Intelligent Reflecting Surfaces in Wireless Communication Systems

Zur Erlangung des akademischen Grades eines

DOKTORS DER INGENIEURWISSENSCHAFTEN
(Dr.-Ing.)

von der KIT-Fakultät für
Elektrotechnik und Informationstechnik
des Karlsruher Instituts für Technologie (KIT)

angenommene

DISSERTATION

von

M.Sc. Yueheng Li
geb. in Jinan, China

Tag der mündlichen Prüfung: 07.03.2023

Hauptreferent: Prof. Dr.-Ing. Thomas Zwick
Korreferent: Prof. Dr. Xiang Wan

Abstract

Accompanied with the development of the wireless communication technologies, the high data traffic is more necessary for civil and industrial applications than ever before. As one of the solutions, signal propagations at higher carrier frequencies are desired to utilize wider unlicensed bandwidth. However, the free space path loss (FSPL) becomes more significant for signal propagation at higher frequencies. As a solution, the concept of an intelligent reflective surface (IRS) has attracted considerable attention recently. By controlling the resonance behaviour of its massive number of micro-component-based unit cells, an IRS reflects the electromagnetic wave from a feeding antenna with electronically controllable beamforming. On the one hand, the promising beamforming targets the desired directions for the concentrated signal power against FSPL. On the other hand, the micro-component-based unit cells use PIN diodes and varactors as traditional solutions, guaranteeing proper cost and power consumption. In the fields of antenna design and communication theory, IRS has accomplished fruitful results. However, the lack of experimental studies restricts the IRS's ability to be utilized in actual situations. This fact motivates the dissertation's investigation of the IRS's system-level performance. The primary objectives are identifying the problems, finding solutions, and proving the feasibility of IRS-based wireless communication systems. According to earlier studies, the IRS can act as a novel alternative antenna array or a signal reflector for channel assistance. To be comprehensive, both application types are investigated. In order to realize this goal, a Ka-band IRS designed by the Southeast University (SEU) from China is implemented for wireless communication system demonstrations operating at 28 GHz following the 3GPP n257 band standard. First, simulation and measurement results are applied to illustrate the IRS beamforming accuracy and robustness. An IRS-based testbed is presented that successfully combines the IRS control chain and signal processing. The IRS is then combined with various modern wireless communication scenarios and technologies, such as hybrid MIMO beamforming, division multiple access, mobile user tracking, etc. The IRS has produced excellent results, proving its

possibility as a wireless communication concept with significant future potential. As the main contribution, the dissertation creates new state-of-the-art and formulates a solid milestone for the IRS research field.

Acknowledgment

I would like to thank Prof. Dr.-Ing. Dr. h.c. Thomas Zwick from the Karlsruhe Institute of Technology for supervising this work while allowing me to be independent and encouraged to explore my ideas. I appreciate Prof. Dr. Xiang Wan from Southeast University for the providing of the implemented IRS, which formulated the fundamentals of this dissertation. I would like to thank Prof. Dr. Tie Jun Cui for reviewing and offering advice on my manuscripts over the past years. The assistance of my colleagues Teng Li, Mohamad Basim Alabd, Lucas Giroto de Oliveira, and Xueyun Long in proofreading the manuscripts and participating in the extensive discussions during my PhD study is deeply appreciated. I also want to thank Maria Jozwika, Frieder Gedenk, and Sven Bettinga for contributing to this dissertation's collaborative outcomes. In general, it is a pleasure to thank all of the IHE colleagues for the encouraging and welcoming environment throughout the entire time. I want to thank Dr. Jerzy Kowalewski and Dr. Joerg Eisenbeis, particularly for the in-depth discussions that helped me choose my research area. IHE technical staff members Andreas Lipp, Ronald Vester, Andreas Gallego, and Mirko Nonnenmacher deserve special recognition for their tireless efforts in implementing my time-consuming requests. I also want to thank Simone Gorre, Marion Jentzsch, and Angela Ziemba for handling my personal affairs, business trips, and project coordination. My parents and my cousin deserve special thanks for supporting me wholeheartedly since I was born. Above all, Xueling Yue has my sincere gratitude for providing me with daily inspiration.

Content

Acronym and Symbols

Acronym

IHE	Institute of Radio Frequency Engineering and Electronics
KIT	Karlsruhe Institute of Technology
MIMO	Multiple-input multiple-output
SISO	Single-input single-output
SIMO	Single-input multiple-output
MISO	Multiple-input single-output
mmw	millimeter wave
BS	Base station
UPA	Uniform planar array
3D	Three-dimensional
2D	Two-dimensional
dB	Decibels
UE	User equipment
IRS	Intelligent reflecting surface
OFDM	Rrthogonal frequency division multiplexing
TDMA	Time division multiple access

FDMA	Frequency division multiple access
CDMA	Code division multiple access
HPBW	Half power beam width
EM	Electromagnetic
Tx	Transmitter
Rx	Receiver
FSPL	Free space path loss
ULA	Uniform linear array
UPA	Uniform planar array
BB	Baseband
DAC	Digital-to-analog converter
ADC	Analog-to-digital converter
DC	Direct current
CSI	Channel state information
MRC	Maximum ratio combination
SNR	Signal-to-noise ratio
SINR	Signal-to-interference-and-noise ratio
1G	The first generation
2G	The second generation
3G	The third generation
4G	The fourth generation
LTE	Long-term evoluation

5G	The fifth generation
6G	The sixth generation
ASK	Amplitude shift keying
FSK	Frequency shift keying
PSK	Phase shift keying
BPSK	Binary phase shift keying
QPSK	Quadrature phase shift keying
QAM	Quadrature amplitude modulation
Q	Quadrature
I	In-phase
MER	Modulation error ratio
LS	Least square
ZF	Zero forcing
MMSE	Minimum mean square error
SIC	Successive interference cancellation
SVD	Singular value decomposition
ICI	Inter carrier interference
ISI	Inter symbol interference
CFR	Channel frequency response
CIR	Channel impulse response
IFT	Inverse Fourier transform
CP	Cyclic prefix

FT	Fourier transform
RLC	Resistor-inductor-capacitor
GPIO	General purpose input and output
DoD	Direction of departure
DoA	Direction of arrival
EIRP	Effective Isotropic Radiated Power
FCC	Federal Communication Commission
RF	Radio frequency
IF	Intermediate frequency
LO	Local oscillator
SDR	Software defined radio
PPS	Pulse-per-second
SPI	Serial peripheral interface
USRP	Universal software radio peripheral
RFSoC	Radio frequency system-on-chip
PC	Personal computer
CPU	Central processing unit
UHD	USRP hardware driver
API	Application programming interface
IP	Internet protocal
USB	Universal serial bus
SCLK	Serial clock

MOSI	Master out slave in
MISO	Master in slave out
CS	Chip select
LoS	Line of sight
WiFi	Wireless fidelity
SQI	Signal quality indicator
RMS	Root mean square
GUI	Graphic user inferface
ASP	Angular speed prediction
AC	Angle correction
NP	Non prediction
DFT	Descrete Fourier transform
IDFT	Inverse descrete Fourier transform
ZP	Zero-padding

Constants

π	3.14159 . . .

Symbols and Variables

Small Letters

r	Distance of the space surrounding an antenna
x	x-axis of the 3D antenna coordinate
y	y-axis of the antenna coordinatea
z	z-axis of antenna coordinate
d	Antenna spacing for an uniform array
e	exponential
m	UPA unit cell index in x axis
n	UPA unit cell index in y axis
a	Flexible variable in general equations
b	Flexible variable in general equations
p	Flexible variable in general equations
k	Number of bits in digital modulation
t	Time
f	Frequency
v	UE movement speed

Capital Letters

D	Largest dimension of an antenna/antenna array
G	Antenna gain
A	Antenna aperture
C	Channel capacity
B	Bandwidth
M	Number of UPA unit cells in x axis

N	Number of UPA unit cells in y axis
N	Antenna aperture
T	Time step between two samples in time domain
S	Total number of sector in hierachical codebook channel estimation
P	Flexible variable in general equations

Greek Symbols

θ	Tilt angle in the 3D antenna coordinate system
ϕ	Rotation angle in the 3D antenna coordinate system
λ	Wavelength
κ	$\frac{2\pi}{\lambda}$
α	Amplitude at the antenna unit
φ	Phase at the antenna unit
Λ	Eigenvalue matrix
ε	Dielectric constant
Σ	Eigenvalue matrix

Mathematical Symbols

$D(\theta, \phi)$	Directivity of an antenna in the direction of θ and ϕ
$E(\theta, \phi)$	Electric field of an antenna in the direction of θ and ϕ
$G(\theta, \phi)$	Gain of an antenna in the direction of θ and ϕ
D_{max}	Maximum directivity of an antenna
E_{max}	Maximum electric field of an antenna

G_{max}	Maximum gain of an antenna
$F(\theta, \phi)$	Array factor of an UPA
e_r	Antenna radiation efficiency
e_a	Aperture efficiency
P_t	Transmit power
P_r	Receive power
G_t	Transmit antenna gain
G_r	Receive antenna gain
d_x	Uniform antenna spacing in x axis
d_y	Uniform antenna spacing in y axis
S_a	Amplitude excitation of the entire antenna array
m	Index of antenna unit along x axis
n	Index of antenna unit along y axis
β_x	Progressive phase of antenna unit in x axis
β_y	Progressive phase of antenna unit in y axis
θ'	Beamforming direction of any antenna array in θ axis
ϕ'	Beamforming direction of any antenna array in ϕ axis
$\boldsymbol{s}_{Rx}$	Received/recovered symbols
$\boldsymbol{F}_{Rx}$	Receiver beamforming matrix
$\boldsymbol{H}$	Channel matrix
$\boldsymbol{F}_{Tx}$	Transmitter beamforming matrix
$\boldsymbol{s}_{Tx}$	Transmitted symbols
$\boldsymbol{w}$	Additive noise
ς_i	The ith eigenvalue
N_s	Number of data streams
M_r	Number of Rx antennas
N_t	Number of Tx antennas
F_{Tx,n_t}	Beamforming coefficient at the n_tth transmit antenna
F_{Rx,m_t}	Beamforming coefficient at the m_rth receive antenna
φ_p	Phase of a phased array unit

d'	Effective antenna spacing
$S11$	Reflection coefficient
$\varphi + d(m,n)$	Additional phase distance for a reflect array unit
$S12$	Transmission coefficient
$\boldsymbol{x}_{Tx}$	Trasnmitted signal after digital signal processing
M_d	The number of receiver digital chains
N_d	The number of transmitter digital chains
$\boldsymbol{H}_d$	Effective digital channel matrix
G_d	Maximum MIMO antenna gain
$(.)^H$	the Hermitian matrix of an argument
P_n	Noise power
$\boldsymbol{I}_a$	Identity maitrx with rank a
σ^2	Noise variance
γ_r	Instantaneous SNR for maximum ratio combinatio at Rx
γ_{m_r}	SNR of each Rx chain for maximum ratio combination
Γ_r	Average SNR of all the Rx chains
$G_{div,r}$	Diversity gain at Rx
γ_t	Instantaneous SNR for maximum ratio combination at Tx
Γ_t	Average signal to noise ratio of all the Tx chains
$G_{div,t}$	Diversity gain at Tx
C_{MIMO}	MIMO channel capacity
E_s	Power of Tx symbols
λ_i	Eigenvlues of a matrix at the ith diagonal element
r_k	Rank of a MIMO channel matrix
b_e	The number of error bits
b_t	The number of total bits
M_{mod}	Number of symbols mapped by the digital modulation
N_m	Total number of received symbols
dI_j	Error distance of a received symbol in in-phase axis
dQ_j	Error distance of a received symbol in quadrature axis

I_j	Position of a reference symbol in in-phase axis
Q_j	Position of a referencesymbol in quadrature axis
$\widetilde{H}$	Estimated channel coefficient
s_{opt_a}	The ath optimum signal at Rx
$g(t)$	Impulse response
$G(f)$	Frequency reponse
$G_{RC}(f)$	Frequency reponse of raise cosine filter
N_c	Total number of subcarriers
f_a	Finite discrete function with index a
C_{cross}	Cross correlation
$\tan\delta$	Loss tangent
R_b	Equivalent resistance under the constraint of b
L_b	Equivalent inductance under the constraint of b
C_b	Equivalent capacitance under the constraint of b
r_1	Illumination distance of the IRS
r_2	Propagation distance of the IRS
G_n	IRS gain with nearfield illumination
G_u	IRS unit cell gain
A_u	IRS unit cell aperture
$E^t_{m,n}(\theta_i, \phi_i)$	Feeding antenna electronic field contribution to IRS unit cell
$E_{m,n}(\theta_i, \phi_i)$	IRS unit cell electronic field contribution
$r'_{m,n}$	Neafield illumination distance to IRS unit cell
η_f	Aperture efficiency for IRS farfield illumination
η_s	Spillover efficiency for IRS nearfield illumination
η_i	Illumination efficiency for IRS nearfield illumination
η_a	Aperture efficiency for IRS nearfield illumination
G_i	Input gain for IRS farfield illumination
G_o	Output gain for IRS farfield illumination
G_f	IRS gain with nearfield illumination
$E(\theta_i, \phi_i)$	IRS electronic field contribution based on incidence angle

$E(\theta', \phi')$	IRS electronic field contribution based on beamforming angle
φ_q	Quantized phase distribution of IRS
φ_e	Quantization error of IRS
θ'_{min}	Minimum IRS beamforming angle
θ'_{max}	maximum IRS beamforming angle
ξ'	Reference wave for IRS single beamforming
ξ''	Reference wave for IRS double beamforming
θ''	IRS beamforming direction for the second beam in θ axis
ϕ''	IRS beamforming direction for the second beam in ϕ axis
θ'_{op}	Optimum IRS beamforming direction
$Q(\theta')$	Quality factor for IRS channel estimation
θ_s	Starting angle of channel estimation area
θ_e	Ending angle of channel estimation area
$P_r(\theta_r, \theta')$	Rx power with beamforming direction to θ' with UE at θ_r
$\boldsymbol{P}_r(\theta_r, \theta')$	Rx power set with beamforming directions to Θ'
σ_t	Threshold for adaptive IRS tracking
P_{Bf}	Reference power with the optimum beamforming direction
θ'_{Bf}	Detected beamforming direction
Θ'	Exhaustive search angle set
$O\{\}$	Complexity indicator
T_{tr}	Training duration
c_f	IRS tracking full scan counter
c_r	IRS tracking rescan counter
t_f	Full scan training time
c_r	Rescan training time
f_s	Time slot of exhaustive search algorithm
N_a	Number of samples for the tracking duration
P_a	Average power of the tracking duration
A_a	Average angle mismatch of the tracking duration
$\theta'_l[]$	Beamforming history list for predictive IRS tracking

T	Time history list for predictive IRS tracking
θ'_d	Beamforming mismatch
θ'_{pr}	Predicted beamforming direction
e	Error for the UE position detection
P_{max}	Local maximum detection for the AC predictive tracking
v_a	Angular speed in predictive tracking
N_I	The number of IRS unit cells
$\mathbf{\Phi}$	Beamforming vectors in IRS MIMO hybrid beamforming
$\bar{\cdot}$	Coefficients derived from averaging
$h_{m_r}^{n_c}$	Channel coefficient on m_rth Rx antenna at n_cth subcarrier
n_c	Subcarrier index
$\boldsymbol{s}^{tr}$	Training symbols
$\boldsymbol{G}_{n_t}$	Generation matrix for the n_t^{th} Tx antenna
$\boldsymbol{F}_{opt}$	Optimum beamforming matrix
$\mathbb{H}$	CIR derived from IDFT of CFR
$\hat{\cdot}$	Coefficients derived from estimation
i_c	Interpolation index

1 Introduction

1.1 Motivation

Since the birth of the first generation (1G) in 1980, mobile communication generations have progressed fast due to the expansion of modern wireless communication technology. As a fresh technology, the 1G network faced reliability and security issues. Consequently, it was superseded in 1991 by the second generation (2G). 2G was dominated by digital signal processing, which improved security and capacity. For 2G, mobile users could send text messages and emails. However, the connection quality remained insufficiently steady, resulting in the third generation (3G). 3G was much speedier than 2G and supported a greater data throughput. For the first time, mobile phones might be used for video calls, file sharing, Internet access, etc. Since then, mobile phones have evolved from telephones to social networking centers. After it, mobile communications had a period of rapid development. By incorporating the fourth generation (4G) standard into mobile phones manufactured in 2013, connection latency, video quality, and loading speed were substantially enhanced [gen]. With the aid of long-term evolution (LTE), the concepts of the cellular network and multiple-input multiple-output (MIMO) technology enabled the transmission of data in greater quantities than ever before, a trend still prevalent in mobile connections today.

The fifth generation (5G) and the sixth generation (6G) are being developed. 5G focuses on applying in industries or merging with other contemporary concepts such as the Internet of Things, smart cities, and military applications. Consequently, more data traffic is necessary. Signal propagation is increased to a higher carrier frequency as a solution. More unlicensed bands and broader bandwidths may be attained at higher frequencies for greater data throughput. In [5Gb], the 5G bands are listed in detail according to worldwide regions. It can be noted that there are several bands between 24 to 30 GHz, and even beyond 30 GHz. These frequencies are called millimeter wave (mmw) since

their wavelengths are close to one millimeter. Nonetheless, signal propagations at higher carrier frequencies are hindered by increased free space path loss (FSPL), which restricts the wireless propagation distance and, therefore, the coverage area. In order to ensure the received power level or signal-to-noise ratio (SNR), extra solutions are necessary. The first approach is to add more antenna units. Accumulating the antenna gain in the desired direction produces a narrower antenna pattern with a larger gain, leading to the beamforming idea from [CZO87]. The second alternative is to enhance the density of cellular networks to decrease the propagation distance, increasing the number of base stations (BSs) in the desired signal coverage region. Both of the approaches above need an expansion of the number of devices, resulting in a rise in cost and energy consumption, which serves as a major barrier to 5G civil use. As a mature technology, LTE already provides a sufficient quantity of data volume and speed for daily life at an affordable price. Therefore, users are less likely to pay a premium for a technology whose advantages are not obvious. This prompted researchers to explore the potential for cost reduction in wireless communication systems.

The first major branch is concerned with system architecture. MIMO technology has dominated digital signal processing since the beginning of the 21st century, according to [GSS+03]. A MIMO system achieves spatial diversity gain by duplicating the same data stream across multiple antenna units, each connected to a digital chain, as an SNR enhancement. Additionally, a MIMO system may increase the channel capacity by delivering multiple data streams through multiple antennas, resulting in spatial multiplexing. However, when the carrier frequency rises, it becomes difficult to maintain full digital beamforming with the MIMO system due to the increased number of antenna units and analog-to-digital converters (ADCs)/digital-to-analog converters (DACs), which significantly increase the cost and power consumption. Analog beamforming, using a phased array as the standard approach, is a different beamforming design. The data stream is split/combined from the multiple antenna components. Then, by altering the phase at the antenna units, the signals are added together in the appropriate beamforming direction. With analog beamforming, signal processing is performed in analog circuits at a lower cost, but only a single data stream can be sent at one moment, which does not meet the requirements of modern wireless communication traffic demands. As a solution, digital and analog beamforming are integrated to create the innovative concept of hybrid beamforming [MRH+17]. Hybrid beamforming may be seen as a compromise

between the two pure beamforming structures, preserving both benefits. In recent years, there has been much research on hybrid beamforming. The primary focuses are channel estimation algorithms and beamforming strategies, which attempt to achieve system performance as close to optimal digital beamforming as possible with lower cost and power consumption [AEALH14].

The second main branch is concerned with antenna design. Typically, a phased array is used as the standard solution for the hybrid beamforming architecture described above. However, a phased array has many phase shifters, which may increase the cost of the system. As a solution, a new antenna array design is referred to as an intelligent reflecting surface (IRS), a programmable metasurface, or a reconfigurable intelligent surface in certain publications. An IRS is a collection of antennas that reflect the electromagnetic (EM) wave from the feeding antenna in the desired direction. It provides electrically steerable beamforming by controlling the micro-component-based unit cells, such as PIN diodes, varactor diodes, and so on. These micro-components have lower cost or power consumption than phase shifters, allowing for the manufacturing of larger arrays at the same or a lower price for arrays with the same gain. IRS was described in [BDRDR+19, CQW+14] and evolved into productive designs at various operating frequencies, different bandwidths, and flexible implementations. Besides an alternative of hybrid beamforming architecture, the IRS also has potentials to replace conventional signal relays using a receive-and-transmit concept. The RIS directly reflects the incidence signal and reflect it to desired destination, without the necessity of any transceiver circuitries. This novel idea effectively enhances the wireless communication channel, which is currently regarded as another attractive research branch.

Both of the subjects above are desired topics that may contribute to the development of wireless communication technologies. Especially if the IRS concept can be utilized in commercial wireless communications, significant cost savings are possible. However, there is still a considerable way to go before accomplishing this goal. From an algorithm perspective, the most prominent articles on system designs concentrated on the theoretical level. Only a few experiments were applied to the presented algorithms to demonstrate their feasibility. Notably, several algorithmic factors are inappropriate for IRS properties, limiting the IRS's capabilities for practical analysis. From the antenna design point of view, numerous varieties of IRSs were constructed without considering their performance in a system, including signal processing. Consequently, it is ques-

tionable if IRSs can be implemented in wireless communication systems and accomplish the functionality required by modern communication scenarios. Motivated by the facts mentioned above, this dissertation focuses on a comprehensive investigation of the utilization of IRS in wireless communication systems.

1.2 State of the art

IRS research has exploded in recent years due to its popularity as a subject of study. The researchers are attempting to build an IRS with various architectures, operating frequencies, bandwidths, and efficiencies. The articles [CQW+14, LC17, LC19, ZCL+18] produced fruitful achievements. By controlling the unit cells' resonance behaviour, the IRS can accomplish beam shaping, and beam steering [YCY+16, WQCC16]. This dissertation is interested in the 3GPP 5G n257 band from 27.5 to 28.35 GHz, within which no suitable IRS was designed.

According to previous studies, IRS applications are split into two groups based on the location of the feeding antenna. The feeding antenna for the first type is positioned in the nearfield of the IRS. Thus, the illumination operates as a point source, with each IRS unit cell having its unique illumination profile. To attain the best antenna gain, the illumination characteristics must be optimized. Therefore, this application type is an alternate design for antenna arrays, as shown in Figure 1.1a. In this case, the IRS and the feeding antenna with the illumination distance r_1 close to it are considered a BS that generates beamforming for the user at a propagation distance r_2. However, the IRS application is more flexible and not solely restricted to antenna array options. As shown in Figure 1.1b, the IRS illumination distance r_1 may also be specified in the farfield area, with D showing the maximum IRS array dimension. In this case, the IRS acts as a signal reflector with beamforming capability to assist the path between the BS and the user, particularly when the line-of-sight (LoS) path is obstructed. State of the art for these two application types is described as follows.

The example of nearfield illumination as an alternative antenna array is discussed first. As stated in [LCZ+16, CQW+14], the nearfield illumination IRS was first referred to as programmable metasurface, which has been demonstrated to be a less expensive alternative to phased arrays. IRS research was mostly focused on antenna design until recent years when new developments were initiated. The

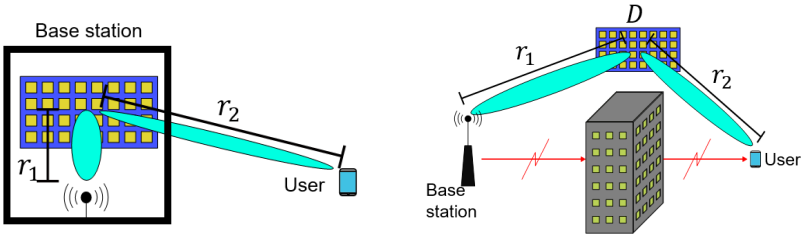

(a) IRS as antenna array.

(b) IRS as signal reflector.

Figure 1.1: IRS application types.

primary proof of concept of the programmable metasurface wireless communication systems has been evaluated in [TSJP16, TLD+19, ZYD+19, ZSW+20, WZC+19, LEK+21, LWE+20, TDC+19]. These investigations are initial studies to exploit IRS as a novel antenna design in SISO wireless communication systems. However, IRS has seldom been incorporated into signal processing methods. As a desirable array of analog beamforming, its combination with MIMO hybrid beamforming is also absent.

According to the history of research, the farfield IRS application as a signal reflector is a relatively fresh concept that was inspired by the near-field IRS application and relay system. It is initially mentioned in 2019 by [BDRDR+19, HZA+19]. Due to the establishment of two wireless communication channels, this concept has been pursued by many theoretical studies. Most of the effort focuses on the theoretical aspects of the technology since it presents new obstacles. Channel estimation techniques, for instance, have been examined in [NKC+19]. For multiuser scenarios, the IRS farfield illumination is integrated with the MIMO system described in [CLCY19]. In [NCCD20], techniques integrating hybrid beamforming and hierarchical codebook channel estimation are developed using several modern wireless communication ideas. However, experimental evaluations are rare at this research stage. An important paper on measurements is [TCC+20], in which a theoretical path loss model for IRS is created and validated with measurements up to 10.5 GHz. At a frequency of 5.8 GHz, [PYT+21] provided measurements for propagation distances up to 500 m. In addition, they implemented data transfer for the SISO scenario, demonstrating considerable promise. In addition to the contributions stated above,

a perfect survey from [DRZD+20] presented a comprehensive review of IRS research. Existing IRS designs, classifications, applications, algorithms, and measurements are summarized and may be referred to for further information.

Except for the successful outcomes discussed before, some practical considerations and limits of IRS-based wireless communication have not been discussed. First, there is no mention of the anticipated IRS size and the corresponding link distance description, particularly for the signal reflector application type. Second, IRS beamforming is achieved by tuning the states of the micro-components on the patch, hence altering the resonance behaviours. In contrast to phase shifters, these components cannot be turned off since the null input voltage is considered one of the phase states. This complicates the implementation of some channel estimate methods based on the sparse array [EMLZ18]. Next, the IRS often has a limited phase resolution for each unit cell, a trade-off for a lower price and a bigger array size. In most visible hybrid beamforming systems, a phased array with high phase resolution is designed, resulting in degraded performance if the respective algorithms are imported directly to IRS. In the end, the medium of the EM wave is illumination through the air, which is less controllable than signal transmission through circuits. This renders IRS beamforming less adaptable and incompatible with all wireless communication designs. These difficulties will be analyzed in this dissertation, and potential solutions will be presented.

1.3 Goal and Organization

This dissertation aims to prove the feasibility and functionality of the low-cost IRS in 28 GHz wireless communication scenarios. Listed below are the chapter-by-chapter objectives and organizational structure.

Chapter 2 introduces the fundamentals of antenna arrays and beamforming. The goal is to discuss the fundamental antenna (array) parameters used throughout the dissertation. Existing beamforming architectures and corresponding channel models are discussed and compared, which will be further adapted to IRS-based models in the following chapter.

The third chapter covers the fundamentals of communication signal processing. The possible methods in each mentioned stage define the general signal

processing flow. The IRS-based wireless communication signals employ these techniques for channel estimation, data recovery, and system evaluation.

Chapter 4 analyzes the IRS's properties. First, the IRS concept and the two types of applications are distinguished. Next, the dissertation implements the technical details of the novel IRS operating at 28 GHz. Then, the theoretical IRS beamforming capability is investigated in terms of various beam-shaping strategies and their robustness against mismatches. Finally, as a benchmark for future IRS evaluations, the challenges and practical considerations of the IRS-based system are addressed in detail.

Chapter 5 introduces the IRS system testbed implemented in this dissertation. A general system block diagram is defined, with brief descriptions of the key functions of each implemented piece of equipment. This chapter describes the coordination and cooperation of devices in IRS-based wireless communication.

Chapter 6 develops IRS beamforming strategies for various wireless communication scenarios. Beginning the measurements is a proof-of-concept SISO model. Then, an exhaustive search and hierarchical codebook algorithms for channel estimation within different IRS systems are investigated. In addition, innovative wireless communication technologies are incorporated into the design. The first IRS-based time division multiple access (TDMA) system is demonstrated and studied, with specifications surpassing LTE beam switching requirements. The 5G beam management strategy is then adapted to produce a real-time IRS tracking system. By implementing the economical IRS, the tracking capability is comparable to conventional MIMO/phased array tracking systems. Furthermore, predictive tracking methods are developed with precise beam alignment to reduce training overhead.

Chapter 7 analysis the first IRS MIMO hybrid beamforming system. A novel channel estimation algorithm is proposed combining analog beam training and interleaved orthogonal frequency division multiplexing (OFDM). The results of channel estimation are utilized for data recovery using various methods. Good results are obtained, which proves the channel estimation's accuracy and the system's feasibility. Different signal processing techniques and MIMO dimensions are measured, compared, and analyzed to provide conclusive evidence. Considerations are paid to both multiuser and singleuser scenarios for completeness.

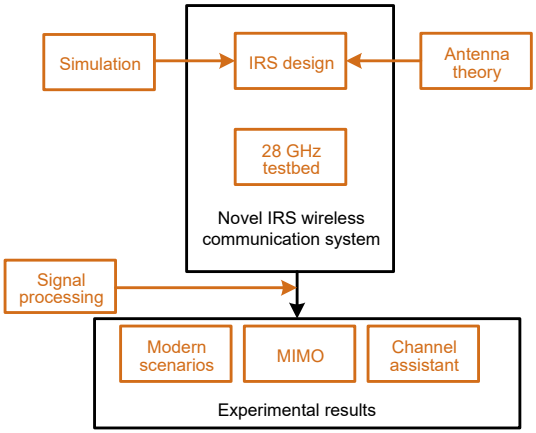

Figure 1.2: A flow graph for the dissertation organization.

Chapter 8 focuses on the studies of IRS farfield illumination applications. Popular IRS signal reflector scenarios, such as IRS-assisted wireless communication, cascaded IRS, and IRS-enhanced MIMO system, are demonstrated and evaluated. The channel model and signal processing algorithms are derived from the IRS nearfield illumination introduced in previous chapters.

Chapter 9 concludes this dissertation by listing the outstanding results and contributions from the previous chapters.

In general, the dissertation organization can be concluded in Figure 1.2. Based on the antenna theory in Chapter 2 and the solid simulation results in Chapter 4, the IRS design is finalized. In combination to the 28 GHz testbed, a novel IRS wireless communication system architecture is demonstrated in Chapter 5. Together with the signal processing methods in Chapter 3, experimental results including modern wireless communication scenarios in Chapter 6, MIMO beamforming in Chapter 7, and channel enhancement in Chapter 8 are realized.

2 Antenna Arrays and Beamforming

This chapter's scope is an introduction to antenna arrays and beamforming fundamentals, which are closely related to the dissertation's IRS topic. The first section presents the fundamentals of antennas in order to formulate general definitions of some crucial parameters. Afterwards, the planar antenna array's geometric and coordination definitions are described in detail. In the end, alternative uniform planar array (UPA) architectures for beamforming generation and properties are introduced, including the general channel model and the specifications for each option.

2.1 Fundamental Parameters of Antennas

This section introduces the fundamental parameters of antennas to clarify the dissertation's general definition of antenna/antenna array. Only the necessary antenna theory parameters are highlighted to accommodate the dissertation's focus rather than all of them. The definition of the antenna pattern, which is essential for the beamforming analysis of IRS, is presented first. Since they represent the performance of an antenna/antenna array, the antenna's directivity and gain are also crucial. Following that, the concept of bandwidth is introduced to aid comprehension of the antenna's operating frequency. Ultimately, the Friis transmission equation is related to the path loss model for IRS, which is essential in later chapters. Professionally, most hints and ideas adhere to the descriptions in [Bal15].

2.1.1 Antenna Pattern

An antenna pattern is a graphical representation of an antenna's radiation properties as a function of space coordinates. The radiation properties are expressed

as a three-dimensional (3D) spatial distribution of radiated energy as a function along a surface with a constant radius, using the coordinate system shown in Figure 2.1. This thesis defines the antenna patch in the xy plane, with the desired power radiating in the $+z$ direction. Furthermore, θ is the tilt angle from the z axis, whereas ϕ is the rotation angle in the xy plane. Coordination can therefore be utilized to denote the associated antenna parameters. In this dissertation, the range of θ is from $-180°$ to $180°$ and the range of ϕ is $-90°$ to $90°$. Combining ellipse shapes illustrates a simplified example of an antenna pattern in Figure 2.1. A power pattern is a graph of the spatial variation of the power density along a constant radius, which is typically plotted on a logarithmic scale in decibels (dB). The field pattern is a plot of the electric field's magnitude as a function of the annular space.

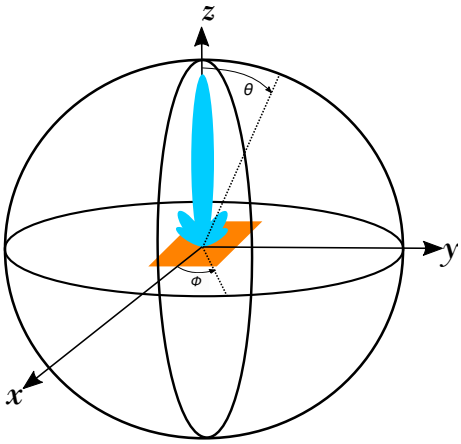

Figure 2.1: 3D coordinate system for antenna analysis.

Antenna Pattern Lobes

An antenna pattern is usually not a simple single shape. Various parts of an antenna pattern are defined as lobes, which can be further classified into main and minor lobes. Figure 2.2 illustrates a two-dimensional (2D) antenna pattern by cutting the xz plane of the coordinate system in Figure 2.1 to simply present antenna pattern lobes. The horizontal coordinate in Figure 2.2 is noted by θ

showing the pattern position, and the vertical coordinate is the magnitude of the antenna pattern based on the specifications.

The main lobe is defined as the lobe containing the direction of maximum radiation. In Figure 2.2 the main lobe is pointing to $\theta = 0°$. Please notice that in some cases, multiple main lobes may exist (e.g., the double main beams generated by the IRS in Figure 4.16). The minor lobe is any lobe except the main lobe. The most important minor lobe is the side lobe, which is usually adjacent to the main lobe and occupies the hemisphere in the direction of the main lobe. Side lobes are normally the largest minor lobes, which should be minimized for antenna design.

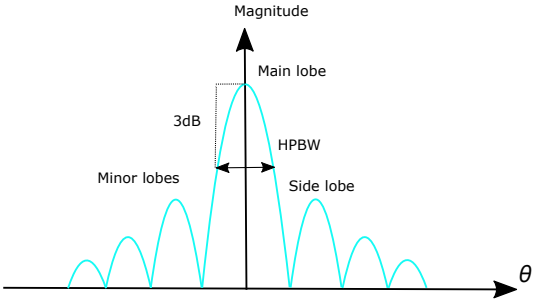

Figure 2.2: 2D plot of the antenna pattern lobes.

In wireless communication systems, signals to different UEs are orthogonalized in domains such as TDMA, frequency DMA (FDMA), and code DMA (CDMA). Therefore, the minor lobes are not introducing critical interferences but decreasing the main power to the desired propagation directions.

Beamwidth

Associated with the antenna pattern is a parameter defined as beamwidth, which indicates the angular separation between the identical points on the opposite side of the pattern maximum. The most widely used beamwidth is half-power beamwidth (HPBW) depicted in Figure 2.2, which is defined in [Bal15] as: In a plane containing the direction of the maximum of a beam, the angle between the two directions in which the radiation intensity is the one-half value of the beam. Therefore, assuming a power pattern is depicted in Figure 2.2, the HPBW is measured at the point where 3 dB is observed to the pattern maximum.

The HPBW is an essential feature for analyzing antenna patterns. It has a trade-off with the main lobe level. Assuming an antenna or antenna array with fixed size, when the main lobe decreases, the HPBW increases and vice versa. In other words, the wider the HPBW, the smaller the pattern maximum.

Field Regions

An antenna designed for wireless communication has to propagate the EM wave to the media, which is commonly through the air. Therefore, analyzing the characteristics of the space surrounding an antenna is critical, which is usually divided into three regions: reactive nearfield, radiating nearfield, and farfield regions.

The reactive nearfield region is defined as the region immediately surrounding the antenna wherein the reactive field predominates. The outer boundary of this region is commonly considered as a distance $r < 0.62\sqrt{D^3/\lambda}$, where D is the largest dimension of the antenna and λ the wavelength. The radiating nearfield region is defined as the region between the reactive nearfield region and farfield region, wherein radiation fields predominate, and the angular field distribution is dependent upon the distance from the antenna. This inter and outer boundary of this region regarding distance is $0.62\sqrt{D^3/\lambda} < r < 2D^2/\lambda$. The farfield region is defined as the region of the field of an antenna where the angular field distribution is essentially independent of the distance from the antenna. The distance is $r > 2D^2/\lambda$ in this case.

The antenna pattern changes in shape with different observation distances. Firstly, The pattern is more spread out and nearly uniform in the reactive nearfield region. Next, the pattern begins to smooth and form lobes in the radiating nearfield region. Finally, the farfield region's pattern is completely formulated with clear main and minor lobes.

In this dissertation, the antenna patterns are default to be in the farfield observation region if further specifications are not mentioned. The reactive and radiating nearfield regions are both regarded as nearfield region for simplicity.

2.1.2 Directivity and Gain

The directivity of an antenna is the ratio of radiation intensity in a given direction from the antenna to the radiation intensity averaged over all directions. The general expression for the directivity and maximum directivity are

$$D(\theta,\phi) = \frac{4\pi\,|E(\theta,\phi)|^2}{\int_{-\pi/2}^{\pi/2}\int_{-\pi}^{\pi}|E(\theta,\phi)|^2\sin\theta d\theta d\phi}. \tag{2.1}$$

$$D_{\max} = \frac{4\pi\,|E_{\max}(\theta,\phi)|^2}{\int_{-\pi/2}^{\pi/2}\int_{-\pi}^{\pi}|E(\theta,\phi)|^2\sin\theta d\theta d\phi}. \tag{2.2}$$

respectively. $E(\theta,\phi)$ is the antenna's electric field, with its square root of the absolute value to be the radiation intensity. Based on the directivity, the gain of an antenna in a given direction is expressed by

$$G(\theta,\phi) = e_r D(\theta,\phi). \tag{2.3}$$

In a similar manner, the maximum value of the gain is

$$G_{\max} = e_r D_{\max}. \tag{2.4}$$

The term e_r denotes the antenna radiation efficiency, which can be determined experimentally. Therefore, the professional definition of antenna gain is the ratio of the intensity, in a given direction θ,ϕ, to the radiation intensity that would be obtained if the power accepted by the antenna were radiated isotropically. In this dissertation, antenna gain G denotes the $G_{\max}$ as default.

The antenna gain is also related to the antenna aperture A expressed as

$$G = e_a A(\frac{4\pi}{\lambda^2}), \tag{2.5}$$

where e_a is the aperture efficiency since there are losses which reduce the antenna gain concerning theoretical value, therefore, one of the general goals for antenna design is the maximization of e_a.

2.1.3 Bandwidth

The bandwidth of an antenna is defined as the range of frequencies within which the antenna's performance, for some characteristics, conforms to a specific standard. These characteristics include beamwidth, gain, etc., which are frequency dependent. However, such characteristics do not necessarily behave in the same manner. In addition, different implementation requirements also lead to different performance analysis standards. Therefore, there is no unique characterization of the bandwidth. The bandwidth of the implemented IRS in this dissertation will be discussed in detail later in Section 4.2 when the specific design is introduced.

2.1.4 Friis Transmission Equation

After understanding the free-air wave propagation behaviours of the antenna, the next setup is to formulate the entire path model considering the existence of transmitter (Tx) and receiver (Rx). As a solution, the Friis transmission equation is suitable for the condition when the Tx and Rx antennas are separated in farfield distance. It defines the relationship between Tx power P_t and Rx power P_r using

$$P_r = P_t G_t G_r (\frac{\lambda}{4\pi r})^2, \tag{2.6}$$

assuming the directions from Tx and Rx antennas are aligned at the maximum directional radiation and reception. The term $(\frac{\lambda}{4\pi r})^2$ is widely known as free space path loss (FSPL), which is an essential parameter while computing the link budget of a wireless communication systems.

2.2 Planar Antenna Array

After clarifying fundamental antenna parameters, this section will introduce an array of multiple antenna units. The unit distribution of an antenna array determines whether it is a uniform or non-uniform array. A uniform array is composed of identical antenna units with the same magnitude and specific progressive phase. In this case, the spacing between antenna units is constant. Due to its simplicity of design, the uniform array architecture is always preferred for IRS. Depending on the geometrical dimension, a uniform array can be further subdivided into a uniform linear array (ULA) and a uniform planar array (UPA). As its name suggests, an IRS is a surface that leads to the UPA structure. Consequently, the mentioned IRS is always a UPA default, which is also the subject of the following section.

2.2.1 Array Factor

To properly describe an antenna array, the 3D coordinate in Figure 2.1 has to be updated. The geometry of the UPA in this dissertation is presented in Figure 2.3. The antenna units are distributed in the xy plane. The antenna spacing along x axis is d_x and along y axis is d_y. For simplicity, assuming $d_x = d_y = d$, the array factor of this UPA is expressed as

$$F(\theta, \phi) = S_a \sum_{m=1}^{M} e^{j(m-1)(\kappa d \sin\theta \cos\phi + \beta_x)} \sum_{n=1}^{N} e^{j(n-1)(\kappa d \sin\theta \sin\phi + \beta_y)}. \quad (2.7)$$

Here, S_a is the amplitude excitation of the entire UPA, m and n are the indexes of array units with M and N the maximum number along each dimension, β_x and β_y are the progressive phases. The phase terms are independent and can be adjusted to generate different main beams in the coordinate. The term κ is a constant defined as $\kappa = \frac{2\pi}{\lambda}$. Firstly, we consider a unique desired main beam generated along $\theta = \theta'$ and $\phi = \phi'$. Therefore the progressive phases become

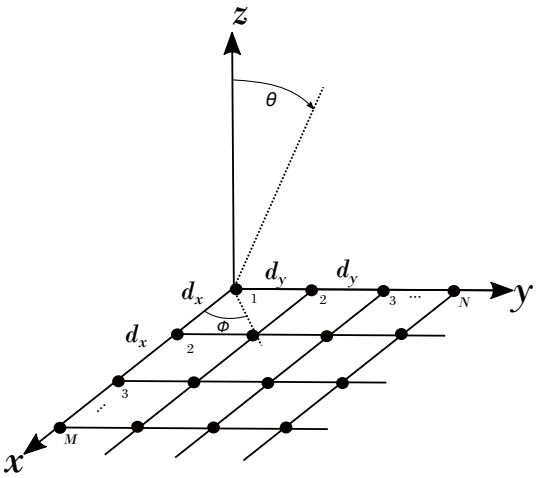

Figure 2.3: UPA 3D coordinate in this dissertation referring to [Bal15].

$$\beta_x = -\kappa d \sin\theta' \cos\phi' \tag{2.8}$$

$$\beta_y = -\kappa d \sin\theta' \sin\phi' . \tag{2.9}$$

They are important terms to formulate the beamforming matrices (mentioned in (2.15) and (2.16)).

2.2.2 Antenna Spacing

As mentioned in Figure 2.2, the antenna pattern contains the main and minor lobes. For an antenna array, there is possibly another undesired lobe known as the grating lobe. For a UPA, the main lobe and grating lobes are located at

$$\kappa d \sin\theta \cos\phi + \beta_x = \pm 2a\pi \qquad a = 0, 1, 2, \ldots \tag{2.10}$$

$$\kappa d \sin\theta \sin\phi + \beta_y = \pm 2b\pi \qquad b = 0, 1, 2, \ldots . \tag{2.11}$$

While the main lobes exist at $a = b = 0$, there are possible grating lobes if the antenna spacing d is greater than λ. In other words, when there are possible values of $\theta \neq \theta'$ and $\phi \neq \phi'$ exist while a and b are non-zero, grating lobes are generated. By simply observing (2.10) or (2.11), it can be concluded that the existence of grating lobe is closely related to the antenna spacing d. As an example, x axis contribution is analyzed by inserting (2.8) into (2.10). For simplicity, we assume $\cos\phi = \cos\phi^{'}$, yielding a single main lobe along ϕ axis. Therefore, (2.10) becomes

$$\frac{d}{\lambda} = \frac{a}{\sin\theta - \sin\theta^{'}}. \tag{2.12}$$

Considering $-90° \leq \theta^{'} \leq 90°$ (assuming the beamforming direction is only on the positive side of z axis in Figure 2.3), the minimum number on the right side of the equal from (2.12) is $\frac{1}{2}$, with $a = 1$ and $\sin\theta = -\sin\theta' = 1$. Thus, if $d < \frac{\lambda}{2}$, the (2.12) can never stand, which means the grating lobes never occurs. Usually, the grating lobe on the xy plane with $|\theta^{'}| = 90°$ is not critical since it is in parallel to the antenna array plane which is in most cases not an interested direction. Therefore, the maximum acceptable antenna spacing is usually said $d = \frac{\lambda}{2}$.

2.3 Beamforming Architectures

After the general UPA definition in the last section, this section aims to the different architectures of UPA with variant features. The main goal of UPA is to realize beamforming and optimize the signal propagation between Tx and Rx by tuning the resonance behaviour of each antenna unit. In this dissertation, the concept of beamforming contains two aspects. Firstly, it represents the power radiation direction of the antenna array pattern derived based on the array factor in (2.7). On the other hand, it represents the signal processing at the Tx and Rx sides, also known as precoding and equalization, respectively. In general, a system including beamforming for both Tx and Rx is expressed as

$$\boldsymbol{s}_{Rx} = \boldsymbol{F}_{Rx}\boldsymbol{H}\boldsymbol{F}_{Tx}\boldsymbol{s}_{Tx} + \boldsymbol{F}_{Rx}\boldsymbol{w}. \tag{2.13}$$

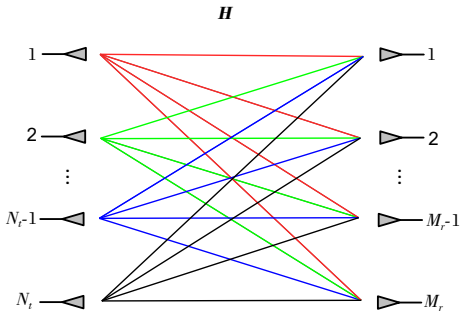

Figure 2.4: Channel model for a multi-antenna system.

For simplicity, each data stream is defined to transmit one symbol at a time/frequency slot, which can be simply extended for the practical signal processing. Therefore in (2.13), $s_{RX} \in \mathbb{C}^{N_s \times 1}$ is the Rx symbols with N_s to be the number of data streams. Similarly, $s_{TX} \in \mathbb{C}^{N_s \times 1}$ represents the Tx signal. $\boldsymbol{F}_{Rx} \in \mathbb{C}^{N_s \times M_r}$ is the beamforming matrix at the Rx side with M_r Rx antennas. Following the same logic, $\boldsymbol{F}_{TX} \in \mathbb{C}^{N_t \times N_s}$ is the beamforming matrix at the Tx side with N_t Tx antennas. The term $\boldsymbol{w} \in \mathbb{C}^{N_s \times 1}$ is the noise vector disturbing the Rx signal. $\boldsymbol{H} \in \mathbb{C}^{M_r \times N_t}$ is the channel matrix formulated by the channel coefficient between each pair of Tx and Rx antennas, which can be expressed by

$$\boldsymbol{H} = \begin{bmatrix} h_{1,1} & h_{1,2} & \dots & h_{1,N_t-1} & h_{1,N_t} \\ h_{2,1} & h_{2,2} & \dots & h_{2,N_t-1} & h_{2,N_t} \\ \vdots & \vdots & \ddots & \vdots & \vdots \\ h_{M_r-1,1} & h_{M_r-1,2} & \cdots & h_{M_r-1,N_t-1} & h_{M_r-1,N_t} \\ h_{M_r,1} & h_{M_r,2} & \cdots & h_{M_r,N_t-1} & h_{M_r,N_t} \end{bmatrix} \tag{2.14}$$

The general channel matrix model can be depicted as Figure 2.4 with complete connections between Tx and Rx antennas. Linear representation is utilized for simple observation, which can effectively be extended/transformed into a planar array. The method to optimize the data propagation between the Tx and Rx regarding $\boldsymbol{H}$ is called beamforming. In the following sections, different architectures of UPA are divided into variant categories based on their beamforming properties, which are defined as beamforming architectures.

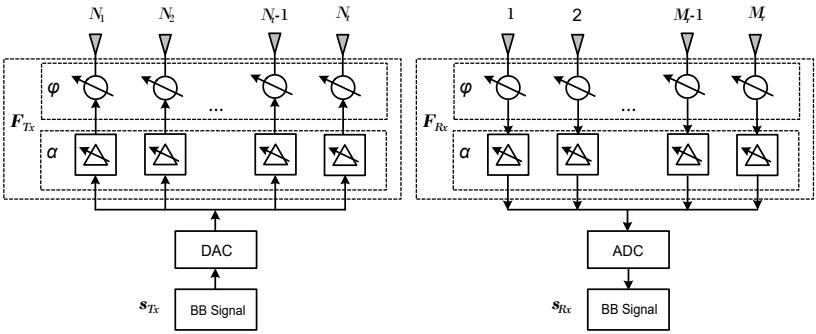

(a) Tx analog beamforming model.

(b) Rx analog beamforming model.

Figure 2.5: General model of analog beamforming.

2.3.1 Analog Beamforming

In analog beamforming, amplitude and phase controls are applied to the analog signals. The general models for analog beamforming are depicted in Figure 2.5a and 2.5b for Tx and Rx, respectively. For simplicity, the frequencies up/down conversions are skipped. Starting with the Tx side, the Tx signal $\boldsymbol{s}_{Tx}$ is generated in baseband (BB) and converted to analog signal using digital-to-analog converter (DAC). For analog beamforming, multiple data streams are not supported, which means $N_s = 1$. Afterwards, the signal is split and distributed to several analog chains. Amplitude and phase controls are available at each analog chain with the factors α and φ. These contributions finally lead to $F_{Tx,n_t} = \alpha_{n_t}^{j\varphi_{n_t}}$ considering antenna index, and formulate the beamforming matrix $\boldsymbol{F}_{Tx}$ altogether. At Rx side, $F_{Rx,m_r} = \alpha_{m_r}^{j\varphi_{m_r}}$ is applied to each Rx analog chain before the signal combination. In the end, with the implementation of an analog-to-digial converter (ADC), the Rx signal $\boldsymbol{s}_{Rx}$ is transferred back to BB.

Analog beamforming can be further divided into the following categories according to the interests of this dissertation.

Phased Array

A phased array is one of the typical analog beamforming architectures. A phased array is an antenna array in which individual radiators may be fed with varying phase shifts. Thus, the typical antenna pattern can be steered. Signal superposition is the fundamental tenet of a phased array. Since all antennas transmit/receive the same signal, if they are adjusted to be progressive phase, the signal will be phase-coherently added to achieve maximum power in the desired direction.

According to Figure 2.3, between the adjacent antenna units, there is uniform antenna spacing d. Such distances lead to different delay profiles for antenna units at different positions. In addition, the effective delay profiles depend on the beamforming direction, as expressed in Figure 2.6. In this example, the x axis is taken from Figure 2.3 for simple representation. To direct the wave from all the M antenna units along the x axis, the effective spacing between antenna units become d' which is the reason for sin and cos terms in the progressive phases (2.8) and (2.9). In the end, for free air signal propagation, the delay is also related to the carrier frequency, which leads to the term κ. Overall, each antenna unit in a UPA is a candidate along the x and y axes. Therefore, the final phase for a phased array unit is expressed as

$$\varphi_p(m, n, \theta', \phi') = -\kappa \cdot (md \sin\theta' \cos\phi' + nd \sin\theta' \sin\phi'), \tag{2.15}$$

For the optimum case, the signal strength at each antenna unit should be uniformly distributed. This is practically hard to be derived upon fabrication due to the hardware imperfection (e.g., fabrication mismatch, variant losses in the circuity), which can be calibrated by α mentioned in Figure 2.5. Usually, the phase adjustments in a phased array architecture are realized by phase shifters, and variable gain amplifiers adjust the amplitudes.

Reflect Array

In [BMK63], the concept of reflect array was proposed as a promising candidate for realizing low-cost, high-gain antennas. This architecture is proposed for numerous applications, including satellite antennas, earth observation, and

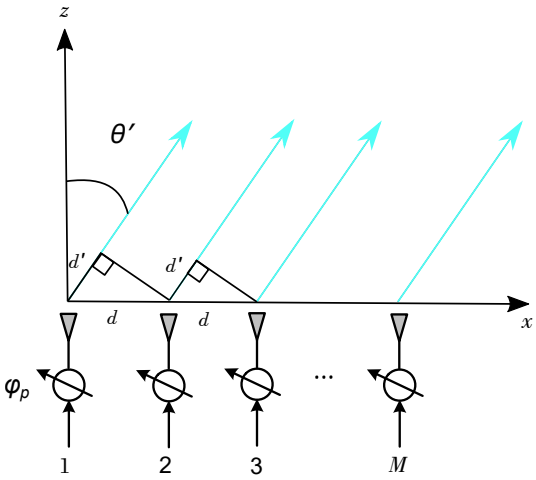

Figure 2.6: Phased array beamforming principle.

telecommunications. Reflect array is motivated by the desire to combine two technologies: reflector antennas and array antennas. In addition, the reflect array is more straightforward to manufacture than conventional reflector antennas, which use a curved surface, such as a parabolic surface, to focus electromagnetic energy.

Beamforming of a reflect array is also accomplished by adjusting the phase delay of each unit cell throughout the UPA. These unit cells' reflection coefficients (S11) dominate performance, as mentioned by their name. Typically, an illumination source feeds EM waves to the UPA through the air and gets reflected with desired beam shaping. For proper beamforming, the phase distribution at each unit cell must be correctly adjusted following

$$\varphi(m,n,\theta',\phi') = -\kappa \cdot (md_x \sin\theta' \cos\phi' + nd_y \sin\theta' \sin\phi') + \varphi(m,n)_d. \quad (2.16)$$

This equation is very similar to the phased array case (2.15), but the term $\varphi(m,n)_d$ is a passive value caused by the variant distance phase introduced by the specific distance between the illumination source and each unit cell. By adjusting the unit cells at a different position, the phases should be changed and hopefully cover the entire 0° to 360° range at the operating frequency. For the amplitude, it is hard to maintain the magnitude of S11 to the same value

over all the phase states. In addition, it is impossible to fabricate components similar to variable gain amplifiers on a reflect array. Furthermore, the amplitude at each unit cell is also related to the incidence and reflection angle. As a result, the amplitude factor α for analogue beamforming is not a fully controllable number. Therefore, instead of making the S11 for all the unit cells uniform, the standard ensures the S11 magnitude is above a required threshold over all the possible phase states and operating frequencies.

Following [Roe09], the unit cell of a reflect array is typically a multilayer structure with a patch on the top layer. The precise number of layers and geometry of the patch depends on the operating frequency and bandwidth designed for various applications. Overall, unit cell designs can be categorized into two primary groups: fixed unit cells and reconfigurable unit cells. Once fabricated, the fixed unit cell has a fixed S11 value. In order to implement the phases of beamforming based on (2.16), each unit cell at a different location must have its geometric specification. [Roe09] provides several methods for achieving this objective by fabricating unit cells with varying sizes, shapes, rotations, and delay lines. On the antenna patch of reconfigurable unit cells, electronically controlled components are soldered. By switching the states of these components, the unit cell's resonance behaviour is altered, resulting in required phase values. For each unit cell in [CERS16], a PIN diode is implemented. This unit cell is expected to achieve a 1-bit phase resolution by alternating between the on and off states. If a higher phase resolution is desired, designs utilizing multiple PIN diodes or varactor diodes are also mentioned in [CERS16]. As a result, more direct current (DC) biases must be buried in the unit cell layers, making design and cost more challenging.

Both fixed and reconfigurable reflect arrays possess advantages and disadvantages. The design for a fixed reflect array is simple and inexpensive. However, beamforming direction is also fixed, resulting in a lack of adaptability. In addition, if beamforming in various directions is required, the array must be mechanically rotated by a motor, resulting in high power consumption. The aforementioned problem is elegantly resolved for a reconfigurable reflect array using DC biases and micro components to control the unit cells. However, the cost is higher than that of a fixed reflect array. Furthermore, optimizing the S11 and bandwidth may be difficult due to the circuitry, resulting in increased design effort.

Transmit Array

A transmit array is another type of analog arrays besides the reflect array. Following the previous section, its beamforming concept and characteristics replicate a reflect array. As the main difference, phase and amplitude are adjusted by refractions rather than by reflections. Therefore, the unit cell designs' transmission coefficient (S12) dominates the array performance. Figure 2.7 depicts the difference between reflect array and transmit array in graphical expression. A transmit array unit cell requires the optimized design of antenna patches for both the top and bottom layers, with one used for receiving and the other for transmitting, to realize the goal of a proper S12. In addition, the wave propagation between the patches must be considered. According to [RCS+10], substrate layers must be chosen carefully to ensure sufficient power transmission as a first option. However, this architecture is predominantly implemented for fixed unit cell designs. When reconfigurable features are desired, DC biases must be woven through the array, and a ground layer is required. This metal ground layer would introduce a high level of reflection, significantly reducing S12. The authors of [DPCD+16] proposed an architecture to realize wave transmission by connecting the receive and transmit patches using a via as a solution. This via is drilled through the ground layer, thereby enhancing transmission.

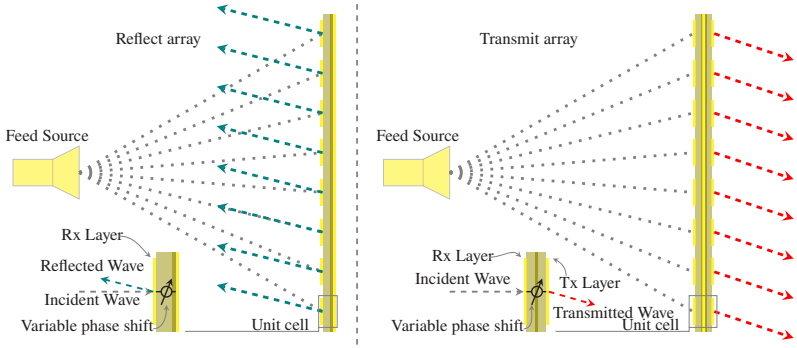

Figure 2.7: Reflect array and transmit array.

Analog Beamforming Comparisons

This section will describe and compare the characteristics of each analog beamforming option. This dissertation focuses on reconfigurable types for reflect and transmit arrays because they enable the desired wireless communication functionalities.

The phased array requires the most circuitry, including DC biases for the phase shifters and analog transmission circuits. Due to the availability of variable gain amplifiers, a phased array does not require many antenna units for adequate power propagation. However, power amplifiers may increase power consumption. In addition, the phase shifters have variable bit resolutions, resulting in beamforming with minimal quantization error. The analog feeding circuits for the reflect and transmit array are replaced by EM wave illumination in the air, which avoids the insertion loss of feeding network, especially for millimeter waves. Due to the limited size of the unit cell, however, the number of micro components that can be soldered on the unit cell is limited, thereby reducing the phase resolution and increasing the quantization error. In addition, the DC biases crossing under the antenna array and the micro-component packages must be considered when optimizing the S parameters. Furthermore, in the absence of power amplification, the reflect/transmit array typically requires a larger size to achieve the same performance as a phased array. Due to the use of inexpensive microcomponents with low power consumption, it is generally believed that reflect/transmit array designs can reduce the system's cost. Inspired by the different beamforming generation principles, reflect array and transmit array also have their features. Reflect arrays are typically simpler to design and fabricate because only one reflectional patch is required. In contrast, a transmit array typically requires a higher number of layers to achieve a comparable bandwidth to a reflect array [DPCD+16]. Unfortunately, the additional layers will decrease the S12 value. Consequently, a transmit array has a higher design complexity and fabrication cost. However, the illumination source of a transmit array is located on the opposite side of the desired beamforming plane, as depicted in Figure 2.7. This eliminates the blind spots in beamforming that a reflect array always experiences.

In conclusion, various analog beamforming architectures have advantages and disadvantages that must be considered based on the system and scenario specifications.

2.3.2 Digital Beamforming

Digital beamforming is another technique for achieving desired signal propagation. Using Rx as an example, Figure 2.8 depicts the general model of digital beamforming. Pure digital beamforming systems necessitate no signal processing in the analog domain, therefore, the number of antennas equals to the number of digital chains with $M_d = M_r$. Instead, signal processing occurs following the ADC for Rx and prior to the DAC for Tx. Digital beamforming achieves the best system performance because the signal processing in BB is not constrained by discrete phase resolution and amplitude levels. Compared to the analog beamforming, the digital beamforming Rx can support the recovery of multiple data streams instead of the single stream in Figure 2.5. This property also leads to the possibility to transmit multiple data streams simultaneously instead of the necessity of time division technologies for the analog beamforming. These is the reason why MIMO architecture (see next section) dominates the modern wireless communication development.

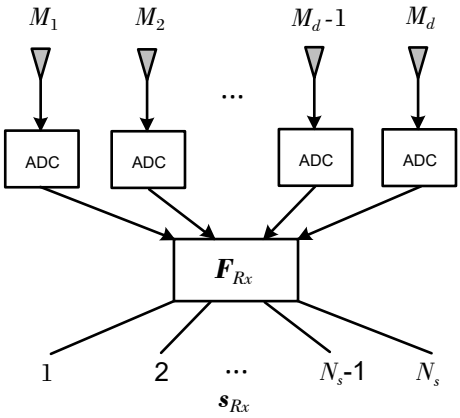

Figure 2.8: Digital Beamforming architecture using Rx as an example.

MIMO Architecture

MIMO architecture is the key technology of digital beamforming. As a popular concept since the beginning of the 21st century, there are different definitions and understanding regarding MIMO architecture [PS01]. In this dissertation,

MIMO is defined as the transmission of data streams from multiple Tx antennas and the reception by multiple Rx antennas. Following the definition of (2.13), MIMO data propagation follows an equation as

$$\boldsymbol{y} = \boldsymbol{H}_d \boldsymbol{x}_{Tx} + \boldsymbol{w}. \tag{2.17}$$

Here, $\boldsymbol{y} \in \mathbb{C}^{M_d \times 1}$ denotes the Rx signal before the Rx digital beamforming with M_d to be the number of Rx digital chains. Similarly, $\boldsymbol{x}_{Tx} \in \mathbb{C}^{N_d \times 1}$ denotes the Tx signal after the Tx digital beamforming with N_d to be the number of Tx digital chains. The matrix $\boldsymbol{H}_d \in \mathbb{C}^{M_d \times N_d}$ is the effective digital MIMO channel matrix formulated by the coefficients between each pair of digital chains of Tx and Rx. The format and model of MIMO channel matrix is similar to (2.14) and Figure 2.4, with $N_d \geq N_s$, and $M_d \geq N_s$. In other words, the data streams carried by Tx symbols $\boldsymbol{s}_{Tx}$ are firstly digitally distributed to N_d number of digital signal chains. In order to properly carry N_s data streams, the number of digital signal chains has to be at least the same as N_s. The same logic takes place at the Rx side, in order to properly recover all the data streams, the necessary condition $M_d \geq N_s$ stands. For a pure digital beamforming system, the (2.13) can be utilized as an expression, with $\boldsymbol{H}_d = \boldsymbol{H}$, and $\boldsymbol{x}_{Tx} = \boldsymbol{F}_{Tx}\boldsymbol{s}_{Tx}$.

A MIMO system has different architectures. From the dimension point of view, the number of digital chains M_d and N_d are positive integers larger or equal to 1. In this dissertation, the general model for MIMO in (2.17) always stands, with notable names for the following conditions:

- when $N_d = 1$ and $M_d > 1$, this special MIMO system is called single input and multiple output (SIMO) system.
- when $N_d > 1$ and $M_d = 1$, this special MIMO system is called multiple input and single output (MISO) system.
- when $N_d = 1$ and $M_d = 1$, this special MIMO system is called single input and single output (SISO) system.

Besides, MIMO can also be divided into singleuser MIMO and multiuser MIMO as presented in Figure 2.9 using downlink mobile communication as an example. For the singleuser MIMO, all the data streams from the BS are assigned for one user, possibly through different spatial paths. This singleuser gets all the MIMO benefits with flexible data propagation algorithms. In this case,

the multiple output of MIMO denotes the multiple antennas at the single user equipment (UE). For multiuser MIMO, a complete MIMO system is divided into sub-MIMO or MISO systems for different UEs. In this case, it must be noticed that the signals lying at the same band for one UE become interference for the other UEs. As a solution, additional schemes such as TDMA, FDMA, or CDMA are required to establish proper links. Moreover, different UEs can not share channel state information (CSI) for channel equalization, further limiting the system's feasibility.

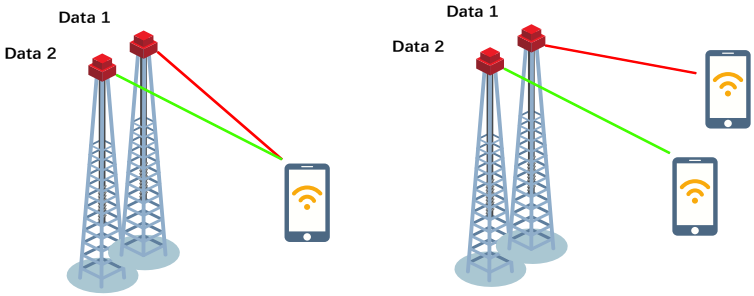

Figure 2.9: Mobile communication scenario in singleuser and multiuser MIMO system from [MIM].

By implementing different signal processing methods, a MIMO system shows variant characteristics, which will be discussed in the following sections.

MIMO Antenna Gain

In a MIMO system, each digital chain is assigned with a DAC/ADC to the BB signal processing as depicted in Figure 2.8. Compared to the analog beamforming architecture as Figure 2.5, a MIMO system can propagate higher power or multiple data streams, known as antenna gain. Its maximum value is related to the number of digital chains expressed as:

$$G_d = N_d M_d. \tag{2.18}$$

MIMO Spatial Diversity

In addition to the simple antenna gain resulting from expanding the number of digital chains, a MIMO system provides additional opportunities for enhancing wireless communication. Multiple receiving or transmitting subsystems combat the fading issue via diversity. There are numerous diversity techniques, such as using different frequencies, coded signals, or time slots. In MIMO systems, spatial diversity is implemented to provide diversity gain. Sending or receiving duplicated data streams in parallel along multiple spatial paths formulated by the different spatial positions of each antenna unit connected to digital signal chains is an example of spatial diversity. Various definitions exist for diversity gain in MIMO. According to [ZAM+18], diversity gain is the reduction of fading caused by the combination of antenna elements that experience different fading. Diversity gain is defined in [div] as the improvement in some resource (typically power) required to meet a specific performance criterion, usually a required bit error ratio (BER). In this dissertation, diversity gain is defined following [Bre03], to increase the system's SNR and thereby increase its reliability. This can be also names as diversity order. MIMO spatial diversity shows different properties at Tx and Rx, which must be discussed separately.

For simplicity, a SIMO system is used as in Figure 2.10 representing the system structure with spatial diversity at Rx. One transmit signal is propagated through the channel $\boldsymbol{H}_d = \boldsymbol{H} \in \mathbb{C}^{1\times M_d}$ and received by M_d receivers assuming pure digital beamforming. For Rx diversity, if we assume there is no additional signal processing at Tx, the data stream or Tx signal is $\boldsymbol{s}_{Tx} = \boldsymbol{x}_{Tx} \in \mathbb{C}^{1\times 1}$, the received signal before any Rx signal processing is $\boldsymbol{y} \in \mathbb{C}^{M_d\times 1}$ should be further combined and then obtains the recovered $\boldsymbol{s}_{Rx} \in \mathbb{C}^{1\times 1}$. By defining the equalization/combining matrix to be $\boldsymbol{F}_{Rx} \in \mathbb{C}^{1\times M_d}$. The output of the combiner can be written as

$$\boldsymbol{s}_{Rx} = \boldsymbol{F}_{Rx}\boldsymbol{y} = \boldsymbol{F}_{Rx}\boldsymbol{H}\boldsymbol{s}_{Tx} + \boldsymbol{F}_{Rx}\boldsymbol{w}. \tag{2.19}$$

There are different combiners for the received signal, including selection combination (SEC), equal gain combination (EGC) and maximum ratio combination (MRC). MRC has the best performance, and its structure is focused on in this dissertation. At Rx, the signals at different digital chains are weighted according to their SNR. The Rx signal with a large SNR has a greater weight, and the other with a lower SNR has a smaller weight. This operation is also introduced as

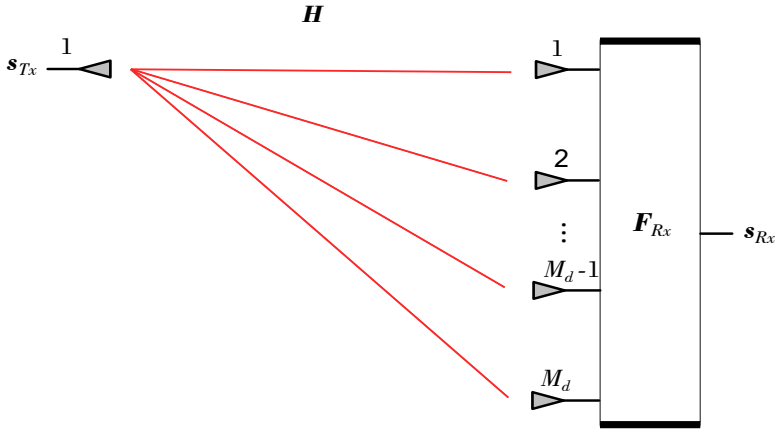

Figure 2.10: Structure of SIMO system with spatial diversity at Rx.

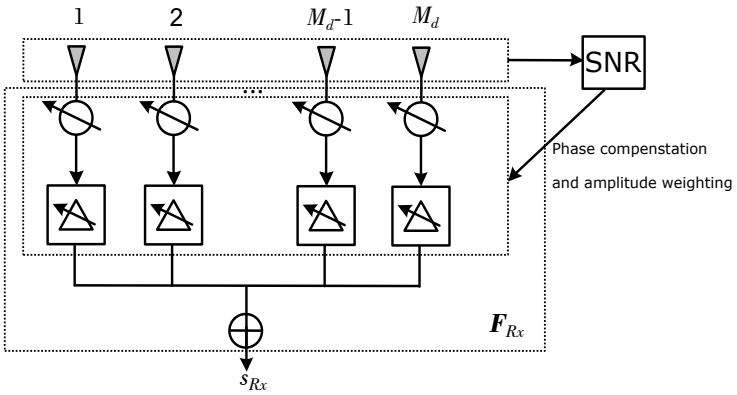

Figure 2.11: Structure for maximal ratio combining (MRC).

an effective matched filtering in some articles. After aligning all the signals in the co-phase, the Rx signal will be multiplied by the corresponding weighting factor. Therefore, the ideal combining matrix based on CSI can be written as:

$$\boldsymbol{F}_{Rx} = \frac{\boldsymbol{H}^H}{||\boldsymbol{H}||} \tag{2.20}$$

in which $(.)^H$ denotes the Hermitian matrix of an argument. Assuming the transmit signal $\boldsymbol{x}_{Tx}$ has unit average power, the instantaneous output SNR is:

$$\gamma_r = \frac{|\boldsymbol{F}_{Rx}\boldsymbol{H}|^2}{\mathbb{E}\{|\boldsymbol{F}_{Rx}\boldsymbol{w}|^2\}} \tag{2.21}$$

The noise power in the denominator of equation (2.21) is given by:

$$\begin{aligned} P_n &= \mathbb{E}\{|\boldsymbol{F}_{Rx}\boldsymbol{w}|^2\} = \mathbb{E}\{|\boldsymbol{F}_{Rx}\boldsymbol{w}\boldsymbol{w}^H\boldsymbol{F}_{Rx}^H|\} = \boldsymbol{F}_{Rx}\mathbb{E}\{\boldsymbol{w}\boldsymbol{w}^H\} \cdot \boldsymbol{F}_{Rx}^H \\ &= \sigma^2\boldsymbol{F}_{Rx}I_{M_d}\boldsymbol{F}_{Rx}{}^H = \sigma^2||\boldsymbol{F}_{Rx}||^2 \end{aligned} \tag{2.22}$$

where $\boldsymbol{I}_{M_d}$ represents identity matrix with rank M_d and σ^2 is the noise variance. Thus, the SNR in (2.21) will be $\gamma_r = \frac{|\boldsymbol{F}_{Rx}\boldsymbol{H}|^2}{\sigma^2||\boldsymbol{F}_{Rx}||^2}$. If the combing matrix is substituted in the SNR:

$$\gamma_r = \frac{|\boldsymbol{H}^H\boldsymbol{H}|^2}{\sigma^2||\boldsymbol{H}^H||^2} = \frac{\boldsymbol{H}^H\boldsymbol{H}}{\sigma^2} = \sum_{m_d=1}^{M_d}\frac{h_{m_d}^2}{\sigma^2} = \sum_{m_d=1}^{M_d}\gamma_{m_d} \tag{2.23}$$

where $m_d \in \{1, 2, ..., M_d\}$ and γ_{m_d} is SNR for each Rx signal. This equation shows that the output SNR is the sum of the SNR at each receiver. The expectation of the instantaneous SNR is $\mathbb{E}\{\gamma_r\} = M_d\Gamma_r$. Γ_r is the average SNR of all the Rx chains. Thus the diversity order $G_{\text{div},r}$ for MRC is:

$$G_{\text{div},r} = \frac{M_d\Gamma_r}{\Gamma_r} = M_d. \tag{2.24}$$

Since the channel with a strong signal contributes more, the weak signal contributes less, and the channel with no signal is completely suppressed. Therefore, MRC is the optimal combiner, capable of achieving the highest system performance. However, this structure requires precise signal phase and amplitude

adjustments, resulting in high complexity. In addition, it is necessary to know each Rx chain's time-varying SNR, which is difficult to measure.

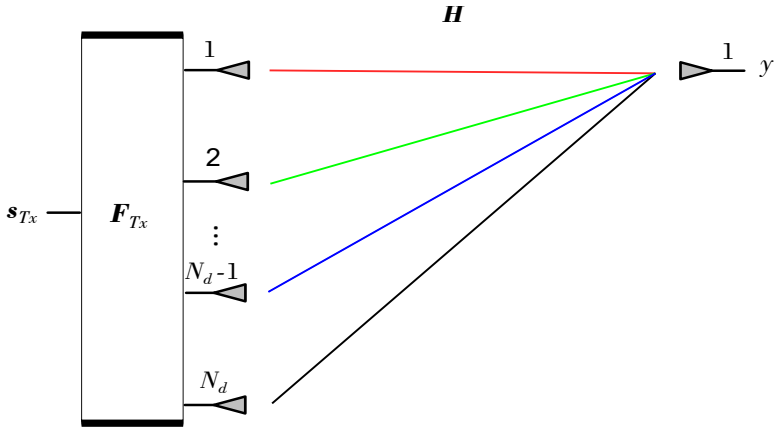

Figure 2.12: Structure of MISO system with spatial diversity at Tx.

Spatial diversity at Tx is realized by transmitting the same data over different digital chains. At Tx side, the knowledge about CSI needs to be discussed as a dominating factor. Starting with the perfect CSI knowledge case, the Tx spatial diversity realization becomes very similar to the Rx case, with the help of a precoding/combiner. As presented in Figure 2.12, the data stream $\boldsymbol{s}_{Tx} \in \mathbb{C}^{1\times 1}$ is sent via N_d digital chains precoded according to the CSI with the matrix $\boldsymbol{F}_{Tx} \in \mathbb{C}^{N_d\times 1}$, then the precoded signal $\boldsymbol{x}_{Tx} \in \mathbb{C}^{N_d\times 1}$ is transmitted and through the channel $\boldsymbol{H} \in \mathbb{C}^{1\times N_d}$. With ideal transmit diversity using CSI at Tx, the precoded matrix will be $\boldsymbol{F}_{Tx} = \frac{\boldsymbol{H}^H}{||\boldsymbol{H}||}$. Thus the received signal $\boldsymbol{y} \in \mathbb{C}^{1\times 1}$ can be formulated as:

$$\boldsymbol{y} = \boldsymbol{H}\boldsymbol{x}_{Tx} + \boldsymbol{w} = \boldsymbol{H}\mathbf{F}_{Tx}\boldsymbol{s}_{Tx} + \boldsymbol{w} = \boldsymbol{H}\frac{\boldsymbol{H}^H}{||\boldsymbol{H}||}\boldsymbol{s}_{Tx} + \boldsymbol{w} = ||\boldsymbol{H}||\boldsymbol{s}_{Tx} + \boldsymbol{w}. \quad (2.25)$$

Without additional signal processing at Rx, $\boldsymbol{y} = \boldsymbol{s}_{Rx}$ stands which recovers the signal directly. To exploit the transmit diversity gain, average SNR γ_t under transmit diversity should also be derived as $\gamma_t = \frac{||\boldsymbol{H}||^2}{\sigma^2}$, where σ^2 is the noise variance. The expectation of instantaneous SNR is $\mathbb{E}\{\gamma_t\} = N_d \cdot \Gamma_t$, where Γ_t

is the average SNR. following the similar logic of diversity order derivation in (2.24), the transmit diversity order can be written as:

$$G_{\mathrm{div},t} = \frac{N_d \cdot \Gamma_t}{\Gamma_t} = N_d. \tag{2.26}$$

For Tx signal transmission without knowledge about CSI, the maximum combination situation to derive $||\boldsymbol{H}||$ from (2.25) does not stand. Instead, at each SISO path from the MISO case, the received signal is

$$\boldsymbol{y} = \frac{\boldsymbol{s}_{Tx}}{\sqrt{N_d}} \sum_{n_d=1}^{N_d} h_{1,n_d}. \tag{2.27}$$

Therefore, the expected average Rx power per assuming unitary transmit power is $\frac{1}{N_d}|\sum_{n_d=1}^{N_d} h_{1,n_d}|^2$, which is rather a new Rayleigh distribution than any diversity gain. As a solution, there exists a method known as space-time coding to realize transmission diversity even without the knowledge of CSI. Since this dissertation is not the main focus, only the concept is raised here, with detailed information in [GSS+03] for readers' interests.

MIMO Spatial Multiplexing

Besides transmitting the same data stream to realize spatial diversity, a MIMO system also realizes spatial multiplexing by transmitting different data streams over different spatial paths simultaneously. This is an important technology to improve the system capacity. An increased data rate can be realized if interference between different signals introduced by the MIMO channel can be eliminated. Assuming pure digital beamforming in Figure 2.13, there are $N_t = N_d$ transmit antennas and $M_r = M_d$ receive antennas. They fomulate a MIMO channel matrix with rank $\min(N_d, M_d)$. In this condition, $N_s = \min(N_d, M_d)$ data streams can be transmitted and recovered for the maximum spatial multiplexing. This ideally leads to a N_s times increase of the spectrum efficiency (bit/s/Hz). Following the general beamforming equation in (2.13), the data stream $\boldsymbol{s}_{Tx}$ is firstly precoded with matrix $\boldsymbol{F}_{Tx}$ which leads to $\boldsymbol{x}_{Tx}$. The signals propagate through the channel matrix $\boldsymbol{H} \in \mathbb{C}^{M_d \times N_d}$. At Rx, the signals $\boldsymbol{y}$ from the MIMO channel $\boldsymbol{H}$ are recovered with the equalization matrix $\boldsymbol{F}_{Rx}$ to the derivation of $\boldsymbol{s}_{Rx}$. There are many methods to realize the signal precoding and

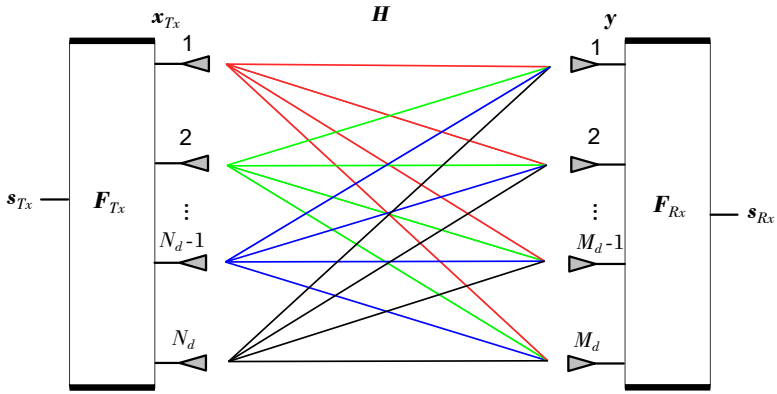

Figure 2.13: Structure of MIMO system with spatial multiplexing.

equalization for MIMO spatial multiplexing. They will be introduced in detail in the Chapter 3.

MIMO Channel Capacity

MIMO technology uses multiple transmit antennas to send signals independently and simultaneously uses multiple antennas at Rx side to receive and restore the original information. Therefore, the data throughput of the system is improved. As known that there is a theoretical boundary for the amount of data that can be passed along a specific channel in the presence of noise which is Shannon's Law:

$$C = B \log_2(1 + \text{SNR}) \tag{2.28}$$

where C is the channel capacity in bits per second, B is the bandwidth in Hertz. The equation shows that the channel capacity is limited by a given bandwidth and the SNR of the signal. For the MIMO system, this equation also stands and is usually written as

$$C_{\text{MIMO}} = B \log_2[\det(I_{M_d} + \frac{E_s}{N_d \sigma^2} \boldsymbol{H}\boldsymbol{H}^H)]. \tag{2.29}$$

Here, E_s denote the power at each Tx symbol and N_d is a weighting for the normalization through the number of Tx digital chains. Using the decomposition rule $\boldsymbol{H}\boldsymbol{H}^H = \boldsymbol{Q}\Sigma\boldsymbol{Q}^H$ with $\boldsymbol{Q}$ to be the unitary matrix satisfying $\boldsymbol{Q}\boldsymbol{Q}^H = \boldsymbol{I}$. Therefore, 2.29 can be transformed to

$$\begin{aligned} C_{\text{MIMO}} &= B\log_2[\det(\boldsymbol{I}_{M_d} + \frac{E_s}{N_d\sigma^2}\boldsymbol{Q}\Sigma\boldsymbol{Q}^H)] \\ &= B\log_2[\det(\boldsymbol{I}_{M_d} + \frac{E_s}{N_d\sigma^2}\Sigma)] \\ &= \sum_{i=1}^{r_k} B\log_2(1 + \frac{E_s}{N_d\sigma^2}\varsigma_i), \end{aligned} \tag{2.30}$$

with ς_i denoting the ith eigenvalues of matrix $\boldsymbol{H}\boldsymbol{H}^H$ and r_k to be the rank of $\boldsymbol{H}$. It can be observed that the MIMO channel capacity highly depends on the eigenvalues of channel matrix $\boldsymbol{H}$.

2.3.3 Hybrid Beamforming

Besides the pure analog and digital beamforming, an architecture that combines both of the technologies above. It is known as hybrid beamforming. In a hybrid beamforming system, the data streams are firstly precoded based on the number of Tx digital chains. Afterwards, the output of these digital chains is connected with analog arrays having larger number of antenna units. The general model of hybrid beamforming is depicted in Figure 2.14. In this condition, the general beamforming equation from (2.13) still stands with some modifications, which leads to

$$\boldsymbol{s}_{Rx} = \boldsymbol{F}_{Rx,BB}\boldsymbol{F}_{Rx,RF}\boldsymbol{H}\boldsymbol{F}_{Tx,RF}\boldsymbol{F}_{Tx,BB}\boldsymbol{s}_{Tx} + \boldsymbol{F}_{Rx,BB}\boldsymbol{F}_{Rx,RF}\boldsymbol{w}. \tag{2.31}$$

The main different is that the beamforming matrices $\boldsymbol{F}_{Tx}$ and $\boldsymbol{F}_{Rx}$ are combined by the digital beamforming matrices $\boldsymbol{F}_{Tx,BB} \in \mathbb{C}^{N_d\times N_s}$/ $\boldsymbol{F}_{Rx,BB} \in \mathbb{C}^{N_s\times M_d}$ at BB in digital domain and analog beamforming matrix $\boldsymbol{F}_{Tx,RF} \in \mathbb{C}^{N_t\times N_d}$/$\boldsymbol{F}_{Rx,BB} \in \mathbb{C}^{M_d\times M_r}$ in analog domain. After the introduction of all the critical beamforming architectures, a detailed definition of the signal processing

symbols in this dissertation is highlighted by this chance. From the Tx, the N_s symbols/data streams are always started with $\boldsymbol{s}_{Tx}$. After the precoding/digital beamforming at Tx, the Tx signals are presented by $\boldsymbol{x}_{Tx}$ based on the number of digital chains N_d at Tx as mentioned in (2.17). After the analog beamforming at Tx, the signals are transmitted by N_t antennas and received by M_r antennas via the channel matrix $\boldsymbol{H}$ from (2.13). The received signal after the Rx analog beamforming at the input of digital chains is defined as $\boldsymbol{y}$ from 2.19. After the equalization/digital beamforming at Rx based on the number of Rx digital chains M_d, the recovered N_s symbols/data streams $\boldsymbol{s}_{Rx}$. There is another effective digital MIMO channel matrix $\boldsymbol{H}_d$ called effective digital channel matrix as defined in (2.17), which is a combined effect of analog beamforming matrices and the channel matrix. It equals to $\boldsymbol{H}$ if pure digital beamforming is considered.

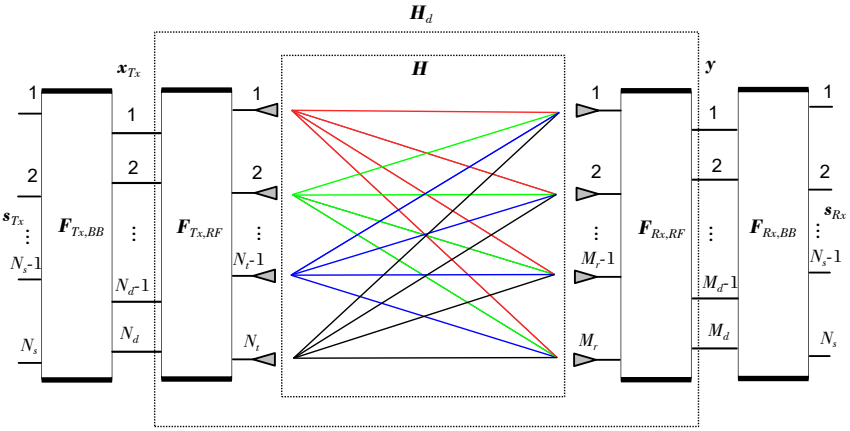

Figure 2.14: System model with hybrid beamforming.

Hybrid Beamforming Architectures

There are different architectures combine digital beamforming and analog beamforming in a hybrid beamforming system. According to [MRH+17], there are two dominating hybrid beamforming architectures: fully connected hybrid beamforming and subarray-based hybrid beamforming. There flow graphs are depicted in Figure 2.15 using the Tx side as an example. For fully connected

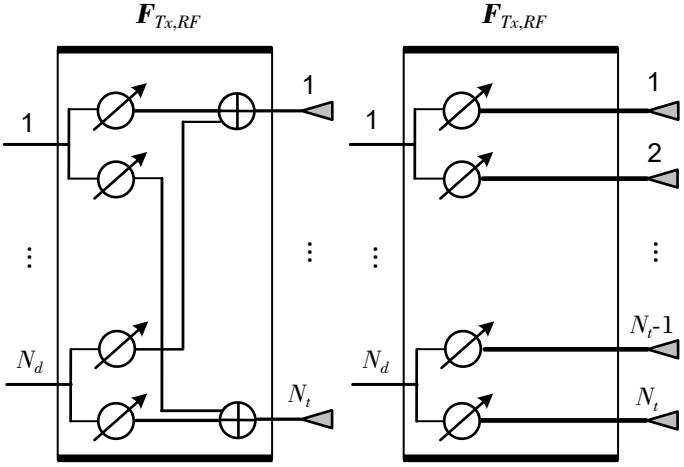

(a) Fully connected hybrid beamforming system.

(b) Subarray based hybrid beamforming system

Figure 2.15: Hybrid beamforming system architectures based on [MRH+17].

architecture in Figure 2.15a, each signal output after the digital beamforming $\boldsymbol{F}_{Tx,BB}$ has access to every antenna unit, which leads to a fully filled analog beamforming matrix $\boldsymbol{F}_{Tx,RF}$. On the other hand, for subarray-based architecture Figure in 2.15b, each antenna is assigned to a specific digital beamforming output signal. In this case, the analog beamforming matrix $\boldsymbol{F}_{Tx,RF}$ has only one non-zero element for each row.

Different hybrid beamforming architectures have different characteristics. In a fully connected architecture, each digital signal chain can access each antenna unit, achieving near-optimal beamforming performance. Compared to pure digital beamforming, analogue circuits' limited amplitude and phase resolution is the only performance detriment. However, this architecture's complex circuitry adds complexity to the design and cost of the system. In contrast, the subarray-based architecture solves this issue by reducing the number of circuitry connections. As a result, each digital chain can only access a limited number of antenna units, resulting in a reduced analog array for each signal. Consequently, beamforming quality is lowered.

2.3.4 Comparison of Beamforming Architectures

All of the aforementioned beamforming architectures have features that can be compared for further observation. Analog beamforming has been widely utilized in the past decade to increase the desired signal strength. Especially, 5G, 6G and future wireless communication systems are operating at a higher frequency with stronger FSPL. In small cell scenarios, an analog array employing massive antenna units to realize beamforming successfully expands the coverage area of a base station. However, because there is only one signal input for an analog array as shown in Figure 2.5, it is insufficient to satisfy the rapid increase of higher data rate, particularly when mobile devices are embedded with advantageous functions such as working, streaming, and gaming. As a solution, the digital beamforming system employing MIMO technology can significantly increase system throughput. However, a pure digital beamforming system requires many digital signal chains. This results in a corresponding rise in DAC/ADC, as shown in Figure 2.8. As a result, a pure digital beamforming MIMO system has a high price and power consumption. Although pure digital beamforming is the ultimate goal of BS due to its superior performance, the manufacturing, device, and power consumption costs make it prohibitively expensive for civil mobile communication companies today. Combining digital and analog beamforming led to the conception of hybrid beamforming as a solution [MRH+17]. With the implementation of hybrid beamforming, sufficient data streams can be carried by digital beamforming and propagated by analog beamforming with decent quality. In other words, the cost of this system is not as high as that of pure digital MIMO beamforming, and it still achieves appropriate signal propagation with an acceptable data rate reduction. As depicted in Figure 2.15, for hybrid beamforming architecture, the subarray-based concept is more desirable because the fully connected version does not offer a significant cost reduction because complex circuitry is still required in this architecture. Recent research has focused on signal processing algorithms for hybrid beamforming architectures. The main goal is to reduce its channel capacity gap to get as close as possible to the optimum digital beamforming performance. [WCLC13] evaluates the algorithmic robustness of hybrid beamforming utilizing a 60 GHz channel model for an indoor environment. In [AEALH14] and [SR15], channel estimation algorithms employing the beam training codebook for various hybrid beamforming architectures have been presented. Using a sparse array, the authors of [EMLZ18] developed hybrid beamforming channel estimation algo-

rithms. In [ZLG+21], channel extrapolation, a relatively new concept, has been analyzed using deep learning. Further algorithms focusing on different modern wireless communication scenarios can be referred to [RWQL17, PGD17]. The feasibility of a 3D hybrid beamforming design for system-level measurements has been evaluated in [JCH+16]. Indoor measurements have been conducted to determine the block and penetration loss in [RPS+18]. Outdoor measurements are also performed in [OOA+15, ZZL+19], whereas the feasibility of mobile communications is discussed in [KLH+16]. The performance degradation caused by the digital chain reduction is minimized due to these studies, which presents a tremendous commercial opportunity for implementing hybrid beamforming technologies.

2.4 Conclusion on this Chapter

This chapter introduces the necessary fundamental parameters of antennas utilized in this dissertation. Notably, 3D geometric coordination is defined as the fundamental environment for antenna analysis in the later chapters. It is further developed to the planar array definition by introducing the beamforming formulation's steering vector and matrix. Then, various existing beamforming architectures are presented and compared. It supports a limited number of data streams but has the lowest complexity for analogue beamforming. Digital beamforming, which is widely employed in MIMO systems, has the potential to realize spatial diversity for SNR or spatial multiplexing for channel capacity improvement. However, MIMO systems that validate digital beamforming suffer from increased circuitry complexity and power consumption, resulting in the hybrid beamforming solution. As a compromise, hybrid beamforming combines digital beamforming and analog beamforming. Its architecture closely resembles IRS-based wireless communication systems, which will be introduced in later chapters. In addition to the beamforming architectures, this dissertation defines the relevant channel models in detail. In general, the channel model is a matrix that depends on the quantity of Tx and Rx chains. The channel matrix size for pure analog and digital beamforming models is determined by the number of antenna units corresponding to the number of digital chains in the digital beamforming model. The channel matrix is essential for calculating the steering matrix/vector in analogue beamforming. In digital beamforming, the channel matrix determines the specifics of digital signal processing, which

will be discussed in Chapter 3. There are two channel matrices in the hybrid beamforming architecture. The first is a channel matrix whose dimensions are determined by the number of antenna units on the analog arrays. The second is referred to as the effective digital channel matrix, an equivalent channel matrix after analog beamforming or, in other words, incorporating the effects of analog beamforming. These are fundamental ideas that should be emphasized throughout the entire dissertation.

3 Communication Signal Processing

This chapter introduces the primary communication signal processing methods, which will be implemented into the IRS systems. They are adapted to the desired system requirements and extended with further novelties. First, a general signal processing following graph is depicted in Figure 3.1, with all the necessary signal processing stages in this dissertation from Tx to Rx included. Starting from the Tx side, the bit sequences are firstly generated and modulated to the Tx symbols/data streams, which is $\boldsymbol{s}_{Tx}$ from (2.13). Afterwards, the data streams in symbol format are precoded, which leads to $\boldsymbol{x}_{Tx}$ from (2.17). At the output of the precoding step, the signals are modulated with the required waveform (singlecarrier modulation or multicarrier modulation), distributed to different N_d digital chains and fed into the DAC. If analog beamforming is considered, it takes place at the output of DAC together with further analog conditioning such as up-conversion and filtering, and the signals are distributed to every Tx antenna unit. Then, the signals are propagated through the wireless channel and captured by the Rx antennas. At the Rx side, analog beamforming (if considered) is firstly operated to transfer the signals to the number of digital chains M_d together with other analog conditioning. Opposite from the Tx side, an ADC is utilized to transform the signal to BB. To properly recover the received signal, timing synchronization is required before all the Rx signal processing. Once the timing offset is eliminated, the waveform demodulator is used as a matched filtering to the Tx waveform, which leads to the derivation of $\boldsymbol{y}$ from (2.17). In this dissertation, the mismatch introduced by the DAC/ADC, matched filtering, and synchronization error are assumed to be minor without giving further attentions in the signal processing. The Rx signal processing contains two possibilities, if training symbols are transmitted, they are utilized to derived the channel coefficients between the Rx and Tx chains which is known as channel estimation. For another option, the Rx signals are further operated with the equalization based on the derived channel coefficients from

channel estimation, as Rx digital beamforming to recover modulated signal $\boldsymbol{s}_{Rx}$ from (2.13). In the end, after the demodulation, the recovered data streams are transferred back to bit format. Detailed methods of each block will be introduced in the following sections by organizing Tx and Rx signal processing together to observe their relationships.

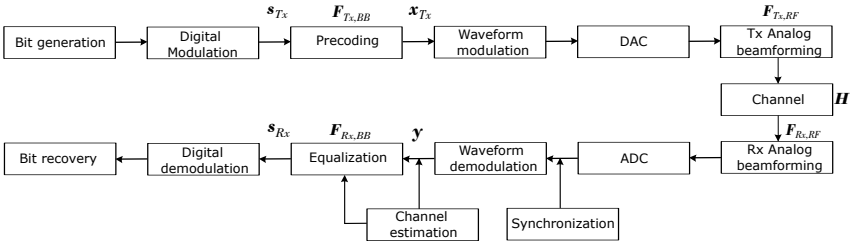

Figure 3.1: The general signal processing chain in this dissertation.

The sections in this chapter are organized based on the corresponded groups in Tx and Rx signal processing. Therefore, the bit generation and recovery are regarded as a pair introduced in Section 3.1. Following the same logic, digital modulation and demodulation are included in Section 3.2, precoding and equalization are presented in Section 3.4, singlecarrier/multicarrier modulation schemes and the corresponding demodulation methods are covered in Section 3.5. The channel estimation and synchronization are individual signal processing blocks introduced individually in the specific sections.

3.1 Binary Sequence Generation and Recovery

Modern wireless communication systems typically involve the transmission of digital data, usually in the form of a binary data stream, i.e. a series of 0s and 1s. In this dissertation, both the training and data bit sequences are generated randomly. Due to the communication system's noise, interference, and other distortions, the recovered bit sequence may have the incorrect values. BER is a general standard for defining system performance. BER is computed by dividing the total number of transmitted bits by the number of Rx bits that have an incorrect decision in comparison to the corresponding bit in the Tx sequence.

$$\mathrm{BER} = \frac{b_e}{b_t}, \tag{3.1}$$

with b_e the number of error bits and b_t the total number of transmitted bits.

3.2 Digital Modulation and Demodulation

With the capability to carry multiple bits on one symbol, digital modulation offers higher information capacity, high data security, faster system availability, and superior communication quality. Therefore, its techniques are more in demand than analog modulation techniques. Depending on the application, there are various digital modulation techniques and combinations thereof.

3.2.1 Digital Modulation Schemes

There exist many digital modulation schemes, for example, amplitude shift keying (ASK), frequency shift keying (FSK), and phase shift keying (PSK). In this dissertation, PSK and ASK are mainly focused on. In general, k bits can be grouped to represent a symbol so that in total, $M_{\mathrm{mod}} = 2^k$ symbols can be mapped correspondingly in modulation. After modulation, symbols can be represented with complex numbers and can be divided into in-phase and quadrature phase components in a constellation diagram.

In PSK, as its name suggests, the phase of the modulated signals are shifted depending on the input. The simplest PSK algorithm is called binary PSK (BPSK), with $k = 1$ and $M_{\mathrm{mod}} = 2$. Since only 1 bit of data is modulated, there are only two required phase states, normally 0 and π. The red symbols depict the constellation diagram in Figure 3.2a for the modulated symbols. BPSK is the most reliable modulation scheme since each symbol's wide detection range (see Section 3.2.2) leads to the minimum BER. However, only 1 bit is modulated in each symbol, which means a minimum data rate. When the specific bandwidth in a communication system is determined, more bits are expected to be transmitted for higher spectrum efficiency. Therefore, another widely used PSK scheme is quadrature PSK (QPSK), with $k = 2$ and $M_{\mathrm{mod}} = 4$. For QPSK, two bits are modulated to one symbol which leads to 4 different combinations

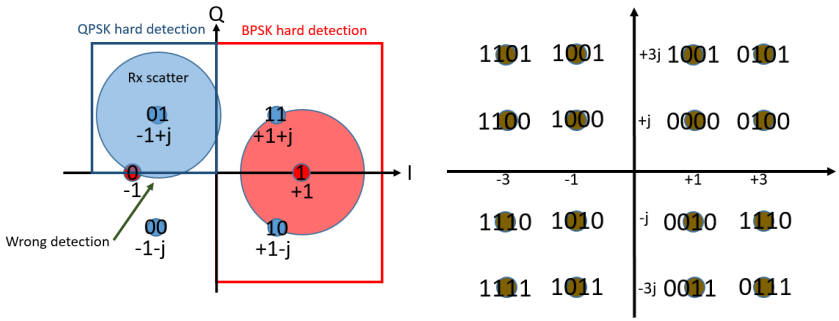

(a) BPSK, QPSK modulation, and hard detection.

(b) 16QAM modulation

Figure 3.2: Digital modulation schemes in the constellation diagram.

11,01,10,00, yielding 4 different phase states, normally $\frac{\pi}{4}$, $\frac{3\pi}{4}$, $-\frac{\pi}{4}$, $-\frac{3\pi}{4}$ based on Gray mapping [LXPY11] presented by the blue symbols in Figure 3.2a. To further increase the data rate, more bits can be added to the modulation leading to 8PSK, 16PSK, etc., with more phase states.

Besides PSK, ASK can also be implemented in digital modulation by changing the amplitude states. Instead of shifting phase states for different symbols, amplitudes are adjusted. Usually, PSK and ASK are combined, which is defined as quadrature amplitude modulation (QAM). This is a format believed to achieve the best spectrum efficiency. With the same modulating bits, QAM can offer a better detection range than a unique shift keying, either PSK or ASK. A typical example of QAM is 16QAM, with $k = 4$ and $M_{\text{mod}} = 16$. The constellation diagram and the corresponding symbols are depicted in Figure 3.2b based on the Gray mapping. There are also other modulation orders for QAM, which will not be all listed in this dissertation. Further information regarding digital modulation can be found in [Xio06].

3.2.2 Demodulation and Hard Detection

Digital modulation occurring at Tx necessitates demodulation at Rx to recover the desired bits. Due to channel-introduced distortions, imperfect channel

estimation and signal recovery, as well as additive noise in the system, the recovered symbols are not optimally distributed at their modulated positions, as shown in Figure 3.2a with blue and red circle areas. Assuming an additive Gaussian white noise channel, the Rx symbols in Figure 3.2a are distributed as large scatters, where most of the spread symbols will land. To recover the bits, a detection method is necessary. This dissertation employs the hard detection method. The idea is to separate the entire constellation diagram into distinguishable ranges. Each range is assigned a unique modulation symbol. Based on the position of each Rx symbol, the hard detection classifies the Rx symbol as the modulation symbol prior to demodulation to bits. As depicted in Figure 3.2a, the blue blanket marks the detection range for a QPSK symbol. The symbols outside this range are interpreted as incorrect, resulting in error bits after demodulation. This is why Gray mapping is advantageous. By using Gray mapping, the neighbouring symbol has only 1 bit difference after the demodulation, which decreases the BER. By observing Figure 3.2a, it can be concluded that for QPSK, the noise amplitude weight in quadrature (Q) or in-phase (I) direction has to be less than $\frac{\sqrt{2}}{2}$ of the symbol power to ensure a correct decision. For BPSK, this ratio becomes 1 due to the less symbols in the entire constellation. In other words, each symbol is distributed with a larger range for hard detection. For 16QAM, this area will be even smaller in comparison to QPSK. This is the reason why BPSK is mentioned to be the most reliable digital modulation scheme. In conclusion, there is a trade-off between spectrum efficiency and BER if digital modulation order M_{mod} is the variable.

3.2.3 Modulation Error Ratio

The BER is one of the conventional parameters to determine the system performance. However, when the system is operating at a high SNR, the BER of the propagation could always be 0, which can not be further differed. Therefore, other standards have to be utilized. This dissertation considered the modulation error ratio (MER) for the Rx signal quality determination. MER is a quantity to describe the average difference between the Rx complex symbols and their associated ideal constellation points as in Figure 3.3. Using QPSK as an example, the blue dots represent the ideal constellation points as a reference, and the black point implies the recovered symbols with distortions. The difference between those two vectors e_j is the error, which contains all the possible dis-

tortions, including Gaussian noise. If, in total, there are N_m restored symbols, the definition of MER in dB can be formulated as:

$$\text{MER} = 10\log_{10}\left\{\frac{\sum_{j=1}^{N_m}(I_j^2+Q_j^2)}{\sum_{j=1}^{N_m}(dI_j^2+dQ_j^2)}\right\}. \tag{3.2}$$

The terms I_j and Q_j denote the reference symbol in the constellation, with dI_j and dQ_j to be the error distance from the Rx symbol to the reference symbol. In this dissertation, MER is computed as a quasi signal-to-interference-and-noise ratio (SINR) or SNR. Since modulated symbols are used as the benchmark, the computed SINR or SNR are based on the symbol power E_s as mentioned in (2.29).

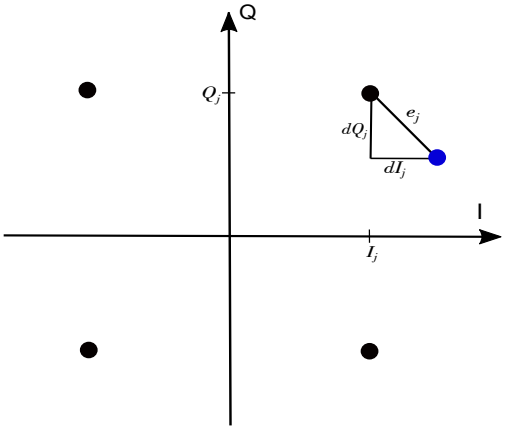

Figure 3.3: Error vector of a received symbol with QPSK constellation.

3.3 Channel Estimation

Before possible signal processing, such as precoding and equalization, channel estimation is required for CSI knowledge. The basic idea of channel estimation is to derive the relationship between the Tx training symbols and Rx symbols. Based on the preliminary information of the training symbols at Rx, a method called least square (LS) channel estimation is operated by straightforward mul-

tiplying the Rx symbols by the inverse of the previously known Tx symbols. For a SISO case, it can be written as

$$\hat{H} = s_{Tx}^{-1} s_{Rx}, \tag{3.3}$$

with $\hat{H}$ to be the estimated channel coefficient. This equation stands for the case singlecarrier modulation scheme is implemented or one subcarrier of multicarrier modulation is considered (see Section 3.5). The LS estimator has a very low complexity when channel statistics are unknown, but it has a high mean square error (MSE). Nevertheless, this is an excellent illustration of the channel estimation principle. Other algorithms in this dissertation are adapted for different system scales or purposes follow the LS algorithm's basic concept but improve their required aspects' performance (see in Algorithm 4).

3.4 Signal Recovery

The channel coefficients influence the propagated signals, necessitating additional signal processing to recover the desired signal. When channel estimation is used to determine the channel coefficients, signal recovery techniques are required to reformulate the desired data streams based on the channel estimation results. In general, the signal processing at the Tx is referred to as precoding, and signal processing at the Rx is referred to as equalization. There are various precoding and equalization techniques deserving of introduction in the following sections that will be utilized in this dissertation.

3.4.1 Equalization

Equalization is a conventional method to recover the signal at the Rx side. Since CSI is usually easily accessible at the Rx, equalization is a widely utilized choice. There exist different equalization methods with different properties. For channel equalization, the number of digital chains at Rx M_d has to be equal to or larger than the total number of data streams N_s for a valid recovery.

Zero Forcing Equalization

In the first place, zero forcing (ZF) equalization is the most straightforward method among all the methods. As its name suggests, the ZF equalization tries to eliminate the effects the channel introduced fully. To achieve this goal, the ZF equalization applies the channel inverse to the received signal. Assuming only equalization is operated in a pure digital beamforming system, $\boldsymbol{F}_{Rx,BB}$ has to fully eliminate the interference introduced by $\boldsymbol{H}_d$. Assuming a pure digital beamforming system, the goal of ZF equalization is to fulfill $\boldsymbol{F}_{Rx,BB}\boldsymbol{H} = \boldsymbol{I}_{N_s}$ for (2.17). Considering the possibility that $\boldsymbol{H}$ is not necessarily an invertible matrix, the zero forcing equalization can be expressed by

$$\boldsymbol{F}_{Rx,BB}^{ZF} = (\boldsymbol{H}^H\boldsymbol{H})^{-1}\boldsymbol{H}^H \tag{3.4}$$

assuming perfect CSI knowledge. It can be seen that the dimensions of $\boldsymbol{F}_{Rx,BB}$ is related to the dimensions of $\boldsymbol{H}$, yielding $M_d \times N_d$, which seems to be conflicting with the definition in (2.13). This is due to the reason that $\boldsymbol{H}$ determines the maximum rank/number of data streams available in the wireless communication system, but the number of data stream N_s is not necessarily reaching this value. As a solution, the data stream vector s_{Tx} and s_{Rx} can be extended with zero padding to the length of N_d and M_d, respectively. This change is equivalent to the reduction of beamforming matrix dimension, leading to the case that some MIMO channels are not occupied. Alternatively, the N_s data streams can be extended to N_d with the duplication of desired symbols, which exactly leads to the MIMO spatial diversity solution mentioned in Section 2.3.2. After the dimension of the vectors/matrices are adjusted, the recovered signal from (2.13) after ZF equalization becomes:

$$\begin{aligned}\boldsymbol{s}_{Rx} &= \boldsymbol{F}_{BB,Rx}^{ZF}\boldsymbol{H}\boldsymbol{s}_{Tx} + \boldsymbol{F}_{BB,Rx}^{ZF}\boldsymbol{w} = (\boldsymbol{H}^H\boldsymbol{H})^{-1}\boldsymbol{H}^H\boldsymbol{H}\boldsymbol{s}_{Tx} + (\boldsymbol{H}^H\boldsymbol{H})^{-1}\boldsymbol{H}^H\boldsymbol{w} \\ &= \boldsymbol{s}_{Tx} + (\boldsymbol{H}^H\boldsymbol{H})^{-1}\boldsymbol{H}^H\boldsymbol{w},\end{aligned} \tag{3.5}$$

It can be observed that under the assumption of perfect CSI knowledge, the ZF equalization eliminates the effects introduced by the channel. However, at the noise term, additional weighting is added, which possibly leads to an increase in noise distortion. This is especially visible if the channel imposes severe attenuation to the signal, when the SNR of the system is low.

Minimum Mean Square Error Equalization

Instead of fully eliminating the channel effect as ZF, the minimum MSE (MMSE) equalization is proposed to minimize the MSE between the Tx and Rx symbols. Therefore, the goal of MMSE equalization is to minimize $\mathbb{E}\{||\boldsymbol{s}_{Rx} - \boldsymbol{s}_{Tx}||^2\}$, which leads to the equalization matrix as

$$\boldsymbol{F}_{BB,Rx}^{MMSE} = (\boldsymbol{H}^H \boldsymbol{H} + \sigma^2 \cdot \mathbf{I}_{\mathbf{N_s}})^{-1} \boldsymbol{H}^H. \tag{3.6}$$

From the equation above, it can be observed that MMSE equalization considers a trade-off between the performance of channel equalization and noise distortion. If the term $\sigma^2 \cdot \mathbf{I}_{N_s}$ trends to null values, $\boldsymbol{F}_{BB,Rx}^{MMSE} = \boldsymbol{F}_{BB,Rx}^{ZF}$. In other words, MMSE converges to ZF when the SNR of the system increases.

Successive Interference Cancellation

Additional algorithms can be implemented upon the channel equalization methods to improve the signal recovery quality. For example, successive interference cancellation (SIC) is a well-known algorithm. For MIMO wireless communication, different signals via different spatial paths lead to interference for other signals. As a solution, if the signals with promising knowledge can be removed firstly at Rx, the amount of interference is reduced. Therefore, the main idea for SIC is that the optimized Rx signal is perceived first, and its contribution is subtracted from the entire Rx signal. Then the second optimized signal is perceived from the rest of the signal, and so on. The flow graph of SIC-based equalization is depicted in Figure 3.4. Take ZF-SIC as an example, the recovered symbols $\boldsymbol{s}_{Rx}$ can be restored after ZF equalization based on (3.5). By taking the optimum recovered signal based on the MER, say it is s_{opt_1} in $\boldsymbol{s}_{Rx} = [s_1, s_2, ..., s_{N_d}]^T$ (assuming $N_s = N_d$ or N_s extension mentioned in (3.5)

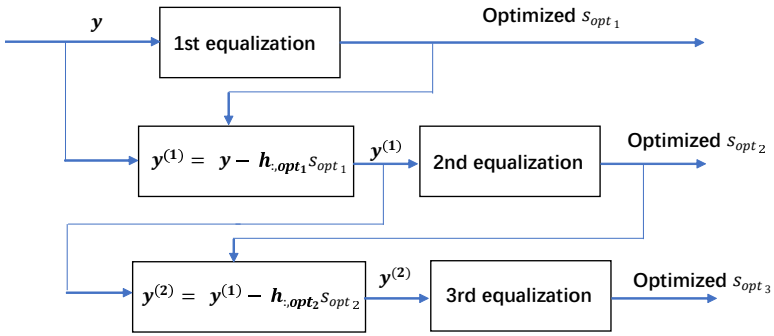

Figure 3.4: Computing procedure of SIC-based equalization.

for simplicity) for the first iteration, the rest of the signal in the first stage is formed by subtracting it from the received signal, that is:

$$\begin{bmatrix} y_1^{(1)} \\ y_2^{(1)} \\ \vdots \\ y_{M_d}^{(1)} \end{bmatrix} = \begin{bmatrix} y_1 - h_{1,opt_1} s_{opt_1} \\ y_2 - h_{2,opt_1} s_{opt_1} \\ \vdots \\ y_{M_d} - h_{M_d,opt_1} s_{opt_1} \end{bmatrix} = \begin{bmatrix} h_{1,1}s_1 + h_{1,2}s_2 + \cdots + \\ h_{1,opt_1-1}s_{opt_1-1} + h_{1,opt_1+1}s_{opt_1+1} + \\ \cdots + h_{1,N_d}s_{N_d} + w_1 \\ h_{2,1}s_1 + h_{2,2}s_2 + \cdots + \\ h_{2,opt_1-1}s_{opt_1-1} + h_{2,opt_1+1}s_{opt_1+1} + \\ \cdots + h_{2,N_d}s_{N_d} + w_2 \\ \vdots \\ h_{M_d,1}s_1 + h_{M_d,2}s_2 + \cdots + \\ h_{M_d,opt_1-1}s_{opt_1-1} + \\ h_{M_d,opt_1+1}x_{opt_1+1} + \cdots + \\ h_{M_d,N_d}s_{N_d} + w_{M_d} \end{bmatrix} \tag{3.7}$$

The term h_{m_d,opt_1} is the channel coefficients at the m_dth Rx antenna while the one with index opt_1 is subtracted. The equation above can be further arranged in matrix form:

$$\begin{bmatrix} y_1^{(1)} \\ y_2^{(1)} \\ \vdots \\ y_{M_d}^{(1)} \end{bmatrix} = \begin{bmatrix} h_{1,1} \cdots h_{1,opt_1-1} h_{1,opt_1+1} \cdots h_{1,N_d} \\ h_{2,1} \cdots h_{2,opt_1-1} h_{2,opt_1+1} \cdots h_{2,N_d} \\ \vdots \\ h_{M_d,1} \cdots h_{M_d,opt_1-1} h_{M_d,opt_1+1} \cdots h_{M_d,N_d} \end{bmatrix} \begin{bmatrix} s_1 \\ s_2 \\ \vdots \\ s_{(opt_1-1)} \\ s_{(opt_1+1)} \\ \vdots \\ s_{N_d} \end{bmatrix} + \begin{bmatrix} w_1 \\ w_2 \\ \vdots \\ w_{M_d} \end{bmatrix} \tag{3.8}$$

That is to say, for the first SIC iteration:

$$\boldsymbol{y}^{(1)} = \boldsymbol{H}^{(1)} \boldsymbol{s_{Tx}}^{(1)} + \boldsymbol{w}^{(1)} \tag{3.9}$$

where $\boldsymbol{s}^{(1)}$ and $\boldsymbol{w}^{(1)}$ are the transmitted signal matrix and the noise matrix without the optimum term, respectively. In this case $\boldsymbol{w}^{(1)}$ may also contain remained interference that will be compensated in next iterations. The term $\boldsymbol{H}^{(1)}$ is the original channel matrix without the optimum receiver column. The above equation can be treated as the new received signal and can be equalized using ZF equalization for the second iteration. This process will repeat until the last signal is recovered. The procedure is the same as ZF-SIC for MMSE-SIC, but the MMSE method is implemented for each equalization step.

3.4.2 Precoding

Besides equalization, the signal can also be precoded at Tx with CSI knowledge. Precoding is a Tx signal processing that affects the maximization of the received signal to a specific receiver while reducing the interference to all other receivers. Following the same logic as equalization, to properly implement precoding, the number of digital chains at Tx N_d should be equal to or more significant than the number of transmitted data streams N_s. Assuming only digital precoding is

utilized in the system, using ZF precoding as an example, the precoding matrix is expressed as

$$\boldsymbol{F}_{BB,Tx} = \boldsymbol{H}^H(\boldsymbol{H}\boldsymbol{H}^H)^{-1} \tag{3.10}$$

The precoded data stream is $\boldsymbol{x}_{Tx} = \boldsymbol{F}_{BB,Tx}\boldsymbol{s}_{Tx}$. If ideally precoded, we have $\boldsymbol{H}\boldsymbol{F}_{BB,Tx} = \boldsymbol{I}_{N_s}$. With precoding, the interferences among different siganls caused by the MIMO channel are eliminated so that there is no need for signal processing at receiver side, leading to $\boldsymbol{F}_{BB,Rx} = \boldsymbol{I}_{N_s}$. Thus, the recovered signal is:

$$\boldsymbol{s}_{Rx} = \boldsymbol{I}_{N_s}\boldsymbol{H}\boldsymbol{s}_{Tx} + \boldsymbol{I}_{N_s}\boldsymbol{w} = \boldsymbol{H}\boldsymbol{F}_{BB,Tx}\boldsymbol{s}_{Tx} + \boldsymbol{w} = \boldsymbol{s}_{Tx} + \boldsymbol{w} \tag{3.11}$$

(3.11) shows that if ideally precoded, the received signal will be the transmitted data stream without changing the noise weight. However, the precoding changes the signal power directly at the Tx, so an equivalent effect still exists. Therefore, MMSE and ZF have the same property for precoding as equalization. The SIC algorithm can also be implemented. For the sake of conciseness, only ZF precoding is introduced in this dissertation.

3.4.3 Singular Value Decomposition

Besides the systems purely using equalization or precoding, these two technologies can exist simultaneously. For example, the method that realizes the optimum system performance is called singular value decomposition (SVD). In linear algebra, the SVD is a factorization of a natural or complex matrix into the product of three matrices, including two unitary matrices and a rectangular diagonal matrix. MIMO signal propagation based on SVD is an effective mathematical technique to maximize the channel capacity. The channel matrix $\boldsymbol{H}$ can also be decomposed with SVD into a set of parallel and independent scalar Gaussian sub-channels as follows:

$$\boldsymbol{H} = \boldsymbol{U}\boldsymbol{S}\boldsymbol{V}^H \tag{3.12}$$

with the Tx subchannel beamforming matrix $\boldsymbol{V} \in \mathbb{C}^{N_d \times N_d}$ and Rx subchannel beamforming matrix $\boldsymbol{U} \in \mathbb{C}^{M_d \times M_d}$. Both of them are unitary matrices with $\boldsymbol{V}^H\boldsymbol{V} = \boldsymbol{I}_{N_d}$ and $\boldsymbol{U}^H\boldsymbol{U} = \boldsymbol{I}_{M_d}$, respectively. $\mathbf{S} \in \mathbb{C}^{M_d \times N_d}$ is a rectangular matrix whose diagonal elements are non-negative real numbers, which are the singular values of the matrix $\boldsymbol{H}$. The diagonal elements are $\lambda_1 \geq \lambda_2 \geq \cdots \geq \lambda_{N_{min}}$, where $N_{min} = \min(N_d, M_d)$ denotes the maximum number of data streams

that can be transmitted. For SVD, the beamforming matrices from (2.13) are expressed by $\boldsymbol{F}_{BB,Tx} = \boldsymbol{V}$ and $\boldsymbol{F}_{BB,Rx} = \boldsymbol{U}^{\boldsymbol{H}}$. This illustrates that for the compensation of transmitting and receiving part of the decomposed channel matrix, CSI at both transmitter and receiver is required. Therefore, assuming pure digital beamforming with $\boldsymbol{H}_d = \boldsymbol{H}$, the received signal with perfect channel estimation can finally be expressed as:

$$\boldsymbol{s}_{Rx} = \boldsymbol{U}^H \boldsymbol{H}\boldsymbol{V}\boldsymbol{s}_{Tx} + \boldsymbol{U}^H \boldsymbol{w} = \boldsymbol{U}^H \boldsymbol{U}\boldsymbol{S}\boldsymbol{V}^H \boldsymbol{V}\boldsymbol{s}_{Tx} + \boldsymbol{U}^H \boldsymbol{w} = \boldsymbol{S}\boldsymbol{s}_{Tx} + \boldsymbol{U}^H \boldsymbol{w} \quad (3.13)$$

With the implementation of SVD beamforming, the received signals are weighted by the eigenvalues from $\boldsymbol{S}$. Normally, its diagonal elements follow a decreasing order. Effectively, this means the received power of each data stream is distributed based on the spatial channel paths' strength, which leads to a water-filling effect and maximizes the spatial diversity in a MIMO system. Recall the MIMO channel capacity equation (2.30), it can be concluded that the eigenvalue matrix $\Sigma = \boldsymbol{S}\boldsymbol{S}^H$. This is evidence that SVD is a method that aims to reach the upper boundary of MIMO channel capacity. The term $\boldsymbol{U}^H$ has unitary power so the noise level is not increasing with the multiplication to $\boldsymbol{w}$.

3.5 Modulation Schemes

Once the data streams are digitally modulated and precoded to form the transmit signals, they have to be modulated to a format that can be transmitted in the time and frequency domain. To properly carry the signals, waveforms have to be chosen carefully to avoid interferences. In this dissertation, singlecarrier and multicarrier modulation are utilized as desired solutions.

3.5.1 Singlecarrier Modulation

Singlecarrier modulation denotes the modulation scheme that exploits the entire utilized bandwidth to transmit signals. Since the signal is regarded as one frame in the frequency domain, it is not necessary to introduce additional frequency domain signal processing to avoid inter-carrier-interference (ICI). On the other hand, different signals are propagated in time domain, which leads

to the necessity to avoid inter-symbol-interference (ISI). The following part of this section is based on [PS01].

The necessary condition to avoid ISI is ensuring a symbol only has a non-zero value at its specific sampling time. Assuming a normalized symbol energy and a single sampling point for each symbol at $a = 0$, the impulse response of the desired time domain signal $g(t)$ based on the Nyquist-ISI criterion can be formulated as

$$g(t = aT) = \begin{cases} 1, a = 0 \\ 0, a \neq 0 \end{cases} \tag{3.14}$$

with a is an integer denoting the sampling point in the time domain, and T is the time step between two samples. The sufficient condition that $g(t)$ satisfies (3.14) is that its Fourier transform follows

$$\sum_{b=-\infty}^{\infty} G(f + b/T) = T. \tag{3.15}$$

The optimum $G(f)$ fulfills this condition considering a bandwidth B

$$G(f) = \begin{cases} T, |f| < B \\ 0, \text{else} \end{cases} \Leftrightarrow g(t) = \frac{sin(\pi t/T)}{\pi t/T}. \tag{3.16}$$

However, a sinc function in the time domain is noncausal, which can not be realized practically. A standard approximate solution to overcome this problem and maintain the required sinc function properties is called raised cosine function. A roll-off factor ζ characterizes it as

$$G_{RC}(f) = \begin{cases} T, 0 \leq |f| \leq \frac{1-\zeta}{2T} \\ \frac{T}{2}\left(1 + cos\left[\frac{\pi T}{\zeta}(|f|) - \frac{1-\zeta}{2T}\right]\right), \frac{1-\zeta}{2T} \leq |f| \leq \frac{1+\zeta}{2T} \\ 0, |f| \geq \frac{1+\zeta}{2T} \end{cases} \tag{3.17}$$

The roll-of-factor of the raised cosine pulse is thereby decisive for the so-called excess bandwidth of the pulse-shaped signal, which measures how much bandwidth the pulse-shaped signal occupies beyond the Nyquist frequency. Several raised cosine pulses with different roll-off-factors can be seen in Figure 3.5, of which $\zeta = 0.35$ is particularly often used in practice. It can be seen that at each sampling point out of the desired symbol position, null values are

always located. For frequency domain signal, instead of a perfect rectangular shaping when $\zeta = 0$, the band leaks more out with increasing ζ.

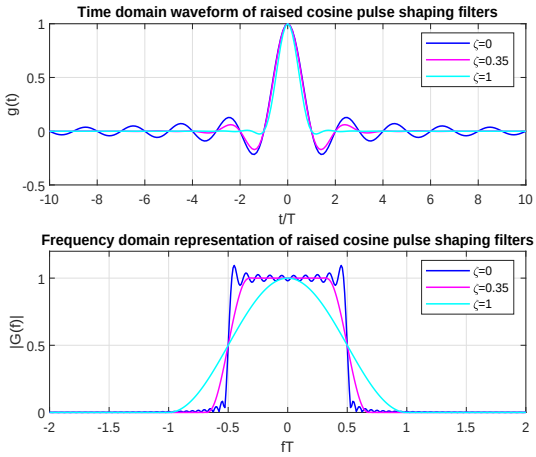

Figure 3.5: Raised cosine impulse response with different roll-off factors.

In digital communications, the raised cosine characteristic is commonly divided into two distinct filters: a pulse-shaping filter on the transmitter side to restrict the signal's bandwidth and a conjugate matched filter on the receiver side to maximize the SNR with its low-pass characteristic. Since the joint characteristic of two filters in series is obtained by convolution of their impulse responses, root-raised-cosine filters are utilized in these situations, resulting in an overall raised cosine characteristic that eliminates ISI. In this case, it is advantageous for the symmetrical pulses to represent their conjugate so that the same filter characteristic can be used on both sides as a pulse-shaping and matched filter. The signal is first sampled and then fed to a finite impulse response filter structure with the desired characteristic to filter the signal in the digital domain on the Tx side. For Rx, the signal is matched filtered and down sampled as a reverse operation of the Tx side.

3.5.2 Multicarrier Modulation

Singlecarrier modulation has the benefit of less complexity. However, in a practical communication channel model, multipath fading introduced by reflection paths between Tx and Rx is very likely to exist. For a singlecarrier system, the channel matrix from (2.13) represents the entire frequency domain channel or a time domain channel matrix for a single tap. Neither of these options can adequately estimate the multipath channel, which turns into interference that degrades the signal recovery quality. The impulse response of a multipath channel has taps at multiple delays, while its frequency response is frequency-selective. As a solution, multicarrier modulation is widely utilized. The bandwidth is divided into N_c subcarriers for the multicarrier modulated signal. A channel matrix known as channel frequency response (CFT) from (2.13) can be estimated at each subcarrier. By operating an inverse descrete Fourier transform (IDFT), the channel model in the discrete time domain is represented by channel impulse response (CIR), which includes N_c samples including delay profiles from multipath contributions.

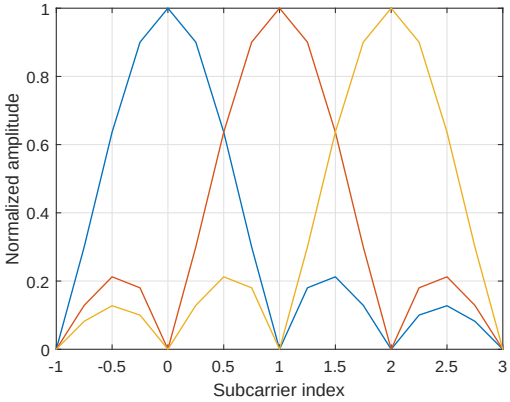

Figure 3.6: OFDM Modulated signals in frequency domain.

Among the existing multicarrer modulation schemes, OFDM is mostly known and regarded as the standard waveform for 5G and 6G mobile communication. OFDM achieves orthogonality in the frequency domain to eliminate critical ICI for multicarrier modulations. The solution is similar to singlecarrier modula-

tion but with sinc shaping in the frequency domain as depicted in Figure 3.6. The N_c subcarriers are uniform distributed over the entire bandwidth B with subcarrier spacing $\frac{B}{N_c}$. The impulse response becomes a rectangular shape by implementing inverse Fourier transform (IFT) to the sinc frequency response. Therefore, OFDM can be realized by implementing the rectangular shape matched filtering and Tx and Rx side. The signal convolution with a rectangular impulse response leads to the original signal. Therefore, if OFDM modulation is used, the flow graph for the multicarrier modulation is presented in Figure 3.7. Firstly, the signals after digital modulation and necessary precoding are aligned to the subcarriers to formulate the frequency domain signal. Afterwards, to realize the data propagation, IDFT is required to transform the signal to time domain following

$$\boldsymbol{x}(a) = \sum_{n_c=1}^{N_c} \boldsymbol{X}(n_c) \exp(j2\pi n_c a/N_c). \tag{3.18}$$

with a and n_c denoting the discrete time domain and discrete frequency domain indexes respectively, with $a \in \{1, 2, ..., N_c\}$, and with $n_c \in \{1, 2, ..., N_c\}$. Then, a cyclic prefix (CP) can be added to overcome ISI introduced by channel delay and parallel-to-serial (P/S) conversion formulates the signal to a proper transmission format before input to the channel. At Rx, serial-to-parallel (S/P) conversion firstly takes place and the CP of the signal is removed before the DFT. Afterwards, frequency deallocation and channel equalization take place to recover the digitally modulated symbols. To utilize OFDM in the proposed beamforming system, the signals at each carrier $\boldsymbol{X}(n_c) = \boldsymbol{x}_{Tx}$ in (2.17), with the channel matrix and Rx signal also changed to discrete frequency domain respectively.

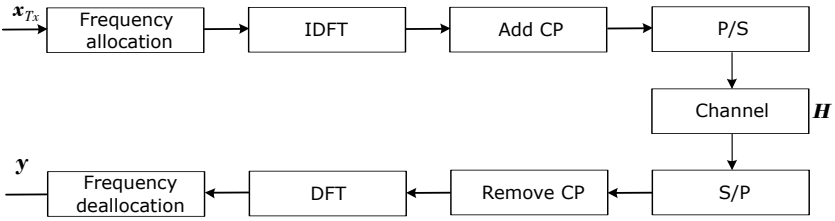

Figure 3.7: Block diagram of OFDM modulation scheme in this dissertation.

3.6 Synchronization

At Rx, synchronization is required to indicate the correct beginning of the desired sequence for all post-processing to operate properly. In this dissertation, the Tx and Rx are assumed to be stationary during the signal processing time. Therefore, the frequency synchronization is ignored. In time domain, Tx and Rx have different timing references. In order to determine a correct starting time for the Rx signal processing, time synchronization is always required. To achieve time synchronization, the cross-correlation between the Tx and Rx signals is computed. Cross-correlation in signal processing is a measure of the similarity between two series as a function of the displacement of one series relative to the other. Therefore, when the convolution of Tx and Rx signals indicates a good match at the cross-correlation output, it indicates the correct position of the desired signal within the entire sequence. For finite discrete functions $f_1, f_2 \in \mathbb{C}^{L\times 1}$ of length L, the cross-correlation is defined as:

$$C_{cross}\,[a] = \sum_{l=0}^{L-1} f_1\,[l]^*\, f_2[(l+a)_{\mathrm{mod}L}] \tag{3.19}$$

The variable a here is the displacement index, also known as lag.

3.7 Conclusion on this Chapter

This chapter provides an overview of this dissertation's communication signal processing techniques. The bits are generated at random before being mapped to symbols based on the desired digital modulation schemes. The training symbols can then be employed for channel estimation to implement signal recovery strategies based on the estimated CSI. Depending on the system's requirements, the symbols can be modulated with either a singlecarrier or a multicarrier. Raised cosine filtering is primarily utilized for single-carrier modulation. OFDM is studied as the standard waveform for multicarrier modulation in 5G. In the following chapter, detailed signal processing either employs the methods described in this chapter or creates novel ideas based on the concepts mentioned above.

4 IRS Modeling in Wireless Communication Systems

As new generations of communication technologies arise, the conflict between the rapidly increasing traffic demand and the cost of the system becomes more apparent. Possible modern wireless communication beamforming architectures are listed and introduced in Chapter 2. In recent years, a novel concept known as intelligent reflecting surface (IRS) has gained traction alongside these existing solutions. The reflect array inspires its structure, but an IRS may support more flexible implementations and algorithms while preserving the low-cost property. This chapter introduces the fundamental concept of IRS, followed by two major application types: yielding IRS as an alternative antenna array and IRS as a signal reflector. The following sections investigate the IRS's beamforming capability in simulation as a fundamental. Based on the theoretical results, the design, model, and beamforming performance of the experimental IRS implemented in this dissertation are described in detail. As a novel concept, there is a lack of discussions regarding the IRS's practical limitations and challenges. Without these considerations, however, there will always exist a gap between the theory and experimental research of IRS. This chapter summarises the challenges posed by IRS based on our experimental research.

4.1 Intelligent Reflecting Surface Basics

An IRS is a surface which reflects the power of the incidence signal with desired spatial distributions to realize algorithms and functions in modern wireless communication scenarios. The key features of an IRS are expressed by the word intelligent. In comparison to the specular reflection created by any metallic surface, the IRS is expected to have the following characteristics:

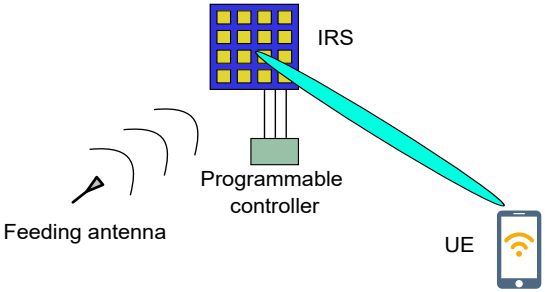

Figure 4.1: General model of an IRS setup from [IRS].

- Following the concept of reflect array in Chapter 2, an IRS is a surface which is divided into many antenna unit cells whose reflectivity can be adjusted individually.
- By adjusting the phases of the unit cells, the direction of reflection of a wave can be specifically set, which leads to the realization of beamforming.
- From the beamforming ability point of view, an IRS should generate desired antenna array patterns to cope with variant wireless communication scenarios. Its ability should be examined from the system point of view, e.g. a valid channel estimation, data propagation, etc.
- From the feasibility point of view, an IRS-based system offers more opportunities compared to the conventional beamforming architectures in Chapter 2. By adjusting the position of the illumination source, the IRS possibly play different roles in a wireless communication system, such as antenna array, hybrid beamforming component, signal reflector, etc.

All of the characteristics mentioned above are regarded as the primary focus of this dissertation. The IRS setup model is depicted in Figure 4.1 according to the IEEE signal processing society's definition. A Tx is considered the source that illuminates the EW wave onto a surface. The surface consists of a large number of unit cells that the programmable controller can individually control. By adjusting the phase distribution of the unit cells appropriately, the desired beamforming is generated, which transmits the signal to the Rx. Please notice

that the IRS can also be equipped on the Rx side. Since the implementations are very similar, IRS is used to reflect the Tx signal and beamform to Rx as a default setting in this dissertation.

4.2 IRS Design

The necessary constraints must be considered to properly design an IRS, including unit cell spacing, IRS size, power reflection efficiency, and the control circuit. These aspects are introduced in this section for the implemented IRS in this dissertation, which is mainly based on the publication from [WXZ+21] with reused texts and figures

4.2.1 Unit Cell Design

The unit cell of the implemented IRS in this dissertation is a 1-bit unit cell. The structure of the proposed IRS is a multilayer printed circuit board. According to the antenna spacing in (2.12), the unit cell has a square shape with 1 mm lengths which is half wavelength for 30 GHz, yielding $d = 5$ mm. Figure 4.2a shows the top layer that consists of a metallic patch and a PIN diode with the type MA4AGP907 from [MA4], which are expected to reflect the incidence EM wave properly. In Figure 4.2b, a fan-shaped structure is used on the bottom layer to choke RF preventing undesired resonance, and a biasing line is used to control voltages for the PIN diode, which finally determines the resonance behaviour of the unit cell. Figure 4.2c illustrates detailed structures of the unit element. The middle layer is the ground layer with drills through the vias from the bottom to the top layer. The first and the third dielectric layers are made from RO4350B (Dielectric constant $\varepsilon = 3.66$, loss tangent $\tan\delta = 0.0037$); the second dielectric layer FB4 ($\varepsilon = 4.3$, $\tan\delta = 0.025$) is used to adhere another two layers. The PIN diode is modeled as a series resistor-inductor-capacitor (RLC) circuit (resistance $R_{\text{on}} = 4.2\ \Omega$, inductance $L_{\text{on}} = 0.05$ nH) when it is turned on, and a shunt RLC circuit ($R_{\text{off}} = 300\,\text{k}\Omega$, capacitance $C_{\text{off}} = 42$ fF) when it is turned off.

The simulation results of the IRS unit cell are provided as follows. When the top layer is illuminated by EM waves polarized in the x-axis as depicted in

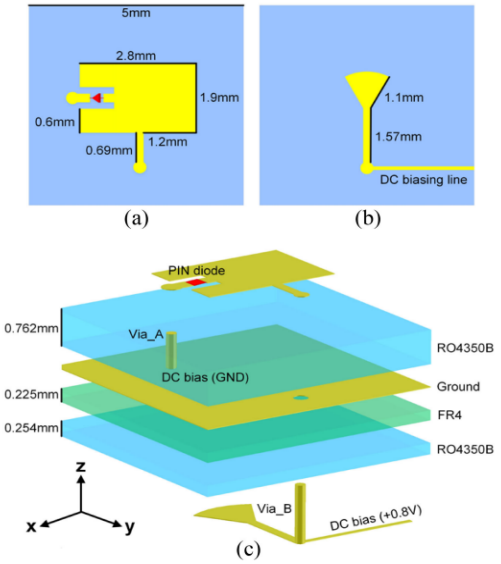

Figure 4.2: IRS unit cell design in this dissertation from [WXZ+21].

Figure 4.3a, the reflected waves will be dynamically affected by switching the PIN diode. This is also the practical setting of the illumination side and polarization. The EM simulation software (CST, Microwave Studio) is used to simulate S11 of the proposed unit cell. During simulations, unit cell boundaries are used in the x and y-axis, and Floquet waveguide ports are used in the positive and negative z-axis to formulate the periodic condition assuming the simulated unit cell is located in a finite antenna array duplicating the same unit cell design. Figure 4.3b gives the simulated S11 when the unit element is illuminated typically by an x polarized plane wave. The on and off states of the unit cells are represented by the blue and yellow curves, respectively. The amplitudes are denoted by Amp and the phases and denoted by Phase in the curves. The results show that the S11 magnitude is generally above 0.8 in the 2 GHz bandwidth from 27 to 29 GHz. Due to the 1-bit unit cell design, the phase difference is expected to be 180° and the simulation results show a phase mismatch less than 20° and matches exactly 180° at the desired 28 GHz. Based on these results, the proposed unit cell design is believed for practical usage.

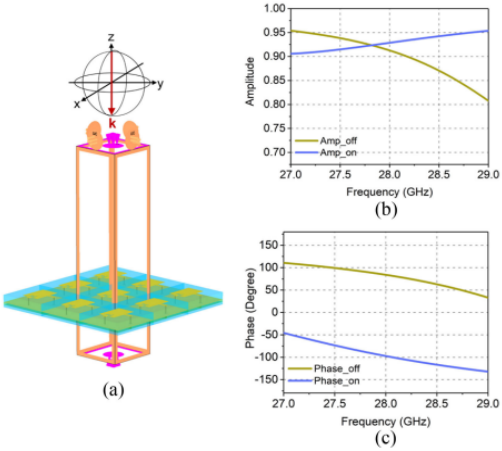

Figure 4.3: IRS unit cell simulation environment and results from [WXZ+21].

4.2.2 Control Board Design

A total number of 400 ($N \times M = 20 \times 20$) unit cells constitute the aperture of the IRS, as shown in Figure 4.4a and b. As aforementioned, each unit cell has on and off states which need a DC bias to control. A digital circuit board with a male connector is designed to output 400 independent DC voltages in parallel. On the back of the IRS, a female connector with the corresponding general purpose input and output (GPIO) pins connecting to the specific unit cells is mounted. By combining the digital circuit board and the IRS through the connectors, 400 units of the BPM can be configured independently and simultaneously. Figure 4.4c shows the appearance of the connectors. With this design, the IRS setup can be placed on a rotatable platform of a microwave anechoic chamber with a horn antenna as a feeding source and measure the array patterns as shown in Figure 4.4d. The entire control board and the IRS operates with a input voltage of 5 V and the average current around 0.78 A depending on the number of PIN diodes in forward states.

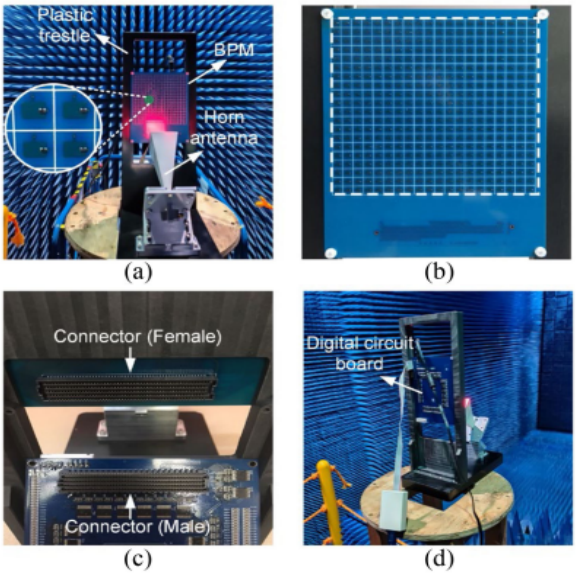

Figure 4.4: Control board design of the IRS from [WXZ+21].

4.2.3 IRS Control Sequence

As mentioned in Section 4.1, to highlight the intelligence of IRS, flexible beamforming generation is required for different wireless communication scenarios. In this dissertation, the IRS is controlled by an Altera Cyclone IV EP4CE30F29C8N FPGA with the Quartus II software can program. It is also the core component of the control board from Figure 4.4. The voltage distribution at the PIN diodes on the unit cells is given by the name coding pattern in this dissertation, which determines the array pattern. The solution is to prestore different coding patterns in the FPGA as a look-up table. With a command sequence correctly sent to the FPGA, the GPIO pins output the required voltage distributions. In this dissertation, a control sequence including 16 bits is designed for the coding pattern command. The first bit is used for error control in command failure and retransmission. The second bit is designed for mode control. The last 14 bits are divided into two groups; every 7 bits denote an angle index using the binary count. The two angles represent different meanings

when the control board works in different models. The IRS works in fixed-angle mode when the second bit is "0". A single beam is generated if the last two angles indicate the same direction. Double beams are generated simultaneously by the IRS if the last two angles indicate different directions. If the second bit is "1", the IRS works in steering mode, with the following two angles indicating the starting and ending angle of the beam steering. Examples are presented in Figure 4.5, with a fixed mode to $-30°$ and steering model from $60°$ to $60°$. Please notice that, as the binary sequence can not express negative angles, the solution is to use the 7 bits indicating the addresses of the coding patterns to different angles. In this example, $-60°$ to $60°$ along θ with $2°$ angle resolution is prestored, leading to 61 different coding patterns. Each coding pattern requires two addresses for the prestored format. Therefore, $-60°$ leads to address 0 and $60°$ address 120, yielding 0000000 and 1111000 for the 7-bit sequence.

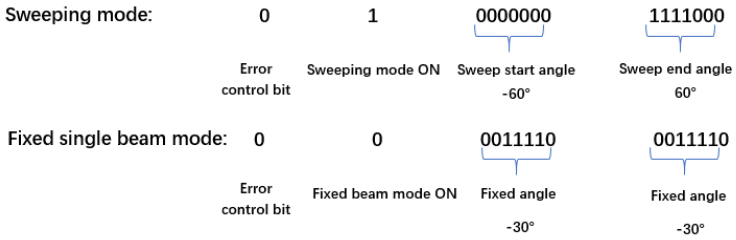

Figure 4.5: Command structure for IRS coding pattern.

4.3 IRS Application Types

Using the novel IRS antenna architecture, experimental measurements are planned as one of the contributions of this dissertation. To achieve this objective, it is essential to comprehend the existing applications of the IRS. Therefore, we define two types in this dissertation based on the location of the illumination source. For the first option, IRS nearfield illumination yields an alternative analog beamforming antenna array. The second option is a low-cost reflective reflector that is facilitated by farfield illumination. In the following sections, we will discuss the technical aspects of these applications.

4.3.1 IRS as Antenna Array

The IRS nearfield illumination indicates the condition that the feeding antenna is located in the nearfield of the IRS. In this condition, IRS is behaving as a low-cost electronically controllable analog beamforming antenna array, which can be a replacement of, for example, phased array from Chapter 2.

IRS Nearfield Illumination Model

Illustrated by Figure 4.6a, an IRS application is depicted assuming a Tx BS using an IRS antenna architecture and a UE as Rx. The feeding source is in the nearfield of the IRS array with an illumination distance r_1 much smaller than the propagation distance from the IRS to the destination r_2. In this dissertation, this geometry is defined as nearfield illumination. Therefore, to evaluate the path model of an IRS-based propagation, the first illumination path follows the nearfield constraints, while the propagation path follows the farfield constraints as mentioned in Section 2.1.1. Effectively, the illumination source behaves like a point source, as depicted in Figure 4.6b. In this condition, the gain of IRS with nearfield illumination G_n assuming a correctly computed distance phase $\varphi(m,n)_d$ from (2.16) can be expressed as [TCC+20],

$$G_n = \frac{G_t G_u d_x d_y |E(\theta',\phi')|^2 A_u^2}{4\pi} \left| \sum_m^M \sum_n^N \frac{\sqrt{|E_{m,n}(\theta_i,\phi_i)|^2 |E^t_{m,n}(\theta_i,\phi_i)|^2}}{r'_{m,n}} \right|^2 . \tag{4.1}$$

In this equation, G_t is the gain of the feeding antenna, assuming IRS is placed at the Tx side, and G_u is the gain of each unit cell. $E(\theta',\phi')$ is the electric field contribution from (2.1) with respect to the reflective beamforming angle θ',ϕ' to the destination. A_u is the aperture of the unit cell. The term in the outer $|\cdot|^2$ denotes the array pattern of the IRS contributed by all the unit cells under nearfield illumination. It can be seen that the array pattern according to the incidence angle θ_i,ϕ_i differs among unit cell indexes m and n. In addition, the contribution from the feeding antenna to each unit cell $E^t_{m,n}(\theta_i,\phi_i)$ also differs. Following the same logic, the distance from the feeding antenna to each unit cell $r'_{m,n}$ varies. The above features are caused by the point source behavior from (4.1). As a result, the path loss model for IRS nearfield illumination can

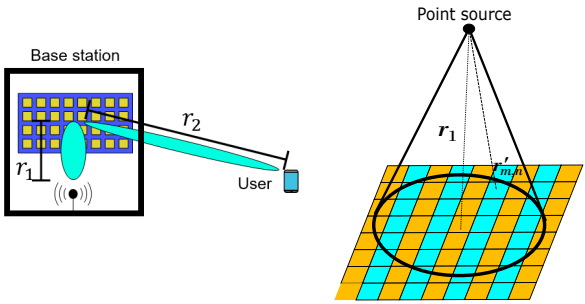

(a) IRS as antenna array.

(b) IRS point source illumination property.

Figure 4.6: IRS nearfield illumination principles.

be derived by replacing G_t from (2.6) to G_n, which copes with the situation that IRS nearfield illumination is a novel alterative antenna architecture.

IRS Illumination Optimization

For the best beamforming condition, all the power from the feeding antenna will be caught by the IRS, and all the unit cells on the IRS have the uniform power reception property. However, this leads to the requirement of a rectangular antenna pattern from the feeding antenna, which is, in practice, not achievable. In addition, the beamwidth and gain of the illumination antenna have a trade-off, as mentioned in Chapter 2. This leads to why each unit cell behaves differently, contributing to the final array pattern as discussed in (4.1) and Figure 4.6. Therefore, optimizing the illumination to IRS is important, especially for the nearfield illumination case. The illumination of IRS depends on the geometry of the IRS setup, which includes many factors such as the size of IRS, the illumination distance, the incidence angle, the relative position of IRS and feeding antenna, etc. Overall, all these parameters can be regarded as parts of the effective aperture efficiency of the IRS. The aperture efficiency η_a for IRS can be further divided into spillover efficiency η_s and illumination efficiency η_i. The spillover efficiency denotes the amount of power caught by the IRS compared to the total incidence power from the feeding antenna. The illumination efficiency

denotes the evenness of the received power at each unit cell over the entire IRS. According to [YYE+10], the relationship between η_a, η_s, and η_i for the IRS nearfield illumination case follows a common behavior. When the feeding antenna is placed closer to the IRS with smaller r_1, the spillover efficiency is high since more power is caught by the array surface. However, due to the beamwidth of the antenna pattern mentioned in Chapter 2, most illuminated power is centralized in the main beam direction. Therefore, when the feeding antenna is placed close to the IRS, the unit cells covered by the mainlobe are strongly illuminated while the others are weakly illuminated. This leads to a degradation of illumination efficiency with worse evenness. Overall, η_s and η_i are two conflicting factors contributing to the η_a. As a result, η_a usually starts with a lower value with shorter r_1 since η_i is poorly guaranteed. It starts to increase and reaches the maximum value as the best trade-off point between η_s and η_i. For longer r_1, too much power leaks away from the IRS and η_a are decreased again. The general task for the IRS illumination optimization is looking for the best trade-off point to achieve the highest η_a. Please notice that for different IRS design and setup, the optimum r_1 varies. Detailed information can be found in [YYE+10] for further interests.

4.3.2 IRS as Signal Reflector

Instead of placing the feeding antenna in the nearfield of IRS, it can also be located in the farfield of IRS. This geometry is defined as farfield illumination in this dissertation. Now, the IRS behaves as a signal reflector instead of an antenna architecture. The IRS farfield illumination model is depicted in Figure 4.7a, with the illumination distance r_1 in the farfield of IRS and comparable to the propagation distance r_2. In this condition, the path model of IRS farfield assisted communication is a cascaded Friis formula (2.6) including two wireless communication paths, yielding

$$P_r = P_t G_t \left(\frac{\lambda}{4\pi r_1}\right)^2 \eta_f \cos\theta_i \cos\theta' A^2 \left(\frac{4\pi}{\lambda^2}\right)^2 \left(\frac{\lambda}{4\pi r_2}\right)^2 G_r. \tag{4.2}$$

The term η_f is the aperture efficiency for the IRS farfield illumination case, and A is the aperture of the entire IRS. For further expression, the gain provided by

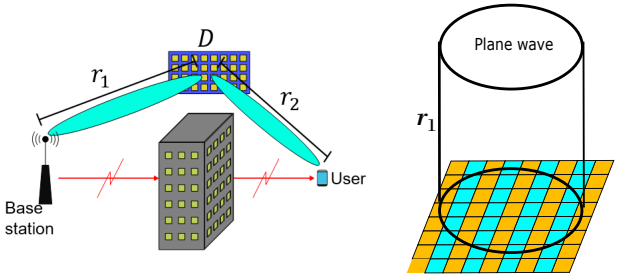

(a) IRS as signal reflector.

(b) IRS plane wave illumination property.

Figure 4.7: Farfield IRS illumination principles.

the IRS can be denoted as a repeater with input gain G_i and output gain G_o, which leads to

$$G_{IRS} = G_i G_o = \eta_f \cos\theta_i \cos\theta' A^2 \left(\frac{4\pi}{\lambda^2}\right)^2. \tag{4.3}$$

For farfield illumination, its property is presented in Figure 4.7b. Due to the farfield illumination, the incidence wave can be regarded as a plane wave, which leads to the condition that the incidence/reflection angle and the antenna pattern for each IRS unit cell can be regarded as a unique value. A plane wave incidence can represent this condition. Following the similar expression as (4.1), the farfield IRS illumination also has its form,

$$G_f = \frac{G_t G_u M^2 N^2 d_x d_y |E(\theta_i, \phi_i)|^2 |E(\theta', \phi')|^2 A_u^2}{4\pi r_1^2}. \tag{4.4}$$

Compared to (4.1), the differences between unit cells vanish. As replacements, $E(\theta_i, \phi_i)$ is used to denote the electric field contribution for all the unit cells based on the incidence angle and similarly for the reflection angle $E(\theta', \phi')$. The variant distances from the feeding antenna to each unit cell can be approximated as r_1, with the difference between each unit cell neglected.

According to the farfield illumination property, the IRS gain, in this case, does not need to/can not be optimized. The spillover efficiency is transformed to the Friis formula, and the illumination efficiency is always 1. In other words, IRS gain optimization is only required for nearfield IRS illumination. On the other hand, in the urban city scenarios, there are lots of shadowing effects due to the existence of objectives (mostly buildings). The farfield IRS illumination from Figure 4.7a exactly solves this problem. Therefore, the shadowing effect between the feeding antenna (BS) and the IRS is assumed to be not existing, since the placement of IRS is flexible to ensure a promising LoS path to the BS. For the shadowing effect from the IRS to the UE, the strongest reflection path will be utilized as the beamforming direction if LoS path is blocked.

4.4 Theoretical IRS Beamforming Studies

Before the IRS is measured in experiments, its beamforming capability should be simulated. This section covers the theoretical analysis of IRS beamforming, including the computation of the IRS beamforming pattern, determination of the phase resolution, and evaluation of robustness. This dissertation focuses on the IRS beam steering in the θ axis, while $\phi' = 0°$ is kept. The reason is, increasing the beamforming direction to 2D only increases the measurement quantity and complexity but does not change the beamforming methods and strategies. For simplicity, beamforming along 1D is an efficient idea for scientific study.

4.4.1 Beam Pattern Generation

As mentioned before, the general IRS beamforming follows the equation (2.16) for the phase distribution computation at each unit cell. The additional phase shift $\varphi(m,n)_d$ represents the distance phase from the feeding antenna to each unit cell depending on $\frac{2\pi r'_{m,n}}{\lambda}$. Therefore for the nearfield illumination case, these terms matter more, since for farfield illumination every $r'_{m,n} = r_1$ which leads to null phase gradient. Based on this computation, the results for the optimum phase distribution are depicted in Figure 4.8a. The settings below are used regarding our interested IRS size: $M = N = 20$, $d = 5\,\text{mm}$, operating frequency at 28 GHz. In this example, the feeding antenna is placed at $\theta_i = -45°$, $\phi_i = 90°$, and $r_1 = 150\,\text{mm}$. The reflective beamforming angle is $\theta' =$

$\phi' = 0°$. However, an IRS in practice can not achieve infinite phase resolution, which means the optimum phase distribution pattern, with the degrees defined by the color by in Figure 4.8a is not achievable. Therefore, quantization is always required to code the optimum phase pattern into discrete values based on the achievable phase resolution. Assuming a 1-bit unit cell, the quantized phase distribution is computed as

$$\varphi_q\left(m,n,\theta',\phi'\right) = \begin{cases} 0, \text{if } -\frac{\pi}{2} < \varphi\left(m,n,\theta',\phi'\right) \leq \frac{\pi}{2} \\ \pi, \text{if } \frac{\pi}{2} < \varphi\left(m,n,\theta',\phi'\right) \leq \frac{3\pi}{2}. \end{cases} \tag{4.5}$$

Afterwards, the quantization phase distribution is depicted in Figure 4.8b,

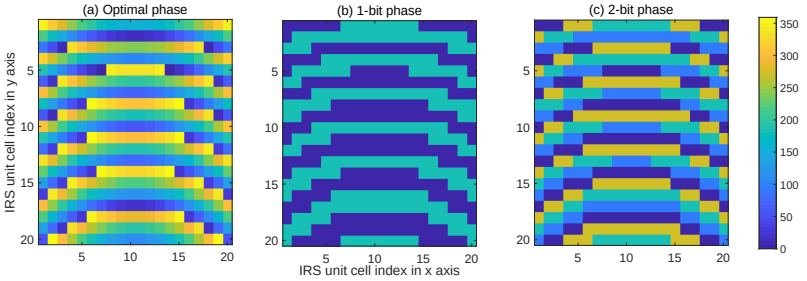

Figure 4.8: IRS phase distribution with different resolutions.

where only 0° and 180° can be observed, yielding the 1-bit IRS. Following the same logic, the coding pattern with 2-bit IRS is presented in Figure 4.8c. As a matter of fact, such quantization leads to some errors that possibly lead to beamforming performance degradation. Therefore, the quantization error in this dissertation is defined as

$$\varphi_e = \frac{1}{MN}\sum_{m}^{M}\sum_{n}^{N}\left|\varphi_q\left(m,n,\theta',\phi'\right) - \varphi\left(m,n,\theta',\phi'\right)\right|. \tag{4.6}$$

In this example, φ_e for 1-bit IRS is around 44° and for 2-bit 21°.

4.4.2 Phase Resolution Determination

Only with the quantization error defined, it is still not clear to see how much loss this error practically leads to. Therefore, the antenna array patterns with the desired beamforming need to be simulated. In the simulation, the feeding antenna power is normalized and uniformly distributed on each unit cell. At each unit cell, a $G_u = 1.4\,\text{dBi}$ is used to cope with the practical IRS unit cell gain in this dissertation. Please notice that the losses caused by the imperfect aperture efficiency, the specular reflection, and fabrication mismatches are not considered in the simulation results. The simulation results are just a simplified model using the quantized phase distribution at each unit cell based on (2.16) and (4.5). Merging the array factor equation (2.7) considering the unit cell distribution, a simplified far-field pattern for the PM beamforming can be expressed as

$$\begin{aligned} E\left(\theta,\phi,\theta',\phi'\right) = S_a \sum_{m=1}^{M}\sum_{n=1}^{N} \exp\big\{j\,\big[\varphi\left(m,n,\theta',\phi'\right) \\ +\kappa D\left(m-1/2\right)\sin\theta\cos\phi \\ +\kappa D\left(n-1/2\right)\sin\theta\sin\phi\big]\big\}\,. \end{aligned} \tag{4.7}$$

In comparison to (2.7), the additional $1/2$ is used to refer to the phase distribution at the center of each unit cell. The gain G_u is expressed by the term S_a for the final pattern derivation. Under these assumptions, the antenna gain of the IRS by merging (4.7) and (2.3) considering lossless condition is presented in Figure 4.9a using different phase resolutions. It can be seen that the optimum case leads to a maximum of 30 dBi antenna gain, with 2-bit phase resolution decreasing 1 dB and 1-bit resolution decreases 3 dB more. Reducing the phase resolution leads to a reduction of the gain at the main beam while increasing the gain at the side lobe. Nevertheless, the sidelobe is more than 10 dB smaller even for the 1-bit phase resolution. In addition, for wireless communication systems, the increase of side lobe is not that critical since it mostly leads to interference for other UEs, which can be eliminated by division technologies. Therefore, the increase of sidelobe level is not a main obstacle in this case. In the simulation, the beam steering works precisely from $\theta' = -60°$ to $60°$. This means reducing the phase resolution in this IRS size is not decreasing the beamforming accuracy. Also, if, in any practical case, the angle accuracy is influenced, the problem can

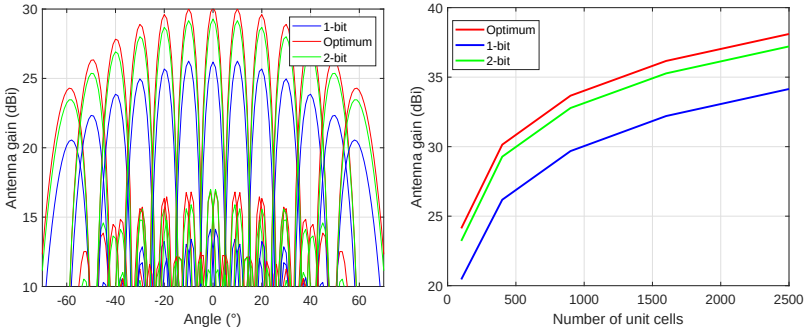

(a) IRS beam steering.

(b) IRS gain vs. size.

Figure 4.9: IRS beamforming simulation using different phase resolutions.

also be solved by using the relative beamforming angle instead of the theoretical ones, which already takes the angle mismatch into account.

The antenna gain can also be studied with different array sizes as presented in Figure 4.9b. It can be observed that the 1 dB and 3 dB degradation between optimum to 2-bit, and 2-bit to 1-bit resolution maintains. These results cope with the fact that the IRS gain is only proportional to the number of unit cells as mentioned in (4.4) and (4.1). Thus, constant gain differences can always be observed at the antenna gain using IRS with 400 and 800 unit cells. In conclusion, the gain reduction caused by the quantization error is not size dependent. This means, theoretically, the additional quantization loss brought by the 2-bit to 1-bit resolution can be compensated by doubling the array size.

In the simulation, designing an IRS with 2-bit phase resolution seems to be attractive by providing higher antenna gain. However, it is no longer that valuable considering practical limitations. Based on [DCDP+17], it can be concluded that a 2-bit unit cell needs a higher number of micro components, which leads to an increased number of DC biases. The placement of these micro components and the crossing of the DC biases increase the design complexity, which usually results in an S11 degradation and bandwidth limitation. These features also bring additional fabrication costs. Comparing previous unit cell designs, the S11 magnitude of the 2-bit unit cell is more than 1 dB lower tha the 1-bit

unit cell [DPCD+15]. In addition, the layers are increased from 4 to 6. All these changes make the implementation of a 2-bit array less satisfactory. In conclusion, the expected 3 dB performance improvement is not possible to be realized even with the sacrifice of bandwidth. Most importantly, there is no evidence to prove that a 2-bit array can be cheaper than a 1-bit array with doubled size. Due to the aforementioned concerns, 1-bit IRS is believed to be more attractive from the realization point of view according to the technology at this stage. Thus, in the latter part of this dissertation, 1-bit IRS is studied.

4.4.3 Beamforming Robustness Analysis

The aforementioned primary simulation results evaluated the possibility of IRS beamforming for future research. In practice, however, numerous mismatches and distortions may impair the ability of IRS beamforming. Consequently, these characteristics must be studied as additional fundamentals for IRS in experimental research.

Illumination Distance

As mentioned in (4.1) and (4.4), the IRS gain is proportional to the square of illumination distance. Besides this effect, it is also important to verify if a longer propagation distance influences the beamforming performance from the phase distribution point of view since the distance phase $\varphi(m,n)_d$ from (2.16) vanishes with larger r_1. Simulation results are provided in Figure 4.10a for the proposed IRS while placing the feeding antenna at $\theta_i = -45°$ and $\phi_i = 0°$, by computing the phase distribution of each unit cell based on (2.16) using different r_1 for the distance phase. It can be observed that the quantization error and the antenna gain fluctuate stronger at shorter r_1 and convergent with longer r_1. This is because, for shorter r_1, the phase difference for each unit cell $\varphi(m,n)_d$ is more significant, leading to more quantization error variances. The quantization error is converged to 44° and the gain to 26.3 dBi with an inversely proportional relationship. This convergence is valid under the previously mentioned assumption that the illumination loss, spillover loss or the path loss are neglected, to purely focus on the effect of illumination distance. The simulation results show that increasing illumination distance is not a problem for the IRS beamforming quality.

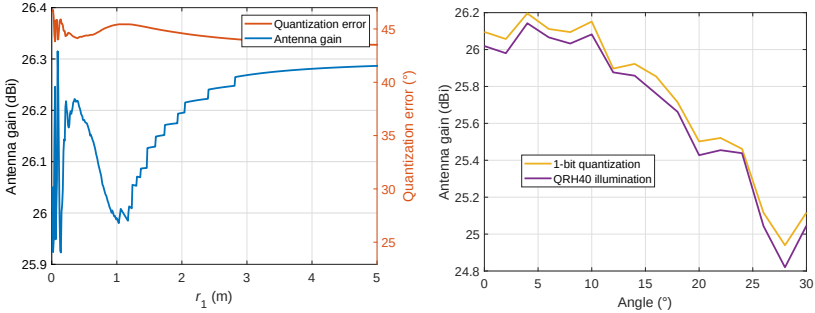

(a) Gain and quantization error vs. illumination distance. (b) Gain at different beamforming angles with/without the illumination loss.

Figure 4.10: IRS beamforming simulation using different phase resolutions.

Illumination Loss

While discussing the aperture efficiency of IRS for nearfield illumination, the concept of illumination efficiency was mentioned. In other words, it leads to beamforming performance degradation due to the power distribution imbalance among the unit cells. This is more effective for the nearfield case as each unit cell's incidence angle differs more from others, as mentioned in (4.1). From Figure 4.11, it can be observed that with $r_1 = 210\,\text{mm}$ and $r_1 = 1\,\text{m}$ the maximum absolute power difference changes less. This simulation was realized considering the effects of the antenna pattern of the QRH40 antenna [QRH] as the feeding antenna to illuminate the unit cells. As a conclusion, the maximum power difference between the best illuminated and the worst illuminated unit cell for $r_1 = 210\,\text{mm}$ is 20.5 dB, while it is only 2.5 dB for $r_1 = 1\,\text{m}$. The amplitude at $r_1 = 1m$ is lower considering a longer illumination distance. The higher power is always concentrated on the left of the IRS due to the placement of feeding antenna at $\theta_i = -45°$ and $\phi_i = 0°$, which is effectively on the left side.

For the simulation results in Figure 4.10b, the $r_1 = 210\,\text{mm}$ is used as a representation since more obvious differences should be observed than $r_1 = 1\,\text{m}$, which is at a distance converging to the farfield condition. As a result, for the beam steering from $\theta' = 0°$ to $30°$ with $2°$ angle step, the loss caused by the

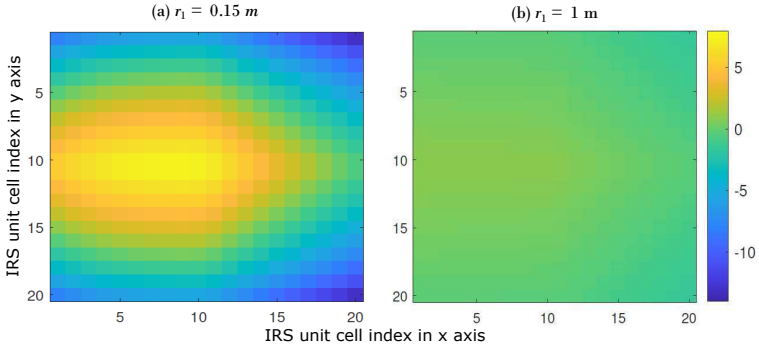

Figure 4.11: Power distribution imbalance at different r_1.

power illumination is less than 0.1 dB in comparison to the pure uniform power distribution, which is a minimal value. In this dissertation, r_1 is never chosen to be less than 150 mm, which keeps the illumination loss low. In conclusion, the non-uniform power distribution leads to acceptable gain degradation for the nearfield illumination case, which is no longer a problem for the farfield illumination case.

Positioning Mismatch

The illumination positioning mismatch may also result in additional distortions. It may be challenging to align the feeding source perfectly, especially when using farfield illumination. If the coding pattern from Figure 4.8 is computed based on a specific feeding antenna position, but the exact location is inaccurate, beamforming performance may suffer. Therefore, it is essential to examine the beamforming's positioning mismatch robustness.

To observe the IRS gain with different positioning mismatch, the antenna gain vs. positioning mismatch in percentage is presented in Figure 4.12a. In this example, $r_1 = 1$ m is used as an example. It can be observed that the IRS beamforming is more sensitive if the positioning mismatch happens towards the IRS direction and performs very robust with positioning mismatch backwards the IRS direction. This again copes with the illumination behaviour that for shorter r_1 closer to near field, the distance phase term varies more, which leads

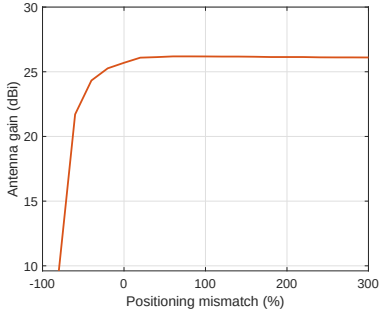

(a) Gain with respect to positioning mismatch.

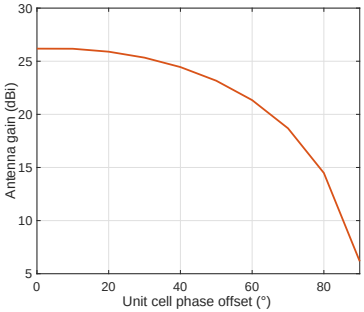

(b) Gain with respect to unit cell phase offset.

Figure 4.12: IRS beamforming simulation with distortions.

to large error if they are not correctly considered. However, for farfield range with longer r_1, the distance phase term for every unit cell becomes more and more uniform, which means that the distance phase from (2.16) is no longer playing an important role. Such property means that the beamforming performance is more sensitive to positioning mismatch for nearfield IRS illumination implementation. However, since the entire setup, including the feeding antenna and IRS, is regarded as an antenna array structure for nearfield illumination, the geometric is always optimized and perfectly aligned without any positioning mismatch.

It is also interesting to note that the optimal antenna gain is not achieved at this example's null positioning mismatch point. This is due to the presence of quantization error. Even if everything is perfectly aligned, the quantization error still causes performance degradation, which may be even less noticeable if the feeding antenna position is slightly off. This is also why the antenna gain in Figure 4.10b varies in different beamforming directions. However, the design of coding patterns cannot rely on the uncertainty of quantization's positive contribution. Consequently, the coding pattern should be computed concerning the correct feeding antenna position. If the beam steering phases are correctly computed, the IRS provides correct beamforming with only minor degradations.

Unit Cell Phase Offset

The last mismatch consideration is about phase mismatch. There are several possibilities leading to a phase mismatch. Firstly, from the design point of view, an IRS usually works in bandwidth, as shown in Figure 4.3. Due to the resonance property, the phase difference can not be guaranteed at 180° through the entire bandwidth. Secondly, the IRS unit cell phase shift is usually controlled by the microcomponent with DC biases as feeding. Along the circuit, there are also other RLC components adjusting the desired feeding voltage and current. However, due to the practical fabrication, especially for the IRS design at mmw frequency, it is sometimes hard to ensure a perfect DC input. Therefore, the microcomponent may not work at its optimum state as a unit cell expects. The possibilities mentioned above require that IRS beamforming is robust against a certain amount of unit cell phase offset. In Figure 4.12b, it shows that with 180-unit cell phase offset°, and 0+unit cell phase offset° for the 1-bit state, the antenna gain degrades. Based on the general IRS design, 30° unit cell phase offset is usually regarded as an acceptable threshold [DPCD+15], which only leads to 1 dB loss. This proves that IRS beamforming is also robust against unit cell phase offset.

4.5 IRS Beamforming Measurement Results

Based on simulations, the previous section examined the theoretical performance of IRS beamforming. The promising results encourage additional attempts to experimentally measure the IRS beamforming capability to finalize its real-world performance and assign different functionalities to various system models.

4.5.1 IRS Nearfield Illumination Beamforming

The measurement results for the IRS as an alternative antenna array with nearfield illumination are first presented based on the previous architecture.

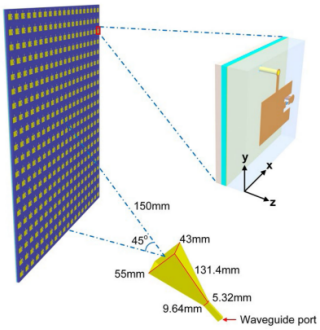

(a) Optimized setup from [WXZ+21].

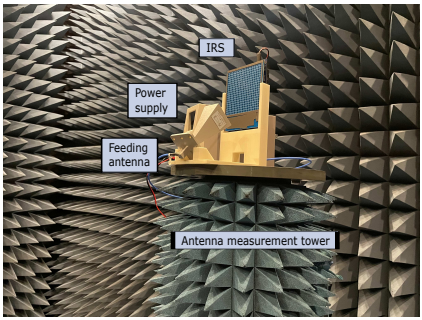

(b) Measurement setup.

Figure 4.13: Setup for IRS beamforming as an antenna array.

Optimized IRS Beamforming Setup

As mentioned above, the aperture efficiency of the nearfield IRS illumination must be optimized. Based on the suggested steps mentioned in [YYE+10], the IRS beamforming setup is optimized as Figure 4.13a. A specifically designed horn antenna is used as the feeding antenna, with its phase centre located at $\theta_i = -45°$ and $\phi_i = 90°$ of the IRS. The distance between the phase centres of the IRS and feeding antenna is $r_1 = 150\,\text{mm}$. The entire setup is placed on a rotating stage of the anechoic chamber for the array pattern measurements as presented by Figure 4.13b. The command determines desired beamforming pattern to the FPGA mentioned in Figure 4.5.

Using this setup, the loss budge parameters are listed in Table 4.1. It can be seen that most of the loss is caused by the spillover after the optimization, which is calculated to be 3.06 dB for the specific geometry. The illumination loss here is 0.26 dB which is slightly higher than the value in Figure 4.10b due to a shorter r_1. The 1-bit quantization error in this case is computed to be 2.27 dB instead of the 4 dB from Figure 4.9a, due to the reason that 4 dB is the maximum quantization loss under theoretical assumptions. In practice, due to the illumination imbalance and spillover loss, the quantization loss is effectively nerved, which also copes with the discussion of why 2-bit phase resolution can

Table 4.1: Loss factors of the measured IRS from [WXZ+21].

Factor	Loss (dB)
Spillover loss	3.06
Illumination loss	0.26
1-bit quantization loss	2.27
Element loss	0.74
Specular reflection, edge diffraction, others	2.72
Total loss	9.05

not be expected to be as favorable as simulation results in Figure 4.9a. The element loss corresponds to the square of the S11 magnitude in Figure 4.3. In addition, due to the incidence angle, a certain amount of power got reflected based on the specular reflection instead of being beamformed. This aspect is concluded with other practical losses for the last item. Overall, the measured gain of IRS at $\theta' = 0°$ is 21.35 dBi, which is 9.05 dB lower than the theoretical value from Figure 4.9, when the aforementioned losses were not considered.

4.5.2 Comparison to Phased Array

Based on the arguments in Chapter 2, an IRS in nearfield illumination case is expected to be a low-cost alternative antenna array architecture with proper beamforming ability. Therefore, the biggest competitor of IRS is the phased array. To have a practical comparison between phased array and IRS, measurement results are presented in Figure 4.14. From the black curve, a maximum of 21 dBi gain can be observed for the beamforming from our proposed IRS. From the red curve, a 16 dBi gain can be observed for the beamforming from a 16×1 phased array with the element gain of each unit to be 4.1 dBi. Based on this measurement benchmark, the pros and cons of IRS and the phased array will be discussed.

It is hard to argue between these two candidates regarding the circuit complexity. The IRS uses unit cell antennas, and the phased array utilizes antenna units like conventional patch antennas. Both of them need digital control circuits for beamforming. An IRS needs more control circuits for the phase switching

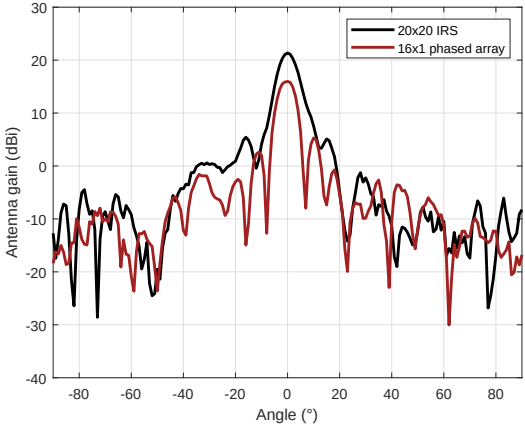

Figure 4.14: Comparison between phased array and IRS

components since more of them are required than a phased array to achieve the same performance. As an example in our setups, based on simulations, a 6×6 phased array is expected to have the similar performance as a 20×20 IRS from the antenna gain point of view. Assuming a 5-bit phase shifter, $6 \times 6 \times 5 = 180$ control lines are needed. For a 20×20 IRS, a larger number of 400 control lines are necessary. However, an IRS eliminates the multiple RF feeding circuit by over-the-air illumination from a horn antenna. Overall, this is quite a balanced competition it is hard to conclude a winner. The biggest advantage of an IRS system is the cost, including price and power consumption. To build up the mentioned phased array, the core component is a 5-bit phase shifter combining analog amplitude tuning ability with the type AWMF-0108 from [AWM]. The PIN diode based IRS element is fabricated with the type MA4AGP907 from [MA4], which is much cheaper even with increased array size. The second benefit is power consumption. Based on the experience from our measurement, the control circuit of the 16 phase shifters needs an input voltage of 10 V with an operating current around 2 A. For the IRS, we use the input voltage of 5 V with an operating current around 0.78 A.

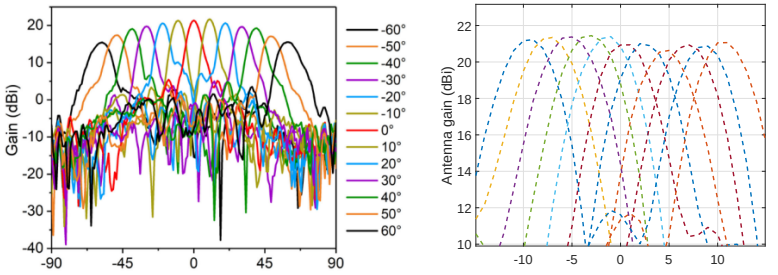

(a) Wide range beam steering from $\theta' = -60°$ to 60° from [WXZ+21].

(b) Examination of $g = 2°$ beam steering angle resolution from [LBE+22].

Figure 4.15: Beam Steering for the measured IRS.

4.5.3 IRS Beam Steering Ability

As a general definition, the beam steering in this dissertation is mainly along θ while keeping $\phi' = 0°$ for simplicity. Based on this definition, the system is easier to set, and the algorithms can be efficiently tested. Figure 4.15a shows the beam steering range for the proposed IRS, with the minimum angle $\theta'_{min} = -60°$ and maximum angle $\theta'_{max} = 60°$ defined. The gain of IRS in this measurement condition decreases with the increasing absolute value of θ' while reaching the minimum value of 15.44 dBi at $-60°$. This is caused by the effective reduction of array aperture with large steering angle mentioned in (4.4). For the same reason, beam steering beyond this defined angle range can not be guaranteed reliable performance. As mentioned in (2.12), the antenna spacing should be further reduced to avoid beam steering blindness and increase the beam steering resolution. However, a unit cell must occupy a certain space, so a limited angle resolution always exists for the beam steering. In this dissertation, $g = 2°$ is defined as the standard. In Figure 4.15b, an example of beam steering with $g = 2°$ is measured as an indication. It can be observed that the beam steering keeps in high quality with precise gain vibration under 1 dB and angle mismatch under 0.5°.

IRS Multibeam

In some situations, a single beamforming direction could be not sufficient for a reliable communication system. For example, if multiple UEs expect the same signal, the IRS is required to realize a broadcasting function but with beamforming ability for a proper SNR. Also, in some cases multipath can be implemented to enhance the capacity. These scenarios lead to the requirement to general multiple beams instead of the single beam from Figure 4.15. Due to the limited size of our proposed IRS and its 1-bit phase resolution, the generation of two beams is analyzed in this dissertation. To generate two beams, the phase distribution from (2.16) has to be modified. Instead of the steering vector of a single beam direction θ' and ϕ', additional angle contributions θ'' and ϕ'' should be considered. If we define the reference wave of single beam case from (2.16) to be

$$\xi' = e^{-j\kappa\cdot(md\sin\theta'\cos\phi' + nd\sin\theta'\sin\phi')}, \tag{4.8}$$

the reference wave for double beam case will be

$$\xi'' = e^{-j\kappa\cdot(md\sin\theta'\cos\phi' + nd\sin\theta'\sin\phi')} + e^{-j\kappa\cdot(md\sin\theta''\cos\phi'' + nd\sin\theta''\sin\phi'')}. \tag{4.9}$$

Here, θ'' and ϕ'' indicate the beamforming direction for the second beam. By abstracting the phase of ξ'' and adding the distance phase term $\varphi(m,n)_d$, the phase distribution for the double beam is derived based on [LWC+14]. In general, multiple beams can be generated by adding and averaging phase contributions from all the desired beam directions. Some examples of double beam combination among the angles $-40°$, $-20°$, $0°$, $20°$, and $40°$ are presented in Figure 4.16. It can be observed that even when one of the two-beam angles is kept constant, and only another is changed, its beamforming direction shifts $3°$ left or right from the desired direction. The reason is, that the phase for each unit cell antenna element is a joint contribution of the two-beam directions. As a consequence, not only is the power spread but also the quality of one beam will be interfered with by another. Nevertheless, this IRS offers clear double beams with good gain, which can be further implemented in required scenarios.

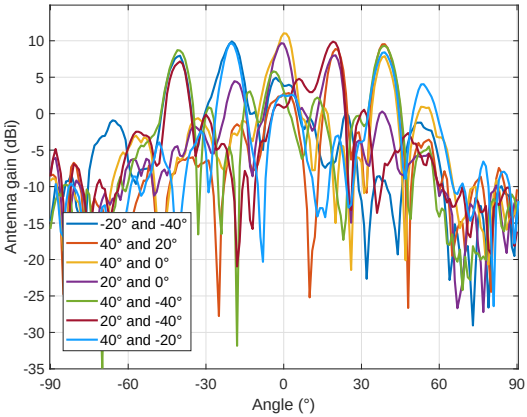

Figure 4.16: Beamforming patterns of IRS generating double beams from [LEK+21].

Broad Beam Generation

In addition to multibeams, time efficiency can be improved in specific applications if an IRS can generate broader beams. For the DoD/DoA estimation, for instance, broader beams can be used as a first approximation of the wireless path's localization. Then, for precise targeting, narrow beams can be employed. Now the problem is how to generate a sufficiently broad beam using IRS to cover a large area. There are several potential candidates for achieving this goal.

- According to antenna theory, a broad beam can be generated by reducing the number of antenna units in an array. As shown in Figure 4.17a, the solution for IRS is to randomly distribute the 1-bit state of the margin units because IRS units cannot be turned off like phased arrays because reflections always exist. The phases of the green units are determined by the computation of (2.16), whereas the phase states of the blue units are determined at random. This equates to a partially utilized IRS.
- Figures 4.17bcd demonstrate alternative methods for generating a broad beam using a sparse array similar to a phased array. Like the previous point, the shutdown/unused units have random state distributions. In b, random and computed units are sequentially distributed throughout the

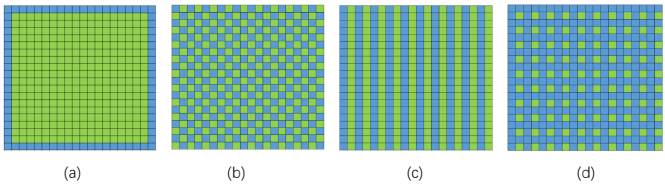

Figure 4.17: Different partial and sparse array options for broad beam generation using IRS.

entire IRS. Option c distributes random and computed units column-wise, one after the other. Only one computed unit in a small area contains 2×2 units for the option d.

- An mentioned in the last section, IRS can generate multiple beams by combining the contribution of their steering matrices based on [LWC+14]. Using this concept as inspiration, if multiple beams are positioned close together, hopefully a broad beam can be created.

The measurement results for the case in Figure 4.17a with different number of computed units are presented in Figure 4.18a. It can be observed that with the more outer units being distributed to random states, the beam gets broader but with fast gain degradation. Detailed parameters are given by Table 4.2. The spare array schemes are presented by Figure 4.18b. Detailed parameters are give by Table 4.3. However, in comparison to Figure 4.18a and Table 4.2, these schemes are not generating sufficient broader beams but sacrifice antenna gain by scattering the power to sidelobes. The measurement results of combining double beams are presented in Figure 4.18c. The solid curves show the combination of two beams with an 8° gap. The dashed curves show the combination of two beams with a 9° gap. For large gaps, the beam will be separated into two parts, and for smaller gaps, the beams are not getting broader. Therefore, the results in these situations are not presented for simplicity. The 8° gap beams average have 19.5 dBi antenna gain and 11° HPBW. The 9° gap beams have 17.3 dBi antenna gain and 15° HPBW. These results outperform the mentioned partial or sparse arrays, which is believed to be a promising way to generate broader beams. As another important point, by combining the broad beams next to each other, they can cover the desired beamforming area smoothly with the maximum degradation around 1 dB.

Table 4.2: Beamforming parameters of partial array

Active units	20×20	18×18	16×16	14×14	12×12	10×10
Antenna gain (dBi)	19.57	19.1	18.88	17.71	17.18	14.3
HPBW (°)	6	7	7	8	11	15

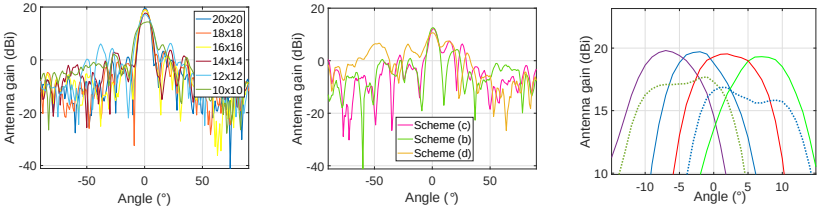

(a) Measured antenna gain of IRS using partial array.

(b) Measured antenna gain of IRS using different sparse array schemes.

(c) Measured antenna gain based on [LWC+14] by combining two beams.

Figure 4.18: Broadbeam generation for the IRS.

4.5.4 IRS Beamforming Flexibility

In the last section, measurements of IRS beamforming under optimal nearfield conditions are analyzed in depth. In this section, the feeding antenna is positioned differently than the optimal geometry, resulting in a greater illumination distance. The purpose is to find if IRS beamforming is flexible enough to generate correct beamforming with varying system settings. The nearfield illumination condition from (4.1) converges to the farfield illumination condition (4.4) as the illumination distance increases. Consequently, the following measurements would be potential evidence of the feasibility of IRS farfield illumination beamforming. This dissertation focuses primarily on single beam steering and broad beam generation because there is no exciting scenario that requires the generation of a double beam for a longer illumination distance.

Table 4.3: Beamforming parameters of sparse array

Scheme	b	c	d
Antenna gain (dBi)	12.55	12.19	10.64
HPBW (°)	7	7	11

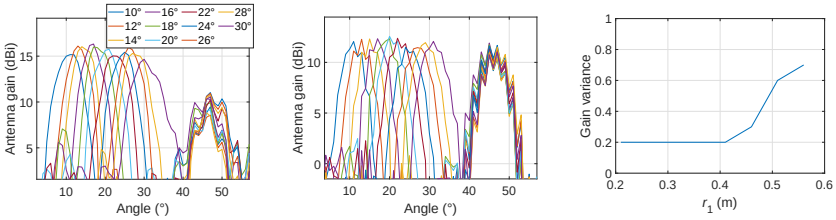

(a) Measurement results with r_1 = 210 mm.

(b) Measurement results with r_1 = 360 mm.

(c) Variance of beamforming gain at different illumination distance r_1.

Figure 4.19: IRS beam steering flexibility analysis.

Beam Steering Flexibility

As a start point, the single beam steering antenna patterns measured in the anechoic chamber is presented in Figure 4.19 with $\theta_i = -45°$ and $\phi_i = 0°$ and the beamforming direction θ' is selected in the range from 10° to 30°. This angle range avoids the shadowing from the feeding antenna and the direction occupation of the specular reflection path. It can be seen that beamforming patterns can be generated with different illumination distances, with two problems visible. Firstly, it can be observed that the gain degrades with a longer illumination distance. The measurements with $r_1 = 210$ mm in Figure 4.19a have smaller gain than the ones in Figure 4.15 with $r_1 = 150$ mm, but larger than the ones in Figure 4.19b with $r_1 = 360$ mm. Based on the model analysis from (4.1), the degradation is caused by additional spillover loss with larger r_1. Secondly, the measured beamforming results become less stable: The measured curves for $r_1 = 360$ mm in Figure 4.19b become less smooth. In addition, some beamforming angles have lower gain than other beamforming directions. For example, $\theta' = 10°$ performs worse than other beams in Figure 4.19a. On the one hand, the placement of the illumination source is not following the optimized condition, leading to performance degradation. On the other hand, it is also contributed by the feeding antenna placed on the same plane of the beam steering. If there are any undesired reflections, they will be more likely to influence the beamforming patterns, making them harder to be generated properly. One of the examples can be observed by the pattern contributions around $\theta' = 45°$ caused by specular reflection, which is a constantly existing term always taking an amount of reflective power. Comparing the specular reflection part in

Figure 4.19a and 4.19b, it can be seen that the specular reflection power for $r_1 = 360\,\text{mm}$ does not decrease with the longer illumination distance, but even slightly increases. This is because when r_1 gets longer, the reflection of each unit cell of IRS is getting closer to a specular reflection to the angle of $\theta' = 45°$.

To analyze the IRS beamforming behavior properly, the variance of beamforming gain among different steering angles are depicted in Figure 4.19c with a fixed feeding antenna angle $\theta_i = -45°$ and $\phi_i = 0°$ and an increasing illumination distance r_1. In conclusion, with the increasing r_1, the variance of the measured beamforming pattern increases. Therefore, further experiments must be verified to see if the beamforming works properly when r_1 is further increased until the farfield condition is approximately reached. Due to the difficulty of measuring antenna patterns in the limited space of the anechoic chamber, further proof is presented in Chapter 8 at the system level.

Broad Beam Flexibility

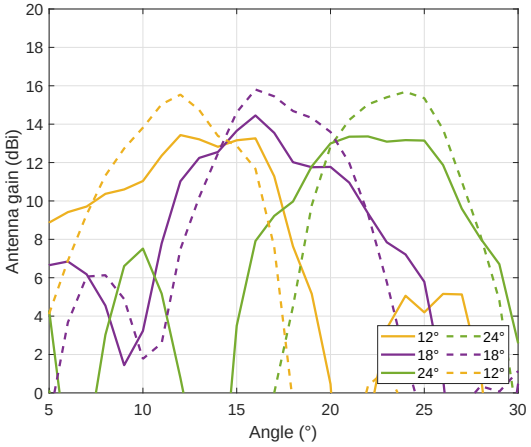

Figure 4.20: IRS beam broadening flexibility.

As mentioned in Figure 4.18, the best solution for the broad beam generation has been figured out for the optimized nearfield IRS illumination. This section

measures the broad beam performance at a different IRS illumination position, yielding the same setting as Figure 4.19a. The measurement results are presented in Figure 4.20 with dashed curves denoting the pencil beams and solid curves denoting the broad beams. Similar to the nearfield IRS illumination, the gain is lower, but the beam width is wider. The average HPBW is 8.5°, while the pencil beam from IRS farfield illumination is around 6°. However, compared to Figure 4.18c, the beams are not broadened as much as the optimized nearfield illumination case, with the coverage also less smooth. This is also caused by similar reasons discussed in Figure 4.19: The additional instability and gain vibration caused by higher spillover loss and undesired reflections. Nevertheless, since the beams are more or less broadened with good coverage ability, further analysis can be done and presented in Chapter 8.

4.5.5 IRS Loss Model Analysis

To implement IRS in different wireless communication scenarios, it is critical to evaluate its path loss model to determine the required Tx power or the maximum propagation distance. The path models mentioned in (4.1) and (4.4) are still at the theoretical level, which should be proved experimentally. From [TCC+20], IRS has been measured in both farfield and nearfield illumination cases. They have mentioned that although these two cases differ in the theoretical equation, the nearfield illumination converges to the farfield case also with r_1 shorter than the farfield margin. Therefore, the equation (4.4) can be approximated as a general equation for IRS beamforming. However, in [TCC+20], a specific incidence and reflection angle is set along the direction of specular reflection. This may lead to over-estimated performance since the reflected power along this direction would contain the specular reflection contributions. In this case, the mismatches and distortion might be masked in the measurements. Therefore, in this dissertation, an average performance through the beamforming angles $\theta' = 10°$ to $30°$ with $g = 2°$ is computed to verify the loss model approximation raised by [TCC+20]. As it assumes, the path loss model of the IRS-assisted signal propagation is raised to be mainly influenced by $(NM/r_1r_2)^2$. We measure multiple points using different r_1 and r_2 in Figure 4.21. In Figure 4.21a, r_1 is shifted with different distances, the blue curve is the measured antenna gain, and the theoretical curve in red is proportional to the factor $(NM/r_1r_2)^2$, with good matches observed. In Figure 4.21b, r_2 is shifted in an indoor system environment

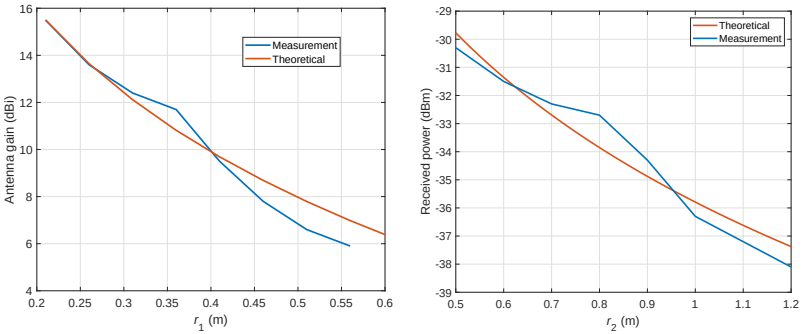

(a) Measurement results with shifted r_1.

(b) Measurement results with shifted r_2.

Figure 4.21: Measurement results for IRS path loss model analysis.

and therefore received signal power is observed (see Chapter 8 for system model descriptions), with also good matches observed. These measurements prove the accuracy of the path loss model published in [TCC+20], (4.1), and (4.4), which builds up solid fundamentals for later analysis.

4.6 Challenges of IRS

After analyzing the beamforming abilities of the IRS, it is believed that IRS can provide the necessary capabilities for various wireless communication scenarios. Therefore, it is essential to experimentally investigate the viability of IRS-based systems, which is the dissertation's primary contribution. Therefore, compared to previous studies, the following chapters discuss some IRS challenges.

4.6.1 Road to Experimental Studies

IRS research has been overgrown in recent years due to its popularity as a topic of study. The IRS study involves two primary research components. The antenna design is in the first direction. The researchers are attempting to design

IRS with various structures, operating frequencies, bandwidths, S11 values, etc. The articles [CQW+14, LC17, LC19, ZCL+18] produced fruitful outcomes. By controlling the unit cells' states, the IRS can achieve beam shaping, and beam steering [YCY+16, WQCC16]. However, the majority of these studies attempt to improve their antenna designs by meeting certain performance criteria, but they rarely examine how the antennas function in the context of the entire system, including signal processing and system coordination. Existing wireless communication systems that employ IRS are presented in [TSJP16, TLD+19, ZYD+19, ZSW+20, WZC+19, LEK+21, LWE+20]. They include some proof-of-concept works and contributions to digital signal processing. However, these works were accomplished with a single IRS and basic experiments, which limits the system's ability to develop more advanced algorithms. Accordingly, the difficulties of implementing MIMO architecture in a system with multiple IRSs are never discussed.

The second IRS research aspect is the study of communication theory. It concentrates on complex mathematical solutions that display improved performance with IRS or multiple IRSs in various communication scenarios. However, since the IRS hardware was not designed at that time, the limitations of practical IRS equipment are generally disregarded by existing algorithms. As a result of [LLdO+22], the following points cover the most significant obstacles:

Firstly, due to the wave reflection principle of IRS and the use of micro components in the design structure, each phase state of each unit cell represents an S11 level that cannot be turned off. This implies that an IRS cannot shut down units like a phased array, and communication algorithms will likely disregard this property. As stated in the existing IRS designs [CQW+14, WXZ+21], the IRS unit cell phase shifts are achieved by electronically controlling the micro components, with inexpensive PIN diodes being the most popular choice. These components alter the resonance behaviour of the unit cells, thereby changing the directivity of reflected beams. Therefore, 0 V is not off for such components but rather one of their resonance states. In addition, because the unit cell always occupies a position in space, signal reflections will always radiate from it. Consequently, such wave illumination through the air cannot be turned off like a phased array element in a circuit. Any channel estimation algorithms attempting to derive the CSI at each IRS element (such as the sparse array concept in [EMLZ18] and channel extrapolation in [ZLG+21]) are either impossible or difficult to implement with reliable performance in this case. Data transmissi-

on methods cannot work properly without accurate CSI at each PM element. In [AEALH14], for example, its algorithms can jointly design the precoding matrix to be as close as possible to the digital optimal precoding. However, the scheme is difficult to implement because it requires complete CSI at each antenna unit to calculate the optimal precoding matrix.

Secondly, as shown in Figure 4.9, it is challenging to design an IRS with a higher phase resolution. Consequently, 1-bit resolution is typically considered, or at most 2-bit resolution if the PIN diode design is to be preserved. This further complicates the direct adaptation of conventional MIMO and hybrid beamforming algorithms. If more PIN diodes are constructed on the IRS unit cell, better phase resolution could be attained; however, this would require highly complicated designs, negating the low-cost advantage of using IRS. Higher or infinite phase resolutions are considered in the current hybrid beamforming algorithms, which may be unsuitable for the IRS case. For example, the minimum phase resolution considered in [AEALH14] is 4 bits, which is more realistic for a phased array but not for an IRS at 28 GHz. As for [SR15], only beam patterns are mentioned to formulate the codebook and are theoretically simulated without mentioning specific information regarding beam generation. Also, in [AEALH14], with fewer RF chains, phase resolution, and array size, the gain of their algorithms become less noticeable. If these numbers are reduced in measurement, the advantages of the implemented algorithms may be hidden by the hardware imperfections caused by real-world IRS.

Lastly, the illumination architecture limits the system configuration when multiple IRSs are necessary. Due to the dependence of IRS beamforming on free-air illumination, the system architecture is less flexible than those considered in theoretical studies. In [AEALH14], the hierarchical codebook algorithm with broader beams is presented as one of the most representative beam training studies. This paper focuses on a hybrid MIMO beamforming architecture in which all digital beamforming chains have access to each sub-array. For IRS, the position of the feeding antenna is crucial for the entire setup, as the free space propagation distance to each unit cell must be accurately computed. Therefore, multiple illumination sources should share the same IRS to create an architecture equivalent to fully-connected hybrid MIMO beamforming. There are bifocal PM solutions described in [NYE13], but the illumination sources must be placed symmetrically from the PM perspective, and the beam scan is highly dependent on the tuning of this spatial distribution. In addition, the interferences

caused by the two illumination sources reduce the beamforming accuracy and resolution, which is insufficient for recalling the algorithms in [AEALH14].

Due to these obstacles, it is difficult or inappropriate to implement existing wireless communication algorithms in IRS-based systems, particularly when the system itself has not been thoroughly studied. This may also explain why IRS-based systems have seldom been studied. In conclusion, since IRS has become a prevalent topic in recent years despite a lack of sufficient research, this dissertation aims to prove its feasibility in wireless communication systems. Following the trend of next-generation systems, the following chapters of this dissertation will focus on multiplexing schemes, mobile communication, MIMO, and hybrid beamforming. This crucial benchmark cannot be bypassed if IRS designs are to remain competitive in the market for future wireless communication technologies. In order to accomplish this, we discuss the key functionalities of a wireless communication system to demonstrate how the IRS beamforming control and signal processing are merged into one system, how the novel channel estimation is operated, and CSI can be derived under the IRS architecture challenges, how the data transmission and recovery can be achieved, and how the feasibility of the entire system is demonstrated. In order to conduct a comprehensive analysis, it is necessary to include theoretical and measurement aspects, to realize proper performance and reasonable complexity.

4.6.2 IRS Practical Considerations

Based on the observations from Figure 4.21 and (4.4), it can be concluded that the Rx power of the IRS-assisted communication system changes with illumination distance, propagation distance, and the IRS size. Since the discussions for Figure 4.21 prove the accuracy of (4.4), it can be implemented as a general approximation for the IRS size, with the received power proportional to $(NM/r_1r_2)^2$. This allows us to estimate the required IRS size for practical cases. Based on the Federal Communication Commission (FCC) effective isotropic radiated power (EIRP) standard, we use 75 dBm as its maximum value. Then based on the received power standards for 5G mobile phones from [pow], we distinguish the signal strengths at different levels. The IRS antenna gain uses the average value derived from Figure 4.19a and proportionally changes based on the $(NM/r_1r_2)^2$. Assuming the number of units along one IRS dimension to be $N = M$, the required number of units for different signal strengths is presented

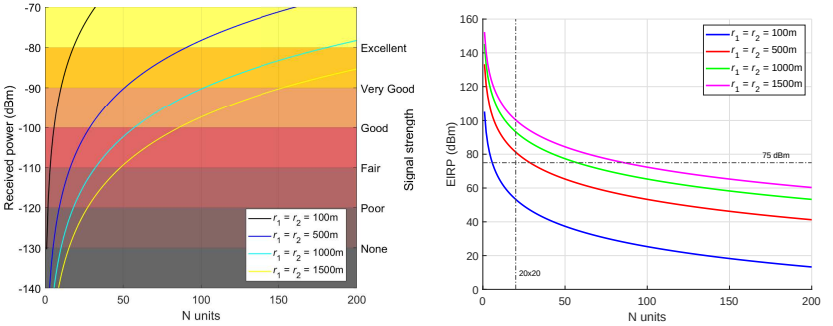

(a) Required number of IRS units for different signal strengths.

(b) Required number of IRS units for different EIRP.

Figure 4.22: IRS size discussions.

in Figure 4.22a, using a few fixed illumination and propagation distances r_1 and r_2 at 28 GHz as examples. In general, a larger IRS supports longer distance and provide larger Rx power. In order to reach a good signal strength, the number of units can also be changed based on how large EIPR can be provided at the base station, as presented in Figure 4.22b. Our implemented IRS size of 20×20 is marked by the dashed line, as well as the 75 dBm EIRP standard.

Another interesting comparison would be using specular reflection as a benchmark. The specular reflection assumes a surface with infinite size, and the destination is precisely at the reflection direction of the incidence wave. In this condition, the received power follows

$$P_r = \left(\frac{\lambda}{4\pi(r_1 + r_2)} \right)^2 G_t G_r P_t . \tag{4.10}$$

Figure 4.23a shows clearly how large an IRS is required to outperform specular reflection based on the distances. For example, when $r_1 = r_2 = 100\,\text{m}$, the IRS has to include $N = 290$ units to achieve the same performance as specular reflection, which is 1100 when $r_1 = r_2 = 1500\,\text{m}$. Figure 4.23b shows how large the IRS should be to achieve the same performance as specular reflection assuming $r_1 = r_2$. It can be observed that a large size of IRS is required to

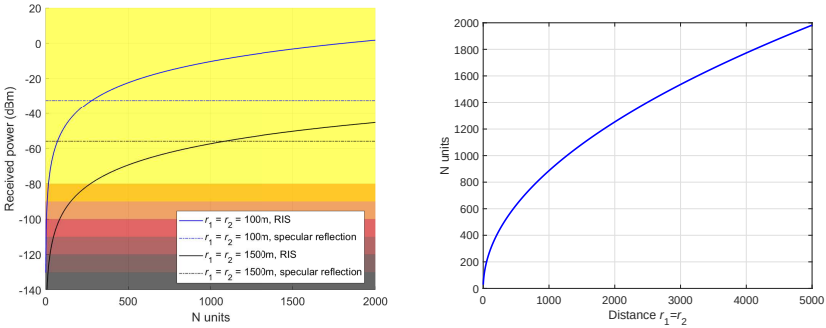

(a) Relationship between IRS and specular reflection.

(b) Required number of IRS units for the same performance as specular reflection.

Figure 4.23: IRS versus specular reflection.

achieve the same performance as specular reflection. However, it is worth a short discussion if IRS and specular reflection are always comparable. First, an IRS provides flexible beamforming but specular reflection with a fixed angle. Second, our IRS model is based on a practical design, but the specular reflection caused by the building should have its lossy coefficient, which is not yet considered. Therefore, the performance of specular reflection can be overestimated at this moment, which could be only used as a benchmark.

By zooming to a single unit with $N = 1$, a single unit is assumed for the IRS. In this case, an antenna gain of 1.34 dBi is derived. Compared to the simulation results for the beamforming patterns using 1.4 dBi for the unit cell gain according to the design in [WXZ+21], only a small mismatch exists. This proves the fact that our proposed IRS has a proper performance and the measurement results have high accuracy.

4.7 Conclusion on this Chapter

This chapter focused on defining the novel architecture for antenna arrays: intelligent reflecting surface. First, its general definition was explained, followed by introducing a promising IRS design operating at 28 GHz, including the unit

cell performance, array architecture, and beamforming method. Then, for further research, the IRS application type is divided into alternative antenna array and signal reflector cases, corresponding to nearfield and farfield illumination, respectively. For nearfield illumination, the feeding antenna is positioned in the near field of the IRS array, and the entire architectural geometry must be optimized. For farfield illumination, the feeding antenna is positioned in the farfield or close to the farfield of the IRS array, and the path loss model is calculated using the cascaded Friis formula. These two application types are important IRS architectures that will be studied in depth using various system models in later chapters.

Before analyzing IRS from a system perspective, its theoretical beamforming performances are simulated, and this chapter proves beamforming's accuracy, resolution, and robustness. The experimental performance of IRS beamforming with the proposed architecture was then validated through measurements. In addition, for cases of optimized nearfield illumination, comparisons to phased arrays and the generation of adaptive beamforming are presented via measurements. They are crucial foundations for the advanced beamforming strategies in the later chapters. Regarding farfield illumination, measurement results proved the beamforming flexibly with variant feeding antenna position converging to the farfield. The accuracy of the path loss models for both IRS application types is proved by referencing the measurement results. Based on these models, it is possible to predict the required IRS size for different illumination distances, propagation distances, Rx and Tx powers based on the measurement results of an IRS of known size. This novel analysis, which has never been discussed in visible publications, helps to determine future IRS demonstration requirements based on real-world conditions.

In addition, the IRS's challenges were discussed in depth. The main issue with the current IRS research stage is the lack of measurement and experimental studies. Thus, numerous algorithms and strategies have not been demonstrated to be effective. This is the crucial motivation for this dissertation, with proof of concepts and adaptive solutions listed in later chapters to address these challenges.

5 28 GHz MIMO Testbed

Before the theoretical studies are validated into experimental analysis, the hardware implemented in this dissertation are described. These devices are essential for the measurement of IRS-based systems. Since different system scenarios are considered, specific system models for each experiment will be introduced in the following chapters. Therefore, this chapter mainly focuses on the general system model and the individual components, which will be combined into complete systems later.

5.1 General System Model

In Figure 5.1, a general system model representing the experimental setup in this dissertation is depicted. The start of the system is a host PC, which realizes the digital signal processing flow represented in Figure 3.1, both in real-time or offline possible. Additionally, it also sends commands to the FPGA, which finally controls the beamforming of IRS, as mentioned in Figure 4.5. In this dissertation, the IRS is placed at the Tx side assuming a BS architecture. Afterwards, software defined radios (SDRs) are used at the Tx and Rx to realize the conversion between BB and intermediate frequency (IF). In this dissertation, the IF frequency is generally centered at 2.66 GHz. Next, the conversion between IF and RF frequency is realized by RF modules, which are the frontend modules at Tx and the backend modules at Rx, including the necessary components such as amplifiers, mixers, and filters. The RF frequency is generally centralized at 28 GHz. Finally, a local oscillator (LO) signal is generated and fed into the Tx and Rx modules equivalently, which avoids phase offset. In the end, the wireless channel is affected by the IRS/IRSs, either with nearfield or farfield illumination cases. In general, to ensure synchronization between Tx and Rx modules, the same pulse-per-second (PPS), 10 MHz reference signals are fed to all used SDRs. The same local oscillator (LO) signal is fed to Tx and Rx

RF modules. The operations above avoid any frequency, sampling, and phase offsets in the system. Furthermore, unless otherwise stated, the henceforth presented results are functions of the measured input power of the Rx SDR. The following sections will introduce the devices mentioned above in detail. For reproducibility, the possible replacements for the devices are also mentioned.

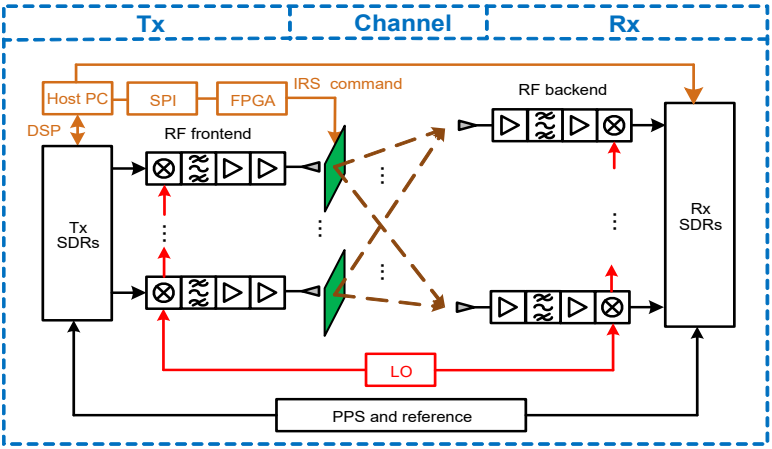

Figure 5.1: The general model for IRS-based communication systems.

5.2 Central Control Unit

In communication systems, the core operations are usually managed by a central control unit, which is realized by a host PC in this dissertation. The host PC in the measurements is equipped with four cores Intel i5-7300U central processing unit (CPU) which operate at 3.33 GHz. Besides, the operating system is a 64-bit version of Ubuntu 18.04.3, and the installed GNU Radio release is the GNU Radio 3.7 Legacy version. The host PC controls the signal generation and signal post-processing using MATLAB, and also controls the SDR operations and sends command for beamforming of IRSs through the serial peripheral interface (SPI) to FPGAs. In general, the host PC can be replaced with any type. With a more powerful CPU, the system can support higher sampling rate leading a wider bandwidth as well as faster signal processing.

5.3 Signal Processing Tool

The generate communication signals, the device utilized in this dissertation is called software defined radio (SDR). This section provides a brief introduction and implementation strategy for the SDR devices utilized in this dissertation. Other radio frequency systems-on-chip (RFSoC) can be utilized and developed to achieve comparable performance as alternative choices.

SDR devices are used to convert signals between BB and IF. Ettus Research's universal software radio peripheral (USRP) X310 devices are being used as a SDR option in this dissertation. Figure 5.2 depicts the USRP platform for designing and deploying next-generation wireless communications systems. In addition to sufficient hardware performance, the open-source software architecture of X310 supports a cross-platform USRP hardware driver (UHD) so that the host PC can access USRP hardware functions, which facilitates GNU Radio as the development framework. Each USRP X310 contains two built-in transceiver card slots for two separate daughterboards that can establish two Tx or Rx digital chains. Multiple USRPs can be connected to an Ethernet switch for parallel operation at higher MIMO orders. To realize a reliable performance, it is default to use only Tx channels or only Rx channels on a single USRP to avoid mutual interference in this dissertation. In order to achieve a high data throughput, the recorded samples are transferred between the USRPs and the host computer via one Ethernet interface per device.

Figure 5.2: USRP X310 from Ettus Research [USR].

The SDRs are controlled by the host PC using the GNU Radio software. Its primary function is to control the transmission of signals. This software can be programmed by Python scripts or a graphical user interface. In Figure 5.3, the control of Tx USRP is used to illustrate an example. As the signal generation

is performed in MATLAB, the GNU Radio flowgraph for the transmitter side consists of only two file sources that read previously generated binary files. Then, using the GNU Radio "Float To Complex"block, the real and imaginary components of the generated complex signal are read from separate files and combined into a stream of complex samples. This complex stream is ultimately sent to the USRP Sink block provided by the "gr-UHD"module, which configures the USRP during initialization and sends the samples to the USRP hardware via Ethernet, where it is converted into an analog signal, fed to the RF frontend module, and transmitted by the antenna. Thus, the UHD: USRP Sink has many configurable parameters that can be matched to the hardware setup, beginning with the device's Internet Protocol (IP) address in the local network and extending to the synchronization options, sample rate, and desired intermediate frequency for the up-conversion. Since the USRP X310 has two daughterboards, each with a TX/RX port and an RX port, the user must specify which subdevices are connected to the antenna setup.

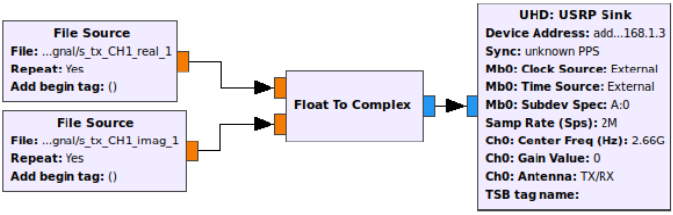

Figure 5.3: An example of GNU Radio flow graph interface for the Tx SDR control.

The blocks in Figure 5.3 are the software's default blocks, which can be utilized directly. There are also opportunities to design a custom block that validates the necessary signal processing. Further information on developing GNU Radio software is available in [Gnu].

Multiple SDRs require synchronization among them for proper functioning. There are two ways to ensure synchronization. For the first solution, the 10 MHz references and PPS signals are generated by an external source. For instance, the OctoClock CDA-2990 from Ettus Research from [Oct] in Figure 5.4 is used for measurement and is a helpful accessory for multi-USRP systems that require synchronization to a common timing source. In this situation, each SDR utilizes the same external reference signal. In the second solution, one

Figure 5.4: OctoClock CDA-2990 from Ettus Research [Oct] connecting with SDRs for synchronization.

SDR uses its internal reference and outputs this signal to all other SDRs via a daisy chain connection. In this instance, all SDRs utilize the external reference signal except for the SDR, which serves as the reference source. Since the OctoClock from Figure 5.4 is a professional tool to provide reference signals, it offers more reliable performance than the daisy chain option, which is why it is favorable in Figure 5.1.

5.4 IRS Control Interface

To realize proper control of the IRS, a reliable interference needs to be established to the central control unit (host PC). As shown in Figure 4.5, beamforming is achieved by controlling the input voltage to the PIN diodes with an FPGA. The connection between the host PC and the FPGA in this dissertation is the MCP2210 USB-to-SPI protocol converter with GPIO Pins from [mcp]. SPI is a high-speed, full-duplex protocol with a master-slave architecture developed on Motorola's MC68HCXX series of processors. In this dissertation, it is used to transmit the command that configures the beamforming pattern of IRS. The device converts the protocol between the computer's USB port and the SPI bus connection to the FPGA. SPI governs the communication between slave and master devices in general. Four logic signals are specified for the SPI bus:

- SCLK: Serial Clock (output from the master)
- MOSI: Master Out Slave In (data output from the master to the slave)

- MISO: Master In Slave Out (data output from the slave to the master)
- CS: Chip Select (Select the slave when multiple slaves exist)

The SPI protocol enables the transmission of binary data bit by bit, as opposed to conventional serial communication, which requires transmitting at least 8 bits of data at once. In addition, the SPI protocol also facilitates data exchange because the data input and output lines are independent, allowing simultaneous data reading and writing. Since the main focus of this dissertation is not the development of SPI, the detailed information is neglected. For further interests, a tutorial [Dha18] can be referred.

5.5 RF Modules

The signal conversion between IF and RF frequency is realized by RF frontend and backend modules designed at IHE, which have been presented in [Eis21]. The circuitry of the modules is presented in Figure 5.5. Each module contains four RF chains connected to four digital chains with the SDR input/output. The inner structure of RF modules is illustrated in Figure 5.6. Starting with the Tx side, the 2.66 GHz IF signal at the output of SDRs is up-converted with RF frontend module to 28 GHz with the mixer HMC264LC3B [HMCb] using twice the local oscillator (LO) frequency, which is 12.67 GHz. After undergoing an RF band pass filtering, the RF signal will be amplified using a low-noise amplifier (LNA) of the type HMC751LC4 [HMCa] and a power amplifier (PA) of the type HMC863ALC4 [HMCc]. The total RF frontend gain is expected to be 32 dB with −7 dBm as the input 1-dB compression point, and the output of the RF frontend module will be connected to the feeding antenna of the IRS. The signal down conversion is the reversion of up-conversion using the RF backend module with an expected gain of 33 dB, and the received baseband signal at the Rx SDRs output will be processed in the host PC. Only LNAs are used in the RF backend module to keep the noise level as low as possible at the Rx. To avoid LO mismatch distortions, the same LO signal with a level between 4 dBm and 8 dBm is fed into the RF front- and backend modules via a splitter. A low pass filter is equipped at the input of Rx SDR to protect the equipment from undesired signal contributions. Based on the final measurements considering additional losses via the circuitry, the average gain of the RF frontend module

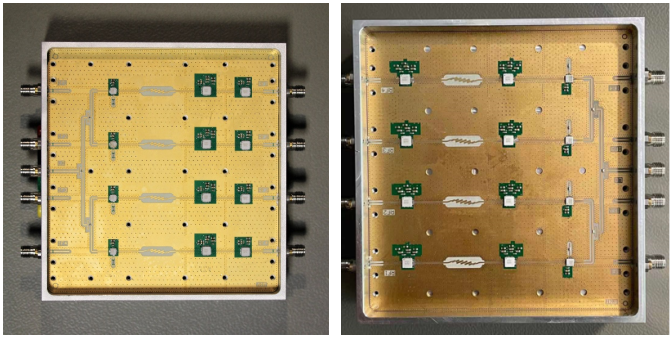

(a) RF frontend module. (b) RF backend module.

Figure 5.5: Photo of RF modules implemented in this dissertation.

chains is around 24 dB, with the difference between each pair of channels less than 1dB. For the RF backend, the gain is around 26 dB. Since the author of this dissertation is not the designer of these modules, only its principles are introduced. For detailed information on the RF modules, please refer to [Eis21]. From the system point of view, the RF modules are replaceable parts which can be adjusted with different system requirements.

5.6 Conclusion on this Chapter

This chapter defines the general system model for the IRS-based wireless communication system, from which the following chapters derive the fundamental system architectures. The system's devices are introduced to validate their coordination and cooperation. This system model provides a potential solution for incorporating IRS into the system and aligning the beamforming control and signal processing chains.

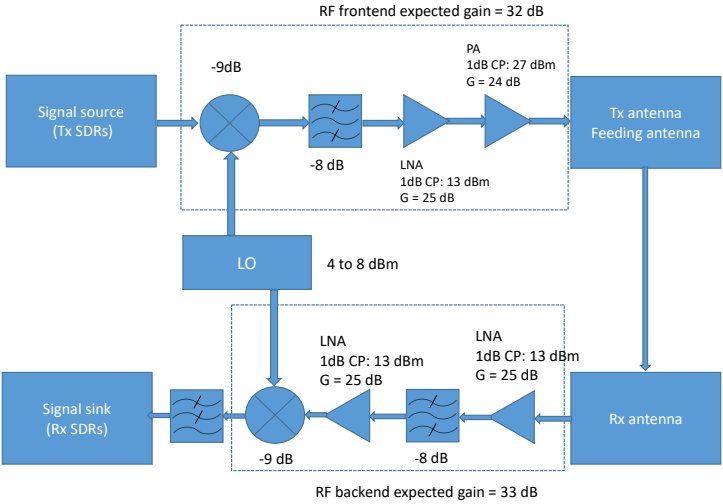

Figure 5.6: Structure of RF frontend and backend module.

6 IRS Beamforming Strategies for Wireless Communication

After proving the capability of IRS beamforming, it is reasonable to believe that an IRS-based wireless communication system merits further investigation. This chapter establishes experimental systems for different communications scenarios utilizing a single IRS as an alternative antenna array using nearfield illumination. The measurement outcomes include primary proof of concept and complex mathematical research.

6.1 IRS Beamforming Strategies and System Performance

In this section, IRS-based systems are established utilizing the beamforming options mentioned in Section 4.3.1. The main task is to prove such systems' basic feasibility for further investigations.

6.1.1 Basic SISO realization using intelligent surface

As the first attempt to prove the functionality of the IRS-based wireless communication system, a SISO system is demonstrated. This section reuses some texts and figures in [LWE+20] © [2020] IEEE. The system model in Figure 6.1 is the simplest version of Figure 5.1, using the hardware components mentioned in Chapter 5. For a SISO chain, only one SDR is required for Tx and Rx side, with one digital chain occupied. Moreover, only one chain from the RF modules is needed. At the Tx side, an IRS is set up using the optimized nearfield illumination as an alternative antenna architecture with beamforming ability and trying to get access to the Rx via wireless path.

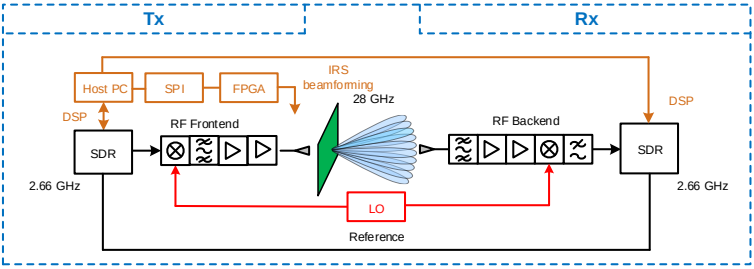

Figure 6.1: The block diagramm of SISO communication system using IRS beamforming from [LWE+20].

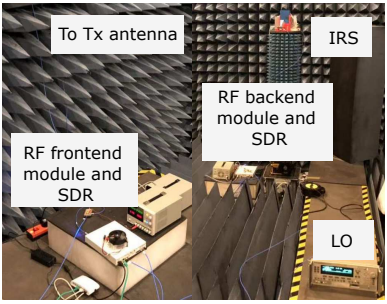

(a) The SISO measurement system in an anechoic chamber from [LWE+20].

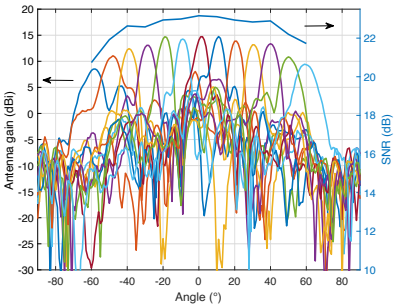

(b) The SISO measurement results and IRS beamforming patterns from [LWE+20].

Figure 6.2: IRS SISO system measurement environment and results.

For the initial attempts to avoid any additional distortion, the system is demonstrated in an anechoic chamber presented in Figure 6.2a, including all the necessary components from Figure 6.1. With a fixed geometric Rx antenna, the IRS Tx is placed on a rotating tower similar to the beam pattern measurements from Section 4.3.1. The Tx signals are QPSK sequences as described in Figure 3.2a. In this model, the general hybrid beamforming equation from (2.31) with $N_s = N_d = 1$ and $M_r = M_d = 1$ stands. Since there is no analog beamforming at the Rx, so the term $\boldsymbol{F}_{Rx,RF}$ can be removed or regarded as $\boldsymbol{F}_{Rx,RF} = \boldsymbol{I}_{N_r}$. The IRS of 400 unit cells determines $N_t = 400$, with the coefficients in $\boldsymbol{F}_{Tx,RF}$ computed based on (2.16) regarding desired beamforming direction. For each beamforming direction, the analog beamforming from the IRS is determined,

which can be regarded as a part of the effective channel for digital beamforming mentioned in (2.17). Therefore, the system leads to an effective SISO chain so the least square channel estimation from (3.3) can be directly used to derive the estimated channel matrix for digital channel matrix $\hat{\boldsymbol{H}}_d$. Afterwards, by utilizing the ZF equalization from (3.5), the recovered signal can be derived, and the quasi SNR can be derived by computing the MER of the recovered symbols sequence using (3.2). The system SNR using the different beamforming patterns can be derived by rotating the tower in corresponding directions. The results are given by the curves in Figure 6.2b with 10° angle resolution from $\theta' = -60°$ to 60°. It can be seen that the measured beamforming patterns match well with the desired beamforming directions. The angle mismatches are smaller than 1° with the highest gain around 14 dB. The solid curve above the farfield patterns in Figure 6.2b expresses the SNR for the corresponding beamforming directions. As an observation, the SNR values are proportional to the measured antenna gain.

Please notice that the measured gain in Figure 6.2b is smaller than the ones in Figure 4.15 because the IRS for this measurement was a prototype for a simple proof of concept. However, in comparison to the double beam measurements from Figure 4.16, the same IRS is used, and reason results are derived: the generated double beams have 3 to 4 dB less gain than the single beam from Figure 6.2b, due to the halved power and quantization errors.

6.1.2 Channel Estimation using IRS

The measurement from the last section was realized by pre-knowledge of the Rx position from the IRS point of view, which is practically unavailable. Therefore, to further realize different wireless communication scenarios, algorithms for channel estimation have to be discovered to determine the IRS's beamforming direction. Due to the challenges mentioned in Section 4.6 regarding the CSI derivation at the IRS unit cells, beam training is a promising way to realize proper channel estimation. In the following sections, different beam training algorithms regarding the feasibility of IRS will be discussed.

Exhaustive Search Algorithm

From the results in the last section, it can be concluded that for the channel estimation of an IRS-based wireless communication system, the final goal is to align the beamforming direction properly and formulate the effective digital channel matrix $\boldsymbol{H}_d$. In other words, since $\boldsymbol{H}_d$ contains the contribution of the IRS beamforming as mentioned in (2.17), it is important to optimize the analog beamforming part first. One of the beam training solutions is known as an exhaustive search. Since the analog beamforming matrix $\boldsymbol{F}_{Tx,RF}$ is realized by tuning the phase states of the IRS unit cells, the optimum combination can be found by exhaustively reviewing all the phase combinations. However, this leads to a very high complexity since, in total, $(NM)^2$ combinations are required to be examined, assuming 1-bit IRS phase resolution. Fortunately, since the wireless communication channels are usually path-dependent, a more efficient solution is to search and determine the optimum path between Tx and Rx instead of exhaustively examining the phase combinations. This leads to the idea of searching for the DoD or DoA. First, an interesting exhaustive search area has to be determined, saying the system is interested in the best path in this range, usually defined by angles. As mentioned in Figure 4.15, the interested beam steering in this dissertation is along one dimension with $\phi' = 0°$ and the starting angle $\theta'_{min} = -60°$ till the ending angle $\theta'_{max} = 60°$ with angle increment of $g = 2°$. Under this assumption, the optimum path can be discovered using a peak detection regarding the metric performance following

$$\theta'_{op} = \text{argmax}_{\theta'} Q(\Theta'), \tag{6.1}$$

with $Q(\Theta')$ to be the quality factor with respect to the beamforming direction set Θ' containing all the possible θ', and θ'_{op} to be the detected beamforming direction implemented in (2.16) to derive the optimized $\boldsymbol{F}_{Tx,RF}$. In this dissertation, three different metrics can be used to indicate the quality factor:

- Rx power: The Rx power P_r from (2.6) can be used as the quality factor to search for the strong existing path. When the beamforming points to a stronger path, the Rx power increases.

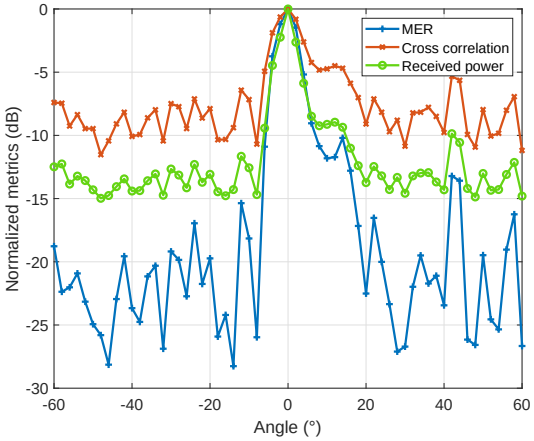

Figure 6.3: Exhaustive search for channel estimation using different performance metrics from [LLdO+22].

- Cross-correlation: The cross-correlation C_{cross} between the Tx and Rx signal can be used as the quality factor based on (3.19). When a stronger path is occupied, the Tx and Rx signals have higher cross-correlation values.

- MER: The MER derived from (3.2) is a reliable quality factor. When the IRS beamforming formulates a better wireless communication channel, the system has better SNR/SINR, which is finally corresponded to a higher MER value.

Using the three metrics for (6.1) as the quality factor, analog beam training can be operated, and the estimated DoD can be derived. The similar system model from Figure 6.2a is set up in an indoor environment without interference from other UE. In this case, all three metrics show consistent performances and indicate the measured DoD at 0° as presented in Figure 6.3 using QPSK as training symbols. The power is proportional to the square of the Rx signal's amplitude, while the cross-correlation is determined by the Rx power multiplied by the power-uniform Tx signal. Consequently, the maximum and minimum values of the cross-correlation quality factors have a smaller difference. When

Table 6.1: Properties of different metrics.

Metric	Advantages	Disadvantages
Rx power	Simple computation	Distorted by interference
Cross correlation	Overcomes some distortions	Convolution with medium complexity
MER	Most accurate	Highest complexity

the IRS beamforming is not directed to the strongest DoD, it is possible to observe that the MER curve overlaps the power curve at higher values but drops more rapidly for lower Rx power. This inconsistency is a result of the multipath indoor environment. When the beamforming direction precisely aligns with the optimal DoD, only the beamforming sidelobes contribute to the reflection path. In these situations, the interference caused by the reflection path is relatively low, and neither the power nor the MER is affected. When the beamforming is aimed in different directions, multipath interference will increase. The additional interference is complexly added to the desired signal, resulting in a combined power value for the Rx power. This value is not necessarily low, as it depends on the phases of these paths. Similarly, interference, a delayed desired signal, also contributes to the correlation. However, such interference results in the rotation of the constellation or the signal spreading after recovery, degrading MER. Therefore, this effect cannot be detected accurately by observing the Rx power, but it becomes more apparent when observing the MER. In addition, the system has additional practical side effects, such as reflections from the transmission lines of the RF modules, leakage between channels, etc. In other words, the system is distorted not only by noise but also by other effects, which is why MER is considered a quasi-SINR and not SNR in this dissertation. Overall, these results illustrate the expected behaviour of the three metrics. Comparing their advantages and disadvantages are revealed by the characteristics listed in Table 6.1. The MER provides the most precise results for computations until the final signal processing step. The Rx power is significantly more efficient because the power value can be easily observed at any stage of the Rx, but it provides the poorest performance, particularly in the presence of interference. Cross-correlation can be viewed as a trade-off between the two alternatives above.

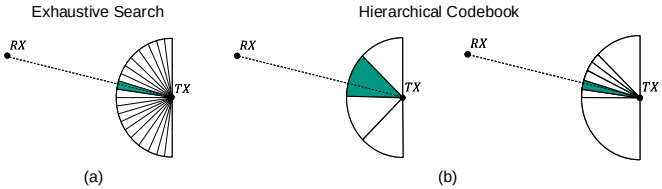

Figure 6.4: Expressions for channel estimation algorithms. (a): Exhaustive search algorithm. (b): Hierarchical codebook algorithm with $S = 4$.

Hierarchical Codebook Algorithm

An exhaustive search algorithm needs to generate all the beamforming patterns. Although the time cost is reduced compared to observing all unit cell phase combinations, it is still a time-consuming algorithm. As a solution, there is another algorithm called hierarchical codebook which increases the time efficiency of beam training by separating the entire area of interest into different sectors [AEALH14]. Based on the reuse of texts and figures from [LLW+21] © [2020] IEEE, this section focuses on how the hierarchical codebook algorithm is realized by IRS channel estimation.

The comparison of exhaustive search and hierarchical codebook algorithm is presented in Figure 6.4. When the DoD is known in an area without its precise position, exhaustive search algorithms scan the pencil beam in this area and find the path based on the metrics mentioned in (6.1). The hierarchical codebook algorithm divides the entire area into a few sectors with a broader range. The peak detection using the metrics first takes place among the S sectors. Once the best sector is determined, higher-level sectors or pencil beams can be used for further searches. In this case, the time efficiency increases since the sectors are usually much broader than a pencil beam coverage which needs fewer time slots to finish the scan of the entire area. For IRS, broader beams can be generated, as mentioned in Figure 4.18c, so an IRS-based system can realize the hierarchical codebook algorithm. In addition to the pencil beams generated in Figure 4.15, an experimental comparison to exhaustive search sharing the similar system model in Figure 6.1 can be achieved.

In this experiment, the Rx power P_r is used as the metric and measured at the Rx SDR input. The DoD is defined to be at an unknown direction within the range from $\theta' = -10°$ to $\theta' = 10°$, and the training duration of $t_s = 0.5\,\text{ms}$

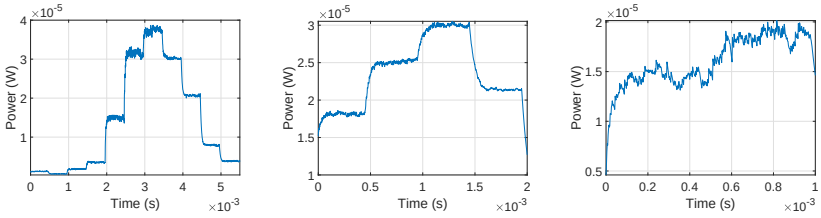

Figure 6.5: Figures for channel estimation measurements. (a): Exhaustive search algorithm. (b)(c): Hierarchical codebook algorithm with $S = 4$ and 2.

is set for each angle for the beam steering. Three different measurements are designed for comparison in Figure 6.5:

- Exhaustive search: From $\theta' = -10°$ to $\theta' = 10°$ with $g = 2$. Figure 6.5a shows the performance of the exhaustive search algorithm with 11 stages observed in 5.5 ms. By implementing a peak detection, the DoD is estimated to be at 2°, corresponding to the 7th stage from the entire scan.

- Hierarchical codebook with $S = 4$: This is realized by using the broad beam from Figure 4.18c with the gap of 8°, which separates the entire area into four sectors. According to the observation, the peak appears correctly at the third sector where 2° is covered. Afterwards, the correct DoD can be discovered by using an exhaustive search from 0° to 4° in the third sector. This procedure requires 3.5 ms.

- Hierarchical codebook with $S = 2$: Broader beams can be generated from Figure 4.18c with the gap of 9°, which separates the entire area into two sectors. According to the observation, the peak appears correctly at the second sector where 2° is covered. Afterwards, the correct DoD can be discovered by using an exhaustive search from 2° to 8° in the third sector. This procedure requires 3 ms.

In general, if we operate the entire beam scanning from $-\theta_s^\circ$ to θ_e° with angle step $g°$. Assuming the time duration for each scanning stage is t, the total required detection time for the exhaustive beam training algorithm is $((\theta_e + \theta_s)/g + 1) \times t$. For hierarchical codebook algorithm with S sectors for the first level and

exhaustive search for the second level, the required detection time is reduced to $((S + (\theta_e + \theta_s)/(S \times g) + 1) \times t$. In practice, the detailed number of term $(\theta_e + \theta_s)/(S \times g)$ should be considered based on the pencil beam width. For example in Figure 6.5b and 6.5c, 3 and 4 number of pencil beams are used since they already covered the determined sector area by observing the beam width in Figure 4.18c and 4.15. In conclusion, hierarchical codebook algorithms with the least number of sections usually have better time efficiency. However, at the same time, it suffers from possibilities for wrong detections. It can be already observed that the power level in Figure 6.5(c) gets less reliable due to the lower Rx power using a broader beam with less gain. In practice, a trade-off needs to be considered. The time consumption can be only reduced when a correct estimation can be guaranteed. Besides, since the received power using a narrow beam is higher, a higher MER should be also expected, which in principle, increases the reliability of the channel estimation. This effectively results in a shortened time slot for each beam training step. Nevertheless, as a prove of concept, this effect is not yet considered in this experiments, which could be included for further studies.

6.1.3 Single Intelligent Surface in Multipath Scenarios

In the scenarios mentioned above, there is only a single dominating wireless path, usually the line of sight (LoS) path between the Tx and Rx. Therefore, the channel estimation results show a unique peak for the DoD in Figure 6.3. However, in wireless communication, many multipath scenarios are much more complex than a single path model. This section will study multipath scenarios to verify how IRS works in these conditions, with reused portions from [LEK+21]

Channel Estimation for Multipath

The aforementioned channel estimation algorithms also work with multipath between Tx and Rx(s). For example, a SISO multipath scenario is depicted in Figure 6.6. Although the SISO architecture maintains, there are two possible paths between them. The experimental system setup is in Figure 6.7a, with the two paths formulated by metallic reflections. A measurement of exhaustive search from $\theta' = -40°$ to $\theta' = 40°$ is implemented with $g = 2°$ presented

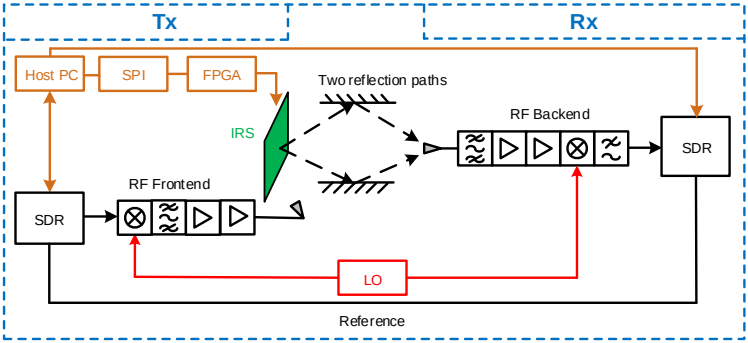

Figure 6.6: The block diagram of IRS wireless communication system under multipath SISO scenario

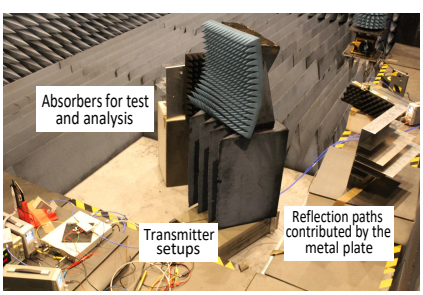

(a) Measurement system setup for SISO multipath scenario.

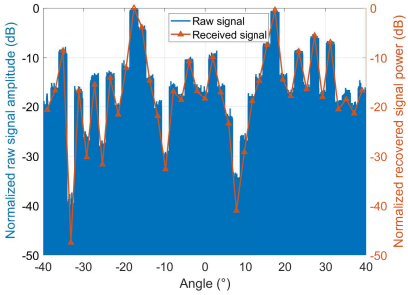

(b) Rx signal quality analysis for exhaustive channel estimation in multipath SISO scenario.

Figure 6.7: IRS multipath SISO system measurement environment and results from [LEK+21].

in Figure 6.7b. The blue bars show the amplitude of the raw Rx signal at the input of the SDR within each training duration observed. The red curve denotes the average desired signal power after post-processing the digital signal at each angle. Due to the environment in the anechoic chamber, there is no other signal source for interference, so a good match happens between the two curves. Most importantly, the peak angles can be found at $-18°$ and $18°$, which are exactly the reflection path created for the multipath SISO system. These measurements show that the beam training algorithm designed for IRS also works when multipath exists.

SISO Multipath Scenario

In a multipath scenario for a SISO system, the signal contributions through the different paths add coherently at Rx. This leads to undesired interferences if there are no additional operations. Nevertheless, if the phase of the two signals can be adjusted and constructively added up, the Rx power increases by $10\log_{10}(a)$ dB (with a to be the number of multipath) if the transmit power is split uniformly to the multipath. Moreover, splitting the power into different directions will increase the robustness of signal propagation, considering the shadowing results from vehicles or buildings. The experiments in this section continue with the system model and setup from Figure 6.6 and Figure 6.7a.

Once the directions of the two paths are estimated by Figure 6.7b, a double beam generated by the IRS from Figure 4.16 can be implemented. The purpose of this experiment is trying to prove that reasonable power relationships exist among measurements in different channel conditions, which provides fundamentals for deep studies in later chapters of this dissertation. Firstly, the Rx power is recorded by blocking one path with the absorber and leaving another free. In other words, the measurement is interested in the Rx power for each path/beam from the IRS double beams. Based on the measurement, the Rx signal powers at the input of Rx SDRs are measured to be -41 dBm and -40 dBm dBm at $\theta' = -18°$ and $18°$ respectively. Next step, both paths are realised and prove the signal combination quality at the Rx. In this measurement, we try to adjust the distances for the two propagation paths to be identical for a perfect signal summation. In principle, if the phases of two signals are matched perfectly, the Rx power should reach -34.5 dBm. However, the measured power is only -36.15 dBm. The phase mismatch causes this loss since at 28 GHz slight distance mismatch still leads to a significant phase difference. As a comparison, instead of the double beam, signal beams pointing to $\theta' = -18°$ and $18°$ provide Rx power of -37.64 dBm and -37.83 dBm respectively. These two values are used as a benchmark that denotes the power of signal transmission through a single path, even with two paths available. It can be seen that using the two propagation paths together with a double beam, the performance surpasses the implementation of a single beam in one particular direction. This result agrees with the concept of phase-coherent channels that can offer additional gain. However, precise phase mismatch adjustment is required compared with incoherent phase conditions. Otherwise, destructive interference happens. This dissertation achieves the proper coherent phase by adjusting proper distance as proof of

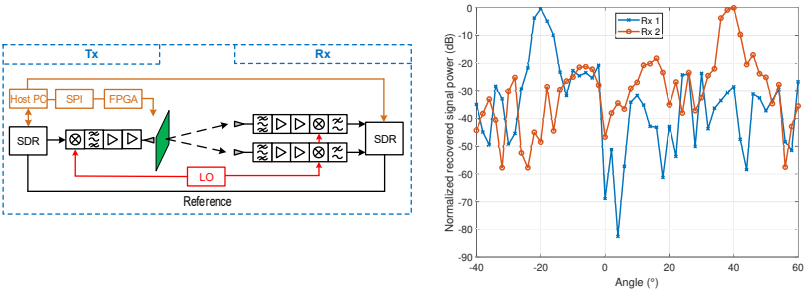

(a) The block diagram of IRS wireless communication system in SIMO scenario.

(b) Rx signal analysis for two Rx channels.

Figure 6.8: IRS multipath SIMO system measurement system model and results from [LEK+21].

the IRS multipath SISO concept. Additional signal processing against multipath fading is not considered. Nevertheless, this setup can improve the SNR by implementing the phase-coherent combination from different paths. Due to the sensitivity of phase-coherent mismatch, it is more likely to place in a stationary scenario like the signal propagation between BS or indoor environment data transmission among different wireless fidelity (WiFi) nodes.

SIMO Multipath Scenario

Besides the multipath between a SISO system, a multipath also exists for a SIMO system. When multiple Rxs require the same signal, the IRS can realize a functionality similar to a broadcasting case with the help of multibeam from Figure 4.16. Assuming two Rx chains with $M_r = 2$, the system is an extension of the SISO model with two Rx spatially distributed at different positions as depicted in Figure 6.8a.

In this experiment, additional analysis is applied for the double beam accuracy of the IRS. Please notice that the IRS in this measurement is also a prototype same as the one implemented in Figure 4.16. As concluded, one of the generated beams suffers from performance degradation due to another beam's interference. Therefore, it is important to verify this effect for proper system

performance. As the initial step, the channel estimation at the two Rxs is presented in Figure 6.8b. It can be seen that the peak power appears at $-20°$ for channel 1 to Rx 1, with the neighboring power at $-22°$ lower than the peak but slightly higher than the one at $-18°$. The dashed curves show the beamforming patterns for the single beams at these three angles in Figure 6.9a. The real angle direction is at $-20°$ given by the dashed straight line based on the beamforming pattern gain. The gain rank of the single beam shows corresponding performance as power from an exhaustive search. As mentioned in the IRS double beam property, changing one of the beam directions may lead to the offset of the second one, even though its direction remains unchanged. As an investigation, by changing only one of the beam direction, we generate three different double beam combinations $-20°, 38°$, $-20°, 40°$ and $-20°, 42°$. The beam offset of $-20°$ can be observed from Figure 6.9(a). Afterwards, we transmit signals from the IRS transmitter to Rx 1, and Rx powers at the input of Rx SDR are shown in Table 6.2. A relationship of Rx power $-20°, 42° > -20°, 40° > -20°, 38°$ is derived. Go back to the beamforming patterns, we can see that this order corresponds correctly to the gain rank of the double beam farfield patterns aligning at $-20°$.

Now we perform the same analysis for Rx 2. In this measurement, we steer the second Rx around $40°$ to show that the IRS beamforming is flexible for any angle direction. As shown in Figure 6.8b, the peak appears at $40°$ for Rx 2. It can be observed that the Rx power at $38°$ is slightly lower than $40°$, but for $42°$, the power degrades largely, which is possibly caused by environmental distortions. As an indication, the practically measured benchmark angle is referred at $39°$ in Figure 6.9(b). Following the same step as fir Rx 1, the Rx power for the three double beam combinations has the order $-20°, 40° > -20°, 38° > -20°, 42°$ with the differences 0.59 dB and 4.76 dB. Again, a larger reduction which is more than the beamforming gain difference, can be observed for the $-20°, 42°$ case. Traceback to the farfield patterns, it can be found that the $-20°, 42°$ combination is pointing in the same direction as the single beam at $42°$, where the power also decreased significantly.

The results lead us to conclude that due to the placement of the devices, such as the looking direction and the height mismatch between the Rx antenna and IRS, it is impossible to repeat the signal transmission conditions precisely as measured for the farfield pattern. Therefore, some unexpected distortions may occur like the results for the beamforming close to $42°$ in Figure 6.9b. However,

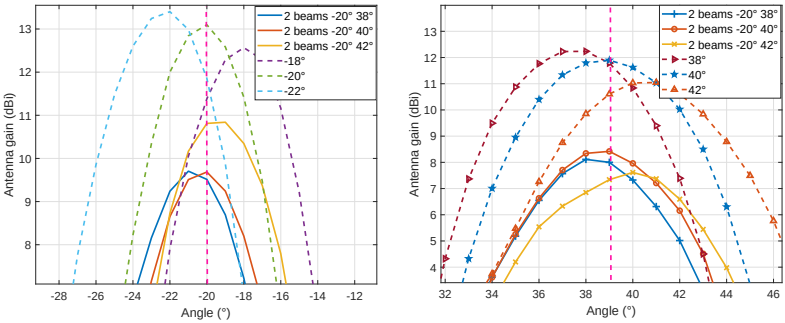

(a) Beamforming patterns around $\theta' = -20°$

(b) Beamforming patterns around $\theta' = 40°$

Figure 6.9: Beamforming patterns of IRS for the SIMO experiment from [LEK+21].

Table 6.2: Rx signal power with different beam angle combinations from [LEK+21].

Angle combination	Rx Power Rx 1	Rx Power Rx 2
$-20°, 38°$	−6.03 dBm	−4.97 dBm
$-20°, 40°$	−5.59 dBm	−4.2 dBm
$-20°, 42°$	−4.53 dBm	−9.46 dBm

the farfield patterns can be utilized as references and they provide excellent indications of the system performance. Given that the Rx power measurements are consistent, it can be concluded that these observations are accurate and that the IRS SIMO system functions appropriately.

6.2 Advanced Communication Technologies using Intelligent Surface

From a system perspective, the primary proofs of the IRS implementation concept have been demonstrated in the previous section. In this section, the system complexity will be increased based on the results of previous successful experiments in order to get closer to modern communication scenarios.

6.2.1 Fast Beam Switching for TDMA

As mentioned in Figure 6.8, an IRS can support broad casting using a multibeam strategy. Due to the implementation of a single IRS, this scenario only applies when multiple destinations require the same data. This is useful for disaster announcement, governmental and general information, which does not occur constantly. However, in most cases, different mobile UEs have data that should not be disclosed or shared with others. Therefore, additional multiplexing technology is required for a system based on the IRS to function under these conditions. In this section, TDMA implementation is detailed. TDMA has the advantages of flexible control, less in-band interference, and bandwidth saving compared with CDMA and FDMA, which is the reason for its considerations in [MZSS16, MDS95, MCR+93, Stu95]. The texts and figures in this section are partially reused from [LEW+21] © [2021] IEEE.

Scenario Formulation

Due to the planar shape of the IRS, it is imagined to be easily mounted on the outer wall of a building as a compact BS depicted in Figure 6.10a. Due to the IRS's planar shape, it is anticipated that it can be easily mounted on the exterior wall of a building as the compact BS shown in Figure 6.10a. If the IRS can implement rapid beam switching among multiple mobile UEs, the TDMA scenario is formulated by distributing the specific time slots for each mobile UE. Utilizing the IRS properties, a cost-effective and adaptable urban mobile radio access network is created. The IRS is expected to provide rapid beam steering settling to achieve such goals. To achieve the highest data throughput, as little time as possible should be wasted between beam steering for time slots between UEs. In the former IRS studies, only the settling time between different beamforming states has been investigated as in [YYX+16, PYXL20, KIT+11]. Its beam steering ability has never been considered in an entire communication system, considering the effects of variant system settings and requirements of signal processing.

The experimental system for the TDMA scenario is very similar to the SIMO multipath measurements in Figure 6.6. To simplify the system complexity, two UEs are used in this experiment. The difference with Figure 6.6 is that the beamforming is not using the double beams generated in Figure 4.18c, but the

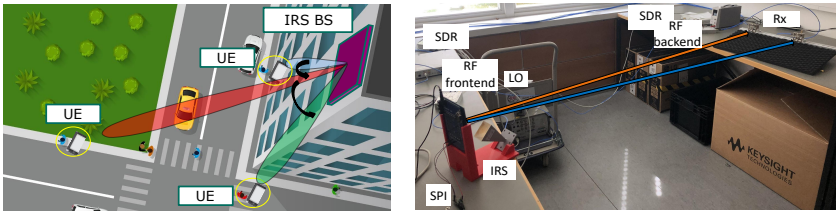

(a) Application scenario of IRS as mobile radio BS switching between highly directional beams towards different spatially separated UEs.

(b) TDMA measurement setup in an indoor environment.

Figure 6.10: IRS TDMA system scenario and experimental setup from [LEW+21].

single steerable beams mentioned in Figure 4.15 at different time slots. The system setup is presented in Figure 6.10b. The QRH40 antennas located at different positions are regarded as separate Rx UEs. Due to the verification of IRS beamforming robustness in the SIMO multipath scenario, the IRS system is set up in an indoor environment, one step closer to practical implementations. Further TDMA operations can be executed with detailed information in the following sections.

IRS Settling Time

Similar to the previous work, it is essential to examine if the implemented IRS can generate/switch beamforming that is fast enough to support TDMA multiuser scenario. If the beam switching is too slow or the reaction between different beam directions takes long time, the TDMA scenario cannot work efficiently. As an examination, Figure 6.11 shows the settling time of the IRS beam switching observed from the oscilloscope. The Tx SDR generates a constant signal, and an oscilloscope is used at the output of the RF backend module for the observations. Although we are transmitting at a constant signal level, it can be seen that the Rx power switches to a lower level as soon as the beam is turned away from the Rx. This switching operation takes 0.33 µs until a constant power level is reached. Our demonstration is one of the fastest beam-switching IRS systems compared with the previous work in [YYX+16,PYXL20, KIT+11], with the minimum of 2 µs was achieved. Additionally, impacts from

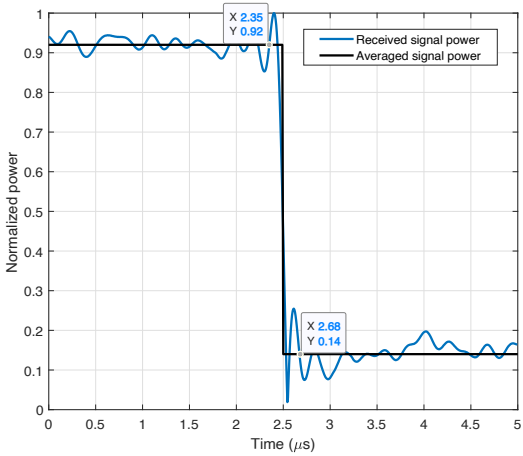

Figure 6.11: Settling time of the IRS beam switching.

the RF modules are also considered, which is the first system point of view analysis. Even though an IRS is proved to achieve fast beam switching as a possible replacement of a phased array, the effects brought by the fast switching and the settling time have never been investigated in a system, which brings novelty to this experiment.

Experimental Results

For this measurement, we assume a scenario where the UEs' positions are unknown initially but stay constant over a certain time. Before data transmission, the dominant DoD is determined for each user by an exhaustive search algorithm introduced in Section 6.1.2. The training data for the DoA estimation consists of QPSK symbols with an RRC pulse shaping filter with a 0.35 roll-off factor, as introduced in Chapter 3. Based on the setup from Figure 6.10b, two Rx antennas are placed at $-1.5°$ and $-11.8°$ with 2 m and 2.03 m distance from the IRS Tx. Figure 6.12a shows the normalized Rx power at each Rx over the DoD. Due to the $g = 2°$ angle resolution, the estimated channel positions are $-2°$ and $-12°$, respectively. The results again prove that the algorithm could precisely identify the dominant DoD towards each UE. The system performance can be

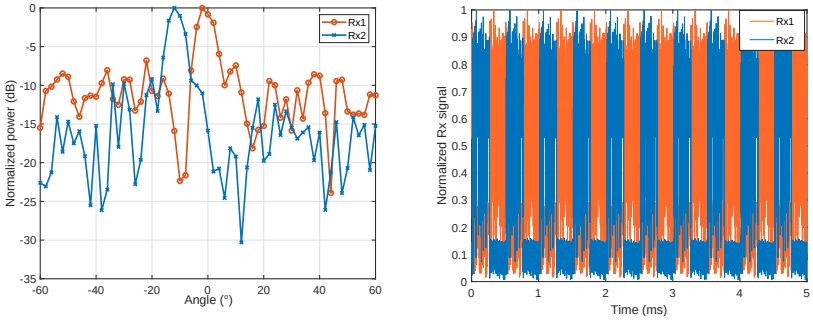

(a) Normalized power curves using IRS exhaustive search algorithm.

(b) Normalized Rx signal before digital signal processing for different users in TDMA scenario.

Figure 6.12: TDMA channel estimation and data propagation results.

further evaluated with a proper settling time proved in Figure 6.12b, with the normalized Rx signal processed in the host PC is presented. In this case, each user occupies a time slot of 0.25 ms for data reception, proving that both users are allocated precisely to scheduled time slots thanks to the fast settling time.

A TDMA system with fast beam switching requires a prompt beamforming system and poses a challenge to signal processing. Considering a constant sampling rate, more swings occur for the same number of symbols being transmitted with a faster switching time. In other words, more symbols are likely to be at the unstable switching edges, as observed in Figure 6.11. This means that the Rx symbols could be no longer clean and distinguishable.

Nevertheless, since we know that the instability starts from the edges, the best solution to avoid undesired bit errors is to use guard symbols at the edges of transmitted frames. The scatter plots in Figure 6.13 show the properties by comparing the 16QAM Rx symbols without and with guard symbols. In this measurement, 125000 symbols have been received from 1000 frames, where each frame occupies 0.25 ms. One guard symbol is used at each edge of the entire frame. Single carrier modulation scheme is considered and an equivalent SISO chain takes place in each TDMA time slot, so the LS method from (3.3) can be directly used for the channel estimation. Afterwards, ZF equalization (3.5) is used to recover the symbols. As a result, the symbols with strong phase

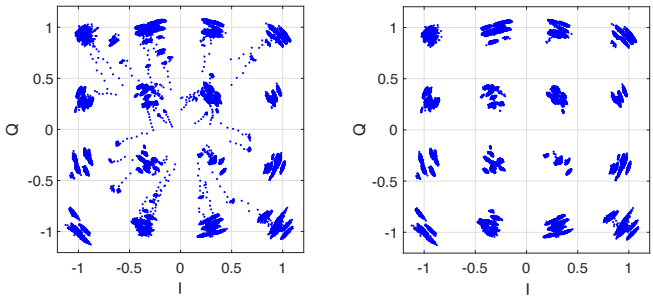

(a) 16QAM without guard symbol (b) 16QAM with guard symbol

Figure 6.13: 16QAM symbols without/with guard symbols

and amplitude mismatches in Figure 6.13a are eliminated in Figure 6.13b. The dispersed distribution of symbols belonging to the same constellation point results from the amplitude and phase fluctuations among the frames for the same user at different sweep slots.

For TDMA, it is also essential to see how fast the beams can be switched to support more users simultaneously. In the following experiments, 125000 Rx symbols with a sampling rate of 2 MHz are analyzed. Five switching speeds of 0.5, 0.25, 0.124, 0.64, and 0.04 ms were measured and correspond to 250, 125, 64, 32, and 20 symbols per frame accordingly, as the symbols are oversampled with four samples per symbol.

Table 6.3 presents BER measurements of QPSK, 8QAMand 16QAM modulated signals without guard symbols, which clearly shows how the BER increases with faster beam switching speed and higher modulation order. In addition, the BER increases more rapidly with shorter switching times, leading to significant performance degradation at 0.04 ms. As a combination of the effects above, the measurements show that if an error-free transmission is required, the fastest beam switching time of QPSK is 0.062 ms. For 8QAM and 16QAM, the time should not be shorter than 0.125 ms and 0.5 ms, respectively. As concluded, the larger BER is likely to result from the instability of the symbols at the edges. To show the effect of guard symbols, Table 6.3 gives the average BER for all investigated modulation schemes in combination with dif-

Table 6.3: Measured BER without/with guard symbols

BER / Time / M	0.5 ms	0.025 ms	0.0125 ms	0.062 ms	0.04 ms
QPSK (M=2)	0/0	0/0	0/0	0/0	5e-5/0
8QAM(M=3)	0/0	0/0	0/0	4.3011e-5/0	4e-4/0
16QAM (M=4)	0/0	1.6e-5/0	1.9355e-4/0	7.7419e-4/0	0.0026/0.0017

ferent switching times. The amount of redundancy caused by guard symbols is 0.8%, 1.6%, 3.2%, 6.4%, 10% for 0.5, 0.25, 0.124, 0.062 and 0.04 ms switching time respectively. As a result, the goal of the error-free transmission is mostly satisfied, except for 16QAM with 0.04 ms, which particularly suffers from a high BER. This shows that the system instability at this switching speed can not serve higher modulation schemes with a dense constellation.

Practical Considerations

Besides the reason for system capability research, the purpose of reaching a faster switching time is to prove the ability to serve more UEs simultaneously with low latency. The system fulfills the requirement of < 10 ms frame or < 1 ms subframe in 5G transmission standard based on [OSAA19], and the 4 ms frame or 0.2 ms subframe duration specified in the TDMA standard. Moreover, the fastest possible switching time at 0.04 ms is much beyond the mentioned TDMA frame and subframe definition supporting future standard improvements. However, the tense of switching time leads to additional BER or guard symbols redundancy. To practically consider the usage of an IRS-based TDMA system, trade-offs of the system parameters such as the requested switching time, the necessary switching time, and acceptance of guard symbol redundancy should be considered based on specific requirements. From the data rate point of view, according to Table 6.3, it is always possible to choose a higher-order modulation scheme if the channel SNR is sufficiently high. Thus, 16QAM is, in our case, the favourable choice except when a 0.04 ms ar faster switching speed is required.

6.2.2 IRS for UE Tracking in Mobile Communication

With the verification of IRS settling time from Figure 6.11, the IRS-based system also has the potential to realize the UE beam tracking, which is more realistic in mobile communication scenarios as an important milestone. This section presents the scenario, theoretical algorithms, and the experimental results for a UE tracking IRS system. These are the fields that have never been studied before in any IRS-based wireless communication system. This section contains reused of texts and figures from [LBE+21] © [2021] IEEE and [LBE+22] © [2022] IEEE.

Scenario Formulation

As a recent popular topic, studies regarding 5G tracking at 28 GHz have been demonstrated in [AAFK20, HLT+18, HTBW20, HTYW19, MSS+17, KTH+17, NMO+20, LHS+17] based on the 3GPP 5G NR standards [GPR+18b, GPR+18a, LGZH20, WLW18]. However, these system architectures suffer from high power consumption and system complexity. As the proper feasibilities of IRS are proved with the experiments in the previous sections, the IRS-based system is expected to realize tracking function for mobile communication scenarios with lower cost and power consumption. Different from a MIMO system, the channel state information between each unit cell to the Rx is not simply accessible due to the IRS difficulties mentioned in Section 4.6. Therefore, the first tracking attempt is also based on beam training ideas from Section 6.1.2. By adaptively adjusting the existing 5G beam management, a novel algorithm for IRS UE tracking is created.

As mentioned in (4.1), the maximum IRS gain can be achieved when the phase distribution from (2.16) corresponds to a beam direction that perfectly matches the DoD. This is true for the case that the exact DoD is the same as the beamforming direction, for example, when the channel estimation algorithms have detected the correct DoD. This optimum condition also stands for the real-time tracking system, saying the actual UE position at θ_r and ϕ_r. The optimum tracking is the realization when $\theta' = \theta_r$ and $\phi' = \phi_r$ for the entire duration. However, this condition can not always be satisfied in a real-time system. The main reason is the limited phase resolution of IRS, as mentioned in Figure 4.15. The visible results from it already show that the beamforming

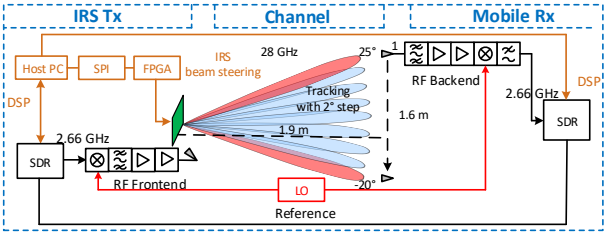

Figure 6.14: System model of the IRS-based beam tracking system at 28 GHz.

of the IRS does not offer full angle resolution due to the quantization error from (4.5). In addition, considering the computation time and interface latency in a practical system, the overhead caused by beam training operations is not negligible. Therefore, a suitable algorithm has to be discovered for IRS based system.

The system model is similar to the SISO case but with a mobile Rx as UE in Figure 6.14. The system was set up in an indoor environment, as shown in Figure 6.15. The IRS Tx, which is assumed to be the BS at a fixed position, steers the beam and tracks the mobile UE, which is represented by a horn antenna moving along a 1.6 m mechanical trace with controllable speed. The vertical distance between the trace and IRS is 1.9 m, yielding a DoD range from 25° to −20° from the IRS point of view.

Adaptive IRS Beam Management Algorithm

In conclusion, the IRS-based tracking system must live with a certain amount of beamforming mismatch for the above situation and still validate the proper signal processing. Therefore, to realize real-time tracking, a new Rx power index $P_r(\theta_r, \theta')$ is introduced. This is the Rx power based on (2.6) using the optimum phase distribution based on (2.16) regarding the beamforming direction θ' while the real UE is located at θ_r. The real-time tracking strategy relies on a permanent observation of $P_r(\theta_r, \theta')$, that is highly dependent on the alignment of the IRS beam direction θ' and the actual target direction θ_r, and can thus serve as a reliable indicator for the tracking mismatch when interpreted over time. As previously mentioned, the term ϕ' is neglected, as it is assumed to be a constant of 0°. A threshold σ_t is necessary to keep the balance

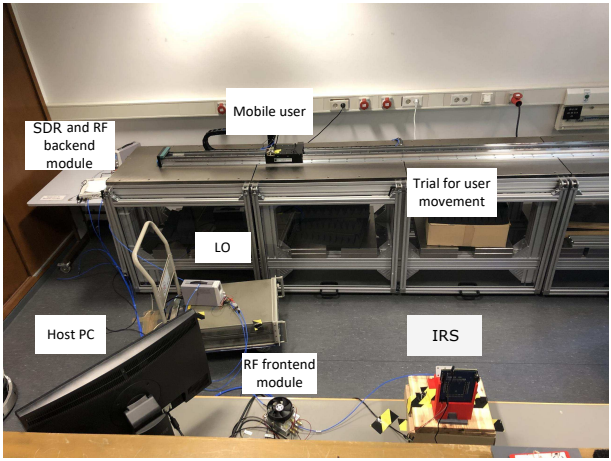

Figure 6.15: Indoor system setup of IRS mobile communication tracking.

between the optimum tracking condition and the introduced training overhead, which is controllable for different tracking requirements and conditions. In this dissertation, we define the threshold to be

$$P_r(\theta_r, \theta') \geq \sigma_t \cdot P_{Bf}, \tag{6.2}$$

where P_{Bf} is the reference power with the optimum IRS beamforming direction from the signal processing point of view. To realize this goal, an adaptive IRS beam management algorithm is created. As presented in Figure 6.16, the beam management is inspired by the 3GPP 5G NR concept from [GPR+18b, GPR+18a, LGZH20, WLW18], with some modifications fitting the IRS system and minimizing the training overhead. Detailed descriptions are presented in Algorithm 1.

To initially determine the first beamforming angle and to start the tracking, it is derived by the exhaustive channel estimation from Section 6.1.2 among the Rx power set $\boldsymbol{P}_r(\theta_r, \Theta')$ with θ' in the entire angle range of $\Theta' = \{\theta_s, \theta_s + g, \theta_s + 2g, ..., \theta_e\}$. This is regarded as an initial detection (full scan) in Figure 6.16. By operating a power peak detection among $\boldsymbol{P}_r(\theta_r, \Theta')$, the beamforming is directed to $\theta' = \theta'_{Bf}$. The entire tracking duration is counted in time domain with t, which is a discrete variable initialized at 0. The updating rate of t depends on how often the system computations take place. The reference power

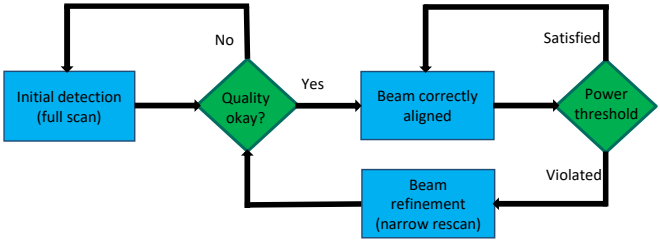

Figure 6.16: The flow graph of beam management.

Algorithm 1 : IRS tracking management and analysis

Input parameters: θ_s,θ_e,g,Q_u,σ_t,k';
$c_f = 0, c_r = 0, t = 0$;
1. Full scan and angle initialization:
$\Theta'_f \in \{\theta_s, \theta_s + g, \theta_s + 2g, ..., \theta_e\}$
$\theta'_{Bf} = \text{argmax}_{\theta'} \boldsymbol{P}_r(\theta_r, \Theta')$;
$c_f = c_f + 1, t = t + t_f$;
2. IRS beam steering to $\theta'[t] = \theta'_{Bf}$ **and quality check**;
if $P_{Bf} = P_r(\theta_r, \theta')[t] \geq Q_u$ **then**
  3. Observation:
  while $P_r(\theta_r, \theta')[t] \geq \sigma_t \cdot P_{Bf}$ **do**
    $\theta'[t] = \theta'_{Bf}$;
    if $P(\theta_r, \theta')[t] > P_{Bf}$ **then**
      $P_{Bf} = P(\theta_r, \theta')[t]$;
    end
  end
  4. Beam refinement:
  $\Theta'_i \in \left\{\theta'_{Bf} - k'/2, \theta'_{Bf} - k'/2 + g, .., \theta'_{Bf} + k'/2\right\}$
  $\theta'_{Bf} = \text{argmax}_{\theta'} P_r(\theta_r, \Theta'_i)$;
  $c_r = c_r + 1$;
  continue
else
  break and back to 1.
end

P_{Bf} is recorded based on the instant Rx power $P_r(\theta_r, \theta')[t]$ and a quality factor Q_u is defined to intercept incorrect detections corresponding to the quality check in Figure 6.16, in case of system operation failure. If the quality check is not passed, a full scan takes place again for the angle initialization. Once the observation stage is entered, the beamforming direction stays only if the instant signal power $P_r(\theta_r, \theta')[t]$ is qualified. There are two possibilities here: Firstly, if the instant power is larger than the reference power, the reference power will be updated to the current instant power. This is designed in case of a slightly suboptimal beam alignment and thus lower Rx power at the start of observation. If the reference power is set incorrectly low, the proper beam alignment during the tracking duration is not well guaranteed. Secondly, if the instant power is higher than the reference power with the threshold ratio $\sigma_t \cdot P_{Bf}$, the observation continues while the beamforming angle is kept. Due to the movement of the mobile UE, once the real-time signal power $P_r(\theta_r, \theta')[t]$ drops below $\sigma_t \cdot P_{Bf}$, the beam refinement is triggered. To minimize the training overhead, a small rescan with the width k' centralized at the last detected direction θ'_{Bf} formulates the new angle set $\Theta'_i \in \left\{\theta'_{Bf} - k'/2, \theta'_{Bf} - k'/2 + g, ..., \theta'_{Bf} + k'/2\right\}$, denoted by the beam refinement (narrow rescan) in Figure 6.16. Again, by operating a peak detection among $\boldsymbol{P}_r(\theta_r, \Theta'_i)$, the beamforming angle θ'_{Bf} is updated and loops back to the beam steering step. Overall, the algorithm relies on a search criterion which has the complexity $O\{n\}$ for each beam refinement iteration.

The following parameters can be implemented to analyse the proposed tracking algorithm's performance. Firstly, the training overhead is defined to be the total training duration spent on beam scans over the entire tracking duration. The total training duration is expressed by

$$T_{tr} = (c_f \cdot t_f + c_r \cdot t_r + (c_f + c_r) \cdot t_d)/T_{total}, \tag{6.3}$$

with c_f and c_r the counters of the number of full scans and rescans in Algorithm 1. Whenever a full scan or rescan happens, the corresponding counter increases by 1. The parameters t_f and t_r can be further extended to $t_f = t_s \cdot ((\theta_e - \theta_s)/g + 1)$ and $t_r = t_s \cdot (k'/g + 1)$, respectively, denoting the required time for the full scan and rescan. Here, t_s is the occupied time slot for each beam direction through the exhaustive search. The term t_d from (6.3) is the computation latency spent for the peak detection, which is required for the detection after each scan. In our system, t_s is set to 0.3 ms and t_d is measured to be 4 ms. The terms $(\theta'_e - \theta'_s)/g + 1$ and $(k'/g + 1)$ denote the number of beamforming candidates in full scans and

refinement scans. Afterward, by dividing with the total tracking time T_{total}, the training overhead is derived.

Secondly, to compute the averaged parameters, the total number of samples along time t is defined as N_a. The average power is then denoted by

$$P_a = \frac{1}{N_a} \sum_{t=0}^{N_a} P(\theta_r, \theta')[t]. \tag{6.4}$$

Following the similar logic, the average angle mismatch A_a is computed based on the beamforming direction differences with real UE position through time, which is expressed as

$$A_a = \frac{1}{N_a} \sum_{t=1}^{N_a} (\theta'[t] - \theta_r[t]). \tag{6.5}$$

GNU Radio Realization

As mentioned in Chapter 5, the system is operated using the GNU Radio software, which drives the SDRs at the host PC. For this experiment, due to the newly created adaptive beam management algorithm, there is no possibility to implement the default signal processing blocks as the example in Figure 5.3. As a solution, a control angle block designed based on the out-of-tree module from the GNU Radio is implemented, following the indications from [Gnu].

Firstly, the logic of the control angle block is introduced. The basic flow graph is presented in Figure 6.17, which can be regarded as a detailed realization of the beam management flow in Figure 6.14. This control angle block implements the core functionality of beam management and aggregates various signal properties to control beamforming and derive the required DoD. It has several operating modes, similar to the SPI functionalities mentioned in Figure 4.5 to trigger beam scanning or fixing. The block switches between two operating states referred to as observation and beam refinement. The observation stage is located at the left part of the flow graph in Figure 6.17. The block constantly compares a client defined signal quality indicator (SQI) to the threshold and reference, corresponding to the observation stage in Algorithm 1. The SQI can

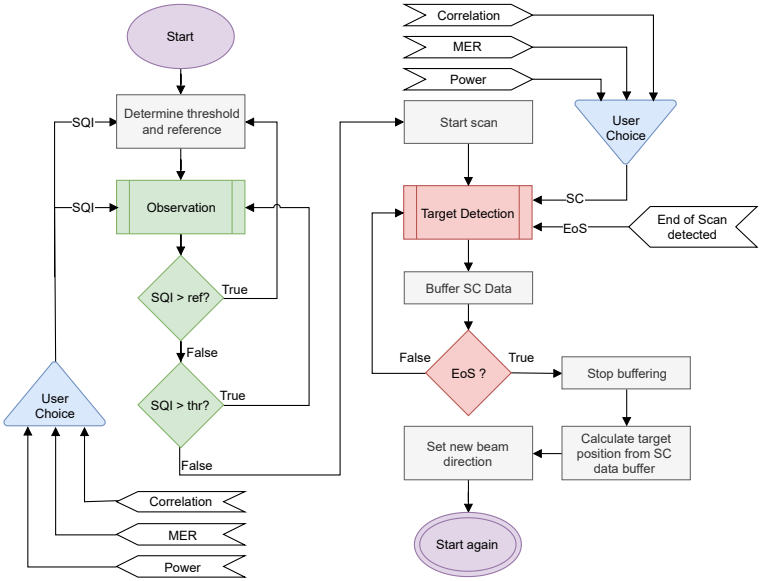

Figure 6.17: Working principle of the control angle block.

be chosen from the metrics mentioned in Table 6.1, and Rx power is used in this experiment. The reference is updated or the processing switches to the beam refinement (right part of Figure 6.17) as soon as the threshold is exceeded. When the block enters the beam refinement state, it sends a beam steering command to the IRS via SPI based on Figure 4.5 and starts buffering the scan data (SC Data) until the scan is complete, in other words, end of scan (EoS). Afterwards, the control angle block evaluates the scanning buffer corresponding to the beam refinement stage in Algorithm 1 and sends a fixed beam command to the IRS to adjust the beam direction for the new θ' after the detection. If any failure occurs that a valid scan is not detected, the target detection will be triggered again.

Next, it is worth discussing the appearance of this control angle block in the GNU Radio graphic interface, which is an excellent chance to present how the out-of-tree modules are designed for our required purposes in this dissertation. The control angle block is a sync block with five input and four output ports in Figure 6.18. The first input port is an asynchronous message port for the general system messages. The second port on the input side is provided for raw symbol

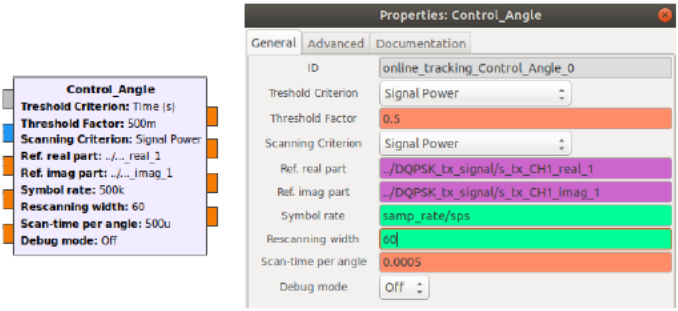

Figure 6.18: Graphic interface of the control angle block.

data. A third port is for the quality metrics input for the system performance evaluation, like MER for correctness observation, whereas a fourth port is available for root mean square (RMS) signal power input. Finally, the fifth input port is an additional control port and is intended to provide information on whether the incoming samples belong to a beam training period or not. The data from all input ports, except for the raw symbol data port, is daisy-chained to the four output ports of the block, attaching GNU-Radio stream tags to the start and end samples of a scanning period for debugging purposes.

As a core component of the IRS tracking as well as the signal processing module in other experiments in this dissertation, the control block is highly configurable from the GNU Radio graphic interface, as shown in Figure 6.18. The block's first input parameter in the GNU Radio context menu is the so-called "Threshold Criterion", which defines the σ_t in the observation stage. It allows the user to select one of the metrics "Signal Power", "Bit Error Ratio", or "Modulation Error Ratio" using a drop-down menu, where the signal power is finally used to observe the $P_r(\theta_r, \theta')[t]$. The "Scanning Criterion" is the third option in the blocks property tab and offers a similar choice for the target detection state, as it defines which signal property should be considered for use with the target detection algorithm. For this input parameter, the options of "Signal Power"," Signal Correlation", and" Modulation Error Ratio" are kept. The following two block parameters are the "Reference real-part" and "Reference imaginary-part" and only need to be specified if the" Signal Correlation" scanning criterion has been selected. The "Symbol Rate", "Rescanning Width k'", and "Scan-time per Angle t_s" parameters also directly influence the behaviour of the block in the

target detection state, as they are used to calculate the number of input samples for a single scanning or rescanning operation. The last option in the block menu offers the user to enable a so-called" Debug Mode", which changes the block behaviour in a way that no SPI commands are sent anymore, which is especially useful when the block should be tested with pre-recorded data in the case that no hardware is attached.

In the end, the complete flowgraph for the online-tracking system as a representative example of GNU Radio signal processing in this dissertation is shown in Figure 6.19, which is structured as follows: All variable definitions and settings are located in the upper left corner, while the transmitter part of the flowgraph is located slightly beneath on the upper right side. The QPSK Rx is located in the centre-left of the flowgraph, together with two "File Sink" blocks to store the raw measurement data and two graphics under interface (GUI) blocks to visualize the data during the measurement. The IRS tracking part of the flowgraph begins directly behind the Costas Loop (a default block from GNU Radio for phase synchronization), where the signal splits up into five different signal processing lines that are directly fed into the "Control Angle" block. The first one goes from the "QPSK MER" block through the differential decoder to the "Bit Error Ratio" block, where the BER is calculated and asynchronously sent to the "Control Angle" block. The second input port of the" Control Angle" block is directly fed by the unnormalized complex symbol output of the Costas Loop. At the same time, the third signal processing line goes through the "AGC3" block (a default block from GNU Radio for gain and decay control) and into the "QPSK MER" block, where MER is calculated from the normalized complex symbols and forwarded to the control angle block after further smoothing by a moving average filter. For the fourth signal processing line, the output of the "Costas Loop" is average filtered using the "RMS" block to calculate the envelope of the RMS symbol magnitude that can then be processed by the "Control Angle" block instead of the actual symbol power. Lastly, the scan detection is implemented with the help of the" Peak Detector 2" block, whose output value is passed to the fifth input port of the" Control Angle" block, indicating whether a beamforming direction is determined or not. The demodulated binary signal, the BER and MER, the RMS symbol magnitude, and the scan detection signal are then passed on to various GUI blocks, allowing the signal quality to be observed during the measurement.

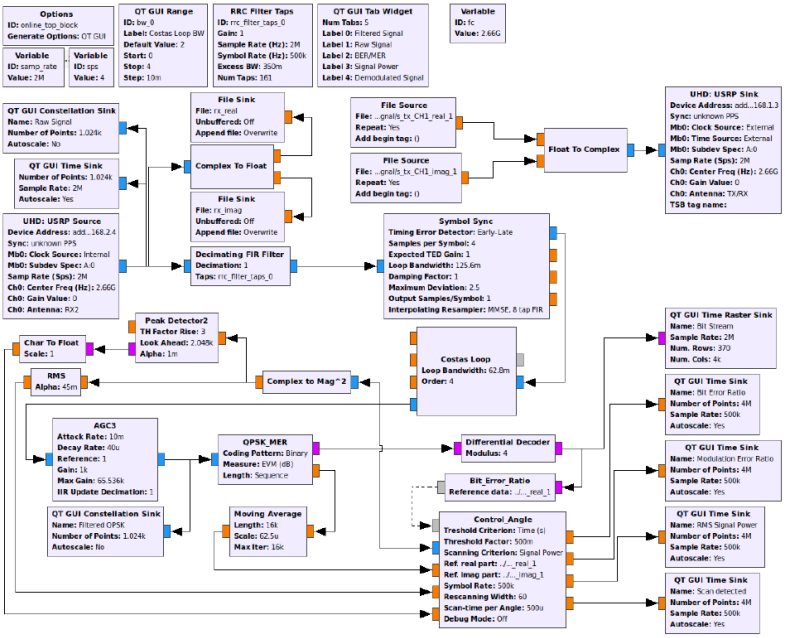

Figure 6.19: Complete GNU Radio flow for the IRS tracking.

Tracking Observation

Figure 6.20 shows a tracking observation of an UE traveling the distance of 1.6 m at a speed $v = 10$ m/min in 9.6 s. The threshold is $\sigma_t = 0.6$ and the angle training width is $k' = 16°$. In Figure 6.20a, The red solid curves show the simulation results of the tracking signal behaviour with the threshold presented by the dashed line. Due to the difficulty of considering all the environment and hardware delay effects, the purpose of the simulation is to prove the basic tracking behaviour. To comparison to the measurement results from the solid blue curve, the trigger positions of the beam refinements are different to align with simulation results due to environmental influences, but the power envelopes are well fitted. Due to the change of link distance, the Rx power reaches its maximum at around 5 s, where the UE approaches the minimum link distance. Meanwhile, the Rx antenna has a fixed facing direction instead of pointing to the IRS Tx constantly, which leads to additional power degradation. Figure

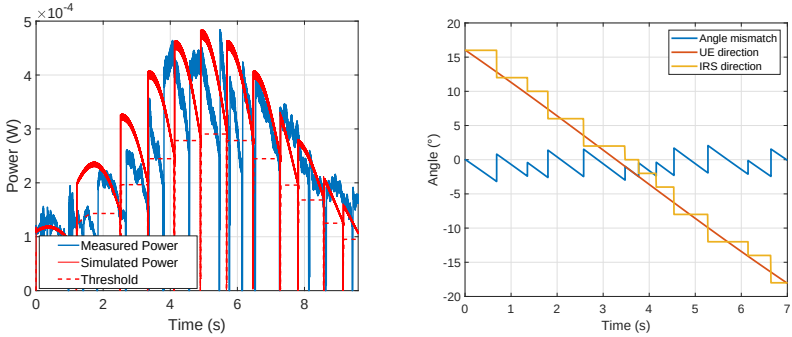

(a) Power vs. Time. (b) Angles vs. Time.

Figure 6.20: Tracking observation for $v = 10$ m/min, $\sigma_t = 0.6$, and $k' = 16°$.

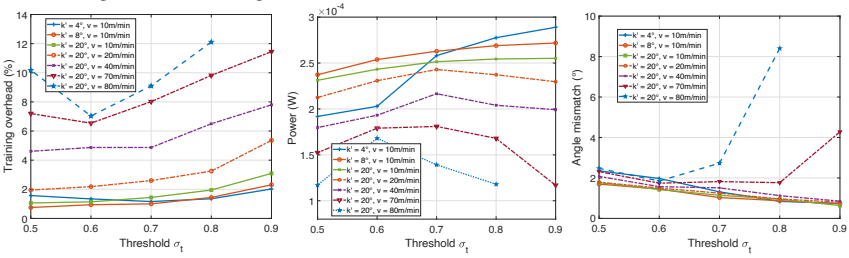

(a) Training overhead results. (b) Average power results. (c) Average angle mismatch results.

Figure 6.21: IRS tracking system performance analysis.

6.20b presents the mismatch between the real UE position and the beamforming direction, with the maximum difference around 2°, which proves that the IRS beamforming system tracks the user with good performance.

System Performance Analysis

Figure 6.21 shows the performance analysis based on the experimental evaluation. The training overhead, average Rx power, and average angle mismatch defined in (6.3), (6.4), and (6.5) are evaluated based on different system settings. In each figure, the observations can be divided into beam refinement/rescan width k' (solid curves) and target speed v (dashed lines) analysis regarding threshold σ_t from 0.5 to 0.9 with 0.1 increment. For training width, the exemplary values

of $k' = 4°, 8°, 20°$ are chosen for evaluation. From Figure 6.21a, it can be observed that the training overhead is directly related to the threshold σ_t, as the beam has to be refined more frequently for higher thresholds. It can also be concluded that a wider training width corresponds to a higher training overhead since more angle steps result in longer scanning times. A special case is $k' = 4°$, where the training overhead increases for σ_t smaller than 0.7. In this condition, the UE leaves the 4° rescanning range when the beam refinement is triggered too late with a low threshold. For speed, $v = 10, 20, 40, 70, 80$ m/min are analyzed. As v increases, the total time to travel the constant distance $d = 1.6$ m decreases. However, for a constant σ_t, the number of beam refinement operations stays the same regardless of the v, as it is mainly related to power observation. Thus, the relative training overhead increases with the target speed, since the training overhead depends on the constant computation latency and IRS beam steering speed. Analogous to the beam training width results, decreasing the threshold leads to less beam refinement operations and less tracking overhead, which is generally true until $v = 70$ m/min. Beyond it, there are increases in training overhead at $\sigma_t = 0.5$, which means the beam allocation becomes less optimal for a fast-moving target with a late beam refinement triggering. From Figure 6.21b, it can be concluded that the average power decreases for lower σ_t since the weaker Rx powers are tolerated before the beam directions are updated. In principle, an increased k' also leads to a lower average power due to a higher training overhead from Figure 6.21a. Again, the unusual behaviour is seen in the 4° curve resulting from losing the target. At $v = 10$ m/min, $\sigma_t = 0.9$ is the best choice since a high power level can be maintained. However, a higher σ_t also means a higher training overhead, especially at a faster v. On the other hand, a lower σ_t leads to a power level degradation. As a result, $\sigma_t = 0.7$ is the best choice as a trade-off to achieve the highest average power. As the special case $v = 80$ m/min, using $\sigma_t = 0.7$ degrades the average power due to frequent scans challenge the system interfaces. In Figure 6.21c, the average angle mismatch is larger with smaller σ_t due to a lower beam refinement rate leads to longer durations with imperfect beamforming alignment. Consistent with Figure 6.21a and Figure 6.21b, for $k' = 4°$ the angle mismatch suddenly increases with σ_t below 0.7.

By observing these figures altogether, the curve with $v = 80$ m/min is a special candidate. The goal of experiments at this speed is to develop the maximum achievable speed of the system, which is also why $k' = 20°$ is utilized in case of target missing problem. At this speed, due to the extremely high beam refinement

rate, the hardware and software interfaces of the system get stressful, with degradation of performance and even unachievable measurement at $\sigma_t = 0.9$. This property is potentially appeared at $\sigma_t = 0.9$ and 0.8 with $v = 70$ m/min in Figure 6.21a, but becomes more obvious at $v = 80$ m/min.

Practical Considerations

According to the analysis of the measurement results above, an adaptive tracking system should be set up as follows. To minimize the beam training overhead, threshold and training width always have to be as low as possible. However, this is contradictory, as the threshold limits the training width. If the threshold is too low, the system might lose the target for low training widths, as presented in Figure 6.21a. On the other hand, if the threshold is too high, beam refinements are triggered too often, leading to high training overhead and challenging communication interfaces, especially at higher speeds. Thus, the maximum user speed must be defined based on a relevant threshold factor and training width to implement the system practically.

As an overview of system performance, we manage to track the user with 80 m/min speed, which corresponds to an angular speed of 37.5°/s. The average angle mismatch through the entire tracking duration is between 0.5° and 2.5° with proper tracking parameter settings not exceeding the interface communication time. According to the measurement results, it can be concluded that the training overhead of the system is between 0.75% to 10%, mainly depending on the speed. These flexible adjustments maximize the data rate instead of wasting resources for beam refinement in unnecessary conditions. Moreover, if a low tracking overhead is requested with sufficient Rx power, this can be managed by putting the IRS BS further away from the movement area, which corresponds to a slower angular speed. As an indication, a vehicle with 33 to 67 km/h speed travelling on a street that is 50 m away from an IRS BSis comparable to our indoor measurement between 20 to 40 m/min as the relative direction to the IRS changes similarly, and could probably be trackable with a training overhead of 2 to 5%. The advantage of such an IRS tracking system is the flexible training overhead. Instead of a fixed number of pilot or beam training slots in conventional solutions, beam training is only triggered when necessary. This adaptive solution is implemented into the novel IRS-based system, which formulates the major novelty.

6.2.3 Predictive Tracking using IRS

The algorithm mentioned above, novel and customized to an IRS-based system, can lower the training overhead through flexible beam management flow. Nevertheless, each beam refinement steps rescan still adds to computation redundancy. As a result, the following predictive algorithms will be shown to prevent beam rescans while maintaining proper tracking performance. This moves Algorithm 1 one step closer to demonstrating the practicality of IRS-based systems for solving real-world issues. The creation of tracking algorithms is thoroughly explained in this section.

Angular Speed Prediction (ASP) Algorithm

Two potential aspects can be investigated to enhance the system's performance, according to the beam management algorithm mentioned in Algorithm 1. The first step in every beam refinement is a rescan, which chooses the best beam from a smaller set of candidates based on the chosen metric. This increases the training overhead because scanning might not always be necessary if enough information about UE movement is available. Second, too many beam refinement scan triggers may cause system failures, leading to additional initializations to adjust the UE position. The training overhead brought by beam refinement rescans is anticipated to be further reduced if algorithms with predictive features can be used to realize beam alignments based on the predicted UE position.

As a solution, the first predictive algorithm being created is called angular speed prediction (ASP) with its descriptions in Algorithm 2. To avoid duplications, the beamforming quality check mentioned Algorithm 1 is removed here but still exists in experiments. Similar to Algorithm 1, for the first step, a full exhaustive scan takes place in order to localize the initial UE position θ' based on the peak Rx power from the set $\boldsymbol{P}_r(\theta_r, \Theta')$, which consumes a time duration of t_f. The counters c_f and c_r record the number of full scans and rescans for later performance analysis. Instantly, the beamforming direction and the time after the peak power detection are recorded and added to the beam tracking history as $\theta'_l[1] = \theta'$ and $T[1] = t$, respectively. The reference power P_{Bf} is recorded after the scan based on the detected θ'_{Bf}, and the observation through time t starts with a predefined threshold σ_t. Same as Algorithm 1, the reference power P_{Bf} is a varying value, which increases along with the Rx power. Due to UE

Algorithm 2 : ASP algorithm

Input parameters: θ_s,θ_e,g,σ_t,k, $c_f = 0, c_r = 0, t = 0$;
1. Full scan and angle initialization:
$\theta' = \theta'_{Bf} = \text{argmax}_{\theta'} \boldsymbol{P}_r(\theta_r, \Theta')$, $c_f = c_f + 1$;
$c_t = c_r + c_f$, $t = t + t_f$, $\theta'_l[1] = \theta'_{Bf}$, $T[1] = t$;
2. Observation and prediction:
$P_{Bf} = P(\theta_r, \theta')[t]$;
while $P(\theta_r, \theta')[t] \geq \sigma_t \cdot P_{Bf}$ **do**
  if $P(\theta_r, \theta')[t] > P_{Bf}$ **then**
    $P_{Bf} = P(\theta_r, \theta')[t]$;
  end
  if $c_t > 1$ **then**
    enter prediction with

$$v_a[c_t] = (\theta'_l[c_t] - \theta'_l[c_t - 1])/(T[c_t] - T[c_t - 1]); \quad (6.6)$$

$$\theta'_{pr}[t] = \theta'_l[c_t] + (v_a[c_t])(t - T[c_t]); \quad (6.7)$$

    $\theta'_{pr}[t] - \theta'_{Bf} = \theta'_d$;
    if $|\theta'_d| \geq g/2$ **then**
      $\theta' = \theta'_{Bf} + g \cdot (|\theta'_d|)/\theta'_d$;
    end
  end
  $t = t + 1$;
end
3. Beam refinement:
$\Theta'_i \in \left\{\theta'_{Bf} - k/2, \theta'_{Bf} - k/2 + g, .., \theta'_{Bf} + k/2\right\}$
$\theta' = \theta'_{Bf} = \text{argmax}_{\theta'} \boldsymbol{P}_r(\theta_r, \Theta'_i)$, $t = t + t_r$;
$c_r = c_r + 1$, $c_t = c_r + c_f$, $\theta'_l[c_t] = \theta'_{Bf}$, $T[c_t] = t$;
back to 2

movement, the beamforming direction θ' is maintained until the Rx power drops below $\sigma_t \cdot P_{Bf}$. As soon as the Rx power $P(\theta_r, \theta')[t]$ falls below $\sigma_t \cdot P_{Bf}$, a beam refinement is triggered and a narrow range exhaustive rescan with width k' is executed consuming a time of t_r. By implementing another peak detection for the Rx power within the angle set Θ'_i, θ'_{Bf} is updated and added to the tracking history in the form of $\theta'_l[c_r], T[c_r]$. When there are more than one recordings in the tracking history list yields $c_t = c_f + c_r > 1$, the angular speed v_a is estimated following (6.6) based on the two latest beamforming angles and time recording with indexes $c_t - 1$ and c_t. Based on this angular speed, the angle prediction through t is computed in (6.7), which hopefully prevents beam refinement rescans. Once the current beamforming direction θ'_{Bf} has a mismatch θ'_d of more than half of the angular step resolution g, beam steering is triggered g degrees towards the predicted direction $\theta'_{pr}[t]$, which is updated without heading to beam rescan. However, the beam rescans can be still activated once the Rx power falls below the threshold, which normally means the prediction is no longer accurately following the UE movement behavior and needs another rescan for adjustment.

Angle Correction (AC) Algorithm

The ASP algorithm described in the last subsections strongly relies on the accuracy of its beam scanning results. Hence, it cannot prevent the prediction from being gradually offset to the actual UE position during the observation phase, as the PM only has a limited angular resolution that already impairs the initial speed estimate. Therefore, a fine-tuning algorithm is required to increase the preciseness of the prediction. As a solution, we developed an angle correction (AC) algorithm which provides additional angle and timing information during the observation stage.

In ASP algorithm we employ an estimator for the target speed that uses two possibly erroneous position measurements from Algorithm 2, $\theta'_l[c_t - 1]$ and $\theta'_l[c_t]$ which can be modeled as follows:

$$\theta'_l[c_t - 1] = \theta_r[c_t - 1] + e[c_t - 1], e[c_t - 1] \sim \mathcal{U}\left[-\frac{g}{2}, \frac{g}{2}\right] \tag{6.8}$$

$$\theta'_l[c_t] = \theta_r[c_t] + e[c_t], e[c_t] \sim \mathcal{U}\left[-\frac{g}{2}, \frac{g}{2}\right] \tag{6.9}$$

with $\theta_r[c_t - 1]$ and $\theta_r[c_t]$ being the real target positions and $e[c_t - 1]$ and $e[c_t]$ being the estimation errors due to to the uniform quantizer nature of the scan. The speed estimation is described as the first order difference quotient with $\Delta t = T[c_t] - T[c_t - 1]$ showing the time interval between two independent angle measurement

$$\begin{aligned} v_a &= \frac{\theta_l'[c_t] - \theta_l'[c_t - 1]}{\Delta t} \\ &= \underbrace{\frac{\theta_r[c_t] - \theta_r[c_t - 1]}{\Delta t}}_{estimate} + \underbrace{\frac{e[c_t] - e[c_t - 1]}{\Delta t}}_{error}. \end{aligned} \tag{6.10}$$

Statistical Considerations

First, we compute the expectation of our velocity estimate

$$\begin{aligned} \mathbb{E}\{v_a\} &= \mathbb{E}\left\{\frac{\theta_r[c_t] - \theta_r[c_t - 1]}{\Delta t} + \frac{e[c_t] - e[c_t - 1]}{\Delta t}\right\} \\ &\overset{(a)}{=} \frac{\theta_r[c_t] - \theta_r[c_t - 1]}{\Delta t} \\ &\quad + \frac{1}{\Delta t} \cdot \Big(\underbrace{\mathbb{E}\{e[c_t]\}}_{0} - \underbrace{\mathbb{E}\{e[c_t - 1]\}}_{0}\Big) \\ &\overset{(b)}{=} \frac{\theta_r[c_t] - \theta_r[c_t - 1]}{\Delta t} \end{aligned}$$

where step (a) is due to the non-statistical character of $\theta_r[c_t - 1]$,$\theta_r[c_t]$ and Δt, in the context of the estimator, and the linearity of the expectation operator. Step (b) due to the fact that the random variables $e[c_t - 1]$ and $e[c_t]$ have the expectation $\mathbb{E}\{e[c_t - 1]\} = \mathbb{E}\{e[c_t]\} = \frac{1}{2}(\frac{g}{2} - \frac{g}{2}) = 0$. This shows that the estimator performs well on average, although the significance of single estimates still has to be examined.

The variance of both $\theta_l'[c_t - 1]$ and $\theta_l'[c_t]$ can be calculated as follows

$$\begin{aligned} \mathrm{Var}\{X_{\mathcal{U}[a,b]}\} &= \frac{(b-a)^2}{12} \\ &\Rightarrow \mathrm{Var}\{\theta_l'[c_t - 1]\} = \mathrm{Var}\{\theta_l'[c_t]\} = \frac{g^2}{12} \end{aligned} \tag{6.11}$$

Assuming that the two separate measurements of $\theta_l'[c_t - 1]$ and $\theta_l'[c_t]$ are statistically independent, we can calculate the variance of the speed estimation as follows

$$\begin{aligned} \mathrm{Var}\{v_a\} &= \mathrm{Var}\left\{\frac{\theta_l'[c_t] - \theta_l'[c_t - 1]}{\Delta t}\right\} \\ &\overset{(a)}{=} \frac{1}{\Delta t^2} \cdot \mathrm{Var}\{\theta_l'[c_t] - \theta_l'[c_t - 1]\} \\ &\overset{(b)}{=} \frac{1}{\Delta t^2} \cdot \left(\mathrm{Var}\{\theta_l'[c_t - 1]\} + \mathrm{Var}\{\theta_l'[c_t]\} - 2\,\mathrm{cov}\{\theta_l'[c_t - 1], \theta_l'[c_t]\}\right) \\ &\overset{(c)}{=} \frac{1}{\Delta t^2} \cdot \left(\mathrm{Var}\{\theta_l'[c_t - 1]\} + \mathrm{Var}\{\theta_l'[c_t]\}\right) \\ &= \frac{g^2}{6 \cdot \Delta t^2} \end{aligned}$$

whereby we made use of the following properties of the variance

(a) $\mathrm{Var}\{a \cdot X\} = a^2 \cdot \mathrm{Var}\{X\}$

(b) $\mathrm{Var}\{X - Y\} = \mathrm{Var}\{X\} + \mathrm{Var}\{Y\} - 2\,\mathrm{cov}\{X, Y\}$

(c) $\mathrm{cov}\{X, Y\} = 0$, if X and Y are statistically independent.

Suppose we now regard the calculated variance as a measure for scattering the estimated speed values around their expectation. In that case, we can conclude that the scattering is directly proportional to the square of the angular resolution and inversely proportional to the square of the time difference between two position measurements. In other words, if no additional steps are taken, shorter time intervals between two angle measurements will significantly worsen the impact of the angle quantization error on the speed estimate. Additionally, this result fundamentally restricts the system's ability to accurately follow highly dynamic target movements because of the fixed angular resolution of the PM.

The system must deal with shorter beam refinement intervals to track dynamic targets because we only use a first-order prediction model, which lowers prediction accuracy and, as a result, the capacity to follow the target with the best beam alignment. This highlights the requirement for an AC algorithm that seeks to correct the quantization errors by retrieving additional angle and timing data during the observation phase.

Algorithm 3 : AC algorithm

2. Observation and prediction:
$P_{max} = 0$, $P_{Bf} = P(\theta_r, \theta'_{Bf})[t]$;
while $P(\theta_r, \theta')[t] \geq \sigma_t \cdot P_{Bf}$ **do**
  if $P(\theta_r, \theta')[t] > P_{Bf}$ **then**
    $P_{Bf} = P(\theta_r, \theta')[t]$;
  end
  if $P(\theta_r, \theta')[t] > P_{max}$ **then**
    $P_{max} = P(\theta_r, \theta')[t]$;
    $\theta'_l[c_t] = \theta'_{Bf}, T[c_t] = t$;
  end
  if $c_t > 1$ **then**
    enter prediction with
    $v_a[c_r] = (\theta'_l[c_t] - \theta'_l[c_t - 1])/(T[c_t] - T[c_t - 1])$;
    $\theta'_{pr}[t] = \theta'_l[c_t] + (v_a[c_t])(t - T[c_t])$; $\theta'_{pr}[t] - \theta'_{Bf} = \theta'_d$;
    if $|\theta'_d| \geq g/2$ **then**
      $\theta' = \theta'_{Bf} + g \cdot (|\theta'_d|)/\theta'_d$, $P_{max} = 0$;
    end
  end
  $t = t + 1$;
end

The beamforming direction should be slightly ahead of the UE movement to derive the highest Rx power for IRS tracking with limited angular step resolution. Consequently, the Rx power will firstly increase to the optimum beamforming direction for the ideal instant $\theta' = \theta_r$, then it starts to decrease until the beamforming direction is updated for the next observation stage. The AC algorithm aims to update the tracking history and keep it as close as possible to this ideal instant. Since the AC algorithm shares the same angle initialization and

beams refinement stages as the ASP algorithm, we only focus on the observation and prediction stage in Algorithm 3. In addition to the ASP algorithm, a local maximum recording P_{max} is defined as a reliable reference in the tracking history list and initialized as 0. For each tracking duration within an unchanged beamforming angle, the Rx power $P(\theta_r, \theta')$ is utilized not only for updating the reference power but also for identifying local maximum power. The direct method to determine the local maximum can be realized by searching for the peak Rx power level and the time index through one tracking observation stage. However, such information brings huge latency to the system since no update can be operated before one observation stage is ended. As a solution, in this dissertation, the local maximum is constantly updated for each time index t. Similar to the threshold floating, once $P(\theta_r, \theta'_{Bf})[t] > P_{max}$, the algorithm regards the instant beamforming angle and time to be the local maximum for the refinement of tracking history. After the beamforming direction is updated satisfying $|\theta'_d| \geq g/2$, P_{max} is set back to 0 since another observation round is started with new local maximum required.

Result Analysis

Due to the measurement systems at different times, the settings for the predictive algorithms are slightly different to Figure 6.14. For a fair comparison, the Algorithm 1 is also repeated in the following results, with the parameters listed in Table 6.4.

All the results are presented in Figure 6.22 with the simulation results from Figure 6.22a to 6.22c, and measurement results from Figure 6.22d to 6.22f. In these figures, blue curves denote the Rx power $P(\theta_r, \theta')[t]$, and the yellow curves show the observation power $\sigma_t \cdot P_{Bf}$. For simulation, the power is a normalized value; for measurement, the power is measured at the input of Rx SDR. Each sudden drop of Rx power indicates one operation of beam refinement. As a benchmark, the tracking algorithm from Algorithm 1 is named a non-prediction (NP) algorithm for detailed analysis.

Starting with simulation, the results of the NP algorithm are presented in Figure 6.22a, with the most beam refinements triggered. In Figure 6.22b, the number of beam refinements is primarily reduced by the ASP algorithm with an exemplary beam refinement at around 5 s. The observation power is reached at this moment,

Table 6.4: System setting parameters

Start angle θ_s	$-60°$
End angle θ_e	$60°$
Angular resolution g	$2°$
Threshold σ	0.65
Beam refinement width k'	$20°$
UE movement speed	10 m/min
UE movement distance	1.53 m
Tracking duration	9.18 s
Bandwidth	1 MHz

and a rescan is triggered to search for the current reliable position information. After this refinement, a sudden power level increase can be seen, which means that the beamforming directions from the last angle steps were sub-optimum due to the prediction mismatch. The solution to this problem can be clearly observed in Figure 6.22c. With the help of the AC algorithm, there is only one necessary rescan at around 2 s to fulfill the triggering of prediction. Afterwards, the local maximum updating of the algorithm offers reliable UE angular speed, angular speed, and position estimation that no further rescans are necessary.

For each tracking algorithm, one example is depicted from Figure 6.22d to 6.22f focusing on the measured Rx power and observation power. In the example from Figure 6.22d, a typical failure can be observed for the beam refinement at approximately 2.5 s. In this case, the real-time computation suffers from a failure that loses the UE position. The more beam refinements are operated over the entire tracking, the more such failures will occur statistically. This shows precisely why beam refinements times are aimed to be reduced in this dissertation. It can be seen in Figure 6.22e that the number of beam refinement rescans is primarily reduced by the ASP algorithm. The rescans are triggered more often during the UE movement away from the IRS BS because fast power degradation makes the threshold levels easier to violate. However, the threshold can not be reduced casually as this increases the probability of losing beam alignment with the target. This problem can be addressed using the AC algorithm in Figure 6.22f. With the angle correction using the constantly updated local maximum, the number of rescans becomes very low also when the UE moves away. However,

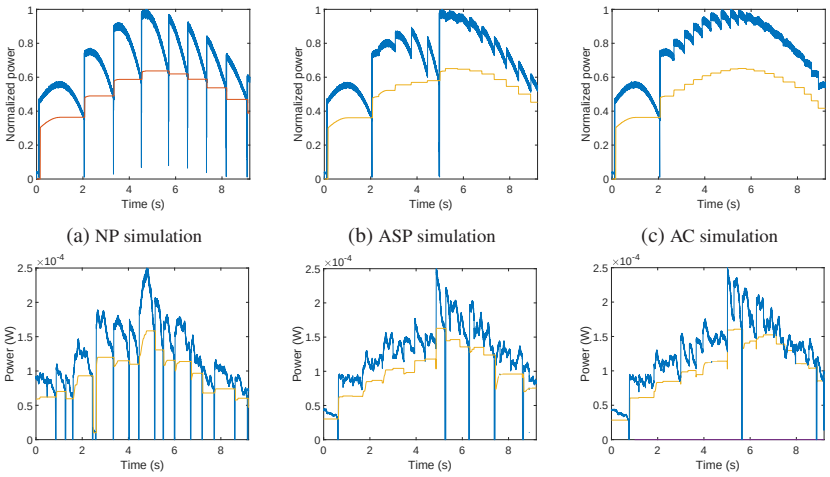

(a) NP simulation (b) ASP simulation (c) AC simulation

(d) NP measurement (e) ASP measurement (f) AC measurement

Figure 6.22: Figures for IRS tracking system performance analysis. (a) to (c): Simulation results. (d) to (f) measurement results. Blue curves denote the Rx power and yellow curve denotes the tracking observation.

due to the noise, a multi-path effect accompanied by the indoor environment, and the target movement contribution towards or away from the IRS, there can still be mismatches, meaning the beam refinements can not be fully eliminated. Nevertheless, the performance improvement is noticeable compared to the other two algorithms. Overall, both Rx power and observation power change as expected for all three algorithms. The measurement results also meet the same conclusion as the simulation results.

To analyze the performance of these tracking algorithms, we calculate the training overhead, average power, and average angle mismatch mentioned (6.3), (6.4), and (6.5). In addition, the average prediction mismatch A_p is computed based on their differences with the real UE position, which is expressed as

$$A_p = \frac{1}{N_a} \sum_{t=1}^{N_a} (\theta'_{pr}[t] - \theta_r[t]). \tag{6.12}$$

As the best candidate, an example of the AC algorithm measurement in Figure 6.22f is presented by Figure 6.23. The red line indicates the UE's actual positi-

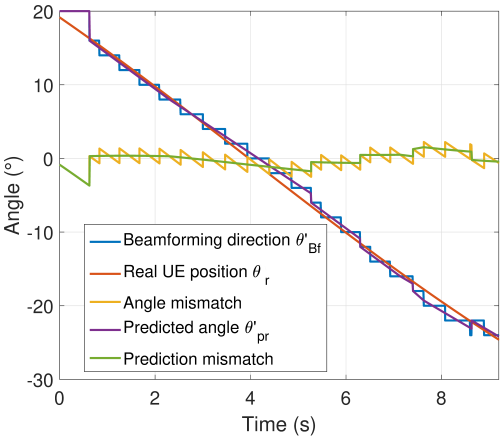

Figure 6.23: Angle analysis for AC algorithm corresponding to Figure 6.22f.

on, and the blue curve depicts the IRS beam steering. The difference between the aforementioned curves expresses the angle mismatch provided by the yellow curve. The green curve represents the prediction mismatch for tracking prediction, and the purple curve depicts the predicted angle. There are slight angle mismatches in prediction and beamforming due to limited IRS beamforming angle resolution. The predicted angle and beamforming direction overlap when the angle initialization and beam refinements are initiated.

As mentioned in the last section, the IRS tracking system with the NP algorithm outperforms former tracking systems with flexible training overhead, which keeps redundancy as low as possible. In Table 6.5, we firstly compare how the novel prediction algorithms further improved the system performance. The performance parameters are derived by averaging the values over several measurements. The training overhead T_{tr} is primarily reduced by the ASP algorithm and further improved by AC, same as the conclusion in Figure 6.22. Correspondingly, higher average power P_a can be derived with lower training overhead since the data propagation during the beam refinement stage is not considered as valid duration. Following the same logic, the angle mismatch A_a is improved by two aspects in the prediction algorithms. Firstly, the latency caused by beam refinement will introduce degradation of angle accuracy. Secondly, with fewer beam refinements, system failures are less likely to occur.

Table 6.5: Comparison for different tracking algorithms

	T_{tr}	P_a	A_a	A_p
NP	1.25%	9.96×10^{-5} W	1.064°	N/A
ASP	0.47%	1.12×10^{-4} W	0.903°	0.801°
AC	0.31%	1.22×10^{-4} W	0.806°	0.714°

The NP algorithm has no prediction mismatch since no predictive computation is operated. The prediction mismatch is lower compared to the practical angle mismatch due to the limited angular step resolution of the implemented IRS and system latency. It can be concluded that the tracking ability is improved with increasing order by NP, ASP, and AC algorithm. The proposed new algorithms improve the performance only with an additional cost of memory for the tracking history and local maximum information.

In the end, a further comparison, including other tracking systems, is shown in Table 6.6 and described as follows. The benchmark literature cover beamforming tracking measurements for variant wireless communication at 28 GHz for fair comparisons. Since the fastest angular speed of 37.5° and the low angle mismatch is already presented in [LBE+21] and Figure 6.21, we focus on the training overhead and the number of beam candidates in this paper. In the previous works, the algorithms are based on implementing a certain number of time slots for tracking localization. In our work, after implementing the AC algorithm, the training overhead maintains low even with the most number of beams in the codebook. The reason is that many scans can be avoided by implementing prediction algorithms. In addition, the property of floating training overhead from [LBE+21] and 6.21 is maintained, which keeps the minimum training time and high tracking accuracy compared with other works using a fixed amount of pre-assigned training slots being operated periodically over time.

6.3 Conclusion on this Chapter

In this chapter, the IRS nearfield illumination application type is concentrated on creating novel wireless communication system models using a single IRS as an alternative antenna array. It is assumed that the IRS is equipped at a

Table 6.6: Comparison to tracking performances in other literatures

	T_{tr}	Beams
This work	0.31%	61 beams from $-60° : 2° : 60°$
[OIA+16, MSS+17]	4/34 slots = 11.67%	16 beams from $(-30° : 10° : 40°) \times (0° : 10° : 10°)$
[KTH+17]	1/50 slots = 2%	48 beams
[NMO+20]	4/50 slots = 5%	28 beams from $(-36° : 6° : 36°) \times (0° : 10° : 10°)$

BS on the Tx side. The measurements began with a SISO proof of concept system with pre-knowledge of DoD, and the system's MERs were measured in different IRS beamforming directions. The accuracy of the DoD estimation was then used to study and validate various IRS channel estimation algorithms, such as exhaustive search and hierarchical codebook algorithms. The ability of IRS beamforming studied from Chapter 4 to accommodate various wireless communication multipath scenarios was further enhanced. Next, the IRS-based system was combined with advanced communication technologies. First, a demonstration of an IRS TDMA system was presented, along with a study of the system's settling time. The IRS was proved to potentially support future developments by realizing TDMA with beam switching speeds faster than LTE specifications. Second, a tracking system was developed using inspiration from IRS's ability to steer a beam rapidly and precisely. The IRS beamforming could track a moving UE with low training overhead and angular mismatch. The 5G 3GPP standards were used to adapt the tracking beam management. The training overhead in a tracking system was further reduced by the design and measurement of prediction algorithms, which also improved the average power reception over the tracking duration.

The main innovation of this chapter is integrating an IRS-based system with contemporary wireless communication technologies. On the one hand, this is a significant milestone which can not be skipped. On the other hand, such experiments drive IRS research up to application levels from independent antenna design or communication theory. The positive outcomes proposed that an IRS might be a viable option for upcoming wireless communication. On the other

hand, considering predictive tracking in measurements proved IRS's capacity to solve real-world scenarios, which had never been covered in previous literatures.

7 Hybrid MIMO Beamforming System using IRS

The development of multiple IRSs in wireless systems can be examined further based on the insensitive studies of a single IRS performance in the previous Chapters. As a result, the hybrid MIMO beamforming system shown in Figure 2.15 is created using the innovative architecture realized by IRSs. This chapter focuses on the channel estimation, data propagation, and signal recovery of the first IRS-based experiment hybrid beamforming system. This chapter contains reuse of texts and figures from [LLdO+22] © [2022] IEEE.

7.1 System and Mathematical Model

In the proposed hybrid MIMO beamforming system using IRS, the wireless transmission link between multiple antenna BS and UE is proposed. Since BS is always immobile, it is easier to be equipped with complex hardware and power supplies. Therefore, the IRSs are designed to operate at the BS side, same as the definition in Chapter 6. On the UE side, multiple antennas are equipped regardless of their type. The transmitted signal covers a certain bandwidth with the OFDM scheme allocated to the subcarriers, as mentioned in Figure 3.6. The system is defined to be stationary within a sufficient time for signal processing. The signal model follows Figure 2.14 to evaluate such a system. The signals are defined to be the allocated symbols at the frequency domain. Therefore, the mathematical model follows the general hybrid beamforming mentioned in (2.31), with the effective channel matrix representing the CFR. In this system, the total number of Tx antenna $N_t = N_d N_I$ formulates the number of rows in $\boldsymbol{F}_{Tx,RF}$, with $N_I = MN$. Due to the architecture property of the IRSs, the proposed hybrid beamforming architecture follows the subarray based model mentioned in Figure 2.15b. Thus, $\boldsymbol{F}_{Tx,RF}$ becomes a diagonal matrix expressed as

$$\boldsymbol{F}_{Tx,RF} = \begin{bmatrix} \boldsymbol{\Phi}_1 & \mathbf{0} & \mathbf{0} & \mathbf{0} & \mathbf{0} \\ \mathbf{0} & \ddots & \mathbf{0} & \mathbf{0} & \mathbf{0} \\ \mathbf{0} & \mathbf{0} & \boldsymbol{\Phi}_{n_d} & \mathbf{0} & \mathbf{0} \\ \mathbf{0} & \mathbf{0} & \mathbf{0} & \ddots & \mathbf{0} \\ \mathbf{0} & \mathbf{0} & \mathbf{0} & \mathbf{0} & \boldsymbol{\Phi}_{N_d} \end{bmatrix} \tag{7.1}$$

considering that each feeding antenna illuminates one IRS. In (7.1), $\boldsymbol{\Phi}_{n_d} \in \mathbb{C}^{N_I \times 1}$ is the analog beamforming vector for the n_dth PM. Considering the definition that only digital beamforming exists at Rx, $\boldsymbol{F}_{Rx,RF}$ becomes an identity matrix with rank $M_d = M_r$ which can be omitted as mentioned in (2.13). In the end, the Rx data stream for the IRS hybrid MIMO beamforming system is

$$\boldsymbol{s}_{Rx} = \boldsymbol{F}_{Rx,BB}\boldsymbol{H}\boldsymbol{F}_{Tx,RF}\boldsymbol{F}_{Tx,BB}\boldsymbol{s}_{Tx} + \boldsymbol{F}_{Rx,BB}\boldsymbol{w}. \tag{7.2}$$

7.2 Interleaved OFDM

One challenge for a MIMO or hybrid MIMO system is to realize channel estimation. This topic has become a trendy research direction in the wireless communication technology field, which is listed in Section 1.2. For a MIMO system, the channel coefficient can not be derived directly using the LS method from (3.3) since the interference from other MIMO channels will contribute to the desired channel coefficient, leading to inaccuracy. This dissertation implements the interleaved OFDM technology for channel estimation. This idea was initially born for radar sensing from [SSBZ13] but can be adapted to communication systems. Based on the fundamental introduction of OFDM from Figure 3.6, the multicarrier modulation can allocate the desired signals at different carriers along the frequency. With the help of OFDM, the signals at different subcarriers are orthogonal with others. Therefore, by distributing different subcarriers at different Tx antennas, the signals are both spatially and frequency orthogonal, leading to the precise derivation of the CSI between each pair of Tx and Rx chains in a MIMO system at the specific subcarrier.

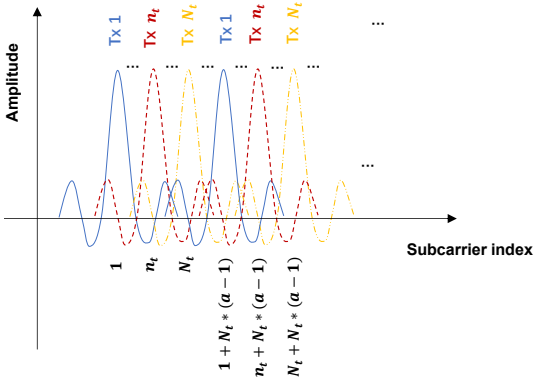

Figure 7.1: Theoretical interleaved OFDM subcarriers at Rx.

The detailed interleaved OFDM technology is introduced as follows. In this dissertation, N_c subcarriers are uniformly assigned in a bandwidth of B. For the sake of conciseness, the OFDM in this chapter mainly focuses on the frequency domain signal processing descriptions with enough cyclic prefix issued to avoid ISI as default. Therefore, the training symbols can be presented as $\boldsymbol{s}^{tr} \in \mathbb{C}^{N_c \times 1}$ covering all the allocated subcarriers. The principle of interleaved OFDM is distributing sparse subcarriers to each Tx antenna without overlapping with other ones. A subcarrier selection matrix $\boldsymbol{G}_{n_d} \in \mathbb{C}^{N_c \times N_c}$ is defined for the n_d^{th} Tx RF chain with $\mathrm{diag}(n_d + N_d * (a-1)) = 1$ and all other elements to be 0, and $a \in \{1, 2, 3, ..., N_c/N_d\}$. Afterward, the training symbols for the n_dth antenna can be be expressed as

$$\boldsymbol{s}_{n_d}^{tr} = \boldsymbol{G}_{n_d} \boldsymbol{s}^{tr}. \tag{7.3}$$

At Rx, each antenna receives signals from all the subcarriers, with each subcarrier containing the channel coefficient contributed by the specific Tx antenna as shown in Figure 7.1. By computing the ratio between received symbol $s_{m_d}^{n_c}$ and training symbols s^{tr,n_c} using the LS method from (3.3) at the n_c subcarrier, the estimated channel coefficients from the digital channel matrix $\hat{\boldsymbol{H}}$ for the m_dth Rx chain at the n_c^{th} subcarriers are

$$\hat{h}_{m_d}^{n_c} = s_{m_d}^{n_c} / s^{tr,n_c}. \tag{7.4}$$

By repeating the same training symbols P times, the final channel coefficient can be computed by averaging

$$\overline{h}_{m_d}^{n_c} = \frac{1}{P} \sum_{p=1}^{P} \hat{h}_{m_d}^{n_c}(p). \tag{7.5}$$

7.3 Hybrid Channel Estimation Algorithm

The problem of digital channel estimation should be resolved with the help of interleaved OFDM technology. The entire channel estimation algorithm for the proposed IRS hybrid MIMO beamforming system still needs to be developed, combining the digital channel estimation with the analog beam training algorithm.

7.3.1 Analog Beam Training

Similar to the derivation of the $\boldsymbol{F}_{Tx,RF}$ from Chapter 6, algorithms such as exhaustive search and hierarchical codebook can also be utilized in the hybrid MIMO beamforming system. However, due to the existence of multiple antenna units, yielding multiple Rx and digital chains based on our singleuser MIMO assumption, the peak detection for the DoD has to be utilized through all the Rx signals. Therefore, the goal for analog beamforming, defined by the quality indicator $Q(\Theta')$ in (6.1), is to maximize the performance over all Rx channels and angles of interest, which mathematically optimizes the set of phases $\varphi\,(m, n, \theta', \phi')$ from (2.16) for $\boldsymbol{\Phi}_{n_d}$. This relationship can be expressed as

$$\begin{aligned} \boldsymbol{\Phi}_{n_d}(m + M * (n-1)) &= \varphi\left(m, n, \theta', \phi'\right) \\ &= \text{argmax}_{\theta', \phi' = 0^\circ} \frac{1}{M_d} \sum_{m_d}^{M_d} Q(\Theta'). \end{aligned} \tag{7.6}$$

7.3.2 Interpolated Digital Channel Estimation

The goal for hybrid beamforming is to minimize the error between the optimum beamforming $\boldsymbol{F}_{opt}$ and $\boldsymbol{F}_{Tx}$ [AEALH14], which can be denoted by $\min \left\| \boldsymbol{F}_{opt} - \boldsymbol{F}_{Tx} \right\|_F$, where $\|\cdot\|_F$ is the Frobenius norm. With the analog beamforming matrix $\boldsymbol{F}_{Tx,RF}$ derived by the analog beam training, the estimated beamforming direction θ'_{n_d} for the n_dth IRS is determined. Therefore, the effective digital channel matrix becomes

$$\boldsymbol{H}_d = \boldsymbol{H}\boldsymbol{F}_{Tx,RF}, \tag{7.7}$$

which is the estimation goal for digital beamforming. Based on the matrix computation, the size of $\boldsymbol{H}_d$ is reduced to $M_d \times N_d$ with the computational cost largely saved. Following (7.3) to (7.5), the channel coefficients at each Rx can be computed. By considering all the subcarriers and averaging through training intervals, we use $\overline{\boldsymbol{H}}_{m_d}$ to denote the channel matrix derived at the m_dth Rx chain. This contains all the digital channel coefficients between the different Tx antennas to the specific Rx antenna due to the interleaved OFDM carriers. To derive the elements from each Tx, the generation matrix in (7.3) can be used and

$$\overline{\boldsymbol{H}}^{\theta'_{n_d}}_{n_d,m_d} = \boldsymbol{G}_{n_d}\overline{\boldsymbol{H}}_{m_d} \tag{7.8}$$

expresses the channel coefficients from the n_dth Tx antenna via the estimated DoD θ'_{n_d} derived from the analog beam training. However, it can be seen that these coefficients only cover the interleaved sparse subcarriers, which are not enough to realize full MIMO gain utilizing the whole bandwidth. Thus, interpolation algorithms are required to derive the full estimated effective digital channel matrix $\hat{\boldsymbol{H}}$ for all the subcarriers.

The interpolation steps can be found in Algorithm 4. For initialization, the number of Tx antennas N_d, Rx antennas M_d, and subcarriers N_c are known. As the input of the algorithm, the measured and averaged $\overline{\boldsymbol{H}}^{\theta'_{n_d}}_{n_d,m_d}$ is loaded, which has zero elements between the valid subcarriers due to the interleaved gaps. After IDFT, the measured CIR $\overline{\mathbb{H}}^{\theta'_{n_d}}_{n_d,m_d}$ is derived. This CIR has a periodic property due to the interleaved subcarriers and down sampling is required to abstract the desired N_c/N_d samples, which yields $\underline{\mathbb{H}}^{\theta'_{n_d}}_{n_d,m_d}$. Afterward, in order to recover the full N_c samples, a zero-padding (ZP) is implemented and the zero-padded-CIR (ZP-CIR) $\hat{\mathbb{H}}^{\theta'_{n_d}}_{n_d,m_d}$ is derived. Finally, the ZP-CIR

undergoes a DFT to produce the CFR and the missing carriers from $\overline{\boldsymbol{H}}^{\theta'_{n_d}}_{n_d,m_d}$ are interpolated yielding channel coefficient estimates $\hat{\boldsymbol{H}}^{\theta'_{n_d}}_{n_d,m_d}$ over all subcarriers. This algorithm is operated through all the M_d Rx chains to get the complete estimated effective channel matrix $\hat{\boldsymbol{H}}$. Detailed analysis of this algorithm will be presented altogether with measurement results in the following sections.

Algorithm 4 : Interpolation Algorithm

Initialization: N_c, M_d, N_d
for $m_d = 1$ *to* M_d **do**
  Input: Measured interleaved CFR $\overline{\boldsymbol{H}}^{\theta'_{n_d}}_{n_d,m_d}$
  1. $\overline{\mathbb{H}}^{\theta'_{n_d}}_{n_d,m_d} =$ **IDFT** $\left\{\overline{\boldsymbol{H}}^{\theta'_{n_d}}_{n_d,m_d}\right\}$
  2. Down sampling $\overline{\mathbb{H}}^{\theta'_{n_d}}_{n_d,m_d}$ **to** N_c/N_d **samples**
  3. Zero padding $\underline{\mathbb{H}}^{\theta'_{n_d}}_{n_d,m_d}$ **back to** N_c **samples**
  4. $\hat{\boldsymbol{H}}^{\theta'_{n_d}}_{n_d,m_d} =$ **IDFT** $\left\{\hat{\mathbb{H}}^{\theta'_{n_d}}_{n_d,m_d}\right\}$
end

7.4 System Description

As an IRS MIMO hybrid beamforming system, it occupies the most number of devices in this dissertation. Therefore, it is essential to describe the detailed settings clearly, to support the further analysis of the results.

7.4.1 Complete System Setup

In this section, the IRS MIMO hybrid beamforming system is introduced as the most advanced setup in this dissertation. In the following result analysis sections, a reduced number of digital chains might be used but can be regarded as partially activating the complete system. The system model of our proposed setup is presented in Figure 7.2. The scenario considers singleuser downlink communication from a BS equipped with $N_d = 3$ IRSs to a full digital UE equipped with $M_d = 4$ receive antennas, corresponding to the same number of

RF channels. The implemented devices follow the ones described in Chapter 5. Two SDRs are required for both Rx and Tx sides to realize this MIMO dimension. The IRS hybrid MIMO beamforming system is demonstrated in an indoor environment via a 2 m link distance, as shown in Figure 7.3. The LoS channel dominates the signal transmission with possible reflection paths in this condition. For OFDM signals, $N_c = 2048$ active subcarriers are assigned in the 1 MHz bandwidth. QPSK symbols are transmitted.

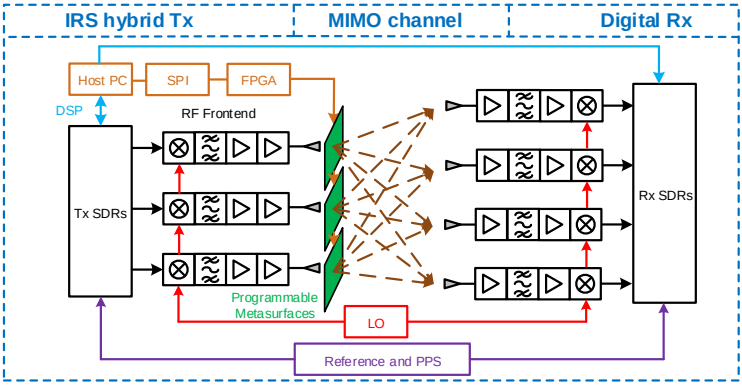

Figure 7.2: System model for PM hybrid MIMO beamforming.

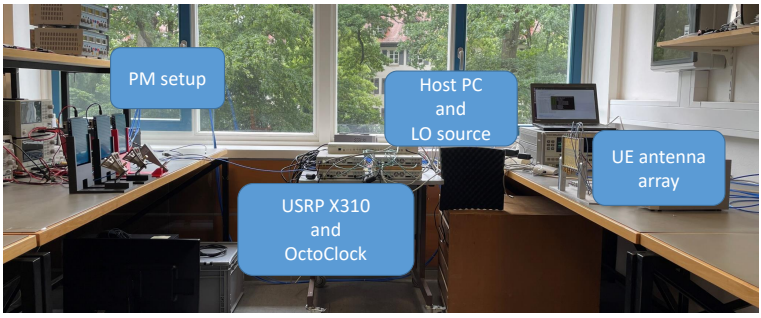

Figure 7.3: Measurement environment for the IRS hybrid MIMO beamforming system for single-user scenario.

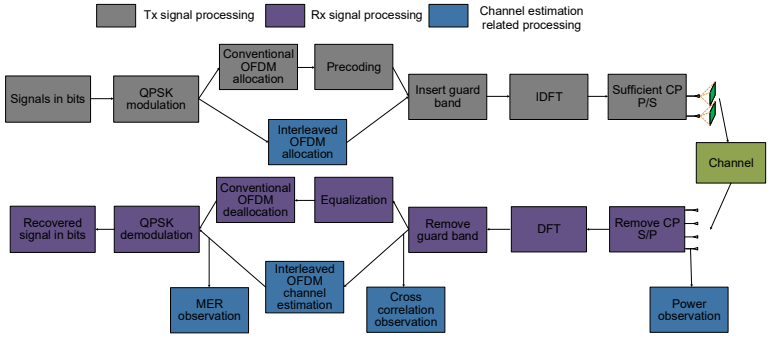

Figure 7.4: General digital signal processing flow graph operated by PC.

7.4.2 Signal Processing Flow

The signal processing flow for the IRS hybrid MIMO system operated in the host PC from Figure 7.2 is depicted in Figure 7.4. The signal processing flows are defined into three aspects: Tx signal processing, Rx signal processing, and channel estimation related processing. The signals for different data streams are initially in bit format and modulated to QPSK symbols, with its generation mentioned in Figure 3.2a. If the training symbols are generated for channel estimation, interleaved OFDM signals are allocated based on the descriptions in the last section to enable frequency and spatial orthogonality among the signals from different IRSs. If the signals are generated for data transmission, conventional OFDM allocation takes place with all the subcarriers allocated with transmitting signals, as mentioned in Chapter 3. Afterwards, precoding is an alternative based on the data transmission methods from (3.11). Then, a guard band can be inserted to avoid interference. Before the signals are fed into antennas, IDFT, sufficient CP, and P/S conversion should be considered. After applying the channel, CP should be removed after the S/P conversion at the Rx side, and DFT converts the signals back to the frequency domain. Since the guard band is filled with null symbols, it can be removed before the post-processing. If the signals are training symbols, interleaved OFDM channel estimation from the last section is operated, and MSE can be computed here to analyze the channel estimation performance. If the signals are received for data transmission, equalization based on the methods from Section 3.4 takes place to derive the recovered signals, which are further deallocated to the

corresponding subcarriers and data streams. After QPSK demodulation, the signals are transferred back to bit format, where the BER can be computed using (3.1). For the beam training metrics introduced in Figure 6.1, the power can be directly analyzed after the Rx antennas to avoid further signal processing. The cross-correlation between the training symbols and the received signal is computed after removing the guard band since this avoids the computation for null subcarriers. The MER has to be analyzed once the QPSK symbols are recovered, which requires the most signal processing blocks but achieves the most reliable performance. For the signal processing order, the communication frame starts with the training symbols. Beam training first takes place, and the OFDM interleaved channel estimation is operated in the optimum DoD beamforming direction. Once the CSI is derived, data transmission takes place.

7.5 Experimental Results

Measurements can be carried out to confirm the accuracy of the algorithms and prove the practicability of the IRS MIMO hybrid beamforming system based on the mathematical model and the algorithms mentioned in the previous sections. The experiment results include comparisons with various digital beamforming methods as well as channel estimation, data propagation, and signal recovery. These research results support the comprehensive study of the IRS hybrid MIMO system.

7.5.1 Channel Estimation Results

Channel estimation, the first step in communication signal processing, must be carried out to estimate the CSI for signal recovery methods. The channel estimation results are divided into analog beam training and interleaved OFDM digital estimation, maintaining the structure from the previous section.

Analog Beam Training

Using the similar beam training strategy mentioned in Section 6.1.2, and combining with the multi-antenna consideration in 7.6, the analog beam training

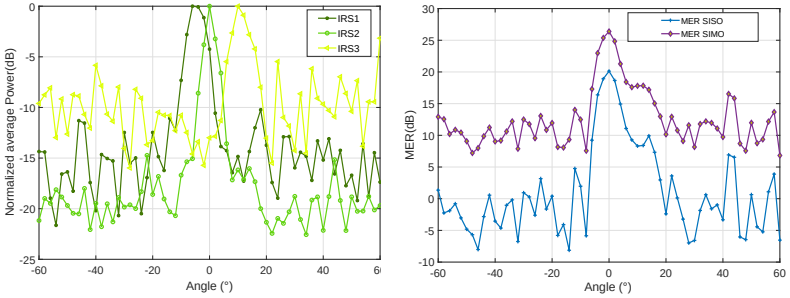

(a) Anaglog beam training results for 3 IRSs at the Tx. (b) Comparison of SISO and MISO beam training.

Figure 7.5: IRS MIMO hybird beamforming system beam training results.

for all 3 IRSs is presented in Figure 7.5a. The DoD from the IRS point of view is measured to be $-4°, 0°$, and $10°$. An exhaustive search algorithm from Section 6.1.2 is implemented for each IRS. Since the properties of different metrics have been discussed in Table 6.1 and Figure 6.3, the averaged power is implemented here as a representation. By making the combined observation for beam training at all the Rx antennas, the delivered results become more reliable due to MIMO gain. Using MER as an example, a comparison of SISO beam training using one of the Rx antennas and the SIMO beam training using the entire Rx array is presented in 7.5b. The ZF equalization from (3.5) is implemented for both cases, and a significant difference can be observed for the SIMO system considering the contribution of 3 Rx chains due to the benefits of MIMO diversity, which makes the channel estimation more robust.

Digital Channel Estimation

Once the analog beamforming part $\boldsymbol{F}_{RF,Tx}$ is derived, the effective digital channel matrix is formulated as (7.7). To have a better visibility, the Algorithm 4 is transformed into the flow graph in Figure 7.6(a). For the first step, the measured and averaged $\overline{\boldsymbol{H}}^{\theta'_{n_d}}_{n_d,m_d}$ can be derived by implementing LS channel estimation (3.3) between each Tx and Rx antenna pairs with the help of interleaved OFDM at the optimum beam training angle duration. By observing Figure 7.6(b) as an example using the subcarriers from $n_c = 1000$ to 1100, $\overline{\boldsymbol{H}}^{\theta'_{n_d}}_{n_d,m_d}$ has zero

elements between the valid carriers due to the interleaved gaps. After IDFT, the measured CIR $\overline{\mathbb{H}}_{n_d,m_d}^{\theta'_{n_d}}$ shows a periodic property observed as three same peaks in Figure 7.6(d) due to the interleaved subcarriers. Each period of CIR shows a single high peak, and a few other smaller peaks due to the domination of LoS transmission and a few weak reflection paths contributed by the indoor environment in this dissertation. Afterward, the under-sampling operation picks the first $N_c/3$ samples of the CIR and undergo ZP back to N_c samples, which leads to the ZP-CIR $\hat{\mathbb{H}}_{n_d,m_d}^{\theta'_{n_d}}$ in Figure 7.6(c). The CIR undergoes a DFT to produce the CFR and the missing carriers from $\overline{\boldsymbol{H}}_{n_d,m_d}^{\theta'_{n_d}}$ are interpolated yielding channel coefficient estimates $\hat{\boldsymbol{H}}_{n_d,m_d}^{\theta'_{n_d}}$ over all subcarriers as shown in Figure7.6(e).

To prove the accuracy of the interpolated channel estimation, channel coefficients are also measured between a single active Tx and Rx chain. In this case, full subcarriers are assigned to this pair of the transceiver chain, which yields measurements through the entire bandwidth expressed by Figure 7.6(e). A good matching between the measured and interpolated channel coefficients can be observed, proving that the CSI can be properly derived efficiently by implementing interleaved channel estimation. Considering all the Tx and Rx combinations of n_d and m_d, the total estimation of the effective channel matrix is denoted as $\hat{\boldsymbol{H}}$. Due to the interleaved OFDM signal processing, all the Tx and Rx chains can be active and operate the computation simultaneously. Moreover, the aforementioned digital signal processing can be operated by using the samples received at the peak angle quality θ'_{n_d} duration from the analog beam training, which further reduces the channel estimation latency.

Determination of OFDM Frame

In order to correctly estimate the channel, it is also necessary to decide how sparse the interleaved subcarriers should be. Two coefficients determine the performance. The first coefficient is the number of subcarriers N_c. With a determined bandwidth, the subcarriers are uniformly distributed with the subcarrier spacing N_c/B. Therefore, the fewer subcarriers distributed, the less CFR needs to be measured. The second coefficient is the interleave index. The minimum interleave index is $i_c = N_d$ to ensure the orthogonality between each Tx antenna. This number can also be increased to reduce the number of measurements. However, changing the coefficients mentioned above should also

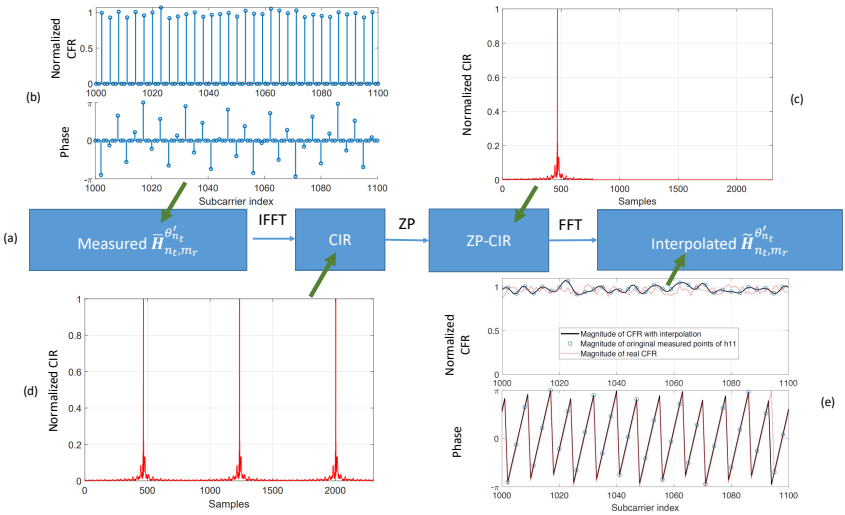

Figure 7.6: Digital channel estimation based on interpolated OFDM carriers. (a) Signal processing flowgraph. (b) Measured interleaved carriers from $n_c = 1000$ to 1100 at one Rx chain. (c) ZP-CIR $\mathbb{H}^{\theta'_{n_d}}_{n_d,m_d}$ after zero-padding (d) CIR $\overline{\mathbb{H}}^{\theta'_{n_d}}_{n_d,m_d}$ after IDFT of $\overline{\boldsymbol{H}}^{\theta'_{n_d}}_{n_d,m_d}$. (e) Estimated $\hat{\boldsymbol{H}}^{\theta'_{n_d}}_{n_d,m_d}$ covering all interested carriers after interpolation.

consider the spacing between the two measured carriers for each Tx antenna. If the frequency gap is too large, there will be missing information leading to an ill-estimated CFR, which results in improper signal recovery.

The number of DFT points decides how many subcarriers are needed to represent CFR. There are upper and lower bounds for determining the DFT points. On one hand, enough subcarrier should fulfill $N_c/B < B_c$, where B_c is the coherence bandwidth. Coherence bandwidth is the bandwidth over which the channel frequency response does not change significantly within it. Otherwise, the subcarrier spacing in frequency becomes too small, and ICI occurs if the channel is time selective or if there are any Doppler shifts. However, since our proposed system is stationary, or at least stationary in a period for signal processing, the upper boundary of N_c is not critical.

The lower boundary of N_c is critical for us due to the required channel estimation accuracy. In order to determine the number of FFT points, the SISO system transceiving with full bandwidth is considered. With LS channel estimation as

in equation (3.3), it is possible to obtain the channel coefficients for the subcarriers. Figure 7.7 shows the phase of the channel matrix with N_c as 64, 128, 256, 512, 1024 and 2048 in measurement, since amplitude is stable in the narrow bandwidth of 1 MHz, its performance is neglected. For lower numbers, e.g. 64, 128, 256, subcarriers cannot represent the whole channel because the spacing between every two points is too large, with the frequency periodicities between the measured points neglected. For example, the curve with 128 subcarrier in Figure 7.7 covers a wide frequency range with a straight line between measured points, which leads to loss of phase information. Subcarriers get enough for higher numbers, and the measured CFRs with 1024 and 2048 subcarriers overlap with the result from 512.

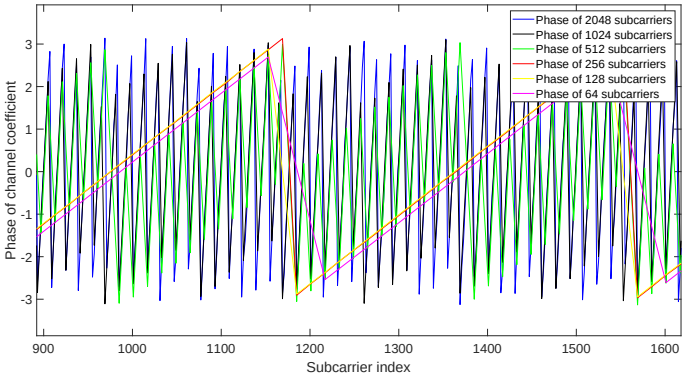

Figure 7.7: Phase of the measured CFR using 64, 128, 256, 512, 1024 and 2048 subcarriers.

However, to implement the proposed interleaved OFDM channel estimation, the interpolation index should also be considered. For ZP-CIR, the interpolated phase will not consider multiple ripples within the two measured points. Therefore, the frequency spacing between the two measured points should not contain multiple frequency periodicities. When interpolating the CFR, the minimum number of interleaved steps is the same as the number of transmit antennas, which is N_d. However, the number of interleaved steps can arbitrarily change and will influence the results' performance. For the completeness of measurement, i_c of 1,2,3,4,6,8 interleave index are measured for the performance of

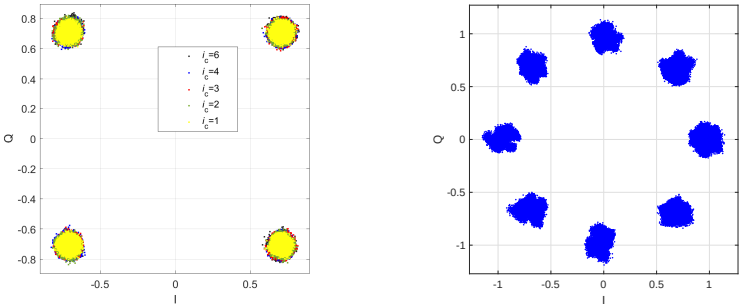

(a) Equalization results using different i_c.

(b) Equalization results with $i_c = 8$.

Figure 7.8: Channel interpolation analysis.

i_c	1	2	3	4	6
MER(dB)	28.84	26.93	26.91	26.64	26.61

Table 7.1: MER of OFDM interpolation using different interleaved factors i_c.

a single Tx and Rx chain for simple representation using $N_c = 2048$. After interpolating the full matrix, equalization can be performed, and the results are shown in Figure 7.8. It can be observed that until $i_c = 6$, the constellation clusters of the recovered QPSK symbols are very similar and overlapping with each other. Therefore, the MER from Figure 7.8a are listed as in Table 7.1.

The results proved that when the interleaved step is smaller, the carriers that needed interpolation are closer, and interpolation will be more precise with higher MER. When i_c is 1, there is no interpolation, and the MER is much higher than the others. When i_c becomes larger, the MER reduces slowly, but until $i_c = 6$, the CFR can be interpolated well, showing very similar constellation clusters in Figure 7.8a. However, when it comes to $i_c = 8$ as in Figure 7.8b, it is impossible to estimate the whole CFR because the spacing between neighbouring estimated points is large such that the spectrum is interpolated incorrectly. This case is the same as using 256 subcarriers to estimate the channel from Figure 7.7. With such large spacing between the measured coefficients, the ambiguities lead to phase rotations, with some symbols at the interpolated carriers wrongly recovered with a wrong phase contribution, as can be obser-

ved in Figure 7.7. In order to interpolate the measured channel coefficients and obtain a proper performance under interleaved OFDM, N_c has to be larger than 2048/6×3 = 1024 since i_c is at least $N_d = 3$ based on the proposed IRS system setup. To achieve a proper performance with reason computational effort, 2048 subcarriers are determined to transmit data in this dissertation.

In the end, the complete frame structure in the frequency domain is therefore determined as in Figure 7.9. In total, 4096 subcarriers are used altogether, including 1792 guard subcarriers at the edges of the spectrum, as a standard strategy in OFDM to avoid frequency leakage. In the middle, 256 subcarriers are spared for DC, which is not transmitting any data because of DC distortion possibly caused by LO self-mixing, which usually happens with SDRs and the implemented RF modules. The DC subcarriers are also neglected in the CFR interpolation. The rest $N_c = 2048$ subcarriers are allocated with data in the frequency domain.

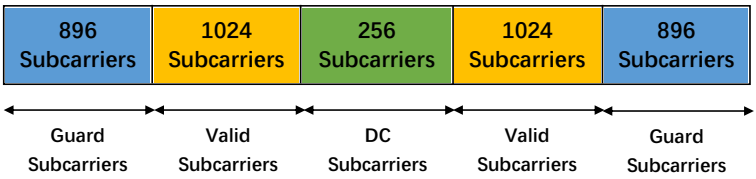

Figure 7.9: OFDM frame structure in this dissertation.

7.5.2 Data Propagation and Signal Recovery

Once the estimated effective channel matrix $\hat{\boldsymbol{H}}$ has been derived successfully, it can be utilized for data propagation and signal recovery. On the one hand, data propagation builds up the last important part of the entire communication system. On the other hand, with the help of signal recovery, the accuracy of the proposed channel estimation algorithm can be proved. Detailed studies are introduced to concretely analyze the system, focusing on different aspects in the following sections.

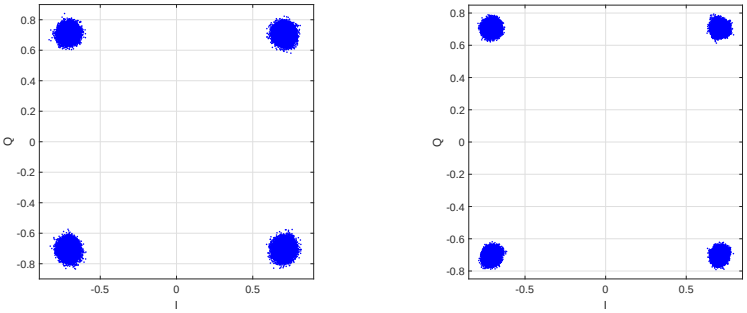

(a) Precoding results for SISO.

(b) Equalization results for SISO.

Figure 7.10: Constellation diagrams for recovered signals.

SISO Results

Firstly, SISO results can be illustrated in Figure 7.10a and 7.10b with signal processing methods of ZF precoding from (3.11) and equalization from (3.5). In this case, $N_d = M_d = 1$, which is very similar to the SISO measurements from Figure 6.1. The measurement is briefly repeated here for the analysis of MIMO gain in comparison with other MIMO dimensions. As a result, their MER, transmit power, and SDR normalized received power are listed in Table 7.1. As the first appearance, the SDR normalized power is an automatically quantized value shown in the host PC. This value is linearly corresponding with a real-world power, with the value 0.5 corresponding to −40 dBm from the input of Rx SDR. In Figure 7.11, it can be observed that with the increase of Rx power, the MER does not increase linearly as SNR. This is caused by the interference from leakage and undesired reflections due to the hardware imperfection that can never be eliminated, with its contribution increasing with the Rx power. These undesired contributions affect the MER with limited performance. Therefore, the MER of the system has a soft upper boundary. Please notice that, with different channels and measurement environments, the same MER value has different corresponding Rx power levels. In other words, the numerical relationship in Figure 7.11 does not always hold, but the curve's trend is constant.

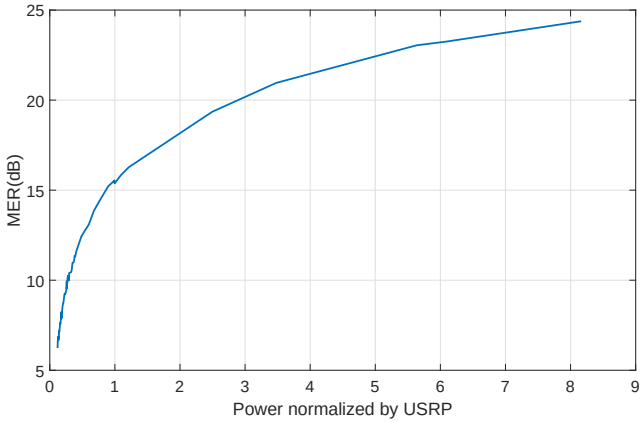

Figure 7.11: An example for relationship of SDR normalized power and System MER.

Go back to the SISO signal recovery in Table 7.2, it can be observed that equalization for SISO outperforms precoding for SISO. The reduced Tx power causes this after the precoding. However, no matter which method is chosen, the ratio between noise and signal will stay the same according to the transmit power. Since the MER is regarded a quasi SNR, the MER from precoding is used as the benchmark for the simulation, which leads to the simulated MER for precoding very close to the measured results in Table 7.2. From this table, the average transmit power for precoding is 8.26 times smaller than the equalization, resulting in 9.2 dB reduction in MER for precoding in simulation. In measurements, the results are affected by the behavior from Figure 7.11. When unitary power is transmitted and equalization is implemented, an MER of 29.9279 dB is derived instead of the theoretical 27.49 + 9.2 = 36.69 dB for equalization case.

	MER(dB)	Transmit power	Received power	Simulated MER(dB)
Precoding	27.63	0.12	1	27.49
Equalization	29.93	1 (unitary)	8.19	36.63

Table 7.2: Results for SISO precoding and equalization.

	MER(dB)	Transmit power	Received power
SIMO equalization	30.27	1	41.39
MISO Precoding	28.32	0.04	1

Table 7.3: Results for MISO precoding and SIMO equalization.

SIMO and MISO Results

After the verification of the system characteristics using a SISO system, the results of SIMO equalization and MISO precoding are shown in Table 7.3. Since only one data stream is transmitted for both cases, the constellation diagram is similar to the ones in Figure 7.10, only with different MERs. Therefore, the figures are omitted for simplicity. For SIMO results, Due to the imbalance of different SISO, the actual total power increasing in the SIMO system is actually 5 times lager. The reason is that the three received signals are in different quality, for channel matrix $\boldsymbol{H}_d = \left[h_{1,1}, h_{2,1}, h_{3,1}\right]^T$ in SIMO situation, the estimated magnitude of channel coefficients of $\hat{\boldsymbol{H}}$ are separately 2.8, 3.3, 4.6, and the worst one was used in the SISO measurement. However, due to the system limitation mentioned above, although MRC could be utilized in this case, only a small amount of SNR increase is visible, which is bounded to 30.27 dB.

For MISO precoding, the gain due to the diversity order can be better visualized. With proper combining scheme, the average power of transmit signal is 0.04, which is 4.36 dB lower than the SISO case in Table 7.1. The Rx power for MISO and SISO has the same normalized value 1, due to the property of precoding from (3.11). Based on the measured MISO MER in Table 7.4, the MISO has 28.32 - 27.63 + 4.36 = 5.05 dB diversity gain, which theoretically should be 4.77 dB. This difference is because the channel SISO used is the second strongest channel in the MISO system. For channel matrix in MISO with $\boldsymbol{H}_d = \left[h_{1,1}, h_{1,2}, h_{1,3}\right]$ and the measured magnitude of the elements in $\hat{\boldsymbol{H}}$ are 2.85, 2.80 ,2.38, which leads to a small extra gain for measurement results.

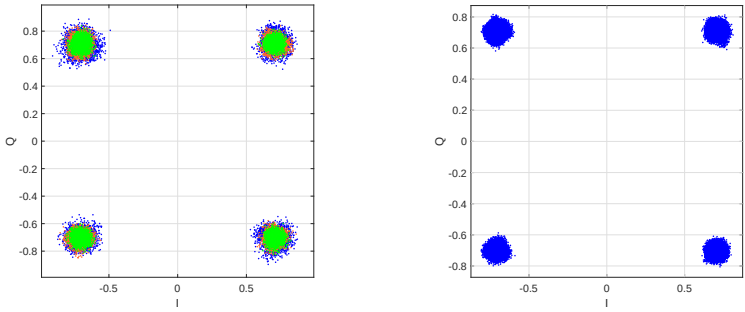

(a) Precoding results for 3×3 MIMO.

(b) Precoding results for 3×3 MIMO after MRC.

Figure 7.12: Constellation diagrams for recovered signals using ZF precoding.

MIMO Results

For the next step, the MIMO dimension of the hybrid beamforming system is increased to different ranks shown in Table 7.4.

	MER(dB) Signal 1	MER(dB) Signal 2	MER(dB) Signal 3	MER(dB) after MRC	Transmit power	Capacity (bit/s/Hz)
MIMO 3×3 precoding	26.72	24.63	22.34	28.03	0.24	14.39
MIMO 3×3 equalization	25.98	25.58	26.36	30.87	3	18.02
MIMO 3×4 equalization	28.37	27.63	27.89	31.40	3	18.27
MIMO 3×3 SVD	29.11	27.67	21.11	N/A	3	19.63
MIMO 3×4 SVD	28.70	27.54	19.62	N/A	3	20.64

Table 7.4: Results for 3×3 and 3×4 IRS hybrid MIMO system

The MER results of ZF precoding for the recovered signals in a 3×3 IRS hybrid MIMO system are 26.72, 24.63, 22.34 dB as in Figure 7.12a with different

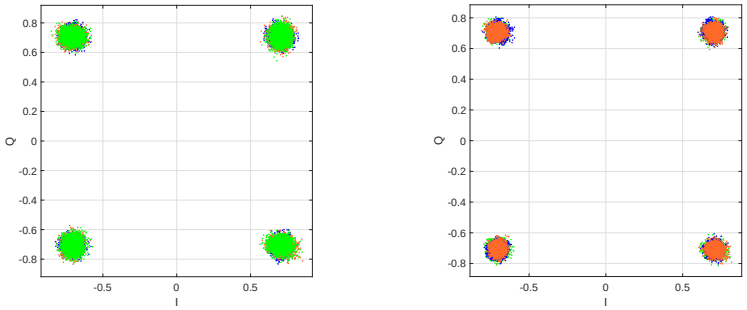

(a) Equalization results for 3×3 MIMO.

(b) Equalization results for 3×4 MIMO.

Figure 7.13: Constellation diagrams for recovered signals using ZF equalization.

colors. For different MER, variant sizes of clusters can be clearly observed. For a 3×3 MIMO system, multiple data streams can be transmitted, and the MER result for each recovered signal should be similar to the MISO precoding result. However, the channel estimation of a 3×3 MIMO matrix leads to more channel coefficients which suffer from more interferences, leading to smaller MERs compared to Table 7.3. If the transmit data stream is the same, it is possible to combine the equalized signal using MRC on the Rx side. After MRC, the combined MER for precoding is 28.0258 dB. An improved MER can be observed in comparison to transmitting different signals at the Tx side, thanks to the transmit diversity gain.

For ZF equalization with the dimension of 3×3, the same problem as ZF precoding remains. The derived MER for each individual recovered signal can not outperform the result in Table 7.3. Again, this is a reasonable trade-off since higher number of data streams can be transmitted simultaneously. As additional analysis, using MRC with the same signal being transmitted, the MER is increased due to the transmit diversity. The same behavior also stands for the 3×4 MIMO dimension. By comparing channel equalization for 3×3 and 3×4 MIMO system, it is obvious that there is more gain for more receivers as shown in Figure 7.13a, 7.13b and in Table 7.4. The QPSK clusters in Figure 7.13b are smaller than the ones in 7.13a, corresponding to larger MER in Table 7.4. Therefore, the improvement of recovered signal quality due to the extension of the MIMO scale can be clearly observed.

For beamforming using SVD, the results are shown in Figure 7.14a and 7.14b. The corresponding MER can be seen in the last two rows from Table 7.4. The water-filling effect can be observed with the 1st recovered signal having the best quality and the third signal having the worst. This meets the fact from (3.13) that the singular values of $\boldsymbol{S}$ decrease from the first-order diagonal element to the lower ones. In Table 7.4, the MIMO channel capacity is computed based on (2.28). For precoding, the channel capacity is the lowest. This is caused by illumination leakage between different IRSs. After the implementation of precoding, the output power at each feeding antenna of IRS differs, which leads to a different power distribution profile to the condition when training symbols with the same power among Tx antennas are transmitted. Therefore, the channel estimation leads to additional mismatches and decreases the channel capacity. For equalization and SVD, the transmit power is three times the unitary power uniformly distributed among the illumination antennas, which solves the problem from precoding. Logically, SVD has the largest capacity among all the results, with 3×4 MIMO outperforming 3×3 MIMO, which is also the design reason for this method. However, SVD has a bad fairness performance for different channels or UEs. In practice, this has to be considered because the total capacity may not be the most significant target under some conditions. Sometimes, it can be more important to avoid bad quality for each channel or UE. Since SVD is a designed algorithm to achieve the maximum spatial multiplexing, the attempt of MRC is not leading to the maximum diversity. Therefore, the MRC results for SVD are not computed.

7.5.3 Digital Beamforming Comparison

Based on the measurement above, the MIMO properties can be visible in the novel IRS hybrid MIMO beamforming system. In order to further prove the system feasibility and the accuracy of the channel estimation algorithm, the performances of ZF and MMSE methods, as well as the combination with SIC, can be studied and verified at the Rx signal. First of all, simulation results based on the measured 3×3 effective matrix $\hat{\boldsymbol{H}}$ are implemented in simulations as in Figure 7.15. The solid red, green, and blue curves are the ZF equalization results for three recovered signals in the MIMO system, and we can see that MMSE equalization outperforms ZF equalization due to the trade-off consideration of noise and interference term mentioned (3.6). When the MER is lower, the

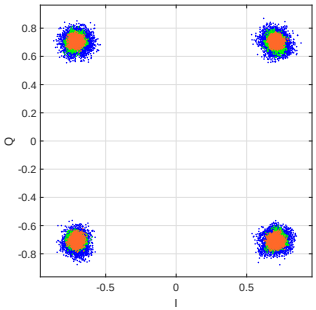

(a) SVD results for 3×3 MIMO when transmitting different data streams.

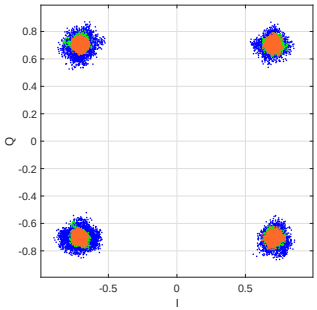

(b) SVD results for 3×4 MIMO.

Figure 7.14: Constellation diagrams for recovered signals using SVD.

difference between ZF and MMSE equalization is more obvious. At higher MER of system, MMSE has only slightly higher performance compared with ZF equalization, since when the noise term is relatively low, MMSE converges to ZF.

SIC equalization algorithm uses iterative computation and recovers the signals one by one, as described in Figure 3.4. It can also be simulated as in Figure 7.15 based on the estimated channel $\hat{\boldsymbol{H}}$. For the first signal results, the MMSE-SIC curve overlaps with MMSE equalization, and ZF-SIC superimposes with ZF equalization because the signal at the first iteration has no previous cancellation of any interference from other signals. Starting from the second signal, equalization methods based on SIC show benefits. Besides, the later the signal is recovered, the higher its improvement since it can be spotted that the difference between SIC and non-SIC equalization is the highest for the third signal. This is because more interference signals are eliminated when subtracting the optimum signal in each iteration. Comparing MMSE-SIC and MMSE-ZF, the improvement of MMSE-SIC against MMSE equalization is lower. This is because MMSE already considers a fair amount of interference that overlaps with some contributions of the SIC method.

Regarding measurements, for the 3×3 MIMO system, the results of different equalization methods are listed in Table 7.5. For ZF-SIC equalization in the 1st iteration, the third signal is the best-equalized signal with the highest MER

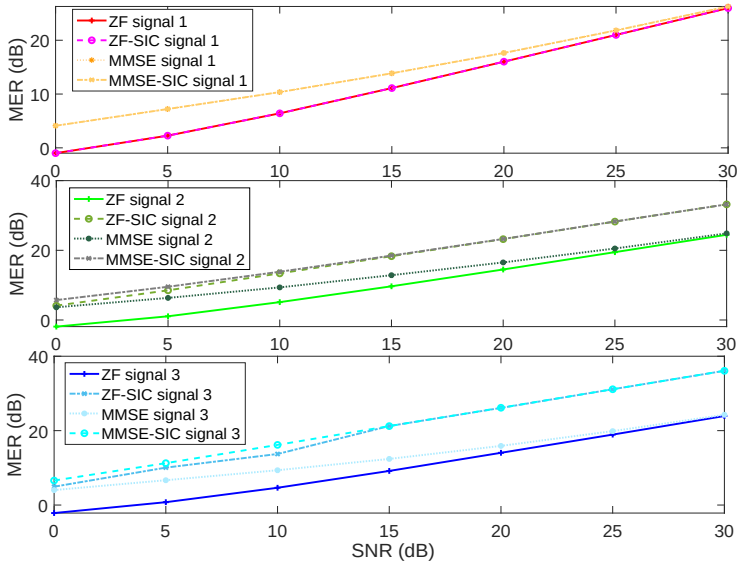

Figure 7.15: Simulation results of different equalization methods in MIMO system for three signals.

MER(dB)	Signal 1	Signal 2	Signal 3
ZF equalization	25.98	25.58	26.36
ZF-SIC equalization	27.15	26.09	26.36
MMSE equalization	26.02	25.61	26.37
MMSE-SIC equalization	27.11	26.84	26.37

Table 7.5: 3×3 MIMO equalization results using different equalization methods

from Table 7.5, and it will be selected and subtracted from the received signal. The resulting signal will perform ZF equalization for the 2nd iteration, and the resulted MER is 27.15 dB and 25.88 dB. Then the first signal has the highest MER and is chosen for the 2nd iteration. Finally, the second signal has an MER of 26.09 dB. MMSE-SIC equalization follows a similar process. In the 1st iteration, the 3rd signal is selected based on Table 7.5 and the resulting MER for 1st and 2nd signals are 26.48 dB,26.84 dB. The second signal is selected

for the 2nd iteration, and the equalized MER for signal 1 is 27.11 dB. For both ZF and MMSE equalization, the improvement for SIC-based equalization can be clearly observed in the 3×3 IRS hybrid MIMO system by comparing the SIC and non-SIC results in Table 7.5. Comparing ZF and MMSE results, MMSE outperforms ZF in all signals and equalization methods. However, the improvement is not very obvious since the proposed system is operating at a high SNR region with low noise and interference term. All the measurement results mentioned above prove that the IRS hybrid MIMO system reacts to the correct behavior of the existing methods and verify the accuracy of the channel estimation.

7.5.4 General Performance

Instead of observing the system performance at a fixed configuration, the average MER derived by ZF equalization is tuned in a broader range by changing the Rx power. This effectively expresses the system performance under different signal strengths. The BER in Figure 7.16a is derived by analyzing 20460 recovered bits based on (3.1). For MER higher than 13 dB, the BER stays 0 for our examined bits. The normalized MSE values in Figure 7.16b are derived by averaging 10230 estimated channel coefficients. The normalized MSE values for the Rx signals are also presented as additional evidence. The normalized MSE values are at levels comparable to [ZLG+21]. All the results mentioned above show that the IRS hybrid MIMO beamforming system challenges are solved, and our proposed hybrid channel estimation algorithm realizes proper data transmission even with the unknown CSI at each IRS unit cell, which solves the challenges properly mentioned in Section 4.6.

7.6 IRS hybird MIMO Beamforming Multiuser Results

For completeness, the proposed system will also be investigated in a multiuser scenario. The difference compared to a singleuser is that the UEs cannot exchange data assuming the mobile communication environment. The system model is similar to Figure 7.2, but the Rx chains can no longer exchange data

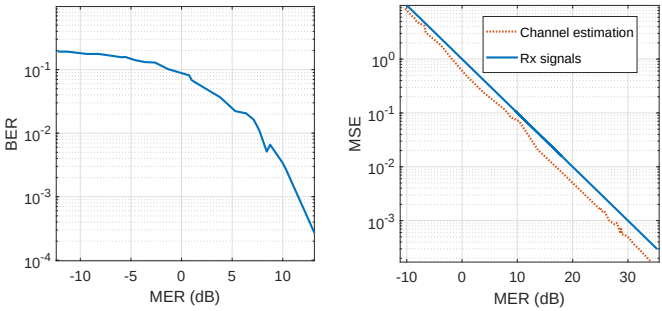

(a) BER results for the proposed hybird MIMO beamforming signal recovery.

(b) MER results for the channel estimation and recovered signals.

Figure 7.16: IRS hybrid MIMO channel estimation performance.

for cooperative signal recovery since independent UEs are considered. In addition, each IRS is not supposed to support all UEs since the spatial positions are considerably distributed. In this experiment, the Rx UEs in Figure 7.17 employ the dielectric resonance antenna designed in [KEJ+20]. The analogue beam training strategy has to be correspondingly modified in this condition. Assuming the estimated DoD from the n_dth IRS to the m_dth UE to be θ'_{m_r,n_t}, the global performance has to be optimized through all the combinations among N_d IRSs and M_d UEs. After this operation, each PM is allocated to a specific user considering $N_d = M_d$ in this experiment. However, there will always be power leakage to undesired users due to the sidelobes of 1-bit IRS beamforming presented in Figure 4.15. Therefore, additional analysis and solutions are required.

7.6.1 Equivalent Multi SISO

The first solution is to regard this multiuser MIMO system as combining several SISO systems since each IRS is responsible for one UE. A simple ZF algorithm based on LS is implemented for channel estimation and signal recovery. However, this will distort the desired signal since the interference from other IRSs is not eliminated. As example is presented in 7.18 using 2 UEs. For both constellation diagrams, the QPSK symbols are spread to sub-QPSK symbols for each

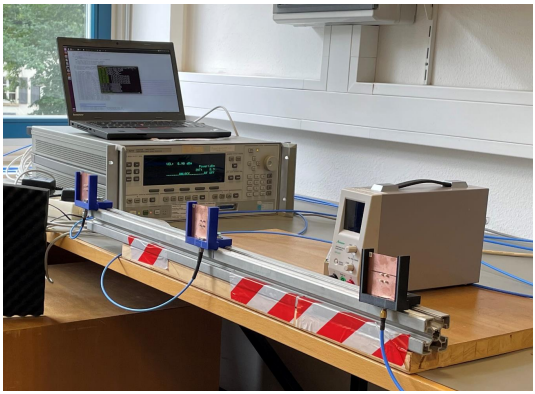

Figure 7.17: Placement of DRA antennas in multiuser scenario.

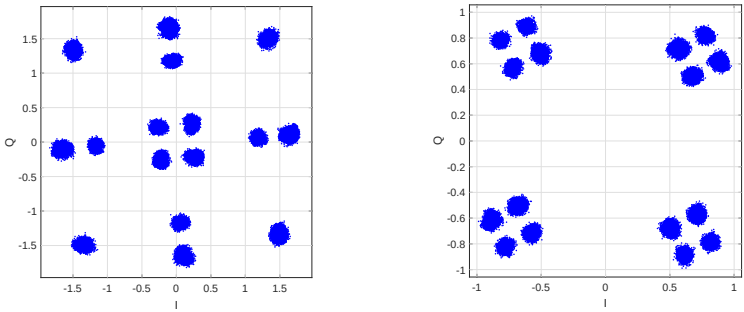

(a) Recovered signal at UE1.

(b) Recovered signal at UE2.

Figure 7.18: Multiuser recovered symbols with interference.

cluster caused by interference from the signal for another UE. UE1 suffers from a higher interference level, leading to a severe spreading of QPSK symbols.

7.6.2 FDMA

It is reasonable to separate the spectrum to different users to avoid interference among the users, which is the FDMA method. For the 3×3 MIMO system, bandwidth is equally divided into three non-overlapping parts, and each pair of Tx and Rx possesses one part. Therefore, the MIMO system can be interpreted

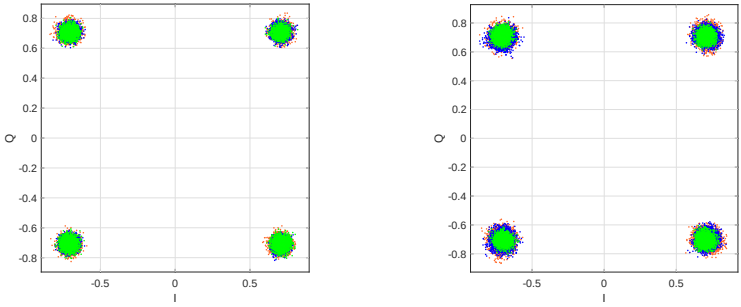

(a) Recovered signal at UE1.

(b) Recovered signal at UE2.

Figure 7.19: Multiuser recovered symbols using FDMA strategy.

as 3 SISO systems, and each SISO system occupies 1/3 of the bandwidth compared with before. Each receiver undergoes its channel estimation and signal recovery, shown in 7.19a. With the FDMA strategy, interference from other UEs is only located at the unused band of the desired signal, leading to high-quality recovered symbols.

7.6.3 Precoding for Interference Cancellation

FDMA method is simple to realize, but this decreases the capacity since only a part of the bandwidth is used for each UE. Another method which solves this problem is precoding for interference cancellation. For precoding, signal processing only takes place at the transmitter side, which fulfills the UE privacy requirement for the multiuser scenario. With ZF precoding at Tx, the interference from the other channel can be eliminated, and the received signal is shown in 7.19b. Different colour represents a different received signal, and their MER can be listed in Table 7.6. It can be seen that the FDMA generally outperforms precoding methods. Because the channel estimation dimension is smaller and there is no interference from undesired channels, resulting in a higher MER. However, precoding enables to occupy the entire bandwidth for each transmitter, increasing the channel capacity and data rate. In this experiment, 1 MHz is occupied based on the frame structure in Figure 7.9, QPSK symbols are transmitted and a guard interval of 20% is added in each OFDM symbol duration.

Considering three data streams in the MIMO dimension, 5 Mbps data rate is achieved for the precoding case. For FDMA, since only 1/3 of the subcarriers are occupied for each data stream, the data rate is reduced to 1.67 Mbps. In conclusion, FDMA eliminates the interference better which realizes a higher system MER with the sacrifice of da ta rate in comparison to the precoding method

MER(dB)	Signal 1	Signal 2	Signal 3	Data rate(Mbps)
FDMA	27.56	28.34	27.98	1.67
Precoding	26.74	24.38	25.11	5

Table 7.6: MER results using FDMA and precoding in multiuser scenario.

7.7 Conclusion on this Chapter

This chapter demonstrated and studied the first IRS MIMO hybrid beamforming system. By investigating the advanced idea, fruitful results were produced. The novel system analysis included data propagation, channel estimation, and signal processing analysis. A novel hybrid channel estimation algorithm was developed by combining beam training and the interleaved OFDM algorithm for channel estimation. Further data recovery was performed using the precisely estimated CSI. Various data recovery techniques and plans were utilized in various MIMO dimensions. The features of various data recovery techniques and MIMO gains were presented clearly and accurately. This proved the new channel estimation algorithm's accuracy and the viability of the newly proposed IRS MIMO hybrid beamforming system. The outcomes provided compelling evidence of the IRS's potential to advance communication in the future. Along with the MIMO singleuser scenarios, the multiuser scenario was successfully studied while considering its specific characteristics.

8 IRS for Channel Assistance

As discussed in Chapter 4, IRS can be divided into near and farfield illumination based on its geometric properties, leading to totally different application types. It is effectively a novel antenna array structure for IRS nearfield illumination, with its implementations intensively studied in Chapter 6 and 7. In this chapter, different scenarios using IRS farfield illumination as a signal reflector will be experimentally studied. In recent years, the topic of IRS farfield illumination has become one of the most popular topics in the wireless communication field. However, there are hardly any experiments considering the IRS difficulties mentioned in Section 4.6, which formulates the primary motivation of this chapter. Based on the general model from Figure 4.7a and the beamforming results from Figure 4.19, the exciting scenario of IRS in this dissertation is divided into four categories: IRS beam training, IRS channel access, cascaded IRS, and IRS channel capacity enhancement, which will be investigated in detail.

8.1 IRS Beam Training

As mentioned in Chapter 6 and 7, analog beam training is verified to be a proper strategy for the derivation of precise DoD of the IRS beamforming, yielding the determination of phase distribution of (2.16), and the analog beamforming matrix $\boldsymbol{F}_{Tx,RF}$ in ((8.1)). For IRS with farfield illumination, the procedure is very similar to the IRS nearfield illumination case, with the analog beamforming taking place at the IRS regarded as a signal reflector. In [BDRDR+19, HZA+19], the channel between Tx and Rx with IRS assistance is described as the multiplication of two channel matrices with Tx to IRS and IRS to Rx. This is an exact model which supports further studies for complex mathematical algorithms. Nevertheless, in this dissertation, a clue to simplify the understanding of IRS assisted channel model is raised. Although the farfield illumination from Tx

to IRS is effectively an additional channel, its contribution is passive if the Tx is assumed to be stationary for the measurement period. In addition, for the first experimental study, it is hard to directly implement the existing theoretical algorithms without proving their feasibilities due to the challenges of IRS beamforming. Therefore, the IRS assisted channel model can be regarded as an extension from the IRS nearfield illumination. For the general IRS scenario in Figure 4.7a, with the previous knowledge of the stationary IRS position at Rx, the most critical task for the IRS beamforming is to generate the beam properly from the IRS to the Rx. Once this goal is achieved, the entire path model can be just regarded as a conventional reflectional path with additional loss factor and phase shift due to the contribution of two LoS paths. Therefore, the digital signal processing will stay the same as IRS near field illumination case, with the contribution of both channel matrices directly considered. For example, if OFDM is implemented for the channel estimation, the derived CIR will have a smaller peak than the direct LoS path due to the additional path loss and reflection loss, and occur at a different time sample due to the changed delay profile. This can be also transferred to an equation point of view as follows:

$$\boldsymbol{s}_{Rx} = \boldsymbol{F}_{Rx,BB}\boldsymbol{H}_2\boldsymbol{F}_{IRS}\boldsymbol{H}_2\boldsymbol{F}_{Tx,BB}\boldsymbol{s}_{Tx} + \boldsymbol{F}_{Rx,BB}\boldsymbol{w}. \tag{8.1}$$

In 8.1, only digital beamforming is defined to be existing at Tx and Rx side. The channels $\boldsymbol{H}_1$ and $\boldsymbol{H}_2$ are the channel from Tx to the IRS, and IRS to the Rx, respectively. The term $\boldsymbol{F}_{IRS}$ represents the IRS beamforming. In comparison to (7.2), the analog beamforming part is moved from the Tx side to the IRS, between the two channel matrices. Therefore, once $\boldsymbol{F}_{IRS}$ can be determined by beam training, the goal of the rest of channel estimation is still the derivation of the estimated effective channel matrix $\hat{\boldsymbol{H}}$ from the combined contribution $\boldsymbol{H}_2\boldsymbol{F}_{IRS}\boldsymbol{H}_2$.

As mentioned in Figure 4.19, an IRS can generate flexible beamforming with an illumination source at a longer distance. However, due to the distance limitation in the anechoic chamber, it was not possible to measure the beamforming pattern for a longer illumination distance r_1. Therefore, we would like to use beam training measurement results to show the possibility of IRS farfield illumination beam training, which simultaneously proves its beam steering ability. Meanwhile, as shown in Figure 4.20, the IRS can also generate broad beams under illumination conditions. Therefore, a comparison between exhaustive search

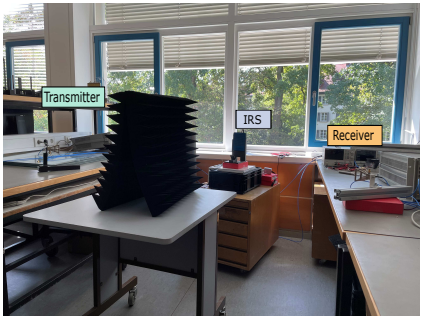

(a) System setup for the IRS farfield beam training.

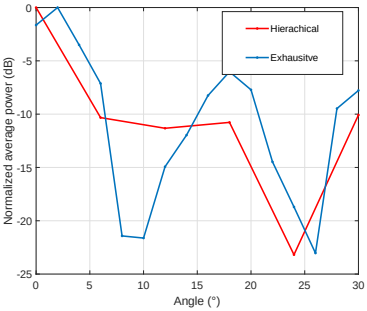

(b) Hierarchical codebook vs. exhaustive search algorithm in IRS channel assisted scenario.

Figure 8.1: IRS assisted system for beam training tests.

and hierarchical codebook algorithm can be investigated for the IRS channel assistant case.

In the first attempt, the entire system model is similar to the one in Figure 6.1. The only difference is that the IRS is placed farther away to achieve the farfield or approximate-farfield illumination, and the directly LoS path from Tx to Rx is blocked, which is why IRS is required to create the reflectional path. For the beam training, the strategy to use pre-stored codebooks is maintained following the instruction from Figure 4.5, with the phase distribution (2.16) computed based on the position of the Tx antenna. The system set up in the indoor environment is shown in Figure 8.1a. The Tx and Rx are presented by the QRH40 antenna. The LoS path between the Tx and Rx is blocked by the absorber and the IRS is required to realize the wireless connection. The goal is to operate beam training at the IRS and search for the optimum beamforming direction from the IRS to the Rx.

The channel estimation results are presented in Figure 8.1b. The hierarchical codebook algorithm uses 6° as the sector resolution and exhaustive search uses 2° as angle resolution. The feeding distance is set to be $r_1 = 1.7\,\mathrm{m}$ which is close to farfield constrain. For simple access, Rx power is utilized as the standard beam training metric. From exhaustive search, the optimum DoD is at 2°, while two other strong paths can be found along 18° and 30°. This is mainly caused by the beamforming performance degradation. Comparing the results

from Figure 4.15 and 4.19, the antenna gain decreases and the sidelobe level increases with longer illumination distance r_1. Therefore, the slidelobe supports data propagation through the possible accesses from the IRS to the Rx, which leads to the fact that the channel estimation results are not as distinguishable as single IRS case as depicted in Figure 6.3. Nevertheless, it is sufficient as a proof of concept. The hierarchical codebook algorithm shows similar performance, the broad beam at 0° indicates the optimum DoD sector, as the secondary peaks at 18° and 30° are also visible. Then the detailed DoD can be found by implementing an exhaustive search around the broad beam sector at 0°. This measurement proves that both the exhaustive search and hierarchical codebook algorithms work for IRS-assisted channel estimation in farfield illumination case.

8.2 IRS Assisted MIMO

Once the beam training is proved, the system can be extended to an IRS-assisted MIMO system, which shares the same architecture as Figure 7.2. The difference is similar, as mentioned in the last section: The analog beamforming part takes place at the IRS part, which is a signal reflector instead of an alternative antenna array. The scenario is depicted in Figure 8.2a. Instead of a single feeding source, multiple sources illuminate multiple RISs at different spatial positions to create multiple paths to the Rx, forming an IRS-assisted MIMO system. With the help of the spatial paths created by the IRS beamforming, MIMO properties can be realized, and the channel capacity can be increased. The measurement setup is presented in Figure 8.2b. In this system, $N_d = M_d = 2$ is utilized, assisted by two IRS for channel assistance creating two spatial paths. Each RIS is assigned with phase distribution regarding (2.16) for one of the Tx antennas as a farfield illumination source. Two QRH40 antennas are placed at the Tx side, with two reflectional paths created by 2 IRSs via a $r_1 = 1.7\,\mathrm{m}$ illumination distance. At the receiver side, an antenna array with two active units are utilized and connected with the RF backend module.

As a transformed system from Figure 7.2, the entire channel estimation, signal propagation, and data recovery steps follow a similar procedure. Firstly, beam training is implemented to search for the correct DoDs from the IRSs to the Rxs, with the feasibility proved in the last section. To avoid undesired duplications,

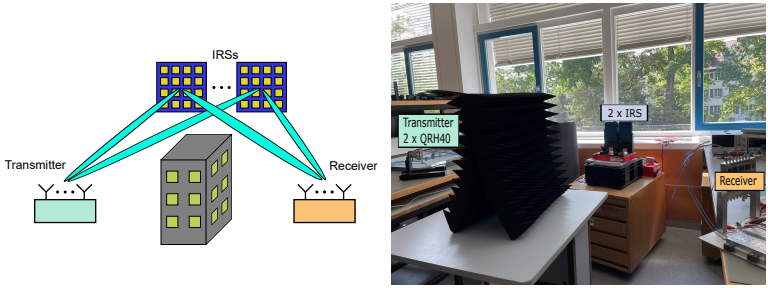

(a) IRS assisted hybrid MIMO beamforming scenario.

(b) IRS assisted hybrid MIMO beamforming setup.

Figure 8.2: IRS assisted MIMO scenario and measurement system.

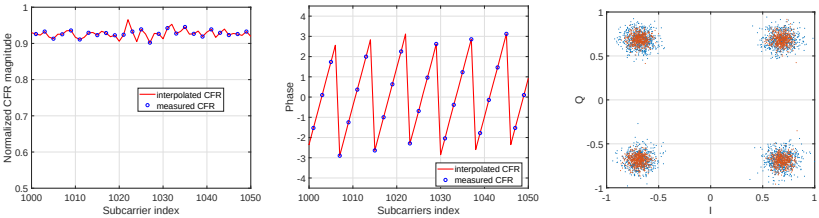

(a) Magnitude of CFR derived from hybrid channel estimation

(b) Phase of CFR derived from hybrid channel estimation

(c) Recovered signals in IRS assisted MIMO scenario.

Figure 8.3: Channel estimation results and signal recovery results for IRS assisted MIMO.

the beam training results will not be shown here, just telling them to be 22° and 28°. After the IRS beamforming $\boldsymbol{F}_{IRS}$ is fixed, interleaved OFDM following Algorithm 4 keeps for the derivation of $\hat{\boldsymbol{H}}$. Measurement results of CFR and CIR are presented in Figure 8.3 following the same definitions in Figure 7.6. The results make good sense, with precise results derived for the data recovery. By utilizing ZF equalization, the two recovered QPSK symbols are shown in Figure 8.3c.

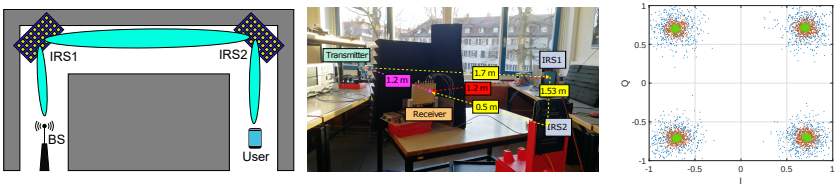

(a) Cascaded IRS scenario. (b) Measurement setup for the cascaded IRS. (c) Recovered signals in IS assisted MIMO scenario.

Figure 8.4: Cascaded IRS scenario, measurement setup, and results.

8.3 Cascaded IRS Communication

Assuming an urban city environment, many buildings are blocking the LoS path between the BS and UEs. It can also be possible that one IRS is not enough to formulate access. As a solution, several IRS can be established in series, leading to the cascaded IRS communication mentioned in [YZZ20]. The architecture is depicted in Figure 8.4a using two IRSs as an example. The Tx antenna firstly illuminates the first IRS. Then, the first IRS generates the reflective beamforming and illuminates the second IRS. In the end, the second IRS generates beamforming to the Rx, which finally formulates the propagation path between the Tx and Rx, located at an objective's counter sides. In this model, the farfield IRS path loss model in (4.4) can be further extended by adding another Friis formula contribution from (2.6). With more IRS into account, the relationship can be just accumulated.

The system setup is presented in Figure 8.4b. A SISO chain is formulated by extending the channel model of Figure 6.1 to Figure 8.4a. At the Tx side, an IRS nearfield illumination is utilized as an alternative option for a Tx antenna with beamforming ability. The distance between the Tx to the first IRS is 1.73 m with the beamforming angle 0° as derived by the exhaustive search DoD estimation algorithm from Section 6.1.2. The distance from the first IRS to the second IRS is 1.53 m, with the DoD estimated to be 26°. In the end, from the second IRS to Tx, the distance is 0.5 m with DoD of 4°. The Rx antenna utilizes the same architecture from Figure 7.3. Please notice that all the DoDs are derived by beam training in this dissertation, which is usually a one-time effort. Due to the stationary property of Tx (BS), and the two IRSs, the DoD should be

Table 8.1: Measurement results of different paths in the cascaded IRS scenario

Rx power(dBm)	MER(dB)	Theoretical path loss(dB)	Relative IRS gain(dBi)
-69.1	29.6	62.97	N/A
-81.7	22	129.11	52.04
-90.9	14.1	186.58	49.73

previously known, and only the DoD from the second IRS to the Rx is always required to be estimated.

Some measurement results are presented in Table 8.1 to analyze the system. The Rx power is measured at the output of the Rx antenna. These are used to analyze the path loss to verify the relative gain of the IRS. For theoretical analysis, the orientation of the Rx antenna is rotated to ensure the optimum power reception. All the IRS unit cell phase distributions follow the computation from (2.16) with the corresponding illumination distance r_1 and the beamforming angle θ'. For the first case, the Tx IRS directly beamforming to the Rx via a 1.2 m propagation distance with a DoD of 46°. Due to the implementation of nearfield illumination for the Tx IRS, the Friis formula is not utilized in this part, which leads to a one-tap path loss equation simply following (2.6) using Tx IRS as an alternative antenna array. Therefore, 62.97 dB loss is added and the final Rx power is −69.1 dBm. For the second case, only one IRS is utilized for channel assistance and propagates the signal directly to the Rx. In total, 1.73 + 1.2 m distance contributes to the two tap FSPL leading to a value of 129.11 dB. By considering the additional loss and the difference of the Rx power in these two cases, the rest of the contribution is introduced by the IRS, which leads to a relative gain of 52.04 dBi, with the incidence and reflection angle taken into consideration. Based on the results from Figure 4.21 and 4.22, the gain for the IRS itself for farfield illumination case is approximately 51 dBi, which is very close to our measured case. For the third case, two IRSs are implemented to build up the communication case, and 1.73 + 1.53 + 0.5 m propagation distance leads to a three-tap FSPL of 186.58 dB in total. Using the same computation method, the IRS derived by comparing to the second case is derived from being 49.73 dBi, which is again very close to the results from Figure 4.21 and 4.22. These measurements prove the feasibility of the cascaded IRS system and provide additional evidence for the correctness of the path loss model in (4.4). In this experiment, the illumination source of the IRS signal reflector is realized

by the another IRS beamforming, which proves the fact that the IRS farfield illumination is flexible with any type of illumination without strict optimization required.

For further study, the MER of the measurement are listed in Table 8.1 by utilizing LS channel estimation (3.3) and ZF equalization 3.5, with their constellation diagrams in Figure 8.4a. As mentioned in (8.1), even with multiple IRS stages, the channel estimation principle stays the same to derive the required CSI. For the MER of the recovered symbols, the non-linear property in Figure 7.11 maintains. Therefore, the differences between MER and Rx power can not be expected to be the same, but the performance degradation logic is correct. In the cascaded IRS wireless communication setup, the MER decreases when the number of IRS stage increases. Such observation is caused by the current limited IRS size. A reflectional path between Tx and Rx always has a longer distance than the LoS path, which brings additional FSPL. The IRS has to provide enough gain to compensate this additional loss, which is one of the challenges mentioned in Figure 4.22. In this dissertation, with the help of multiple IRS stages, the goal is to establish the cascaded IRS communication path as a proof of concept rather than chasing for an enlarged Rx power. Hopefully, the Rx power can be enhanced with IRS with a larger size or better design with a higher S11 in the future.

8.4 IRS Enhanced System

In the previous sections, the IRS is used to validate the wireless communication channel when the LoS channel is blocked. For IRS, another popular scenario aims to enhance the MIMO spatial multiplexing depicted in 8.5a. As mentioned in Section 2.3.2, additional channel capacity can be derived by utilizing multiplex spatial paths between Tx and Rx. If the IRS can provide a solid channel, the channel capacity can be enhanced even though the LoS path exists. This is especially helpful for mmw wireless communication when spatial multiplexing caused by reflections is hard to be achieved due to the severe FSPL and reflection loss, which may lead to a very ill-conditioned channel. This is the reason that IRS is believed to support the scenario mentioned above.

The system model is depicted in 8.5b. To utilize the two spatial paths, a 2×2 MIMO system is created, which fulfills the minimum required rank for ZF equa-

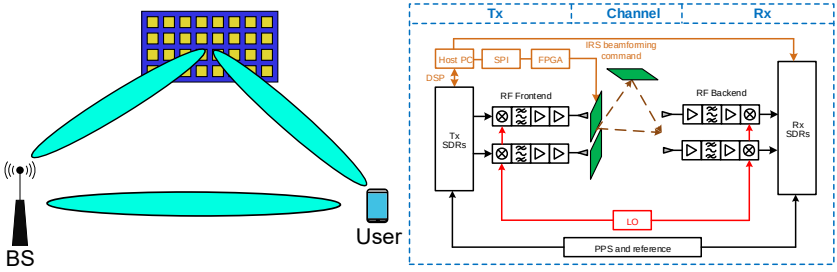

(a) IRS enhanced MIMO scenario.

(b) IRS enhanced MIMO system.

Figure 8.5: IRS enhanced MIMO scenario and system setup.

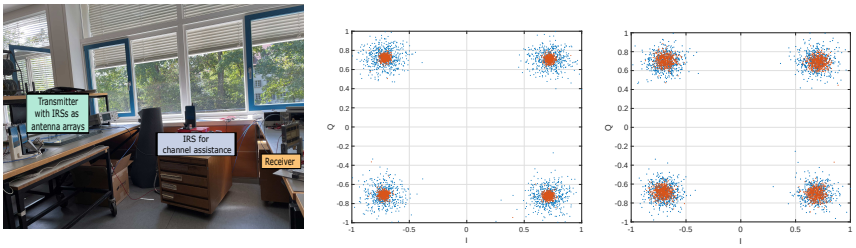

(a) IRS enhanced MIMO measurement environment.

(b) The first recovered signal.

(c) The second recovered signal.

Figure 8.6: Recovered signals for RIS enhanced MIMO system.

lization mentioned in 3.5. To realize proper beamforming, the BS is equipped with two IRS with nearfield illumination as alternative antenna arrays, which can generate precise beamforming with lower system complexity. With the help of beam training, the DoD of from the Tx to the IRS assisted path and the LoS path can be determined. Utilizing the interleaved OFDM channel estimation, the 2×2 channel matrix can be derived for data recovery. Afterwards, the BS generates two beams separately via the IRS assisted path and the LoS path for comparison. Only the essential results and analysis are given below to avoid undesired duplications with previous chapters.

To compare the results, two different channel utilization conditions are presented in Figure 8.6 regarding the recovered data. The measurement environment in Figure 8.6a is very similar to Figure 8.2b with the blocking objective remo-

ved. The Tx antennas are replaced with nearfield illumination IRS, for precise beamforming selecting between LoS and reflection path between Tx and Rx. For the first experimental condition, both IRS enhanced path and the LoS path are utilized by the BS beamforming. The LoS path has an estimated DoD of −26°, and the LoS path is at 10°. The illumination distance r_1 is 1.73 m and the propagation path r_2 is 0.95 m. The LoS path has a 1.5 m link distance. Two BS IRSs generate beamforming to the Rx for the second experimental condition using the LoS path. It can be seen that when both beams are using the LoS path to the Rx, the recovered signals have worse performance (blue symbols) than the case where different propagation paths (red symbols) are utilized. This means the IRS enhanced case is better than the signal propagated on the same LoS path. Using SVD regarding the estimated channel, the singular values also clearly present the channel ranks. The IRS enhanced channels have singular values of 3.9 and 1.2. The LoS path contributes the 3.9 since it is stronger than the IRS reflectional path based on the evidence from Figure 8.4b. For both LoS utilization cases, the singular values are 5.9 and 0.6. The LoS path is duplicated and utilized, leading to a significant value, and the second channel becomes very weak. This means the full MIMO multiplexing and diversity can not be achieved. After the signal recovery using ZF equalization, the average MER for the IRS enhanced case is 23 dB, while the LoS path case is only 17 dB. The Rx power for these two cases averaging through the two Rx antennas is −52.5 dBm for IRS enhanced case and −50.9 dBm for LoS case. The values show that even though higher Rx power is derived by utilizing the LoS path, the signal quality/MER can not be enhanced. The results have the similar observation as Table 7.3, with the correlation of channels playing an important role. In the end, after computing the channel capacity using the afore-measured data, the IRS enhanced case achieves 17.7 bit/s/Hz, and the LoS case achieves 12.2 bit/s/Hz. This copes with the expectation that IRS can enhance the MIMO capacity.

8.5 Conclusion on this Chapter

As a very recent and popular concept, the IRS farfield illumination is regarded as one of the most popular communication relay architectures for channel assistance. This chapter focuses on the missing consideration of practical implementations for this novel concept. Instead of focusing on the complex mathematical model, the realization of the system experiment was achieved,

which is an essential milestone for further studies. The aspects of channel estimation, wireless communication with IRS access, cascaded IRS system, and IRS-enhanced MIMO system were studied. With the algorithms developed from the previous chapters, the challenges of IRS working as a signal reflector were solved and experimental systems were demonstrated. All the aspects mentioned above derived good results, which proved the feasibility. For future tasks, detailed mathematical solutions can be developed to further improve the system performance and to overcome the obstacles resulting from the limited IRS size.

9 Conclusion

With the development of wireless communication technologies, the novel concept of an intelligent reflecting surface was created. Due to the utilization of the micro-component-based unit cells, the IRSs offer commercial potential to reduce the wireless communication system's price and power consumption. Studies on the IRS are primarily focused on two factors, which result in two different application types. The first type is an alternative antenna array with electronically controllable beamforming ability. The second type is a signal reflector to assist or enhance wireless communication channels. However, due to a lack of experimental studies, it was still unclear whether IRS-based wireless communication systems could operate as expected, realize the theoretical algorithm, and satisfy the needs of contemporary communication purposes. In this dissertation, one step further in investigating the viability and functionality of IRS-based systems at the experimental level was achieved. The outcomes established new research benchmarks and realized significant steps toward achieving IRS's practical implementations. In conclusion, the dissertation's main contributions can be summarized as follows:

- IRS beamforming viability was intensively discussed to develop solid foundations for experimental studies. Under distortions and imperfections, IRS beamforming's robustness was investigated. Modern wireless communication requirements were discovered to be compatible with advanced IRS beamforming capabilities like fast beam steering and switching and multi/broad beam generation. Additionally, adaptive algorithms were used to address and overcome the challenges associated with IRS beamforming in wireless communication. The results of the measurements, which were used to answer practical questions, were used to define and prove the IRS models.
- To realize experimental studies close to the real-world scenarios, IRS wireless communication testbed is demonstrated at 28 GHz. Promising

solutions to coordinate IRS beamforming control loop and communication signal processing were presented.

- Innovative IRS beamforming strategies were created and experimentally evaluated. The IRS-based TDMA fast beam switching system was successfully demonstrated. This system achieved high-quality signal propagation among multiple UEs and offered beam switching speeds faster than those required by LTE. Additionally, mobile communication was first employed to track UEs utilizing the IRS system. The demonstrated system achieved accurate mobile UE tracking with a low training overhead by utilizing a beam management method modified from the 5G 3GPP standard. Although the low-cost IRS was used to construct the system, its specifications were comparable to existing MIMO/phased array tracking systems. This system was further developed with the help of predictive beam refinement algorithms. Due to the training overhead being reduced by predicting the beamforming direction for the mobile UE, better performances were obtained throughout the tracking duration.

- IRSs were first combined with MIMO hybrid beamforming. The novel IRS MIMO hybrid beamforming, considering as the most advanced IRS-based wireless communication testbed at this research stage, was created. The analog beam training algorithm and the interleaved OFDM algorithm were combined to create a new channel estimation algorithm for the proposed system. This concept overcame the problems with IRS hybrid MIMO channel estimation with the proper complexity. Various signal recovery methods and MIMO dimensions were tested to study the data propagation based on the estimated CSI. For the sake of completeness, both the single-user and multiuser conditions were taken into account. The signals could then be recovered with the appropriate SNR, allowing us to observe the characteristics of the implemented signal processing techniques. These results showed that the new system could work and that the new channel estimation algorithm was accurate.

- The IRS channel assistant concepts were proved and analyzed. The IRS application as a signal reflector supports many exciting scenarios that have never been tested through experiments. In this dissertation, a few candidates were selected as representations for deep analyses, including IRS-assisted wireless communication, cascaded IRS, and IRS-enhanced MIMO systems. The channel estimations and signal propagations for IRS

channel assistant architectures were able to achieve reliable performances thanks to the development and adaptation of the channel model and algorithms. Also, the channel capacity was increased by using the useful reflection path created by the IRS instead of putting all of the signal power on the line-of-sight path, especially for the MIMO system with the IRS.

This dissertation's experimental studies of IRS in wireless communication systems have yielded positive results. They offer convincing evidence of the feasibility and functionality of wireless communication technologies based on the IRS. If similar architectures are desired for system extension, algorithm development, or commercial implementation, these studies fill in the missing aspects of the current IRS studies, which may be regarded as promising benchmarks.

References

[5Gb] 5G spectrum access. https://www.itu.int/dms_pub/itu-r/oth/0a/0E/R0A0E0000C60001PDFE.pdf.

[AAFK20] Irmak Aykin, Berk Akgun, Mingjie Feng, and Marwan Krunz. Mamba: A multi-armed bandit framework for beam tracking in millimeter-wave systems. In *Proc. of the IEEE INFOCOM 2020 Conference, Toronto, Canada*, 2020.

[AEALH14] Ahmed Alkhateeb, Omar El Ayach, Geert Leus, and Robert W Heath. Channel estimation and hybrid precoding for millimeter wave cellular systems. *IEEE Journal of Selected Topics in Signal Processing*, 8(5):831–846, 2014.

[AWM] Awmf-0108 beamformer ic. https://www.anokiwave.com/products/awmf-0108/index.html.

[Bal15] Constantine A Balanis. Antenna theory: analysis and design. 2015.

[BDRDR+19] Ertugrul Basar, Marco Di Renzo, Julien De Rosny, Merouane Debbah, Mohamed-Slim Alouini, and Rui Zhang. Wireless communications through reconfigurable intelligent surfaces. *IEEE access*, 7:116753–116773, 2019.

[BMK63] D Berry, R Malech, and W Kennedy. The reflectarray antenna. *IEEE Transactions on Antennas and Propagation*, 11(6):645–651, 1963.

[Bre03] DG Brennan. Linear diversity combining techniques. *Proceedings of the IEEE*, 91(2):331–356, 2003.

[CdOVR16] Guilherme R Colen, Lucas Giroto de Oliveira, AJ Han Vinck, and Moises V Ribeiro. A spectral compressive resource allocation technique for plc systems. *IEEE Transactions on Communications*, 65(2):816–826, 2016.

[CERS16] Eduardo Carrasco, Jose A Encinar, and Y Rahmat-Samii. Reflectarray antennas: A review. In *Forum for Electromagnetic*

Research Methods and Application Technologies (FERMAT), volume 16, 2016.

[CLCY19] Jie Chen, Ying-Chang Liang, Hei Victor Cheng, and Wei Yu. Channel estimation for reconfigurable intelligent surface aided multi-user mimo systems. *arXiv preprint arXiv:1912.03619*, 2019.

[CQW+14] Tie Jun Cui, Mei Qing Qi, Xiang Wan, Jie Zhao, and Qiang Cheng. Coding metamaterials, digital metamaterials and programmable metamaterials. *Light: Science & Applications*, 3(10):e218, 2014.

[CZO87] Henry Cox, Robertm Zeskind, and Markm Owen. Robust adaptive beamforming. *IEEE Transactions on Acoustics, Speech, and Signal Processing*, 35(10):1365–1376, 1987.

[DCDP+17] Fatimata Diaby, Antonio Clemente, Luca Di Palma, Laurent Dussopt, Kien Pham, Erwan Fourn, and Ronan Sauleau. Design of a 2-bit unit-cell for electronically reconfigurable transmitarrays at ka-band. In *2017 47th European Microwave Conference (EuMC)*, pages 1321–1324. IEEE, 2017.

[Dha18] Piyu Dhaker. Introduction to spi interface. *Analog Dialogue*, 52(3):49–53, 2018.

[div] Receive diversity. `https://www.comm.utoronto.ca/~rsadve/Notes/DiversityReceive.pdf`.

[DPCD+15] Luca Di Palma, Antonio Clemente, Laurent Dussopt, Ronan Sauleau, Patrick Potier, and Philippe Pouliguen. 1-bit reconfigurable unit cell for ka-band transmitarrays. *IEEE Antennas and Wireless Propagation Letters*, 15:560–563, 2015.

[DPCD+16] Luca Di Palma, Antonio Clemente, Laurent Dussopt, Ronan Sauleau, Patrick Potier, and Philippe Pouliguen. Circularly-polarized reconfigurable transmitarray in ka-band with beam scanning and polarization switching capabilities. *IEEE Transactions on Antennas and Propagation*, 65(2):529–540, 2016.

[DRZD+20] Marco Di Renzo, Alessio Zappone, Merouane Debbah, Mohamed-Slim Alouini, Chau Yuen, Julien De Rosny, and Sergei Tretyakov. Smart radio environments empowered by reconfigurable intelligent surfaces: How it works, state of research,

and the road ahead. *IEEE journal on selected areas in communications*, 38(11):2450–2525, 2020.

[DTY+19] Jun Yan Dai, Wankai Tang, Liu Xi Yang, Xiang Li, Ming Zheng Chen, Jun Chen Ke, Qiang Cheng, Shi Jin, and Tie Jun Cui. Realization of multi-modulation schemes for wireless communication by time-domain digital coding metasurface. *IEEE Transactions on Antennas and Propagation*, 68(3):1618–1627, 2019.

[Eis21] J. Eisenbeis. *Hybride Beamformingsysteme niedriger Komplexität für den Mobilfunk*. PhD thesis, Karlsruhe Institute of Technology, Karlsruhe, 2021.

[EMLZ18] Joerg Eisenbeis, Tobias Mahler, Pablo Ramos Lopez, and Thomas Zwick. Channel estimation method for subarray based hybrid beamforming systems employing sparse arrays. *Progress In Electromagnetics Research C*, 87:25–38, 2018.

[FCC] 5G nr physical layer/waveforms. `https://transition.fcc.gov/oet/ea/presentations/files/apr19/3.0-5G-and-above-6-{G}{H}z-Measurements.pdf`.

[gen] Generations of mobile networks: Explained. `https://justaskthales.com/en/generations-mobile-networks-explained/`.

[GJJV03] Andrea Goldsmith, Syed Ali Jafar, Nihar Jindal, and Sriram Vishwanath. Capacity limits of mimo channels. *IEEE Journal on selected areas in Communications*, 21(5):684–702, 2003.

[Gnu] Gnu radio tutorials. `https://wiki.gnuradio.org/index.php/Tutorials`.

[GPR+18a] Marco Giordani, Michele Polese, Arnab Roy, Douglas Castor, and Michele Zorzi. Initial access frameworks for 3GPP NR at mmwave frequencies. In *2018 17th Annual Mediterranean Ad Hoc Networking Workshop (Med-Hoc-Net)*, pages 1–8. IEEE, 2018.

[GPR+18b] Marco Giordani, Michele Polese, Arnab Roy, Douglas Castor, and Michele Zorzi. A tutorial on beam management for 3GPP NR at mmwave frequencies. *IEEE Communications Surveys & Tutorials*, 21(1):173–196, 2018.

[GSS+03] David Gesbert, Mansoor Shafi, Da-shan Shiu, Peter J Smith, and Ayman Naguib. From theory to practice: An overview of mimo

space-time coded wireless systems. *IEEE Journal on selected areas in Communications*, 21(3):281–302, 2003.

[HLT+18] Björn Halvarsson, Kjell Larsson, Magnus Thurfjell, Kimmo Hiltunen, Khanh Tran, Paulo Machado, Daniel Juchnevicius, and Henrik Asplund. 5G nr coverage, performance and beam management demonstrated in an outdoor urban environment at 28 GHz. In *2018 IEEE 5G World Forum (5GWF)*, pages 416–421. IEEE, 2018.

[HMCa] Hittite / analog devices hmc751lc4. https://www.mouser.de/hittite-hmc751lc4/?gclid=CjwKCAjwiJqWBhBdEiwAtESPaNVusBWXoKoyF_7tfIokJCapYgqOuJ-ZRohl57yQuRvBZzVtkhBHRoC0PcQAvD_BwE.

[HMCb] Hmc264lc3b. https://www.mouser.de/ProductDetail/Analog-Devices/HMC264LC3B?qs=pceeu5JH%2FH%252Bwz3tovyb2ww%3D%3D&gclid=CjwKCAjwiJqWBhBdEiwAtESPaIeQKncxZQBGxewg4KvsahRCpM-JaF4Q4GIrAjEXx6SWkXPtIH5RkhoCL2YQAvD_BwE.

[HMCc] Hmc863alc4. https://www.micro-semiconductor.com/products/ADI(Analog-Devices,Inc.)/HMC863ALC4.

[HTBW20] Karsten Heimann, Janis Tiemann, Stefan Böcker, and Christian Wietfeld. Cross–bearing based positioning as a feature of 5G millimeter wave beam alignment. In *2020 IEEE 91st Vehicular Technology Conference (VTC2020-Spring)*, pages 1–5. IEEE, 2020.

[HTYW19] Karsten Heimann, Janis Tiemann, Davit Yolchyan, and Christian Wietfeld. Experimental 5G mmwave beam tracking testbed for evaluation of vehicular communications. In *2019 IEEE 2nd 5G World Forum (5GWF)*, pages 382–387. IEEE, 2019.

[HZA+19] Chongwen Huang, Alessio Zappone, George C Alexandropoulos, Mérouane Debbah, and Chau Yuen. Reconfigurable intelligent surfaces for energy efficiency in wireless communication. *IEEE Transactions on Wireless Communications*, 18(8):4157–4170, 2019.

[IRS] Ieee signal processing cup 2021. https://signalprocessingsociety.org/community-involvement/ieee-signal-processing-cup-2021.

[JCH+16] Jinyoung Jang, MinKeun Chung, Seung Chan Hwang, Yeon-Geun Lim, Hong-jib Yoon, TaeckKeun Oh, Byung-Wook Min, Yongshik Lee, Kwang Soon Kim, Chan-Byoung Chae, et al. Smart small cell with hybrid beamforming for 5G: Theoretical feasibility and prototype results. *IEEE Wireless Communications*, 23(6):124–131, 2016.

[KEJ+20] Jerzy Kowalewski, Joerg Eisenbeis, Alisa Jauch, Jonathan Mayer, Marius Kretschmann, and Thomas Zwick. A mmw broadband dual-polarized dielectric resonator antenna based on hybrid modes. *IEEE Antennas and Wireless Propagation Letters*, 19(7):1068–1072, 2020.

[KIT+11] Hirokazu Kamoda, Toru Iwasaki, Jun Tsumochi, Takao Kuki, and Osamu Hashimoto. 60-GHz electronically reconfigurable large reflectarray using single-bit phase shifters. *IEEE transactions on antennas and propagation*, 59(7):2524–2531, 2011.

[KLH+16] Yungsoo Kim, Hyun-Yong Lee, Philyeong Hwang, Ranjeet Kumar Patro, Jaekon Lee, Wonil Roh, and Kyungwhoon Cheun. Feasibility of mobile cellular communications at millimeter wave frequency. *IEEE Journal of selected topics in Signal Processing*, 10(3):589–599, 2016.

[KTH+17] Daisuke Kurita, Kiichi Tateishi, Atsushi Harada, Yoshihisa Kishiyama, Shoji Itoh, Hideshi Murai, Arne Simonsson, and Peter Ökvist. Outdoor experiments on 5G radio access using distributed mimo and beamforming in 28-GHz frequency band. In *2017 IEEE 28th Annual International Symposium on Personal, Indoor, and Mobile Radio Communications (PIMRC)*, pages 1–6. IEEE, 2017.

[LBE+21] Yueheng Li, Sven Bettinga, Joerg Eisenbeis, Jerzy Kowalewski, Xiang Wan, Xueyun Long, Teng Li, Alisa Jauch, TieJun Cui, and Thomas Zwick. Beamsteering for 5G mobile communication using programmable metasurface. *IEEE Wireless Communications Letters*, 2021.

[LBE+22] Yueheng Li, Sven Bettinga, Joerg Eisenbeis, Jerzy Kowalewski, Xiang Wan, Xueyun Long, Teng Li, Alisa Jauch, TieJun Cui, and Thomas Zwick. Predictive tracking implementation for mobile communication using programmable metasurface. IEEE, 2022.

[LC17] Shuo Liu and Tie Jun Cui. Concepts, working principles, and applications of coding and programmable metamaterials. *Advanced optical materials*, 5(22):1700624, 2017.

[LC19] Lianlin Li and Tie Jun Cui. Information metamaterials–from effective media to real-time information processing systems. *Nanophotonics*, 8(5):703–724, 2019.

[LCZ+16] Shuo Liu, Tie Jun Cui, Lei Zhang, Quan Xu, Qiu Wang, Xiang Wan, Jian Qiang Gu, Wen Xuan Tang, Mei Qing Qi, Jia Guang Han, et al. Convolution operations on coding metasurface to reach flexible and continuous controls of terahertz beams. *Advanced Science*, 3(10):1600156, 2016.

[LEK+21] Yueheng Li, Joerg Eisenbeis, Jerzy Kowalewski, Xiang Wan, Xueyun Long, Jozwicka Maria, Lucas Giroto de Oliveira, Tijun Cui, and Thomas Zwick. Ka-band programmable metasurface demonstrations in wireless communication scenarios. In *15th European Conference on Antennas and Propagation (EuCAP)*. IEEE, 2021.

[LEW+21] Yueheng Li, Joerg Eisenbeis, Xiang Wan, Sven Bettinga, Xueyun Long, Mohamad Basim Alabd, Jerzy Kowalewski, Tie Jun Cui, and Thomas Zwick. A programmable metasurface based tdma fast beam switching communication system at 28 GHz. *IEEE Antennas and Wireless Propagation Letters*, 2021.

[LGZH20] Yu-Ngok Ruyue Li, Bo Gao, Xiaodan Zhang, and Kaibin Huang. Beam management in millimeter-wave communications for 5G and beyond. *IEEE Access*, 8:13282–13293, 2020.

[LHS+17] Kjell Larsson, Björn Halvarsson, Damanjit Singh, Ranvir Chana, Jawad Manssour, Minsoo Na, Changsoon Choi, and Sungho Jo. High-speed beam tracking demonstrated using a 28 GHz 5G trial system. In *2017 IEEE 86th Vehicular Technology Conference (VTC-Fall)*, pages 1–5. IEEE, 2017.

[LLdO+22] Yueheng Li, Xueyun Long, Lucas Giroto de Oliveira, Joerg Eisenbeis, Mohamad Basim Alabd, Sven Bettinga, Xiang Wan, Tie Jun Cui, and Thomas Zwick. Programmable metasurface hybrid mimo beamforming: Channel estimation, data transmission, and system implementations at 28 GHz. *IEEE Systems Journal*, 2022.

[LLW+21] Yueheng Li, Xueyun Long, Xiang Wan, Joerg Eisenbeis, Sven Bettinga, Tiejun Cui, and Thomas Zwick. Realization of efficient channel estimation using programmable metasurface. In *2021 IEEE USNC-URSI Radio Science Meeting (Joint with AP-S Symposium)*, pages 66–67. IEEE, 2021.

[LWC+14] Yun Bo Li, Xiang Wan, Ben Geng Cai, Qiang Cheng, and Tie Jun Cui. Frequency-controls of electromagnetic multi-beam scanning by metasurfaces. *Scientific reports*, 4(1):1–7, 2014.

[LWE+20] Yueheng Li, Xiang Wan, Joerg Eisenbeis, Xueyun Long, Maria Jozwicka, TieJun Cui, and Thomas Zwick. A novel wireless communication system using programmable metasurface operating at 28 GHz. In *2020 International Conference on Microwave and Millimeter Wave Technology (ICMMT)*, pages 1–3. IEEE, 2020.

[LXPY11] Zaishuang Liu, Qiuliang Xie, Kewu Peng, and Zhixing Yang. Apsk constellation with gray mapping. *IEEE communications letters*, 15(12):1271–1273, 2011.

[MA4] Ma4agp907. `https://www.macom.com/products/product-detail/MA4AGP907`.

[mcp] MCP2210. `https://www.microchip.com/en-us/product/MCP2210`.

[MCR+93] M Mazzella, M Cohen, D Rouffet, M Louie, and KS Gilhousen. Multiple access techniques and spectrum utilisation of the GLOBALSTAR mobile satellite system. In *Fourth IEE Conference on Telecommunications 1993*, pages 306–311. IET, 1993.

[MDS95] Kris Maine, Carrie Devieux, and Pete Swan. Overview of IRIDIUM satellite network. In *Proceedings of WESCON'95*, page 483. IEEE, 1995.

[MIM] Tag:mimo. `http://teletopix.org/tag/mimo/page/2/`.

[MRH+17] Andreas F Molisch, Vishnu V Ratnam, Shengqian Han, Zheda Li, Sinh Le Hong Nguyen, Linsheng Li, and Katsuyuki Haneda. Hybrid beamforming for massive mimo: A survey. *IEEE Communications magazine*, 55(9):134–141, 2017.

[MSS+17] Jun Mashino, Kei Satoh, Satoshi Suyama, Yuki Inoue, and Yukihiko Okumura. 5G experimental trial of 28 GHz band super

wideband transmission using beam tracking in super high mobility environment. In *2017 IEEE 85th Vehicular Technology Conference (VTC Spring)*, pages 1–5. IEEE, 2017.

[MZSS16] Guowang Miao, Jens Zander, Ki Won Sung, and Slimane Ben Slimane. *Fundamentals of mobile data networks*. Cambridge University Press, 2016.

[NCCD20] Boyu Ning, Zhi Chen, Wenrong Chen, and Yiming Du. Channel estimation and transmission for intelligent reflecting surface assisted thz communications. In *ICC 2020-2020 IEEE International Conference on Communications (ICC)*, pages 1–7. IEEE, 2020.

[NKC+19] Qurrat-Ul-Ain Nadeem, Abla Kammoun, Anas Chaaban, Merouane Debbah, and Mohamed-Slim Alouini. Intelligent reflecting surface assisted wireless communication: Modeling and channel estimation. *arXiv preprint arXiv:1906.02360*, 2019.

[NMO+20] Nobuhide Nonaka, Kazushi Muraoka, Tatsuki Okuyama, Satoshi Suyama, Yukihiko Okumura, Takahiro Asai, and Yoshihiro Matsumura. 28 GHz-band experimental trial at 283 km/h using the shinkansen for 5G evolution. In *2020 IEEE 91st Vehicular Technology Conference (VTC2020-Spring)*, pages 1–5. IEEE, 2020.

[NYE13] Payam Nayeri, Fan Yang, and Atef Z Elsherbeni. Bifocal design and aperture phase optimizations of reflectarray antennas for wide-angle beam scanning performance. *IEEE Transactions on Antennas and Propagation*, 61(9):4588–4597, 2013.

[Oct] Octoclock-g cda-2990. `https://www.ettus.com/all-products/octoclock-g/`.

[OIA+16] Tatsunori Obara, Yuki Inoue, Yuuichi Aoki, Satoshi Suyama, Jaekon Lee, and Yukihiko Okumurav. Experiment of 28 GHz band 5G super wideband transmission using beamforming and beam tracking in high mobility environment. In *2016 IEEE 27th annual international symposium on personal, indoor, and mobile radio communications (PIMRC)*, pages 1–5. IEEE, 2016.

[OOA+15] Tatsunori Obara, Tatsuki Okuyama, Yuuichi Aoki, Satoshi Suyama, Jaekon Lee, and Yukihiko Okumura. Indoor and outdoor

experimental trials in 28-GHz band for 5G wireless communication systems. In *2015 IEEE 26th Annual International Symposium on Personal, Indoor, and Mobile Radio Communications (PIMRC)*, pages 846–850. IEEE, 2015.

[OSAA19] Aymen Omri, Mohammed Shaqfeh, Abdelmohsen Ali, and Hussein Alnuweiri. Synchronization procedure in 5G NR systems. *IEEE Access*, 7:41286–41295, 2019.

[PGD17] Sohail Payami, Mir Ghoraishi, and Mehrdad Dianati. Hybrid beamforming for downlink massive mimo systems with multiantenna user equipment. In *2017 IEEE 86th Vehicular Technology Conference (VTC-Fall)*, pages 1–5. IEEE, 2017.

[pow] What's my cell signal strength? `https://powerfulsignal.com/cell-signal-strength/`.

[PS01] John G Proakis and Masoud Salehi. *Digital communications*, volume 4. McGraw-hill New York, 2001.

[PYT+21] Xilong Pei, Haifan Yin, Li Tan, Lin Cao, Zhanpeng Li, Kai Wang, Kun Zhang, and Emil Björnson. Ris-aided wireless communications: Prototyping, adaptive beamforming, and indoor/outdoor field trials. *IEEE Transactions on Communications*, 69(12):8627–8640, 2021.

[PYXL20] Xiaotian Pan, Fan Yang, Shenheng Xu, and Maokun Li. A 10240-Element Reconfigurable Reflectarray with Fast Steerable Monopulse Patterns. *IEEE Transactions on Antennas and Propagation*, 2020.

[QRH] Qrh40. `https://www.rfspin.com/product/qrh40/`.

[RCS+10] Colan GM Ryan, Mohammad Reza Chaharmir, JRBJ Shaker, Joey R Bray, Yahia MM Antar, and A Ittipiboon. A wideband transmitarray using dual-resonant double square rings. *IEEE Transactions on Antennas and Propagation*, 58(5):1486–1493, 2010.

[Roe09] Antoine G Roederer. Reflectarray antennas. In *2009 3rd European Conference on Antennas and Propagation*, pages 18–22. IEEE, 2009.

[RPS+18] Vasanthan Raghavan, Andrzej Partyka, Ashwin Sampath, Sundar Subramanian, Ozge Hizir Koymen, Kobi Ravid, Juergen

Cezanne, Kiran Mukkavilli, and Junyi Li. Millimeter-wave mimo prototype: Measurements and experimental results. *IEEE Communications Magazine*, 56(1):202–209, 2018.

[RWQL17] Yuwei Ren, Yingmin Wang, Can Qi, and Yinjun Liu. Multiple-beam selection with limited feedback for hybrid beamforming in massive mimo systems. *IEEE Access*, 5:13327–13335, 2017.

[SR15] Jaspreet Singh and Sudhir Ramakrishna. On the feasibility of codebook-based beamforming in millimeter wave systems with multiple antenna arrays. *IEEE transactions on Wireless Communications*, 14(5):2670–2683, 2015.

[SSBZ13] Christian Sturm, Yoke Leen Sit, Martin Braun, and Thomas Zwick. Spectrally interleaved multi-carrier signals for radar network applications and multi-input multi-output radar. *IET Radar, Sonar & Navigation*, 7(3):261–269, 2013.

[ST12] Warren L Stutzman and Gary A Thiele. *Antenna theory and design*. John Wiley & Sons, 2012.

[Stu95] Mark A Sturza. Architecture of the TELEDESIC satellite system. In *Proceedings of the International Mobile Satellite Conference*, volume 95, page 214, 1995.

[TCC+20] Wankai Tang, Ming Zheng Chen, Xiangyu Chen, Jun Yan Dai, Yu Han, Marco Di Renzo, Yong Zeng, Shi Jin, Qiang Cheng, and Tie Jun Cui. Wireless communications with reconfigurable intelligent surface: Path loss modeling and experimental measurement. *IEEE Transactions on Wireless Communications*, 20(1):421–439, 2020.

[TDC+19] Wankai Tang, Jun Yan Dai, Mingzheng Chen, Xiang Li, Qiang Cheng, Shi Jin, Kai-Kit Wong, and Tie Jun Cui. Programmable metasurface-based rf chain-free 8psk wireless transmitter. *Electronics Letters*, 55(7):417–420, 2019.

[TLD+19] Wankai Tang, Xiang Li, Jun Yan Dai, Shi Jin, Yong Zeng, Qiang Cheng, and Tie Jun Cui. Wireless communications with programmable metasurface: Transceiver design and experimental results. *China Communications*, 16(5):46–61, 2019.

[TSJP16] Xin Tan, Zhi Sun, Josep M Jornet, and Dimitris Pados. Increasing indoor spectrum sharing capacity using smart reflect-array.

In *2016 IEEE International Conference on Communications (ICC)*, pages 1–6. IEEE, 2016.

[USR] Usrp x310. https://www.ettus.com/all-products/x310-kit/.

[WCLC13] Sau-Hsuan Wu, Lin-Kai Chiu, Ko-Yen Lin, and Tsung-Hui Chang. Robust hybrid beamforming with phased antenna arrays for downlink sdma in indoor 60 GHz channels. *IEEE transactions on wireless communications*, 12(9):4542–4557, 2013.

[WLW18] Lili Wei, Qian Clara Li, and Geng Wu. Initial access techniques for 5G nr: Omni/beam sync and rach designs. In *2018 International Conference on Computing, Networking and Communications (ICNC)*, pages 249–253. IEEE, 2018.

[WQCC16] Xiang Wan, Mei Qing Qi, Tian Yi Chen, and Tie Jun Cui. Field-programmable beam reconfiguring based on digitally-controlled coding metasurface. *Scientific reports*, 6(1):1–8, 2016.

[WXZ+21] Xiang Wan, Qiang Xiao, Ying Zhe Zhang, Yueheng Li, Joerg Eisenbeis, Jia Wei Wang, Zi Ai Huang, Han Xiao Liu, Thomas Zwick, and Tie Jun Cui. Reconfigurable sum and difference beams based on a binary programmable metasurface. *IEEE Antennas and Wireless Propagation Letters*, 20(3):381–385, 2021.

[WZC+19] Xiang Wan, Qian Zhang, Tian Yi Chen, Lei Zhang, Wei Xu, He Huang, Chao Kun Xiao, Qiang Xiao, and Tie Jun Cui. Multichannel direct transmissions of near-field information. *Light: Science & Applications*, 8(1):1–8, 2019.

[Xio06] Fuqin Xiong. *Digital Modulation Techniques, (Artech House Telecommunications Library)*. Artech House, Inc., 2006.

[YCY+16] Huanhuan Yang, Xiangyu Cao, Fan Yang, Jun Gao, Shenheng Xu, Maokun Li, Xibi Chen, Yi Zhao, Yuejun Zheng, and Sijia Li. A programmable metasurface with dynamic polarization, scattering and focusing control. *Scientific reports*, 6(1):1–11, 2016.

[YYE+10] Ang Yu, Fan Yang, Atef Z Elsherbeni, John Huang, and Yahya Rahmat-Samii. Aperture efficiency analysis of reflectarray antennas. *Microwave and Optical Technology Letters*, 52(2):364–372, 2010.

[YYX+16] Huanhuan Yang, Fan Yang, Shenheng Xu, Yilin Mao, Maokun Li, Xiangyu Cao, and Jun Gao. A 1-Bit 10 x 10 Reconfigurable Reflectarray Antenna: Design, Optimization, and Experiment. *IEEE Transactions on Antennas and Propagation*, 64(6):2246–2254, 2016.

[YZZ20] Changsheng You, Beixiong Zheng, and Rui Zhang. Wireless communication via double irs: Channel estimation and passive beamforming designs. *IEEE Wireless Communications Letters*, 10(2):431–435, 2020.

[ZAM+18] Ali Zaidi, Fredrik Athley, Jonas Medbo, Ulf Gustavsson, Giuseppe Durisi, and Xiaoming Chen. *5G Physical Layer: principles, models and technology components*. Academic Press, 2018.

[ZCL+18] Lei Zhang, Xiao Qing Chen, Shuo Liu, Qian Zhang, Jie Zhao, Jun Yan Dai, Guo Dong Bai, Xiang Wan, Qiang Cheng, Giuseppe Castaldi, et al. Space-time-coding digital metasurfaces. *Nature communications*, 9(1):1–11, 2018.

[ZLG+21] Shun Zhang, Yushan Liu, Feifei Gao, Chengwen Xing, Jianping An, and Octavia A Dobre. Deep learning based channel extrapolation for large-scale antenna systems: Opportunities, challenges and solutions. *IEEE Wireless Communications*, 2021.

[ZLS+19a] Deyou Zhang, Ang Li, Mahyar Shirvanimoghaddam, Peng Cheng, Yonghui Li, and Branka Vucetic. Codebook-based training beam sequence design for millimeter-wave tracking systems. *IEEE Transactions on Wireless Communications*, 18(11):5333–5349, 2019.

[ZLS+19b] Deyou Zhang, Ang Li, Mahyar Shirvanimoghaddam, Yonghui Li, and Branka Vucetic. Exploring aoa/aod dynamics in beam alignment of mobile millimeter wave mimo systems. *IEEE Transactions on Vehicular Technology*, 68(6):6172–6176, 2019.

[ZSW+20] Hanting Zhao, Ya Shuang, Menglin Wei, Tie Jun Cui, Philipp Del Hougne, and Lianlin Li. Metasurface-assisted massive backscatter wireless communication with commodity wi-fi signals. *Nature communications*, 11(1):1–10, 2020.

[ZYD+19] Jie Zhao, Xi Yang, Jun Yan Dai, Qiang Cheng, Xiang Li, Ning Hua Qi, Jun Chen Ke, Guo Dong Bai, Shuo Liu, Shi Jin,

et al. Programmable time-domain digital-coding metasurface for non-linear harmonic manipulation and new wireless communication systems. *National Science Review*, 6(2):231–238, 2019.

[ZZL+19] Ruoqiao Zhang, Jianyi Zhou, Ji Lan, Binqi Yang, and Zhiqiang Yu. A high-precision hybrid analog and digital beamforming transceiver system for 5G millimeter-wave communication. *IEEE Access*, 7:83012–83023, 2019.

Publication List

Journals

1. **Li, Y.**, Eisenbeis, J., Wan, X., Bettinga, S., Long, X., Alabd, M. B., ... & Zwick, T. (2021). A programmable-metasurface-based TDMA fast beam switching communication system at 28 GHz. *IEEE Antennas and Wireless Propagation Letters*, 20(5), 658-662.
2. **Li, Y.**, Bettinga, S., Eisenbeis, J., Kowalewski, J., Wan, X., Long, X., ... & Zwick, T. (2021). Beamsteering for 5g mobile communication using programmable metasurface. *IEEE Wireless Communications Letters*, 10(7), 1542-1546.
3. **Li, Y.**, Long, X., de Oliveira, L. G., Eisenbeis, J., Alabd, M. B., Bettinga, S., ... & Zwick, T. (2022). Programmable Metasurface Hybrid MIMO Beamforming: Channel Estimation, Data Transmission, and System Implementations at 28 GHz. *IEEE Systems Journal*.
4. **Li, Y.**, Bettinga, S., de Oliveira, L. G., Eisenbeis, J., Alabd, M. B., ... & Zwick, T. (2022). Predictive Tracking Implementation for Mobile Communication Using Programmable Metasurface. *Manuscript accepted by IEEE China Communications*.
5. Giroto de Oliveira, L., Antes, T., Nuss, B., Bekker, E., Bhutani, A., **Li, Y.** Diewald, A., ... & Zwick, T. (2022). Doppler shift tolerance of typical pseudorandom binary sequences in PMCW radar. *Sensors*, 22(9), 3212.
6. Alabd, M. B., Nuss, B., de Oliveira, L. G., Diewald, A., **Li, Y.**, & Zwick, T. (2022). Modified Pulse Position Modulation for Joint Radar Communication Based on Chirp Sequence. *IEEE Microwave and Wireless Components Letters.*
7. Wan, X., Xiao, C., Huang, H., Xiao, Q., Xu, W., **Li, Y.**, ... & Cui, T. (2022). Joint modulations of electromagnetic waves and digital signals on a single metasurface platform to reach programmable wireless communications. *Engineering*, 8, 86-95.

8. Eisenbeis, J., Pfaff, J., Karg, C., Kowalewski, J., **Li, Y.**, Pauli, M., & Zwick, T. (2020). Beam pattern optimization method for subarray-based hybrid beamforming systems. *Wireless Communications and Mobile Computing*, 2020.
9. Eisenbeis, J., **Li, Y.**, Kowalewski, J., Kretschmann, M., & Zwick, T. (2020). Analog 28 GHz LOS MIMO relay system using a 90° hybrid coupler. *IEEE Antennas and Wireless Propagation Letters*, 19(4), 571-575.
10. Wan, X., Xiao, Q., Zhang, Y. Z., **Li, Y.**, Eisenbeis, J., Wang, J. W., ... & Cui, T. J. (2021). Reconfigurable sum and difference beams based on a binary programmable metasurface. *IEEE Antennas and Wireless Propagation Letters*, 20(3), 381-385.

Conferences

1. **Li, Y.**, Long, X., Wan, X., Eisenbeis, J., Bettinga, S., Cui, T., & Zwick, T. (2021, December). Realization of Efficient Channel Estimation using Programmable Metasurface. *In 2021 IEEE USNC-URSI Radio Science Meeting (Joint with AP-S Symposium) (pp. 66-67). IEEE.*
2. **Li, Y.**, Eisenbeis, J., Kowalewski, J., Wan, X., Long, X., Jozwicka, M., ... & Zwick, T. (2021, March). Ka-band programmable metasurface demonstrations in wireless communication scenarios. *In 2021 15th European Conference on Antennas and Propagation (EuCAP) (pp. 1-5). IEEE.*
3. **Li, Y.**, Eisenbeis, J., Michev, R., Alabd, M. B., & Zwick, T. (2020, March). Measurement-based misalignment analysis of dual-polarized 2× 2 los mimo system at 28 ghz. *In 2020 German Microwave Conference (GeMiC) (pp. 152-155). IEEE.*
4. **Li, Y.**, Wan, X., Eisenbeis, J., Long, X., Jozwicka, M., Cui, T., & Zwick, T. (2020, September). A novel wireless communication system using programmable metasurface operating at 28 GHz. *In 2020 International Conference on Microwave and Millimeter Wave Technology (ICMMT) (pp. 1-3). IEEE.*
5. Eisenbeis, J., **Li, Y.** , López, P. R., Fischer, J., & Zwick, T. (2019, March). Comparison of hybrid beamforming systems using phase shifters and

switches. *In 2019 12th German Microwave Conference (GeMiC) (pp. 40-43). IEEE.*

6. de Oliveira, L. G., Nuss, B., Alabd, M. B., **Li, Y.**, Yu, L., & Zwick, T. (2021, March). MIMO-OCDM-based joint radar sensing and communication. *In 2021 15th European Conference on Antennas and Propagation (EuCAP) (pp. 1-5). IEEE.*